



# Fast Determination of Soil Behavior in the Capillary Zone Using Simple Laboratory Tests

**Xiong Xhang, Ph.D., P.E.**

**Lin Li, Graduate Student**

*University of Alaska Fairbanks*

**Robert L. Lytton, Ph.D**

*Texas A&M Univeristy*

**December 2012**

**Prepared By:**

**Alaska University Transportation Center  
Duckering Building Room 245  
P.O. Box 755900  
Fairbanks, AK 99775-5900**

**Zachry Department of Civil Engineering  
Texas A&M University  
3136 TAMU  
College Station, TX 77843-3136**

**INE/AUTC 13.14**

**REPORT DOCUMENTATION PAGE**

Form approved OMB No.

Public reporting for this collection of information is estimated to average 1 hour per response, including the time for reviewing instructions, searching existing data sources, gathering and maintaining the data needed, and completing and reviewing the collection of information. Send comments regarding this burden estimate or any other aspect of this collection of information, including suggestion for reducing this burden to Washington Headquarters Services, Directorate for Information Operations and Reports, 1215 Jefferson Davis Highway, Suite 1204, Arlington, VA 22202-4302, and to the Office of Management and Budget, Paperwork Reduction Project (0704-1833), Washington, DC 20503

1. AGENCY USE ONLY (LEAVE BLANK)

2. REPORT DATE

3. REPORT TYPE AND DATES COVERED

December 2012

4. TITLE AND SUBTITLE

**Fast Determination of Soil Behavior in the Capillary Zone Using Simple Laboratory Tests**

5. FUNDING NUMBERS

DTRT06-G-0011  
AUTC# 410025

6. AUTHOR(S)

Xiong Zhang, Ph.D., P.E. and Lin Li, Graduate Student, University of Alaska Fairbanks  
Robert L. Lytton, Ph.D, Texas A&M University

7. PERFORMING ORGANIZATION NAME(S) AND ADDRESS(ES)

Alaska University Transportation Center  
P.O. Box 755900  
Fairbanks, AK 99775-5900

8. PERFORMING ORGANIZATION REPORT NUMBER

INE/AUTC 13.14

9. SPONSORING/MONITORING AGENCY NAME(S) AND ADDRESS(ES)

Research and Innovative Technology Administration (RITA) (USDOT)  
1200 New Jersey Ave, SE, Washington DC 20590  
Zachry Department of Civil Engineering, Texas A&M University  
3136 TAMU, College Station, TX 77843-3136

10. SPONSORING/MONITORING AGENCY REPORT NUMBER

11. SUPPLEMENTARY NOTES

12a. DISTRIBUTION / AVAILABILITY STATEMENT

No restrictions

12b. DISTRIBUTION CODE

13. ABSTRACT (Maximum 200 words)

Frost heave and thaw weakening are typical problems for engineers building in northern regions. These unsaturated-soil behaviors are caused by water flowing through the capillary zone to a freezing front, where it forms ice lenses. Although suction-controlled tests are the standard for characterizing unsaturated soils, such testing is too laborious, time-consuming, and costly for routine engineering projects. Characterizing the stress/strain behavior for only one unsaturated soil can take up to three years, and moisture content measurements are unreliable. This research team seeks to develop a method for rapidly determining and analyzing unsaturated soil behavior through a new approach, the Modified A shake table model of a single pipe embedded in a frozen silt layer overlying a liquefiable sand layer adjacent to a river channel. In these experiments, the loads induced on the bridge foundations by unfrozen and frozen ground crust will be measured from two shake table tests by means of strain gauges. State Surface Approach. The MSSA can potentially reduce the time required to characterize unsaturated soils to a few weeks, as well as provide more reliable measurements and more representative soil behavior. If successful, this research will produce a useful tool for geotechnical engineers, allowing fast, practical, and more comprehensive soil characterization for more complicated soil behavior problems.

14. KEYWORDS: Frost heaving (Jbyfh), Frost heaving soils (Rbespfd), Soil stabilization (Fcbys)

15. NUMBER OF PAGES

16. PRICE CODE

N/A

17. SECURITY CLASSIFICATION OF REPORT

Unclassified

18. SECURITY CLASSIFICATION OF THIS PAGE

Unclassified

19. SECURITY CLASSIFICATION OF ABSTRACT

Unclassified

20. LIMITATION OF ABSTRACT

N/A

### **Notice**

This document is disseminated under the sponsorship of the U.S. Department of Transportation in the interest of information exchange. The U.S. Government assumes no liability for the use of the information contained in this document.

The U.S. Government does not endorse products or manufacturers. Trademarks or manufacturers' names appear in this report only because they are considered essential to the objective of the document.

### **Quality Assurance Statement**

The Federal Highway Administration (FHWA) provides high-quality information to serve Government, industry, and the public in a manner that promotes public understanding. Standards and policies are used to ensure and maximize the quality, objectivity, utility, and integrity of its information. FHWA periodically reviews quality issues and adjusts its programs and processes to ensure continuous quality improvement.

### **Author's Disclaimer**

Opinions and conclusions expressed or implied in the report are those of the author. They are not necessarily those of the Alaska DOT&PF or funding agencies.

# SI\* (MODERN METRIC) CONVERSION FACTORS

## APPROXIMATE CONVERSIONS TO SI UNITS

Symbol	When You Know	Multiply By	To Find	Symbol
<b>LENGTH</b>				
in	inches	25.4	millimeters	mm
ft	feet	0.305	meters	m
yd	yards	0.914	meters	m
mi	miles	1.61	kilometers	km
<b>AREA</b>				
in <sup>2</sup>	square inches	645.2	square millimeters	mm <sup>2</sup>
ft <sup>2</sup>	square feet	0.093	square meters	m <sup>2</sup>
yd <sup>2</sup>	square yard	0.836	square meters	m <sup>2</sup>
ac	acres	0.405	hectares	ha
mi <sup>2</sup>	square miles	2.59	square kilometers	km <sup>2</sup>
<b>VOLUME</b>				
fl oz	fluid ounces	29.57	milliliters	mL
gal	gallons	3.785	liters	L
ft <sup>3</sup>	cubic feet	0.028	cubic meters	m <sup>3</sup>
yd <sup>3</sup>	cubic yards	0.765	cubic meters	m <sup>3</sup>
NOTE: volumes greater than 1000 L shall be shown in m <sup>3</sup>				
<b>MASS</b>				
oz	ounces	28.35	grams	g
lb	pounds	0.454	kilograms	kg
T	short tons (2000 lb)	0.907	megagrams (or "metric ton")	Mg (or "t")
<b>TEMPERATURE (exact degrees)</b>				
°F	Fahrenheit	5 (F-32)/9 or (F-32)/1.8	Celsius	°C
<b>ILLUMINATION</b>				
fc	foot-candles	10.76	lux	lx
fl	foot-Lamberts	3.426	candela/m <sup>2</sup>	cd/m <sup>2</sup>
<b>FORCE and PRESSURE or STRESS</b>				
lbf	poundforce	4.45	newtons	N
lbf/in <sup>2</sup>	poundforce per square inch	6.89	kilopascals	kPa
<b>APPROXIMATE CONVERSIONS FROM SI UNITS</b>				
Symbol	When You Know	Multiply By	To Find	Symbol
<b>LENGTH</b>				
mm	millimeters	0.039	inches	in
m	meters	3.28	feet	ft
m	meters	1.09	yards	yd
km	kilometers	0.621	miles	mi
<b>AREA</b>				
mm <sup>2</sup>	square millimeters	0.0016	square inches	in <sup>2</sup>
m <sup>2</sup>	square meters	10.764	square feet	ft <sup>2</sup>
m <sup>2</sup>	square meters	1.195	square yards	yd <sup>2</sup>
ha	hectares	2.47	acres	ac
km <sup>2</sup>	square kilometers	0.386	square miles	mi <sup>2</sup>
<b>VOLUME</b>				
mL	milliliters	0.034	fluid ounces	fl oz
L	liters	0.264	gallons	gal
m <sup>3</sup>	cubic meters	35.314	cubic feet	ft <sup>3</sup>
m <sup>3</sup>	cubic meters	1.307	cubic yards	yd <sup>3</sup>
<b>MASS</b>				
g	grams	0.035	ounces	oz
kg	kilograms	2.202	pounds	lb
Mg (or "t")	megagrams (or "metric ton")	1.103	short tons (2000 lb)	T
<b>TEMPERATURE (exact degrees)</b>				
°C	Celsius	1.8C+32	Fahrenheit	°F
<b>ILLUMINATION</b>				
lx	lux	0.0929	foot-candles	fc
cd/m <sup>2</sup>	candela/m <sup>2</sup>	0.2919	foot-Lamberts	fl
<b>FORCE and PRESSURE or STRESS</b>				
N	newtons	0.225	poundforce	lbf
kPa	kilopascals	0.145	poundforce per square inch	lbf/in <sup>2</sup>

\*SI is the symbol for the International System of Units. Appropriate rounding should be made to comply with Section 4 of ASTM E380.  
(Revised March 2003)

## **ACKNOWLEDGMENTS**

The authors wish to express their appreciation to the AKDOT&PF for their support throughout this study, as well as Alaska University Transportation Center (AUTC). The authors would also like to thank Eric's Machine shop for the help on the test equipment modification and Andy Chamberlain for his contribution on lab testing.

## EXECUTIVE SUMMARY

Frost heave and thaw weakening are typical problems in northern regions. It is well known that frost heave is caused by water flow through capillary zone to a freezing front where it forms ice lenses (Guymon et al. 1984; 1993; Henry and Holtz 2001; Henry and Stormont 2002) and the s. Investigation of soil behavior in the capillary zone is in the range of unsaturated soil mechanics and the unsaturated transmission of water is the key to understand the frost heave problem.

Bishop and Donald (1961) developed the first suction controlled triaxial test apparatus for testing on unsaturated soils. Since then, suction controlled tests have been extensively used and now have become a standard for characterization of unsaturated soil behavior (Delage 2003). Most important concepts for unsaturated soil mechanics were developed based upon results from suction controlled tests. However, tests for unsaturated soils are usually laborious, time-consuming, costly, and may not be justifiable for routine engineering projects. Due to the lengthy testing process, the test results, especially for the water content change, are not reliable or simply not available. The lack of reliable experimental data has posed great difficulties in developing coupled hydro-mechanical models for unsaturated soils.

The objective of this proposed research was to develop a method to rapidly determine and analyze the unsaturated soil behavior. In this study, a new image based method was developed by integrating photogrammetry, optical-ray tracing, and least square estimation techniques to measurement the total and localized volume change during triaxial testing. High-suction tensiometers were developed for measuring suction changes in undrained compression tests for unsaturated soils. Locally available Fairbanks silt was used for the undrained isotropic compression and shear tests to characterize the constitutive behavior of the soil. The test results were used for constitutive modeling of the elasto-plastic behavior for the soil based upon the Modified State Surface Approach recently developed by the PIs (Zhang and Lytton 2007a, 2007b, 2008, 2009a, 2009b, 2009c, 2009d, and 2009e).

It was proved that this new method allows the use of conventional triaxial testing apparatus for saturated soils for the testing on unsaturated soils. The new approach can reduce the testing time required to characterize behavior for unsaturated soils

from approximately two to three years to a couple of weeks with more reliable measurement and more representative soil behavior.

## TABLE OF CONTENTS

Disclaimer .....	i
Acknowledgements .....	ii
Executive Summary .....	iii
Table of Contents .....	vi
List of Figures .....	viii
List of Tables .....	xii
List of Appendices .....	xii

### CHAPTER

I INTRODUCTION.....	1
General.....	1
Research Objectives.....	2
Research Methodology .....	2
II LITERATURE REVIEW .....	6
General.....	6
Triaxial Testing on Unsaturated Soils .....	6
<i>Volume Measurement Methods</i> .....	8
<i>High-suction Tensiometer</i> .....	26
Constitutive Modeling of Unsaturated soils .....	36
III DEVELOPMENT OF A NEW VOLUME MEASUREMENT METHOD .....	47
General.....	47
Principle of Photogrammetry.....	48
Optical-ray Tracing Technique.....	52
Proposed Method .....	54
<i>Camera Calibration</i> .....	55
<i>Triaxial System Setup</i> .....	57
<i>Image Capturing and Orientation</i> .....	59
<i>3D Reconstruction of Acrylic Cell</i> .....	60
<i>Refraction Correction</i> .....	62
<i>Least Square Optimization</i> .....	64
Method validation.....	65
<i>Validation on Stainless Steel Cylinder</i> .....	66
<i>Validation on Saturated Sand Specimen</i> .....	74
Error Sources .....	77
Differences from Existing Image Based Methods.....	79
Conclusions .....	82
IV DEVELOPMENT OF A NEW HIGH-SUCTION TENSIO METER .....	84

General.....	84
High-suction Tensiometer Fabrication.....	84
High-suction Tensiometer Saturation.....	92
High-suction Tensiometer Calibration.....	93
Maximum Attainable Suction.....	95
Conclusions.....	96
V RESEARCH PROGRAMME AND PRESENTATION OF TEST RESULTS ..	97
General.....	97
Sample Preparation.....	97
<i>Soil Properties</i> .....	99
<i>Specimen Compaction and Moisture Equalization</i> .....	100
SWCC.....	101
Triaxial Testing.....	105
Presentation of Test Results.....	112
<i>Soil Water Retaining Curve</i> .....	112
<i>Undrained Isotropic Compression Test Results</i> .....	115
<i>Undrained Shear Test Results</i> .....	123
VI CONSTITUTIVE MODELLING .....	128
General.....	128
Modified State Surface Approach .....	134
Analysis of an Undrained Test Using MSSA .....	137
Determining Parameter Values in BBM by Combining the MSSA and Newton Method .....	139
VII CONCLUSIONS AND RECOMMENDATIONS .....	139
Conclusions .....	139
Recommendations .....	140
REFERENCES .....	143
APPENDICES .....	156

## LIST OF FIGURES

Figure		Page
2.1	Schematic plot of suction controlled triaxial apparatus.....	7
2.2	Triaxial test apparatus for saturated soils .....	8
2.3	Double-wall cell method.....	10
2.4	GCTS differential pressure transducer.....	11
2.5	Test apparatuses used by Zhang et al.....	11
2.6	Air pressure/volume controller.....	13
2.7	Configuration of the test equipment with GDS air pressure/volume controller....	13
2.8	Local strain transducers from GDS.....	14
2.9	Setup for LVDT method.....	15
2.10	Axial strain measurements for LVDT method.....	15
2.11	Radial strain measurements for LVDT method.....	16
2.12	Schematic plot of the laser scanner method.....	17
2.13	Laser scanner method setup.....	17
2.14	Pinhole camera model.....	18
2.15	Two-dimensional system model.....	19
2.16	Volume measurement based on images.....	20
2.17	2D image based method.....	20
2.18	Setup on soil specimen for local strain measurement.....	21
2.19	Schematic plot of the system setup for X-ray CT method.....	23
2.20	System setup for X-ray CT method.....	23
2.21	A horizontal CT slice.....	24
2.22	DIC pixel subset matching.....	26
2.23	Configuration of the 3D DIC method.....	26
2.24	Tensile strength of water.....	28
2.25	Schematic plot of the tensiometer developed by Ridley and Burland.....	30
2.26	Tensiometer developed by Ridley and Burland.....	31
2.27	Tensiometer saturation device.....	31
2.28	Inside of the tensiometer saturation device.....	32
2.29	Tensiometer developed by Guan and Fredlund.....	33
2.30	Tensiometer and saturation cup by Guan.....	33

2.31	Tensiometer developed by Meilani et al	34
2.32	Tensiometer developed by Tarantino and Mongiovi	35
2.33	Tensiometer developed by Take and Bolton	35
2.34	Tensiometer developed by Lourenco et al	35
2.35	Experimental tests establishing the concept of state surface	37
2.36	Suggested stress paths to determine model parameters for the BBM	39
2.37	Typical isotropic compression tests	40
2.38	Drying-wetting test results ( $s = s_0 = \text{constant}$ )	41
2.39	Wetting collapse tests	41
2.40	Idealized results for wetting collapse of a soil	42
2.41	Yield surface in the p-q-s space in the BBM	43
3.1	Principle of the Photogrammetry	48
3.2	Coordinate systems	49
3.3	Snell's law	53
3.4	Lens distortion	55
3.5	Calibration targets (from Photomodeler)	56
3.6	Testing system setup	58
3.7	Typical camera stations	60
3.8	Deformation of confining chamber under pressure	61
3.9	Optical-ray tracing based on Snell's law	62
3.10	Camera and lens	65
3.11	System setup	67
3.12	Cell deformation due to applied confining pressure	69
3.13	3D coordinates of the targets on specimen surface	70
3.14	3D coordinates comparison for the 16 cross sections	71
3.15	Membrane and sand used for specimen preparation	75
3.16	Comparison of volume change	76
3.17	Soil deformations under shear load	77
4.1	EPXO pressure transducer	85
4.2	Principle of pressure measurement based on Wheastone Bridge	85
4.3	Schematic plot of the tensiometer	86
4.4	Preparation for tensiometer fabrication	87
4.5	Tensiometer fabrication	89

4.6	Layout of the stainless steel ring.....	89
4.7	Grommet fabrication by using silicone rubber.....	91
4.8	High-suction Tensiometer.....	92
4.9	Tensiometers installation.....	93
4.10	Calibration results of two tensiometers.....	95
4.11	Maximum attainable pressures.....	96
5.1	Location of the used Fairbanks silt.....	98
5.2	Fairbanks silt.....	98
5.3	Particle size distribution of Fairbanks silt.....	99
5.4	Compaction curve.....	99
5.5	Specimen preparation.....	101
5.6	Pressure plate test for determination of SWCC.....	103
5.7	Use of salt solution for determination of SWCC.....	104
5.8	Testing system from GCTS.....	106
5.9	Membrane mounting on specimen.....	107
5.10	Tensiometer installation.....	107
5.11	Triaxial test setup.....	108
5.12	Isotropic loading paths.....	110
5.13	Soil specimen after testing.....	112
5.14	SWCC of Fairbanks silt.....	113
5.15	Soil water retaining curve under different confining stresses.....	113
5.16	Soil suction equalization during isotropic compression and shear test.....	116
5.17	Tensiometer response to sudden increase or decrease of confining pressure.....	118
5.18	Suction changes due to variation of net confining stress.....	119
5.19	Volume change due to variation of net confining stress under different water contents.....	120
5.20	Casagrande method for determination of yield stresses.....	121
5.21	Yield stresses based on Casagrande method.....	122
5.22	Suction changes due to variation of volume.....	122
5.23	Deviator stress versus axial strain under different moisture conditions.....	124
5.24	Specific volume change versus axial strain under different moisture conditions.....	125
5.25	Change of matric suction under different strain levels.....	126

5.26	Change of matric suction due to shear loading under different moisture conditions.....	127
6.1	Principle of the MSSA.....	6
6.2	Shape of the state boundary surface for the BBM.....	6
6.3	Analysis of an undrained test using the MSSA.....	6
6.4	Analysis of multiple undrained tests with identical stress histories.....	6
6.5	Analysis of multiple undrained tests with different stress histories.....	6
A.1	Container with and without water.....	6

## LIST OF TABLES

Table		Page
3.1	Camera calibration parameters.....	66
3.2	Measurement accuracy under different confining pressures.....	71
3.3	Measurement accuracy under shear load.....	76
4.1	Tensiometer calibration.....	94
5.1	Soil properties of Fairbanks silt.....	100
5.2	Osmotic suction for several salt solutions.....	105
5.3	Loading paths for specimens with different initial suctions.....	111
B.1	Camera stations.....	1
B.2	3D coordinates for measurement points on cell wall.....	1
B.3	Regression parameters for acrylic cell wall.....	1
B.4	Point information on each corresponding image.....	1
B.5	First optical-ray tracing (air to acrylic cell) results.....	1
B.6	Second optical-ray tracing (air to acrylic cell) results.....	1
B.7	Least square estimation for the point.....	1

**LIST OF APPENDICES**

	Page
Appendix A.....	80
Appendix B.....	80

## **CHAPTER I**

### **INTRODUCTION**

#### **GENERAL**

Frost heave and thaw weakening are typical problems in northern regions. It is well known that frost heave is caused by water flow through capillary zone to a freezing front where it forms ice lenses (Guymon et al. 1984; 1993; Henry and Holtz 2001; Henry and Stormont 2002) and the s. Investigation of soil behavior in the capillary zone is in the range of unsaturated soil mechanics and the unsaturated transmission of water is the key to understand the frost heave problem.

Since Bishop and Donald developed the first suction controlled triaxial test apparatus, suction controlled tests have been extensively used and now have become a standard for characterization of unsaturated soil behavior. Most important concepts for unsaturated soil mechanics were developed based upon results from suction controlled tests. However, suction controlled tests are too laborious, time-consuming, and costly, and cannot be justified for routine engineering projects. It is not uncommon to take months or 2-3 years to characterize the stress-strain behavior for one unsaturated soil. In addition, measurements of soil behavior are very unreliable and might be incorrect.

The objective of this proposed research was to develop a method to rapidly determine and analyze the unsaturated soil behavior. The research was based on the Modified State Surface Approach, which is recently developed by the PIs (Zhang and Lytton 2007a, 2007b, 2008, 2009a, 2009b, 2009c, 2009d, and 2009e), to investigate the unsaturated soil behavior.

#### **RESEARCH OBJECTIVES**

The main objectives of this project were to, 1) develop a triaxial test apparatus with suction measurement ability, 2) systematically study the behavior of silty soils in Alaska under undrained conditions, 3) validate the concept that simple undrained

loading tests can be used as an alternative to suction-controlled triaxial tests to investigate unsaturated soil behavior.

## **RESEARCH METHODOLOGY**

To meet the objectives of this study, the following major tasks were accomplished:

- Task 1:Literature Review
- Task 2:Development of Test Apparatus
- Task 3:Development of a New Volume Measurement Method
- Task 3:Validation of the Concept and Characterization of Soil Behavior
- Task 4: Data Processing and Analyses
- Task 5:Draft of Final Report and Recommendations

### **Task 1: Literature Review**

The purpose of this task was to review the previous studies and current progress in laboratory characterization and constitutive modeling of unsaturated soils. In terms of laboratory characterization of unsaturated soil behavior, the emphasis was put on the existing methods of volume measurements of unsaturated soils since the suction-controlling methods are now well-established. The principle of high suction tensiometers and its development were also reviewed since they were needed in the undrained compression and shear tests were performed with measurements of suction changes. Finally, the historical developments of constitutive models for unsaturated soils were critically reviewed. All these reviews were presented in Chapter II

### **Task 2: Development of Testing Apparatus**

In this task, high-suction tensiometers were developed for measuring suction changes in undrained compression tests for unsaturated soils. After being fabricated, high suction tensiometers were calibrated and installed in the existing triaxial test apparatus for testing purpose. The methods proposed by Ridley and Burland (1993)

and Tarantino and Mongiovi (2003) were used. Efforts in this topic were reported in Chapter III.

### **Task 3: Development of a New Volume Measurement Method**

A new method was developed in this study to measure both the total and local volume change of unsaturated soils specimens during triaxial testing by integrating photogrammetry, optical-ray tracing, and least square estimation. The method, when combined with the Modified State Surface Approach, allowed use of the traditional triaxial testing apparatus to characterize unsaturated soil behavior for constitutive modeling purpose with the minimal modifications. Chapter IV described the principle of the proposed method as well as detailed mathematic derivations and tests performed for the method validations.

### **Task 4: Characterization of Soil Behavior**

Fairbanks silt was used to validate the concept and then for the systematical testing program. Basic soil properties of the selected soil such as Atterberg limits and gradation were determined. A series of undrained isotropic compression and shear tests at different moisture contents were performed to characterize the constitutive behavior of the soil.

### **Task 5: Data Processing and Analyses**

Test results from the extensive testing program outlined in the previous section were used to calibrate the model parameters in the Barcelona Basic Model. The model parameters were the used to predict the soil behaviors and compared with the test results from which some discussions were made.

### **Task 6: Draft of Final Report and Recommendations**

A final report was drafted upon the completion of data analyses. The report will include a literature survey and investigation of the results of other researchers, a

description of the research methods and approach for this project, the test procedures and results, the findings of this research project, and suggestions for further study. The recommendations of use of test results for further study of frost heave problem in Alaskan soils were provided as well.

## CHAPTER II

### LITERATURE RIVIEW

#### GENERAL

In this chapter, literature review on the topics related to this research project is presented. The reviews focused on the following areas: exiting laboratory methods to characterize constitutive behavior for unsaturated soils, development of high suction tensiometers for direct suction measurements, and existing constitutive models for unsaturated soils. At present, suction-controlled triaxial tests are extensively used to characterize constitutive behavior for unsaturated soils. The equipment needed for unsaturated soil characterization differs from the traditional triaxial test apparatus for saturated soils in two aspects: the volume measurement system and the suction control system. While the adoption of the axis-translation technique for suction control is simple and well established, the measurement of volume change for unsaturated soil specimen during triaxial testing remains a great challenge. Consequently, a comprehensive literature review specially on existing volume change measurement methods for triaxial tests on unsaturated soils was conducted. Different from the existing research, this research uses the undrained test to characterize constitutive behavior for unsaturated soils. High-suction tensiometers were used to monitor suction changes during triaxial testing. Literature on development of high-suction tensiometers were also collected and summarized. Finally, existing theories for constitutive modeling of unsaturated soils were reviewed in the last section.

#### TRIAXIAL TESTING ON UNSATURATED SOILS

Triaxial test has been widely used to evaluate the unsaturated soil behavior. Bishop and Donald (1961) developed the first suction controlled triaxial apparatus. Since then suction-controlled tests have been extensively used and now have become a standard for characterization of unsaturated soil behavior (Delage 2003). Most important concepts for unsaturated soil mechanics were developed based upon results from

suction controlled tests. Figure 2.1 shows a Schematic plot of a suction controlled triaxial test Apparatus (Bishop &Donald 1961). It differs from the traditional triaxial test apparatus for saturated soils in two aspects: the double-wall volume measurement system and the suction control system using the axis-translation technique. While the adoption of the axis-translation technique for suction control is simple and well established, the measurement of volume change for unsaturated soil specimen during triaxial testing remains a great challenge. A comprehensive literature review on existing volume change measurement methods for unsaturated soil specimen during triaxial testing is presented as follows.

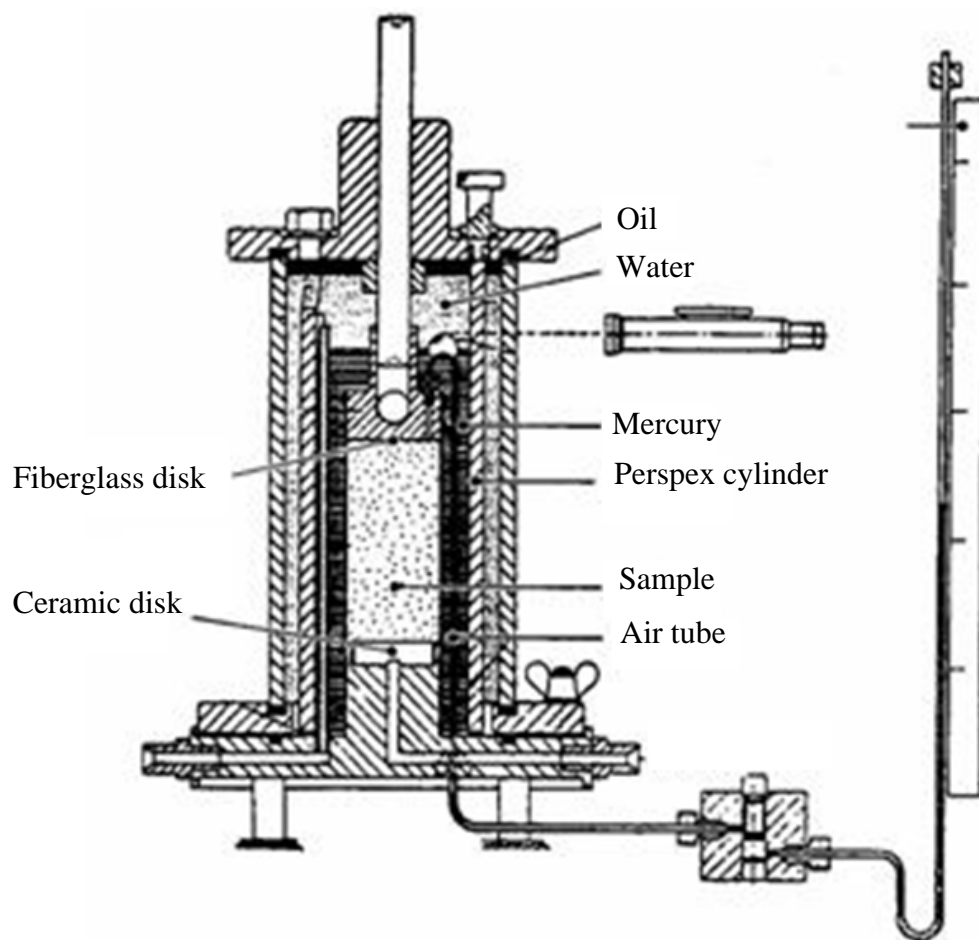


Figure 2.1 Schematic plot of suction controlled triaxial apparatus  
(Bishop &Donald 1961)

## Volume Measurement Methods

A saturated soil is a two-phase system which included water and soil solids. For triaxial tests on saturated soil, the volume change of the sample is usually monitored by pore-water volume exchange. Figure 2.2 shows the setup of a conventional triaxial test apparatus for saturated soils. An unsaturated soil is commonly referred to as a three-phase system which included water, air and soil solid and the total volume change of unsaturated specimen is no longer equal to the pore water volume change. As a result, conventional method to measure the volume change for saturated soils is no longer applicable for unsaturated soils. In the past few decades, many research efforts have been directed to develop alternative volume measurement methods for unsaturated soil in triaxial tests. Geiser et al. (2000) summarized the existing methods for measuring volume change of unsaturated soil specimens, which can be broadly classified into three categories: (i) measurement of the cell fluid, (ii) direct measurement of the air and water volumes, and (iii) direct measurement on the soil specimen.



Figure 2.2 Triaxial test apparatus for saturated soils

#### *Measurement of the Cell Fluid*

The principle of this method is to deduce unsaturated soil volume changes from volume changes in the confining cell liquid. Although the principle is simple, several problems are often associated with this method, such as immediate expansion of cell wall caused by a pressure increase, Plexiglas creep under constant stress, and possible water leakage. Theoretically speaking, a conventional triaxial cell for saturated soils can be used if carefully calibrated. However, the accuracy of the method highly depends on the quality of the calibration procedure, the volume capacity and the precision of the measurements. Ideally, numerous calibrations are needed, as corrections depend on time, stress path and stress level (Lade 1988). Bishop and Donald (1961) added an inner cylinder sealed to the outer cell base to minimize the liquid volume (double-wall cell) as shown in Figure 2.1. To enhance accuracy, mercury was used as the cell fluid between the inner cylinder and the specimen which could prevent the air diffusion through the rubber membrane in long term. Water was used as the outer liquid while the mercury was enclosed in an internal jacket with the cell pressure applied to both sides of the jacket. To prevent expansion or contraction of the inner cell as a result of changes in the cell pressure, a hole was cut at the upper part of the inner cell wall to maintain equal pressure in both the inner and outer cells. A stainless steel ball floating on the mercury surface was used to indicate the mercury level. The variation of the mercury level in the inner cell was monitored by a cathetometer which is mounted at the front of the testing system. The overall volume change of the soil specimen was then deduced by the rise or fall of the mercury vertical level in the inner cylinder. Further improvements to the inner cylinder technique have been introduced by other researchers (Wheeler 1988, Cui and Delage 1996, Rampino et al. 1999, Ng et al. 2002, and Zhang et al. 2011). Wheeler (1988) designed a double-wall cell to minimize the confining liquid in which an inner cylinder was sealed to both the top and the base of the cell. Both of the inner and outer cells were completely filled with water. Equal cell pressures were applied to the inner and outer cells to avoid deformation of the inner cell. Soil volume change was then inferred from the volume leaving or entering the inner cell. Cui and Delage (1996) replaced mercury with water for safety reasons. Rampino et al. (1999) designed an air-filled cell instead of water-filled to protect it from explosion by using an iron shield surrounding the cell. Ng et al. (2002) developed an open-ended, bottle-shaped aluminum inner cell to measure the volume change of unsaturated soil during

testing as can be seen in Figure 2.3. The use of aluminum can significantly reduce the water absorption compared with acrylic materials. A high-accuracy differential pressure transducer was used to record the pressure difference between the water inside the open-ended inner cell and the water inside a reference tube in which a constant water pressure was maintained. The deformation of the soil sample will result in a water level change in the inner cell which could be reflected by the pressure difference between the inner cell and the reference tube. Figure 2.4 shows a differential pressure transducer used for double cell manufactured by GCTS. Zhang et al. (2011) used an ultra-high accuracy laser displacement sensor to measure the water level changes resulting from the volume change of the soil specimen. The system setup is shown in Figure 2.5 which consists of an open inner cell, outer cell, an external measurement cell connected to the open inner cell, and a laser transducer fixed above the measurement cell. The laser transducer transmits a laser beam to the water surface and reflected back to the sensor to monitor the water level change in the measurement cell which is then converted into specimen volume change.

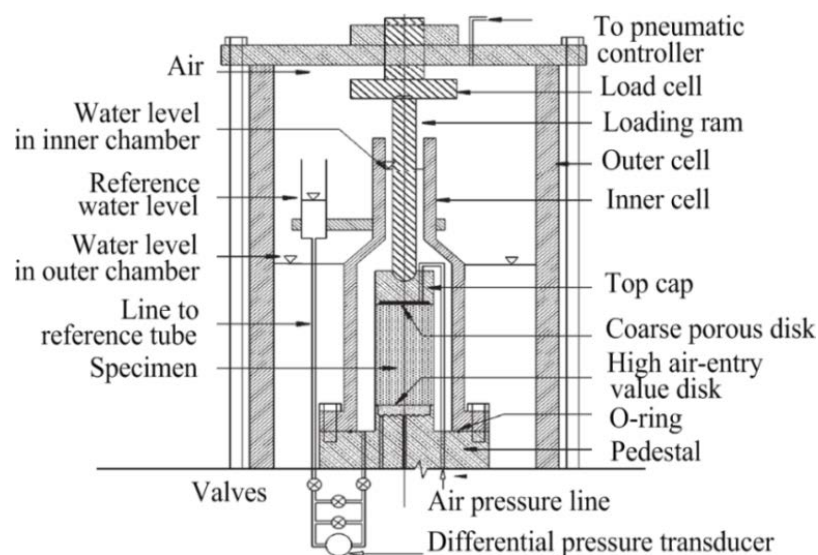


Figure 2.3 Double-wall cell method with differential pressure transducer (Ng et al. 2002)

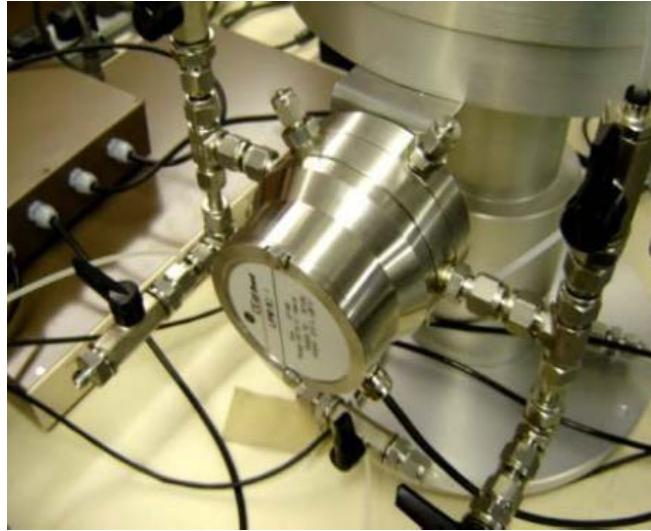


Figure 2.4 GCTS differential pressure transducer

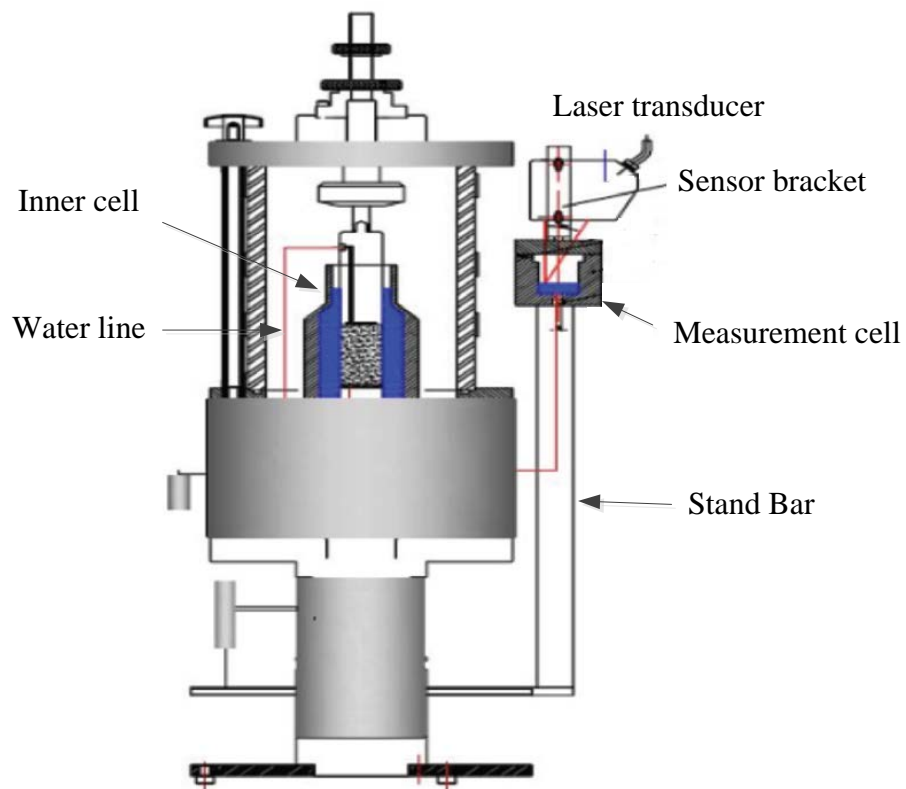


Figure 2.5 Test apparatuses used by Zhang et al. (2011)

So far, double-wall cell method is the most widely used method for triaxial testing on unsaturated soils. However, this method requires major equipment modifications and is therefore expensive. A double-wall cell testing system typically costs \$150,000 and is complex to operate. It cannot eliminate errors from the deformations of the top and the base of the cell. In addition, the air bubbles are difficult to remove and water used

required to be de-aired. Also for the acrylic inner cell, water absorption is affected by pressure, temperature, and time, making the calibration of the system very difficult. For small specimens (38 mm in diameter), errors due to this absorption can be significant. Larger specimen however requires longer testing time which increases creep. Steel inner cell can be an alternative to solve the problem. However, for this non-transparent inner cell, it is difficult to examine the existence of air bubbles in the cell. The double-wall cell has been extensively used for unsaturated soil testing in the past five decades. A carefully calibrated GDS double-wall cell can measure total volume change to an accuracy of 0.25%.

#### *Direct Measurement of the Air and Water Volumes*

In this method, volume change of a soil specimen is obtained by measuring the air and water volume changes separately and adding them together. It requires adding an air-volume controller filled with air instead of water. Figure 2.6 is a typical Air Pressure/Volume Controller from GDS. To be successful, this method requires the air phase to be continuous. This method is sensitive to small temperature and atmospheric pressure changes. In addition, undetectable air leakage and diffusion through tubes, connections, and high-air-entry disk can also influence the accuracy of the measurements. The errors can be significant for consolidated drained tests, which often takes months to complete. Furthermore, excess pore air pressure can be generated during the test and lead to misleading volume changes. Various improvements were proposed to overcome these limitations. Geiser (1999) proposed a mixed air and water controller that allows reduction of air volume to the tubing only to minimize the errors from changes in atmospheric pressure and temperature. GDS adds a U-shaped observation tube filled with ethanol to their volume controller for pore air to maintain the pore air always at atmospheric pressure. Although these improvements are available, direct measurement of the air and water volumes is not extensively used by researchers at present. Laudahn et al. (2005) proposed the use of GDS Air Pressure/Volume Controller for measuring pore-air volume changes in drained tests under atmospheric conditions as shown in Figure 2.7.

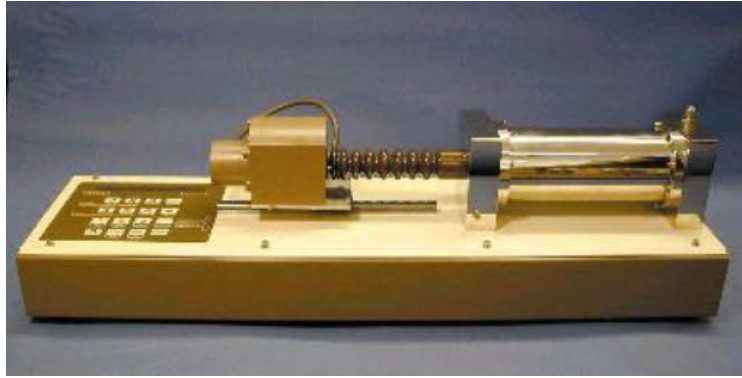


Figure 2.6 Air pressure/volume controller (GDS)

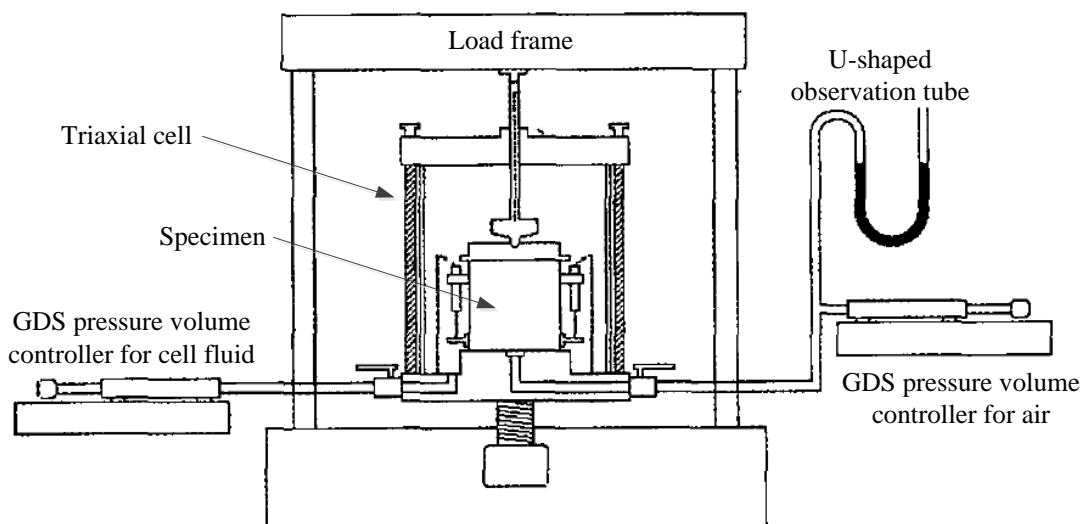


Figure 2.7 Configuration of the test equipment with GDS air pressure/volume controller (Laudahn et al. 2005)

### *Direct Measurement on the Soil Specimen*

In this method, soil volume change is computed from the direct measurements of axial and radial specimen displacements. This category can be further divided into contact and non-contact methods.

#### *Contact method*

The contact method is a commonly used method in which local displacement sensors are directly attached onto the specimen (Figure 2.8) to measure axial/radial deformations during the test (e.g., Clayton et al. 1989, Blatz and Graham 2000, and Sun et al. 2003). Generally, radial displacements are measured at one to three discrete points and assumptions are made as to the shape of the specimens to assess the volumetric strain as shown in Figure 2.9. This method is normally applicable only for rigid specimens with small deformations. Measurements become meaningless as a means of measuring soil volume change, for example, if a shear plane forms across the specimen. It also requires use of specially designed sensors such as miniature LVDTs (Costa-Filho 1982; Klotz and Coop 2002) and Hall Effect transducers (Clayton and Khatrush 1986). Errors could be raised due to seating, closing of gaps between components, and axial and radial alignment. Generally less than three measurements can be made due to the limited space inside the cell. Hird and Hajj (1995) proposed use of proximity transducers mounted on a rigid tube around the sample to provide an output voltage proportional to the distance of a lightweight conductive target placed on the specimen as shown in Figures 2.10 and 2.11. Generally, this type of transducer is not waterproof and has to be sealed in housing. Another major drawback is that the target must be aligned with the sensor, which is difficult to satisfy.



Figure 2.8 Local strain transducers from GDS

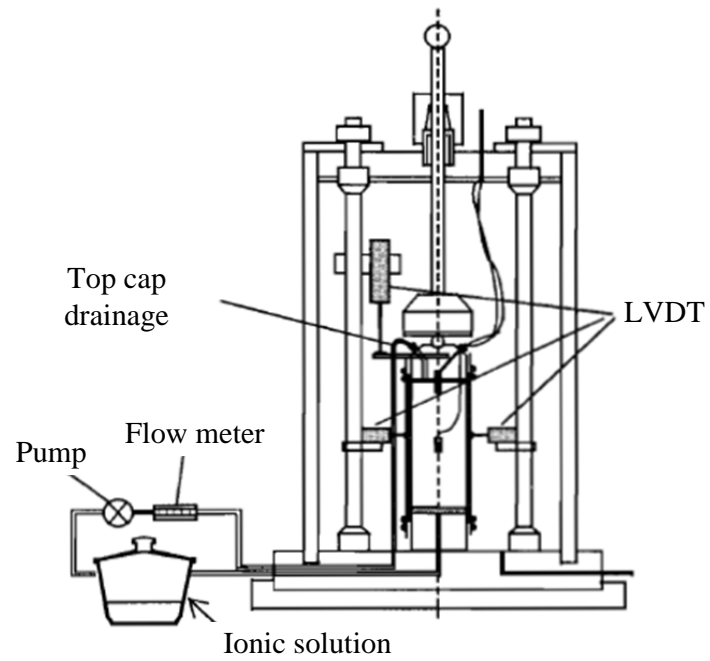


Figure 2.9 Setup for LVDT method (Blatz and Graham 2000)

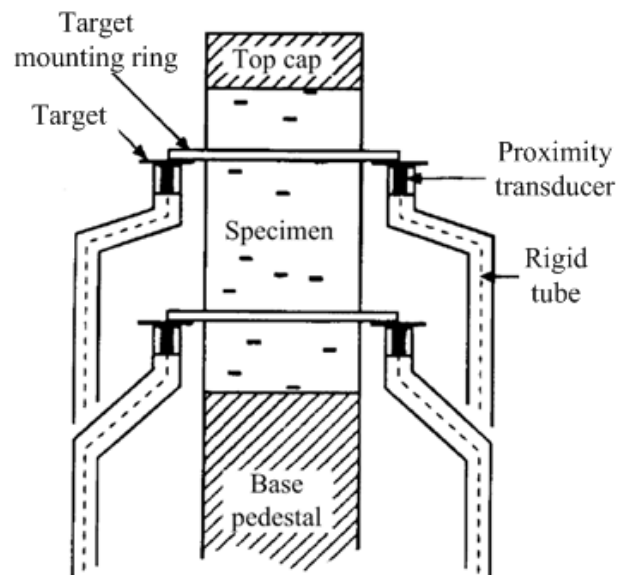


Figure 2.10 Axial strain measurements for LVDT method (Hird and Hajj 1995)

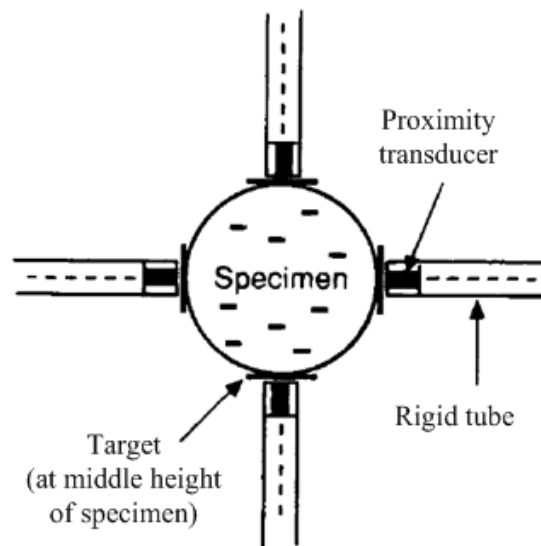


Figure 2.11 Radial strain measurements for LVDT method (Hird and Hajj 1995)

#### *Non-contact method*

Romero et al. (1997) reported the use of an electro-optical laser scanner to determine the lateral profiles of specimen for radial deformation as shown in Figures 2.12 and 2.13. It also allowed detection of non-uniformities and localized deformations along the two diametrically opposite sides of the specimen. The technique requires costly modification (> \$20,000) and sophisticated installation procedures as shown in Figure 2.13. A triaxial cell needs to be modified by opening a flat window for the laser ray. In addition, this method needs to deal with the refraction from the cell wall and the confining fluid, which has been neglected.

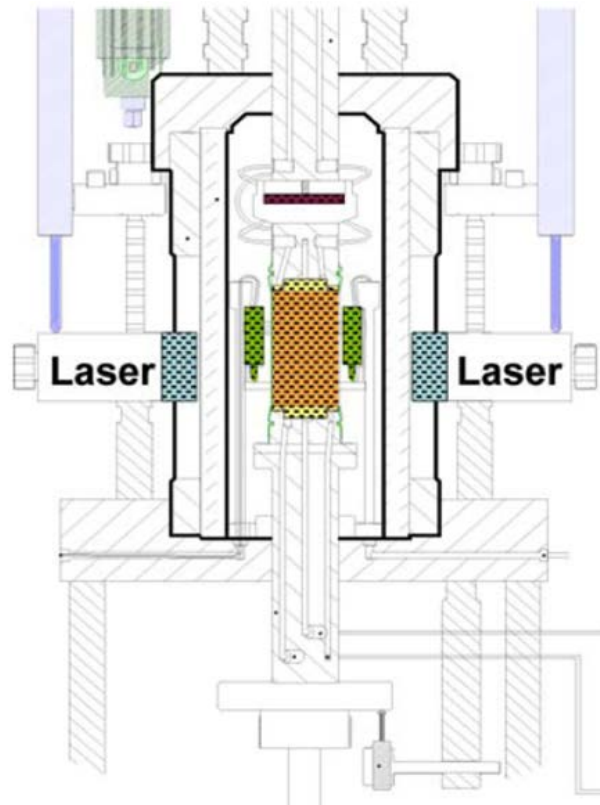


Figure 2.12 Schematic plot of the laser scanner method (Romero et al. 1997)



Figure 2.13 Laser scanner method setup (Romero et al. 1997)

Digital Image Analysis (DIA) with refraction correction is another non-contact approach to measure soil volume change during testing by using images captured by cameras (Macari et al. 1997, Gachet et al. 2010). Pinhole camera model was adopted for this method as shown in Figure 2.14. However, when a photo is taken for a 3D object using a digital camera, a 2D image is obtained and the depth of the object is lost. As shown in Figure 2.14, object A and B product same picture on the image plane even though they are in different size and from different distance. In order to make correct measurements, the orientation (including position and shooting direction) of the camera relative to the object have to be known in order to reconstruct its 3D dimensions.

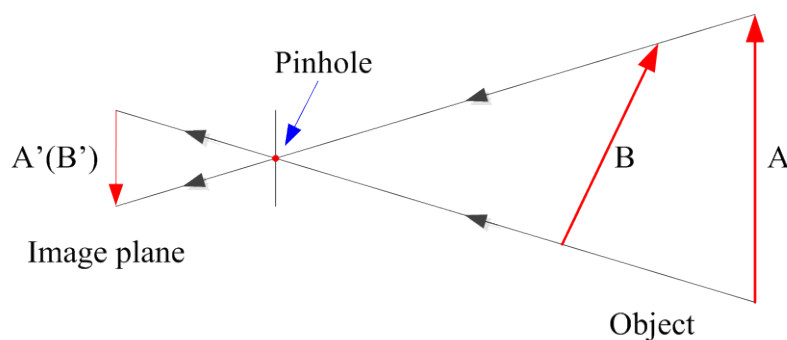


Figure 2.14 Pinhole camera model

For soil triaxial testing as shown in Figure 2.2, the presence of the confining acrylic chamber and the confining water in the line of vision between the camera and the soil specimen creates an apparent magnification of the specimen which must be accounted for if high accuracy is expected. Parker (1987) developed a two-dimensional model to use DIA with 2D refraction corrections to measure soil deformations in a conventional triaxial test cell. Macari et al. (1997) proposed a further improvement as shown in Figure 2.15. An idealized pinhole camera model is installed “far away” from the soil specimen. Then, a series of images were captured during testing as shown in Figure 2.16. For a digital image, every pixel in the image has a corresponding gray value (varied from 0 to 255, with 0 being black and 255 being white) which is dependent on its brightness. Based on the significant change of gray values for pixels at the edges of soil sample, the edges can be determined as shown in Figure 2.16. Then, volume of soil sample can be determined based on the shape change of the sample. To apply this method, system calibrations must be performed first and several

implicit requirements must be satisfied: (1) the soil specimen and the confining acrylic chamber are perfectly cylindrical and installed vertically; (2) the digital pinhole camera is placed perfectly at the horizontal direction and its shooting direction exactly passes through the center of the chamber; (3) the soil specimen is installed exactly at the center of the confining chamber and the relative positions of the camera, the chamber, and the soil specimen are accurately known; (4) deformation of acrylic cell wall under water pressure is negligible; and (5) when soil deforms, the deformations occur homogeneously along the radial directions. With these assumptions, the Snell's law is applied twice to determine the positions of the points on the surface of soil specimen. None of these conditions can be met in real conditions. The results of the image-based volume measurements depend greatly on how well the model conditions are satisfied throughout the test. Gachet et al. (2010) applied this method to determine volume changes of an unsaturated soil from its lateral profiles. The system setup for this DIA method is presented in Figure 2.17.

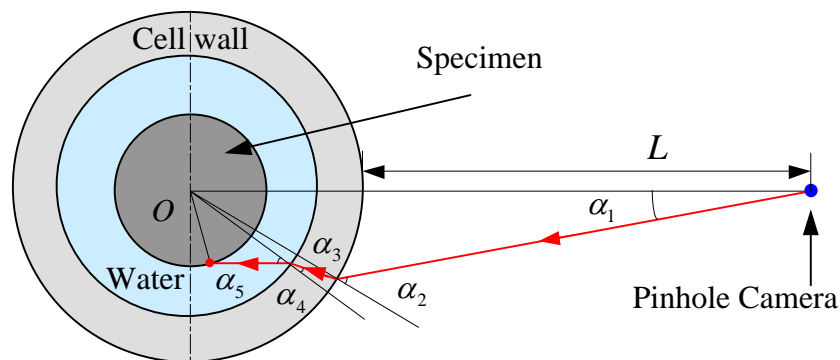


Figure 2.15 Two-dimensional system model (Macari et al. 1997)

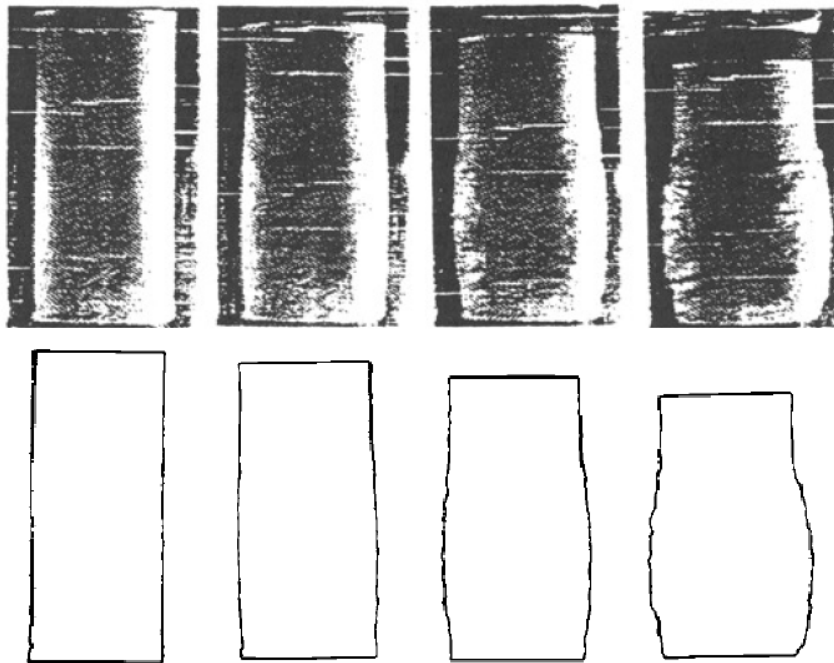


Figure 2.16 Volume measurement based on images (Macari et al. 1997)

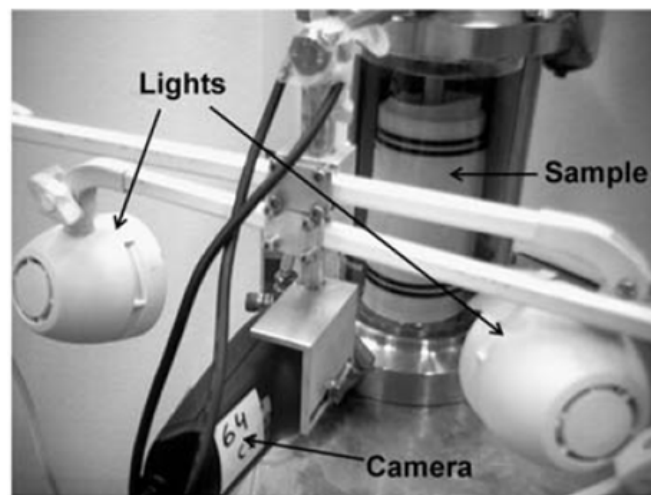


Figure 2.17 2D image based method (Gachet et al. 2010)

Besides been used for volume measurement during triaxial testing, DIA can also been used to detect strain localization (Lin and Penumadu 2006, Sachan and Penumadu 2007). The system setup for this strain localization method by using DIA is similar to Figure 2.17. The only difference between the total volume and local strain measurement by using DIA is the setup on sample surface. In order to do a local strain measurement, as shown in Figure 2.18, grid points are required to be marked on latex membrane which covered sample surface. By tracking the movement of these grid

points with a high resolution camera, strain localization can then be determined. Before measurement by using this method, the whole system needs to be carefully calibrated as addressed by Sachan and Penumadu (2007). Similar to the total volume measurement by using DIA, the strain localization measurement inherits all the requirements for total volume measurement by using DIA method which could not be perfectly satisfied. In addition, this method cannot provide measurements for the whole soil specimen since back of the soil specimen is blocked by itself. Lin and Penumadu (2007) used this method to analyze a series of combined axial-torsional tests for kaolin clay under undrained conditions. It was found that for a spacing of 10 mm between the grid points, the obtained accuracies of measurement are 0.2 mm and 0.3 mm in the vertical and circumferential direction, respectively.

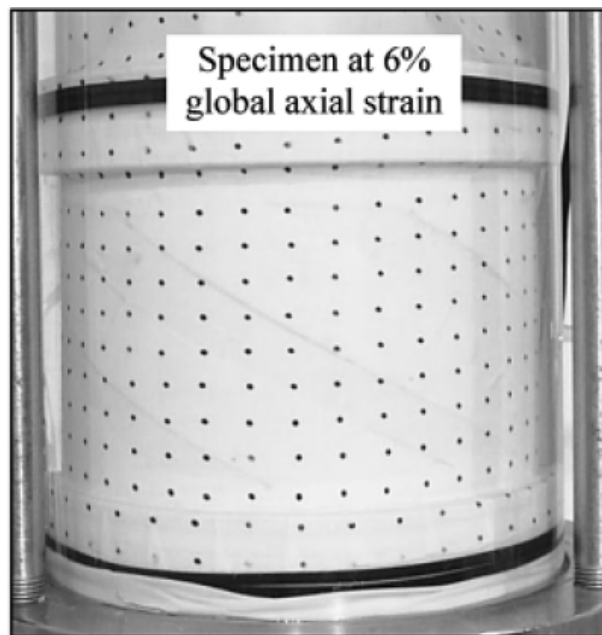


Figure 2.18 Setup on soil specimen for local strain measurement  
(Sachan and Penumadu 2007)

#### *Methods Especially Developed for Measuring Strain Localizations*

Even if a soil element is subject to a homogeneous stress at its boundary, localized strain concentration can occur and propagate into zones of localized shear deformation or shear band because of the inevitable non-uniformity of the mass and stiffness of the material. As a result, the meaning of stress and strain variables derived

from boundary measurements of loads and displacements is only nominal. The only way to understand localized deformation is to measure the full field of deformation in the specimen (Viggiani and Hall, 2008). Several methods have been developed to track shear band including X-ray Computerized Tomography (CT), Digital Image Analysis (DIA) with Refraction Correction, and Digital Image Correlation (DIC). These methods can potentially be used to measure the total and local volume changes for unsaturated soil specimen during triaxial testing. A brief literature review of these methods in geomaterials studies is presented as follows.

X-ray CT is a nondestructive imaging technique to detect the internal structure of an object using an X-ray source. The system setup for this strain localization measurement can be found in Figures 2.19 and 2.20. When X-ray beam passes through an object, some photons are either scattered or completely absorbed, resulting in the attenuation of the intensity of beam. The amount of attenuation depends upon the photon energy, the chemical composition, and the density of the object. This attenuation can be well captured by a camera. A typical image obtained through X-ray CT method of a soil slice is shown in Figure 2.21. By interpreting the beam intensity data, information regarding the internal structure of an object can be obtained. The information is presented as two dimensional cross sections or stacked to develop 3D renderings of the object for which total and local volume change can be deduced. Roscoe (1970) used X-ray radiography to measure two dimensional (2D) strain fields in sand. From the early 1980s, X-ray tomography was used by Desrues and coworkers (Desrues 1984, Colliat-Dangus et al. 1988, and Desrues et al. 1996) and later by Alshibli et al. (2000) and Lenoir et al. (2010) to provide valuable 3D information on evolution of void ratio inside a shear band and its relation to critical state.

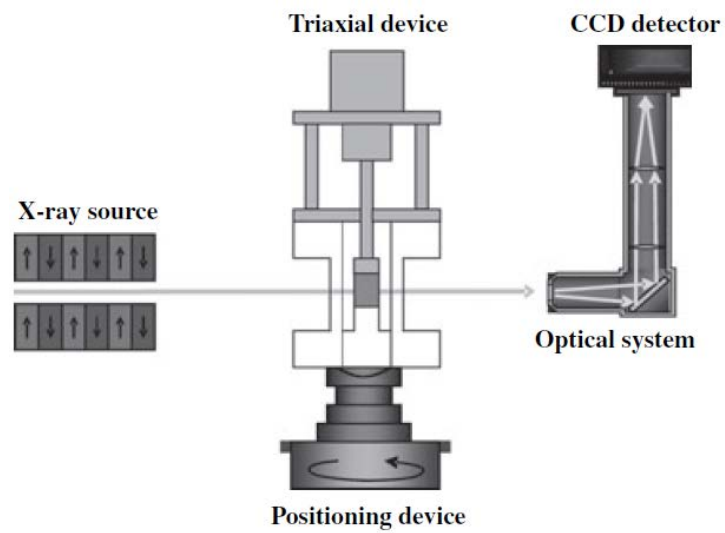


Figure 2.19 Schematic plot of the system setup for X-ray CT method (Lenoir et al. 2010)

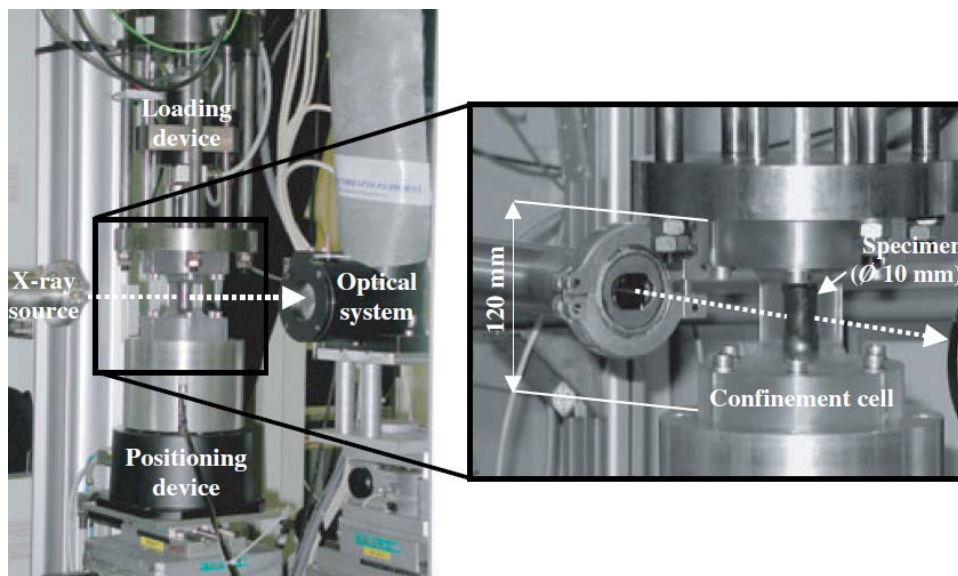


Figure 2.20 System setup for X-ray CT method (Lenoir et al. 2010)

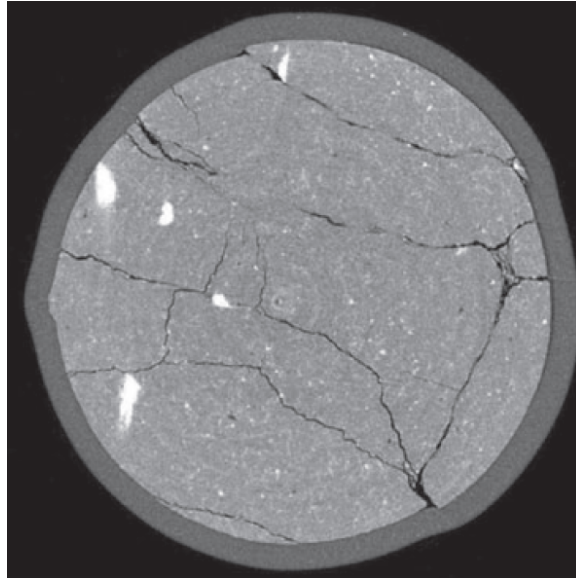


Figure 2.21 A horizontal CT slice (Lenoir et al. 2010)

In the past 30 years, using X-ray CT has changed from a pioneering high-tech experimental approach to a well-recognized powerful experimental method. The accuracy could be as high as several microns for small-size soil specimens. The major disadvantage of X-ray CT technique for triaxial soil testing is that it is too expensive. Since the steel and water attenuates the intensity of X-ray beam, conventional triaxial test apparatus cannot be used with X-ray CT for soil testing. A completely different new system such as the one at Washington State University (Razavi 2006) is therefore needed for real-time soil characterizations during shearing with controlled confinement. At present very few such systems are available in the US. In addition, suction controlled triaxial tests for unsaturated soils are often time-consuming (2-3 months/test), which makes its use more expensive. Although possible and having many advantages, it is impractical to use the X-ray CT test to characterize real-time stress-strain behavior for unsaturated soils.

Digital image correlation (DIC) is another non-contact method to detect local strain of soil sample during triaxial testing based on images captured by cameras. DIC measures displacements across an object surface based upon the assumption that all soils have their own unique textures in the form of different-colored grains and the light and shadow formed between adjacent grains when illuminated. These textures include numerous small clusters of uniquely colored pixels called subsets and their

corresponding gray level variations represent unique mathematical entities that can be tracked during a deformation process. Figure 2.22 shows fractions of two images for a sand specimen before and after deformation (Rechenmacher and Medina-Cetina, 2007). By best matching the pixel subsets through minimization of an error measure, such as normalized cross correlation (Sutton et al. 2000), subset straining and/or rotations can be captured and measured. The pixel subset matching can be intensively performed so that nearly full-field displacement information can be obtained. Initially DIC displacements are analyzed incrementally from images taken at short time steps using a single digital camera at a fixed location which is similar to DIA method. As a result, only 2D analysis can be performed. White et al. (2003) presented a DIC method for soil volume measurement which used digital images and particle image velocimetry analysis for measuring soil deformation. Orteu (2009) and Rechenmacher and Medina-Cetina (2007) reported use of 3D-DIC to match pixel subset patterns reflected on surfaces of 3D objects in which the 3D object shape is discerned by utilizing two obliquely oriented digital cameras as shown in Figure 2.23. Based upon the 3D spatial information of the object, 3D displacements between consecutive sets of images are computed using the DIC concepts described above. Results indicated the vertical and horizontal displacements could be measured to an accuracy of  $\pm 0.02$  mm. However, the DIC method does not have a component to take the refraction into considerations and therefore cannot directly be used with the conventional triaxial test apparatus for saturated soils to measure the soil volume change. Rechenmacher (2006) and Rechenmacher and Medina-Cetina (2007) eliminated the refraction effect by carrying out triaxial tests under vacuum confinement without the use of a conventional confining cell. As a result, the confining pressure that can be applied is limited to one atmosphere. The DIC method was only used to measure local volume change (deformation) for a small area of soil specimen and cannot be used to measure displacements for the whole soil specimen.

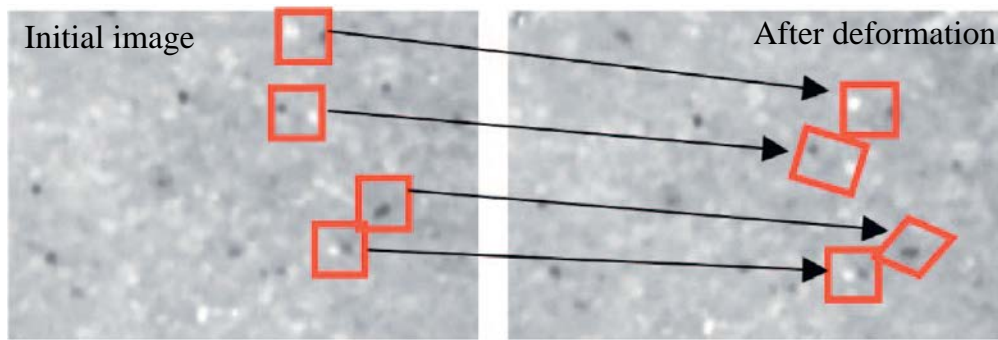


Figure 2.22 DIC pixel subset matching



Figure 2.23 Configuration of the 3D DIC method (Orteu 2009)

In a summary, according to the above discussions, at present there is no simple and cost-effective method to accurately measure the total and local volume change for unsaturated soil specimen during triaxial testing. There is a great need for research in this area.

### **HIGH SUCTION TENSIOMETER**

At present most researchers use suction-controlled consolidated drained tests to characterize constitutive behavior for unsaturated soils. This type of tests normally is very time-consuming due to the low permeability of unsaturated soils, especially at the high suction range. For example, it took Sivakumar (1993) 959 days to complete 30 suction-controlled consolidated drained tests for compacted speswhite kaolin. It

took Sharma (1998) 801 days to complete 20 suction-controlled isotropic consolidated drained tests for two compacted expansive soils. Different from the existing research, this research uses the undrained test to characterize constitutive behavior for unsaturated soils. In the past few decades, a great effort has been dedicated to measure the matric suction of unsaturated soils. Reviews of conventional suction measurement methods on unsaturated soil can be found in Fredlund and Rahardjo (1993), Ridley and Burland (1993), and Rahardjo and Leong (2010). High-suction tensiometers were considered to be most suitable for measuring suction changes during triaxial testing. A literature review on matric suction measurement by using tensiometers is presented as follows.

#### *Principle of High-suction Measurement*

Basically, the theory of suction measurement by using tensiometers is based on the tensile strength of water. As addressed in Guan and Fredlund (1997), the tensile strength is defined as the stress of a liquid at which the liquid ruptures or cavitates. Cavitation starts as vapor bubbles begin to form in water which is triggered at gaseous or other hydrophobic surfaces. The vapor bubbles are commonly referred as potential cavitation nuclei. Water usually cavitates when the hydrostatic pressure is close to the vapor pressure. However, if the radii of cavitation nuclei are sufficiently reduced, water will have the ability to sustain a high tension without cavitation. As can be seen in Figure 2.24, due to the surface tension of water, there is a raise of water level in the glass tube which is referred as capillary behavior. Water underneath the meniscus and above the water level in the tank is under tensile strength which can be determined through Equation 2.1. Thus, if the radius of the glass tube is reduced to a very small value, water in the tube can sustained a very high tensile strength based on Equation 2.1.

$$S_w = \frac{2T_s}{r} \quad (2.1)$$

where,

$S_w$  = tensile strength of water,

$T_s$  = surface tension of water, and

$r$  = radius of the glass tube.

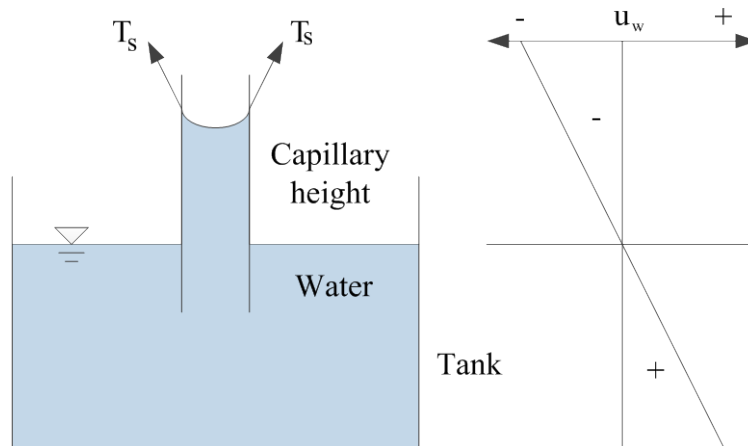


Figure 2.24 Tensile strength of water

Knapp et al. (1970) reported a maximum attainable tensile strength in water ranged approximately from 1.3 to 27 MPa. Zheng et al. (1991) detected a tensile stress of 140 MPa, which is believed to be very close to the maximal tension that water can hold, in a single crystal of water.

#### *Existing High-suction Tensiometers*

For conventional tensiometers, negative pressure measurement is limited to approximately -90 kPa due to the cavitation of water in the tensiometer (Fredlund and Rahardjo 1993). So, the application for conventional tensiometers is limited to be used on unsaturated soils with low matric suction (less than 100 kPa). The first attempt to direct measurement on soil suction higher than 100 kPa was achieved by Ridley and Burland (1993) in Imperial College. It was found that during the use of pressure plate for suction measurement of a Kaolin sample, a water pressure ranging from -100 to -300 kPa was detected by a reservoir transducer after an instant reduction of the air pressure in the chamber to an atmospheric level. This phenomenon was also found during the measurement of pore water pressure of a saturated soil specimen (equilibrium pore water pressure of 20 kPa) under stress path with a confining pressure of 400 kPa by using pore water pressure sensor PDCR 81.

Under undrained condition, when the confining pressure was released relatively slowly to atmospheric pressure, a reduction in probe pressure was also detected and stabilized at -365 kPa. The high negative pressure in the probe slightly decreased and maintained for about two hours before jump to -100 kPa. Inspired by this phenomenon, by replacing the porous stone of PDCR 81 with a 15 bar ceramic disc, a new suction probe for measuring matric suction of unsaturated soil was developed which could reach a negative pore water pressure as high as 1370 kPa. However, the high mortality of the PDCR 81 due to seal between the silicon diaphragm and the underneath Pyrex cylinder forced the author to use a pressure transducer with a strong joint which is Entran EPX-500 as a replacement. After trying several designs, a new high-suction tensiometer was developed which is shown in Figures 2.25 and 2.26. A 15 bar air-entry value ceramic disc with housing was sealed to the transducer. The diaphragm of the pressure transducer responds to the pressure applied. Beneath the ceramic disc, the thickness of the water reservoir was minimized to 0.1 mm. This new tensiometer could give a reliable measurement up to -1500 kPa with a response time within five minutes. Beside this, a special saturation device was also designed and fabricated as shown in Figure 2.27 in which a 19 bar pressure was applied. The tensiometer was mounted in a hole at the center of a plinth and rested on a soft spring, with the porous stone facing upwards and slightly proud of the plinth as shown in Figure 2.28. After saturation, soil specimen was then placed on the plate. Due to the presence of spring, tensiometer would move downward as a result of the weight of the sample. In this way, a good contact between the soil specimen and the tensiometer could be ensured.

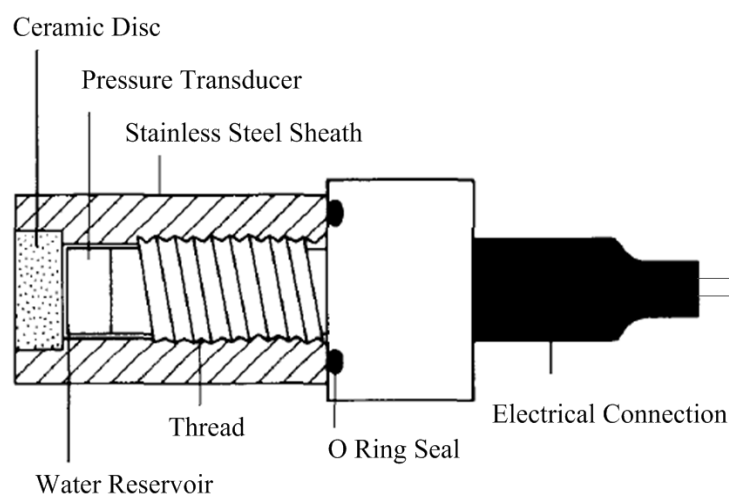


Figure 2.25 Schematic plot of the tensiometer developed by Ridley and Burland (1993)

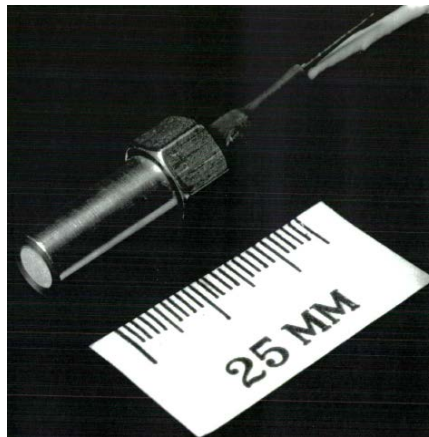


Figure 2.26 Tensiometer developed by Ridley and Burland (1993)



Figure 2.27 Tensiometer saturation device (Ridley and Burland 1993)

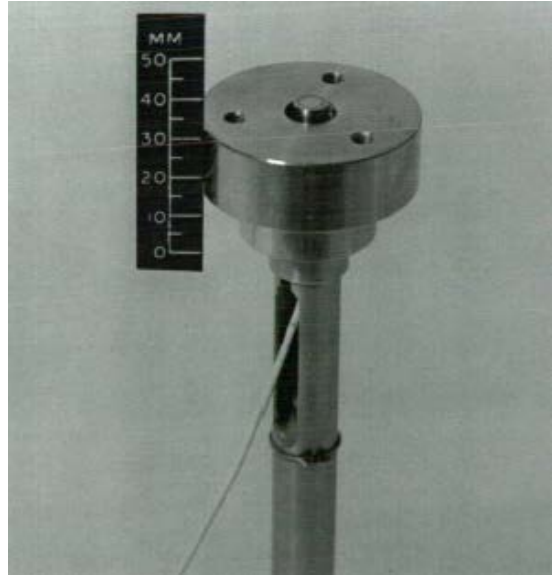


Figure 2.28 Inside of the tensiometer saturation device  
(Ridley and Burland 1993)

However, due to the thread-type transducers were used by Ridley and Burland 1993, it was difficult to saturate the tensiometer. Also, the surfaces of the threads may constitute an important source of potential cavitation nuclei (Guan 1996). Since 1993, more of these high suction tensiometers have been developed and successfully used in laboratory and field experiments. In University of Saskatchewan, Guan and Fredlund (1997) reported the development of a tensiometer (Figure 2.29) based on a pressure transducer (150 bar, without thread) manufactured by Entran Devices, Inc., Fairfield, USA (Model EPN-0762AI\* - I50SY) instead of using a thread-type transducers. The pressure transducer diaphragm is 7 mm in diameter. The transducer and housing were assembled under water to leave a water-saturated chamber with a clearance between transducer and ceramic disk of 0.1–0.5 mm which could reduce the time needed for the saturation process. Also, a saturation cup for this tensiometer, in which a pressure up to 150 bar can be applied, was fabricated as shown in Figure 2.30. By apply six cycles of -85 to 12000 kPa pressure, the tensiometer was saturated and could be used to measure the matric suction of clay soil up to -1250 kPa.

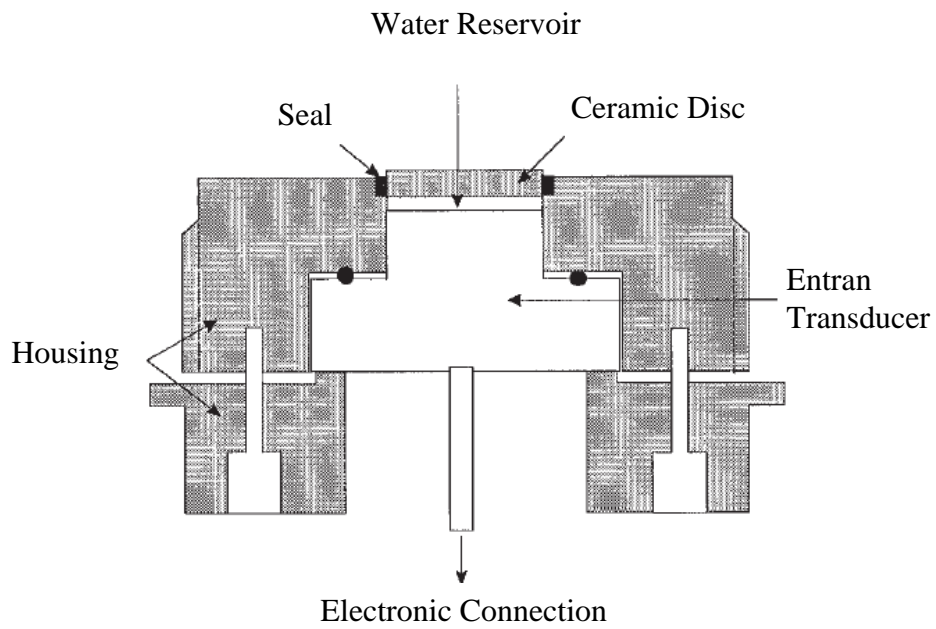


Figure 2.29 Tensiometer developed by Guan and Fredlund (1997)

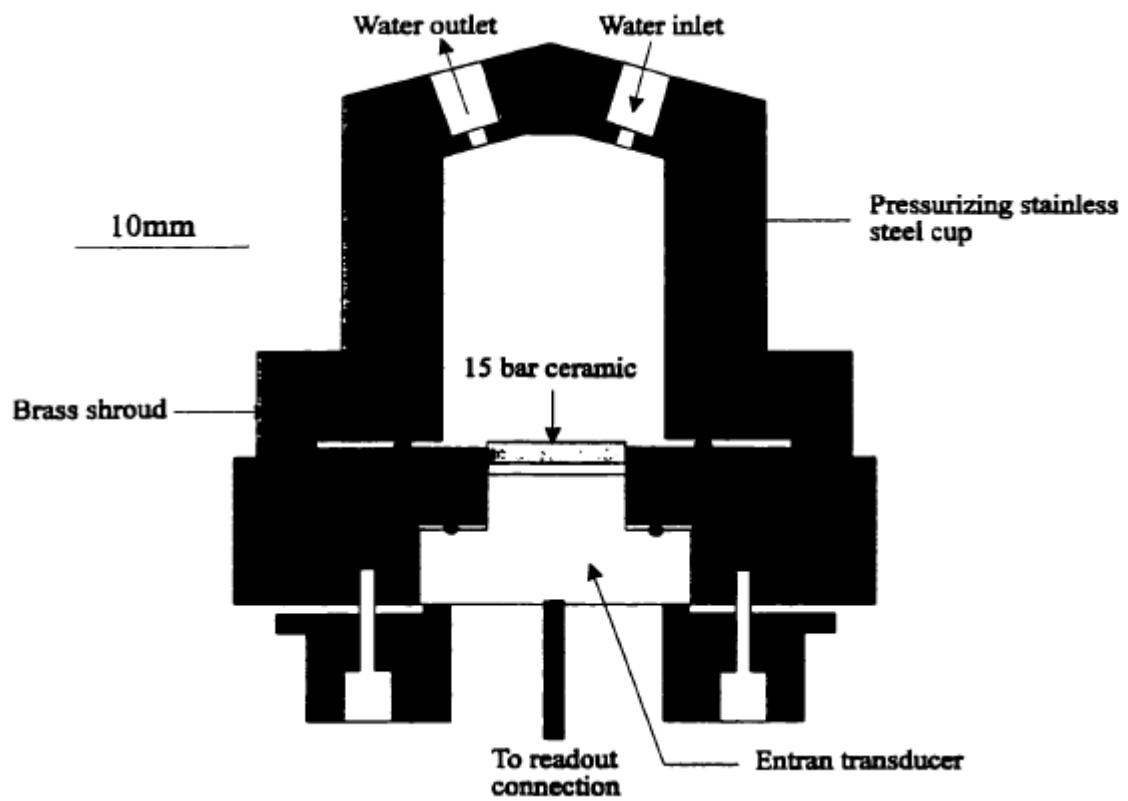


Figure 2.30 Tensiometer and saturation cup by Guan (1996)

Meilani et al. (2002) presented the development of a tensiometer (Figure 2.31) based on PDCR 81 pressure transducer. A 5 bar air entry ceramic disc thinned to 1 mm was used to reduce the long response time introduced by using high air entry ceramic disc. By applying a pressure of 800 kPa for four days, the tensiometer can then be saturated. Then, the tensiometer can be used to measure matric suction of unsaturated soil up to -400 to -500 kPa. Similar designs can also be found for tensiometers developed by Tarantino and Mongiovi (2002) as shown in Figure 2.32, Take and Bolton (2003) as shown in Figure 2.33 based on an Entran EPB stainless steel diaphragm pressure transducer and Lourenco et al. (2006) as shown in Figure 2.34. For all these tensiometers, a similar structure could be found which comprises (1) a pressure transducer for pressure measurement, (2) a high air entry disc to prevent tensiometer cavitation at low suction, (3) a water reservoir to generate a negative water pressure which can be detected by the pressure transducer. Differences among the tensiometers are mostly related to the dimensions, materials used and sealing characteristics.

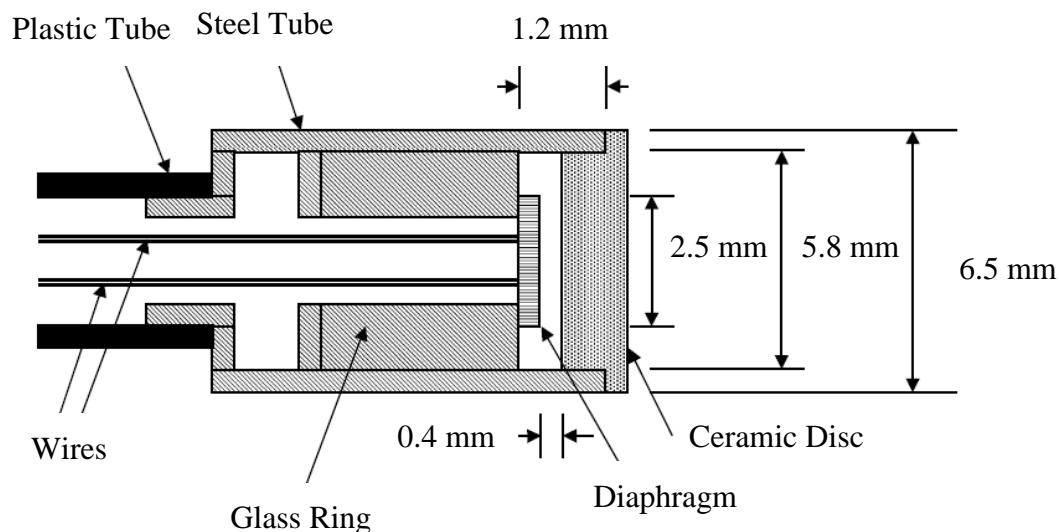
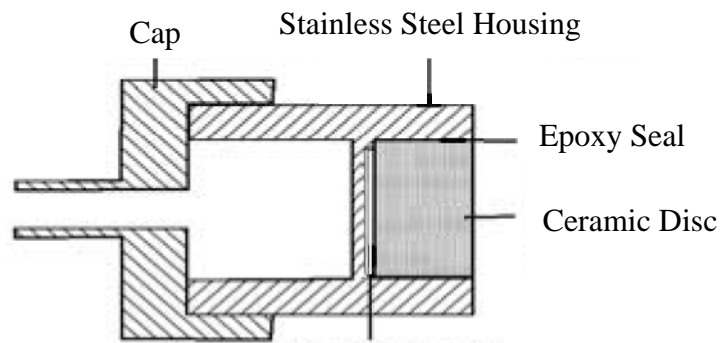


Figure 2.31 Tensiometer developed by Meilani et al. (2002)



Pressure Diaphragm and Water Reservoir

Figure 2.32 Tensiometer developed by Tarantino and Mongiovi (2002)

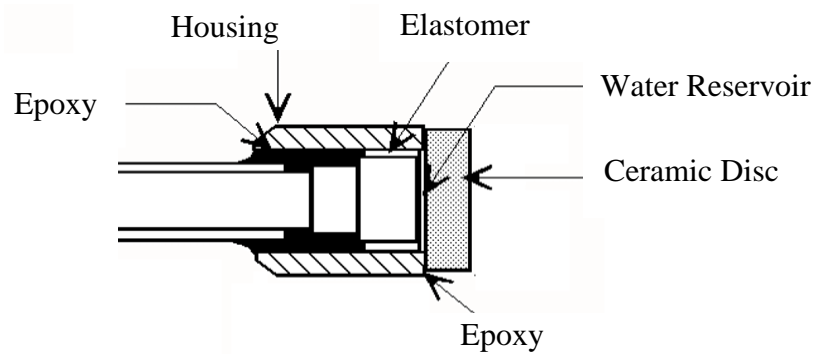


Figure 2.33 Tensiometer developed by Take and Bolton (2002)

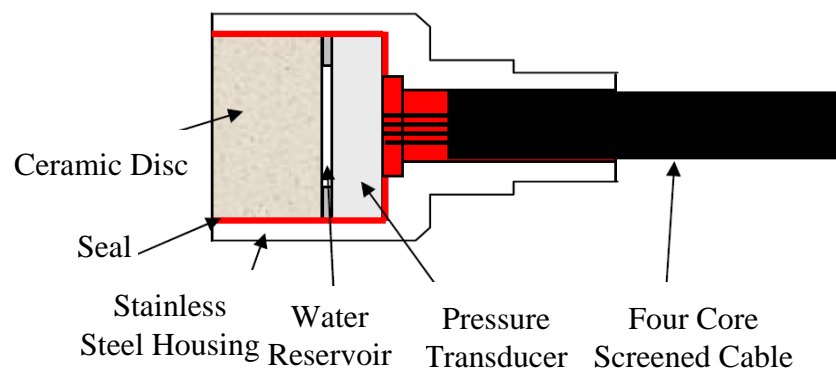
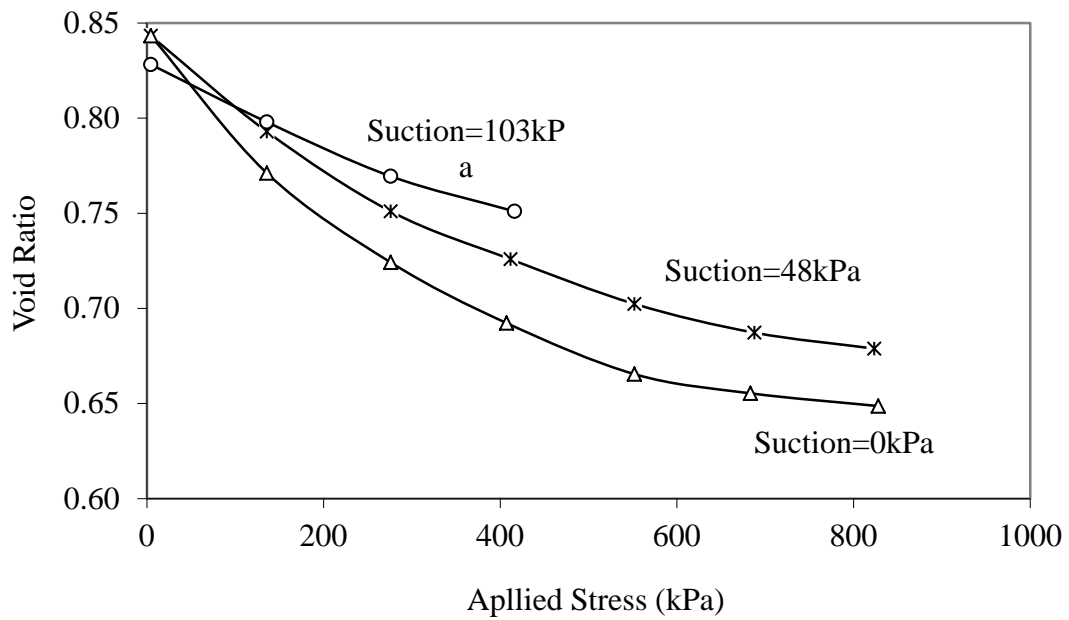


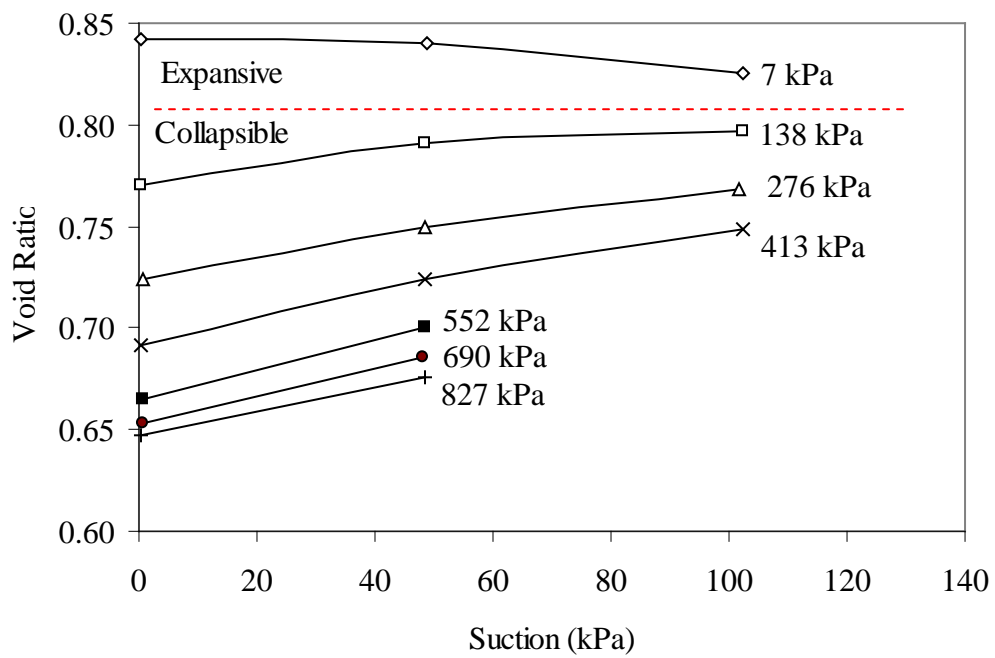
Figure 2.34 Tensiometer developed by Lourenco et al. (2002)

## CONSTITUTIVE MODELING OF UNSATURATED SOILS

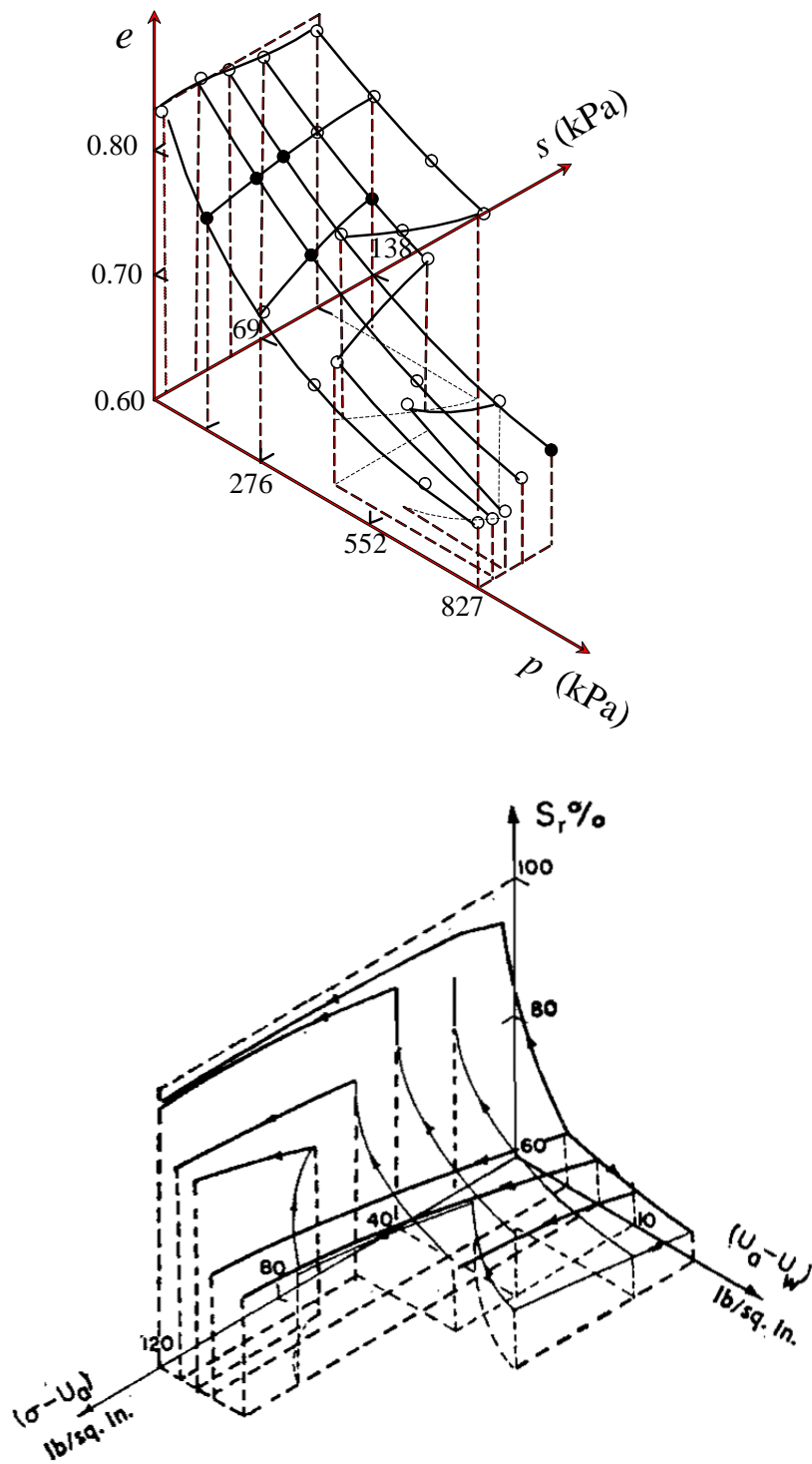
Early researchers attempted to extend the effective stress principle for saturated soils into the research on unsaturated soils (Bishop et al. 1960; Aitchison and Donald 1956; Aitchison 1961; Jennings and Burland 1962; Matyas and Radhakrishna 1968). The difficulty in finding a single equivalent effective stress to explain unsaturated soil behavior, has progressively resulted in the adoption of two stress state variables (i.e. net normal stress  $p$  and matric suction  $s$ ), as a necessary framework to describe unsaturated soil behavior (Fredlund and Morgenstern 1977, Fredlund 1979; Fredlund et al. 1978; Fredlund and Hasan 1979). Based upon the results from suction controlled consolidated drained tests as shown in Figure 2.35, Matyas and Radhakrishna (1968) proposed the concept of state surfaces to relate void ratio and degree of saturation to two stress state variables  $p$  and  $s$ . The theoretical and experimental justifications of using two independent stress state variables were further reinforced by Fredlund and Morgenstern (1977). Based on the concepts of two stress state variables and state surfaces, Fredlund and his coworkers developed a comprehensive theoretic framework for unsaturated soils (Fredlund and Rahardjo 1993) in which the volumetric behavior and shear strength are described entirely separately. The use of unique state surfaces to explain unsaturated soil behavior was called the state surface approach (SSA) and used extensively by many early researchers (Matyas and Radhakrishna 1968; Lloret and Alonso 1980; Lloret and Alonso 1985; Fredlund and Hasan 1979; Fredlund and Rahardjo 1993). The SSA is essentially an elastic analysis of unsaturated soil behavior (Alonso et al. 1987, 1990; Wheeler 1996).



(a) Constant suction compression curve



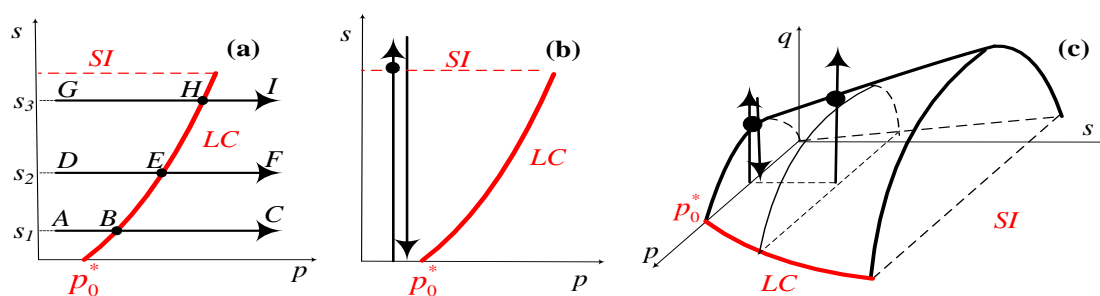
(b) Plot of (a) on the e-s plane



(c) Three dimensional plots of the results

Figure 2.35 Experimental tests establishing the concept of state surface  
(Matyas and Radhakrishna 1968)

However, unsaturated soils often demonstrate irrecoverable behavior, which cannot be explained by the SSA. Furthermore, long experience with both saturated and unsaturated soil has emphasized the important link between volume change and shearing (Alonso et al. 1987, 1990; Wheeler 1996). The weaknesses of the SSA had led to many attempts to develop generalized elasto-plastic critical state constitutive models for unsaturated soils in late 1980s. In 1990, Alonso et al. (1990) proposed the first EP model for unsaturated soils, which was later called the BBM (Alonso et al. 1999). The most important feature of the BBM was the introduction of an LC yield curve in the  $p$ - $s$  plane on which the yield stress increases with the increase of suction, as shown in Figures 2.36a and 2.36b. The model was then extended to triaxial stress states by assuming elliptical yield curves at constant suctions in the  $q$ - $p$ - $s$  stress space as shown in Figure 2.36c. Figures 2.36a through 2.36c show the stress paths (straight lines with arrows) proposed by Alonso et al. (1990) to determine the model parameters for the BBM, which are suction-controlled isotropic compression tests, constant load drying-wetting tests, and suction-controlled triaxial shear tests, respectively. In such tests, only one stress variable, either  $p$  (Figure 2.36a) or  $s$  (Figure 2.36b) or shear stress  $q$  (Figure 2.36c), is changed, while the other stress variables remain unchanged in order to eliminate the hydro-mechanical coupling effects of unsaturated soils and make the test results easy to analyze. These stress paths are propounded according to the principle of divide-and-conquer approach and are typical in the characterization of unsaturated soil behavior although other similar stress paths were also used (Alonso et al. 1994; 1999; Wheeler 1996; Wheeler and Sivakumar 1995; Cui and Delage 1996; Sharma 1998; Hoyos 1998).



(a) SCTX/ISC(vary  $p$  only); (b) SWCC (vary  $s$  only); (c) SCTX/TS (vary  $q$  only)

Figure 2.36 Suggested stress paths to determine model parameters for the BBM



$$dv^e = -\kappa_s \frac{ds}{s + p_{at}} \tag{2.6}$$

$$dv = -\lambda_s \frac{ds}{s + p_{at}} \tag{2.7}$$

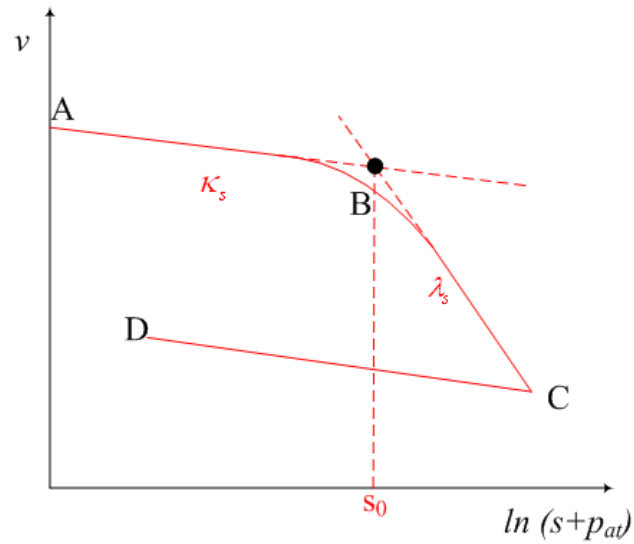


Figure 2.38 Drying-wetting test results ( $s = s_0 = \text{constant}$ )

Figure 2.39 shows the results for wetting collapse tests from some soils. This phenomenon was modeled by selection the  $N(s)$  and  $\lambda(s)$  as shown in Equations 2.4 and 2.5.

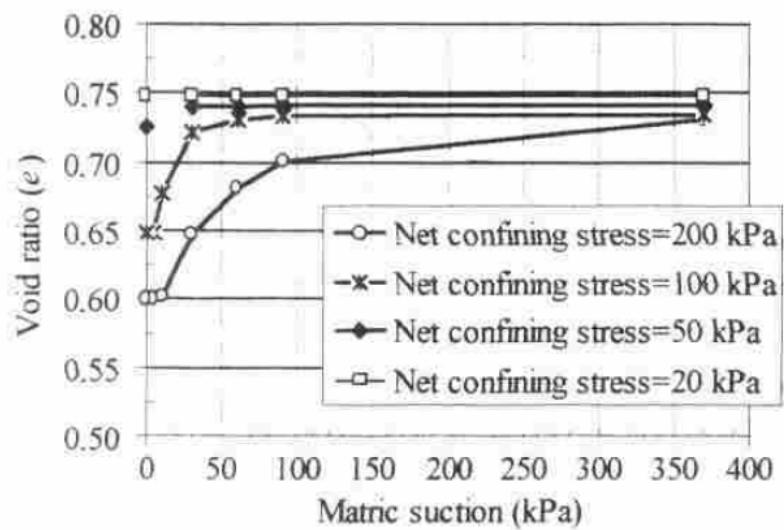


Figure 2.39 Wetting collapse tests

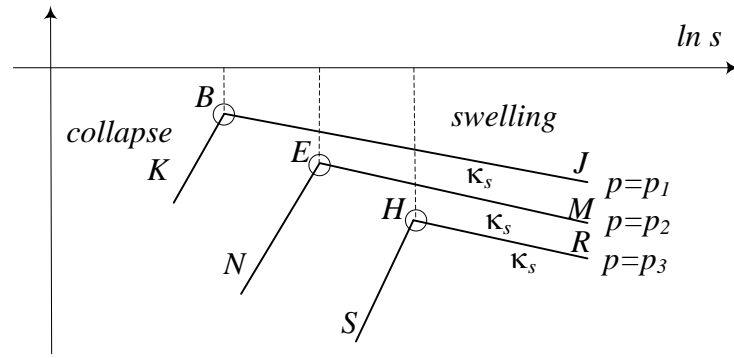


Figure 2.40 Idealized results for wetting collapse of a soil

The yield curves as shown in Figure 2.36 therefore have the following expressions:

$$p = p^c \left[ \frac{p_0^*}{p^c} \right]^{\frac{\lambda(0) - \kappa}{\lambda(s) - \kappa}} \quad (2.8)$$

$$s = e^{\frac{c_3 - c_1}{(\lambda_s - \kappa_s)}} - p_{at} = \text{constant} \quad (2.9)$$

The model was then extended to triaxial stress states by assuming elliptical yield curves at constant suctions in the  $q$ - $p$ - $s$  stress space. The yield surface as shown in Figure 2.41 has the following expression:

$$q^2 - M^2(p + p_s)(p_0 - p) = 0 \quad (2.10)$$

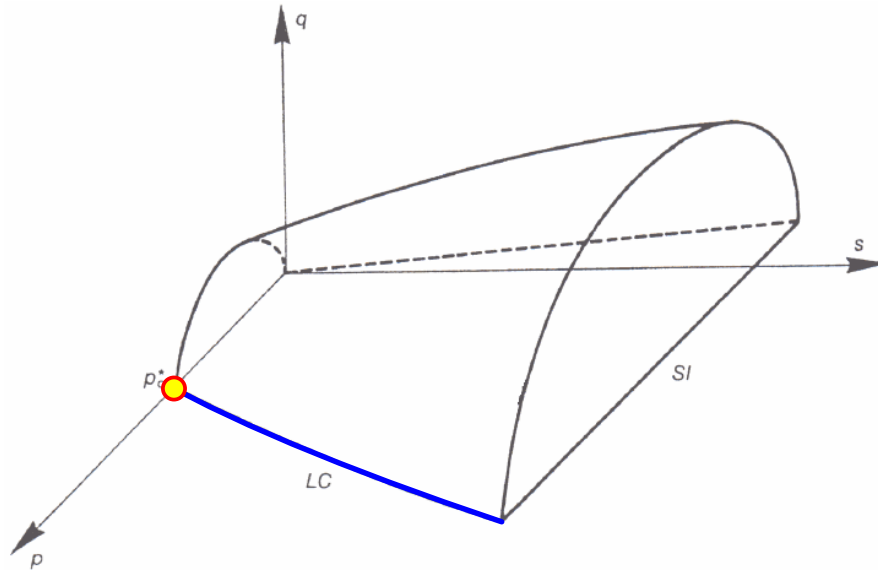


Figure 2.41 Yield surface in the p-q-s space in the BBM

The elastic deviatoric strain is calculated using the following equations:

$$d\varepsilon_s^e = \left( \frac{1}{3} G \right) dq \quad (2.11)$$

By assuming a non-associated flow rule, the plastic deviatoric strain using the following equation:

$$\frac{d\varepsilon_s^p}{d\varepsilon_{vp}^p} = \frac{2q\alpha}{M^2(2p + p_s - p_0)} \quad (\text{Non-associated flow rule}) \quad (2.12)$$

The following hardening laws are used to calculate the plastic volumetric strains.

$$\frac{dp_0^*}{p_0^*} = \frac{v}{\lambda(0) - \kappa} d\varepsilon_v^p \quad (2.13)$$

$$\frac{ds_0}{s_0} = \frac{v}{\lambda(0) - \kappa} d\varepsilon_v^p \quad (2.14)$$

The BBM successfully explained many features of unsaturated soils and received extensive acceptance. Since then many EP models have been developed (Alonso et al. 1994; 1999; Wheeler 1996; Wheeler and Sivakumar 1995; Cui and Delage 1996; Wheeler et al. 2003; Gallipoli et al. 2003; Sheng et al. 2004; 2008; Sanchez et al. 2005; Sun et al. 2008). Review of these EP models for unsaturated soils can be found in Delage and Graham (1995), Gens (1995), Wheeler and Karube (1995), Vanuat (2004), and Gens et al. (2006). Sheng et al. (2004) concluded that, from the EP theory point of view, all existing EP models have a similar framework and can be considered variants of the BBM. Gens et al. (2006) also considered that most existing EP models kept the same core of basic assumptions in the BBM, and sought to improve some of the limitations in the BBM as follows:

1. Overcome the difficulties in the transition between unsaturated and saturated states by using alternative stress variables [11, 47, 51, 58]. Some researchers used stress variables other than net normal stress and matric suction (such as Bishop's stress with  $\chi \square = S_r$ ) to realize a smooth transition between unsaturated and saturated states. However, this makes the representation of the stress paths more complex or impossible since data on water content is often not available or unreliable [12].
2. Develop a coupled hydraulic model which can consider the coupling between the mechanical and hydraulic behavior. Wheeler and Sivakumar [44] first pointed out that the BBM cannot be used to predict undrained conditions since there is no relationship was developed to describe the EP variations of the water phase. Wheeler [40] and Dangla et al. [46] were the first researchers who included hydraulic components in their constitutive models for unsaturated soils. Vaunat et al. [49] presented the first full attempt to couple hydraulic behavior with a mechanical model for unsaturated soils. This approach has been extensively used by many other researchers [11, 50, 56, 59-62], and is able to predict the irreversible change of degree of saturation during cyclic wetting and drying. Zhang and Lytton [70] however found that the proposed approach fails when the soil is subjected to an undrained loading-unloading process.

3. Development of constitutive models for unsaturated expansive soils. The BBM was developed for collapsible soils and slightly expansive soils [9]. It has limitations in modeling the behavior of highly expansive soils [41-43], particularly the dependency of swelling strains and swelling pressures on the initial state [71] and on the stress path [72] as well as strain accumulation during suction cycles [73-74]. Gens and Alonso [41] presented a conceptual basis for a model for expansive soils, which was improved by Alonso et al. [42]. Alonso et al. [43] suggested further improvements, and the revised version is called the Barcelona Expansive Model (BExM). Recently, Sanchez et al. [63] developed a formulation based on generalized plasticity concepts while keeping the same basic features and assumptions in the BExM. Zhang and Lytton [14-15] pointed out that shapes of yield curves are closely related to the soil behavior under isotropic conditions and the existence of the SI and SD curves in the BExM has not been experimentally verified. In addition, many researchers reported that compacted soil demonstrated expansive soil behavior under low confining pressure and collapsible soil behavior under high confining pressures [25-26]. It is therefore important to explain both expansive and collapsible soil behavior in a unified model. However, the BBM and BexM are vastly different.
4. Inclusion of non-mechanical (such as thermal variable on the stress-strain behavior for unsaturated soils [75-81]). This is mainly attributed to the fact that expansive clays are now widely used as waste-isolation barriers in the deep nuclear waste disposal technology, which is most viable means of disposing of high-level energy- or defense- radioactive waste [82].

None of the above problems have been solved. Of the four problems listed above, the second problem is most critical as the effect of load application is often idealized into two processes [83]: undrained loading and dissipation of excess pore water pressure (or suction). Solving the undrained conditions must precede the dissipation of excess pore water pressure (or suction). Without ability to predict undrained conditions, the existing models cannot be used for engineering purpose [68]. The fourth problem is a coupled thermo-hydro-mechanical stress (THM) problem which cannot be solved before the first three problems are solved.

In recent years, some researchers worked on the renewal of the Bishop's effective stress [84-85]. For example, recent work by Lu [84] shows that matric suction is not a stress variable. Khalili et al. [85] argued that the Bishop's effective stress in fact can explain those experimental results if EP behaviors are recognized. Regardless of these arguments, the BBM [9] is also well-accepted by researchers who used the Bishop-type effective stress for the constitutive modeling purpose [11, 12, 54-56, 58-60, 65, 85] and results from the SCTX tests are unanimously used for development and verifications of constitutive models for unsaturated soils (e.g. [84, 85]). This might be the reason why in the state-of-the-art report [8], it is suggested that the BBM should be considered as a canon of unsaturated soil mechanics.

## CHAPTER III

### DEVELOPMENT OF A NEW VOLUME MEASUREMENT METHOD

#### GENERAL

In the past few decades, several methods such as local strain measurement, double cell, digital image and laser profiling have been developed to measure the volume change of soil specimen during triaxial test. All these methods have their limitations. Till now, measuring the volume change of unsaturated soil is still a great challenge for researchers. In this study, an optical method was developed to reconstruct 3D model of unsaturated soil specimen during testing. For this method, the conventional triaxial test apparatus for saturated soils can be used without any modification. This was achieved by integrating photogrammetry, optical-ray tracing, and least-square optimization to reconstruct 3D model for unsaturated soil specimen during testing. The following sections introduce the proposed method and two proof-of-concept validation tests.

General principles applied in this method are discussed in details which included camera calibration, orientation and refraction correction for three dimensional (3D) coordinates computation. To apply this method, camera was calibrated first to determine the interior orientation parameters. Then, based on photogrammetry, soil specimen as well as the acrylic cell was imaged for the determination of the geometric properties of acrylic cell. After this, 3D coordinates of object in water can be estimated by using least square method with help of refraction correction. With this method, quantitative 3D measurement is possible. A method validation on a stainless steel cylinder and a case study on soil specimens were also performed and test results by using this method are presented as well.

#### PRINCIPLE OF PHOTOGRAMMETRY

Photogrammetry is a method to determine the 3D coordinates of points on an object using photographic images taken from different orientations. As a non-contact 3D measurement technique, photogrammetry is widely used in different fields, such as topographic mapping, architecture, engineering, manufacturing, quality control, and geology. Its principle can be described by using a stereopair as shown in Figure 3.1. In photogrammetry, ideal pinhole camera model was adopted. Images taken from different positions are different for the same object (Figure 3.1a). The differences can be used to calculate the orientations of the camera from where the images are taken (orientation process). Usually, for a specified image (Figure 3.2a), the upper left corner was set as the origin of the 2D pixel coordinate system. Pixel position  $(m_o, n_o)$  of a certain point in this image were identified and converted to  $(x_e, y_e)$  on its 2D image coordinate system (Figure 3.2b) by using Equation 12. In this image coordinate system, principal point was set as the origin of the coordinate system. For a single image, a local 3D coordinate system can be built as shown in Figure 3.2d. Origin of the coordinate system is set at the perspective center of the camera. Imagine the object has a coordinate system in which the XY plane lies on the imaging surface and the Z axis lies along the optical axis of the camera. In this local coordinate system, the coordinates of the object on the image plane can be expressed as  $(x_o, y_o, -f)$ .

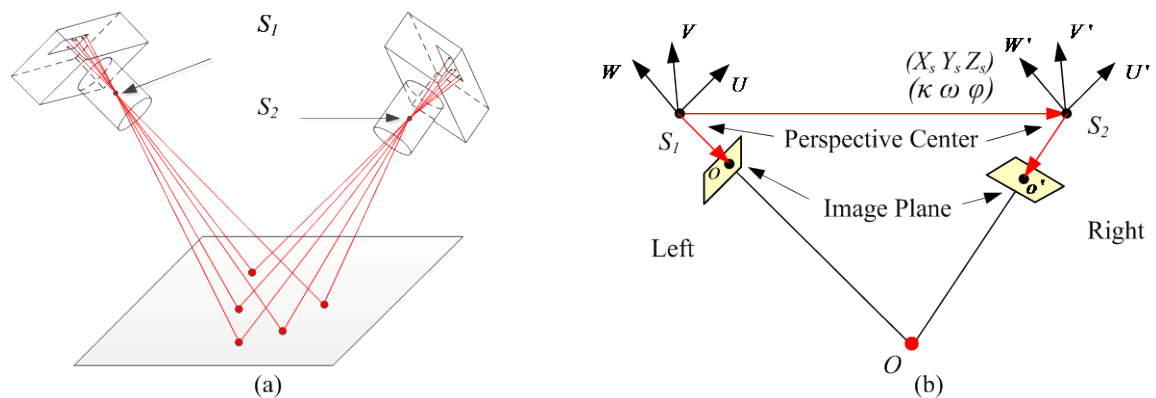


Figure 3.1 Principle of the Photogrammetry

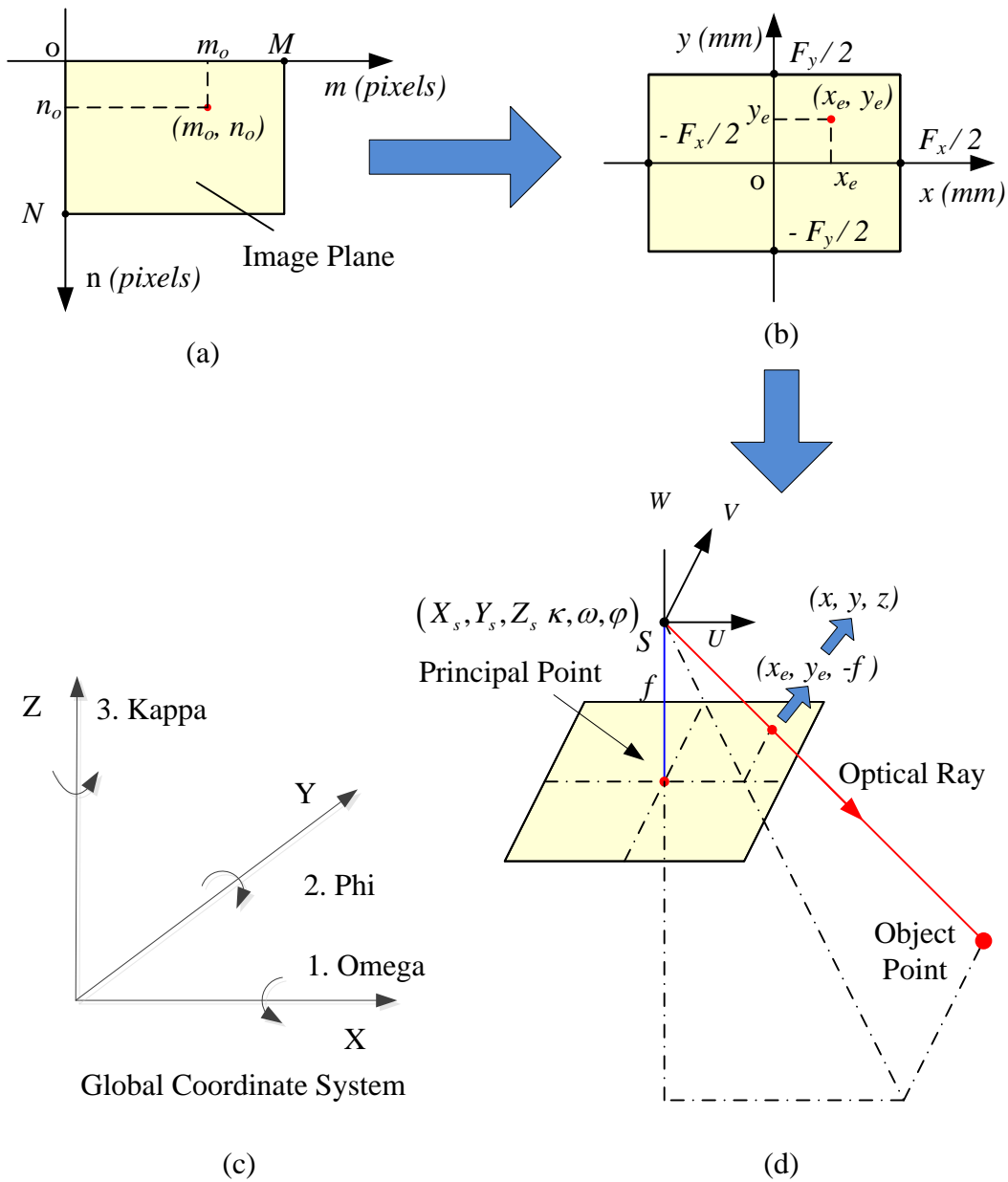


Figure 3.2 Coordinate systems: (a) Pixel coordinate system; (b) Image coordinate system; (c) Global coordinate system; (d) Local coordinate system

$$\begin{cases} x_e = \frac{m_o}{M} * F_x - P_x \\ y_e = -\frac{n_o}{N} * F_y + P_y \end{cases} \quad (3.1)$$

where,

$x_e, y_e$  = image coordinates in x and y directions,

- $m_o, n_o$  = pixel coordinates in x and y directions,  
 $M, N$  = total pixel numbers in x and y directions,  
 $F_x, F_y$  = format size in x and y directions, and  
 $P_x, P_y$  = principal point value in x and y directions.

Usually, this local coordinate system is required to be converted to the global coordinate system as shown in Figure 3.2c with an origin difference of  $(X_s, Y_s, Z_s)'$  and rotational angles of  $(\kappa, \omega, \varphi)'$ . The 3D coordinates and directional angles in the global coordinate system can be determined as  $(X_s, Y_s, Z_s)'$  and directional angles of  $(\kappa, \omega, \varphi)'$ . Then, in the global coordinate system, the 3D coordinates of the point of interest on the image plane can be calculated through Equation 3.2.

$$\begin{pmatrix} x \\ y \\ z \end{pmatrix} = \begin{pmatrix} a_1 & a_2 & a_3 \\ b_1 & b_2 & b_3 \\ c_1 & c_2 & c_3 \end{pmatrix} \begin{pmatrix} x_e \\ y_e \\ -f \end{pmatrix} + \begin{pmatrix} X_s \\ Y_s \\ Z_s \end{pmatrix} \quad (3.2)$$

where,

$$\begin{pmatrix} a_1 & a_2 & a_3 \\ b_1 & b_2 & b_3 \\ c_1 & c_2 & c_3 \end{pmatrix} = \text{rotation matrix which can be determined from Equation 3.3.}$$

$$\begin{pmatrix} a_1 & a_2 & a_3 \\ b_1 & b_2 & b_3 \\ c_1 & c_2 & c_3 \end{pmatrix} = \begin{pmatrix} \cos \varphi \cos \kappa & \sin \omega \sin \varphi \cos \kappa + \cos \omega \sin \kappa & \sin \omega \sin \kappa - \sin \varphi \cos \omega \cos \kappa \\ -\cos \varphi \sin \kappa & \cos \omega \cos \kappa - \sin \omega \sin \varphi \sin \kappa & \sin \varphi \cos \omega \sin \kappa + \sin \omega \cos \kappa \\ \sin \varphi & -\sin \omega \cos \varphi & \cos \omega \cos \varphi \end{pmatrix} \quad (3.3)$$

Thus, for the point of interest on an image plane, the directional unit vector of the traced optical ray is obtained and shown in Equation 3.4 with a start point of  $(X_s, Y_s, Z_s)'$ . So, the function for the traced optical ray  $\vec{i} = (\alpha_a, \beta_a, \gamma_a)'$  in the global coordinate system can be written as Equation 3.5.

$$\vec{i} = \begin{pmatrix} \alpha_a \\ \beta_a \\ \gamma_a \end{pmatrix} = \frac{1}{\sqrt{(x-X_s)^2 + (y-Y_s)^2 + (z-Z_s)^2}} \begin{pmatrix} x-X_s \\ y-Y_s \\ z-Z_s \end{pmatrix} \quad (3.4)$$

$$\frac{x-X_s}{\alpha_a} = \frac{y-Y_s}{\beta_a} = \frac{z-Z_s}{\gamma_a} \sqrt{\quad} \quad (3.5)$$

As can be seen in Figure 3.1b, for a single object point “*O*”, its projection on the left and right image are “*o*” and “*o'*”. Vectors  $\overline{S_l S_r}$ ,  $\overline{S_l o}$  and  $\overline{S_r o'}$  are in the same plane. So, a nonlinear equation (coplanarity equation in Photogrammetry) was obtained which is shown in Equation 3.6.

$$\overline{S_l S_r} \cdot (\overline{S_l o} \times \overline{S_r o'}) = \begin{vmatrix} X_s & Y_s & Z_s \\ U & V & W \\ U' & V' & W' \end{vmatrix} = X_s V W' + U V' Z_s + U' Y_s W - X_s V' W - U Y_s W' - U' V Z_s = 0 \quad (3.6)$$

To determine the orientation of the two cameras, the 3D coordinates of the principle point for camera station on the left can be set as (0,0,0) with rotation angle of (0,0,0). The six unknown parameters for the other camera station need to be identified which are coordinates of perspective center ( $X_s, Y_s, Z_s$ ) as well as three Euler angles ( $\kappa, \omega, \varphi$ ) of right camera. Any one of  $X_s, Y_s, Z_s$  can be set as given value which specified the scale for the object coordinate system. For the left five unknowns, theoretically, five corresponding optical rays are sufficient to yield a finite number of solutions. Since there are numerous pairs (far more than five) of corresponding points on the two images, the redundancy in information can be used to perform an optimization analysis to accurately determine the camera orientation so that the errors in measurement are minimal. In addition, multiple images can be taken from different orientations with sufficient overlap, which can provide more redundant equations, to improve the accuracy of the result. Once the camera orientations are determined, for a point of interest, optical rays can be constructed from the perspective centers of the cameras through image plane to the point on the object which is so-called “forward intersection”. The forward intersection process is performed by using Equation 3.6 (collinearity equations). For each corresponding point in a stereopair, four collinearity

equations were available. Any three of those equations can be used to determine the 3D coordinates of the point in object coordinate system.

$$\begin{cases} x = -f \frac{a_1(X - X_s) + b_1(Y - Y_s) + c_1(Z - Z_s)}{a_3(X - X_s) + b_3(Y - Y_s) + c_3(Z - Z_s)} \\ y = -f \frac{a_2(X - X_s) + b_2(Y - Y_s) + c_2(Z - Z_s)}{a_3(X - X_s) + b_3(Y - Y_s) + c_3(Z - Z_s)} \end{cases} \quad (3.7)$$

As a noncontact 3D measurement technique, photogrammetry is used in different fields for more than 160 years and proven to be able to provide measurements with high accuracy. However, for volume measurement on unsaturated soil, due to the refraction at the interfaces of air-chamber and chamber-water, light is bended which cause image point shift in the image plane as shown in Figure 2.2. Therefore, collinearity condition is disturbed and photogrammetry is no longer suitable for measuring the soil specimen in the acrylic confining chamber during triaxial testing. Therefore, for the proposed method, photogrammetry is used to determine camera orientations and shape and location of the confining acrylic chamber. 3D coordinates of object in water cannot be directly determined through triangulation due to refraction. However, although the optical rays bended when reached the two refraction interface (air to acrylic cell and acrylic cell to water), rays still can be traced based on Snell's law which is discussed in details as follows.

### **OPTICAL-RAY TRACING TECHNIQUE**

Optical-ray tracing technique is proposed to take into account the effect of the refraction. It is well known that the refraction of optical ray at the interface of different media follows Snell's law as shown in Figure 3.3 and Equation 3.8.

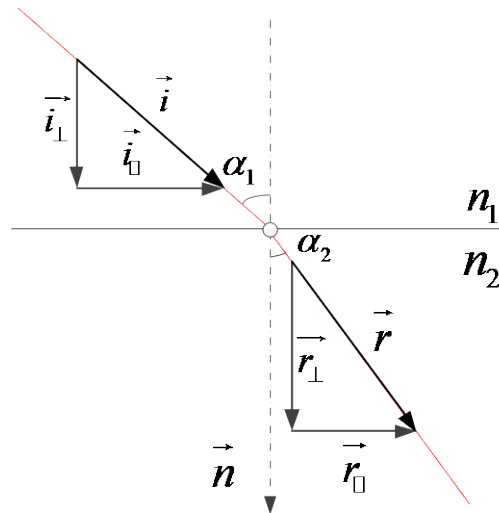


Figure 3.3 Snell's law

$$n_1 \sin \theta_1 = n_2 \sin \theta_2 \quad (3.8)$$

where,

$$\begin{aligned} n_1, n_2 &= \text{refraction index, and} \\ \theta_1, \theta_2 &= \text{incident angle and refraction angle.} \end{aligned}$$

As can be seen in Figure 3.3, direction vectors of incident and refracted rays are  $\vec{i}$  and  $\vec{r}$ . The direction change of optical ray after refraction follows Snell's law. The refracted ray  $\vec{r}$  can be split into a tangent and normal part which is shown in Equation 3.9. Same split can be applied to incident ray  $\vec{i}$ , Equations 3.10 and 3.11 can be drawn. Because of Snell's law, the tangent part of the refracted ray can be obtained as shown in Equation 3.11. Since  $\vec{r}_{\parallel}$  and  $\vec{i}_{\parallel}$  are parallel and point in the same direction, Equation 3.13 can be obtained based on Equation 3.12.

$$\vec{r} = \vec{r}_{\perp} + \vec{r}_{\parallel} \quad (3.9)$$

$$\vec{i}_{\parallel} = \vec{i} - \vec{i}_{\perp} = \vec{i} - \cos \alpha_1 \vec{n} \quad (3.10)$$

$$\sin \alpha_1 = \frac{|\vec{i}_\perp|}{|\vec{i}|}, \sin \alpha_2 = \frac{|\vec{r}_\perp|}{|\vec{r}|} = |\vec{r}_\perp| \quad (3.11)$$

$$|\vec{r}_\perp| = \sin \alpha_2 = \frac{n_1}{n_2} \sin \alpha_1 = \frac{n_1}{n_2} |\vec{i}_\perp| \quad (3.12)$$

$$\vec{r}_\perp = \frac{n_1}{n_2} \vec{i}_\perp = \frac{n_1}{n_2} (\vec{i} - \cos \alpha_1 \vec{n}) \quad (3.13)$$

Also,

$$\vec{r}_\perp = \cos \alpha_2 \vec{n} = \sqrt{1 - \left(\frac{n_1}{n_2}\right)^2 \sin^2 \alpha_1} \vec{n} \quad (3.14)$$

Then,

$$\vec{r} = \frac{n_1}{n_2} \vec{i} + \left( \sqrt{1 - \left(\frac{n_1}{n_2}\right)^2 \sin^2 \alpha_1} - \frac{n_1}{n_2} \cos \alpha_1 \right) \vec{n} \quad (3.15)$$

As can be seen in Equation 3.15, as long as the incident ray, normal vector of the refractive surface, and the refractive indices of the two media are given, the optical ray after refraction can be determined which is referred as optical-ray tracing in this paper.

## PROPOSED METHOD

With the development of image sensors, qualities of digital photographs for photogrammetry are getting better in resolution which would bring better accuracy for 3D geometry measurement. The procedures of the proposed optical method are as follows: (1) Camera calibration; (2) Testing system setup (post measurement targets on the acrylic cell wall, test specimen, and the load frame); (2) Image capturing and orientation; (3) 3D reconstruction of the acrylic cell wall; (4) Optical-ray tracing; and (5) Least square estimation for the determination of 3D coordinates. For this method, images can be captured at any orientation to obtain best quality and accuracy. Also, each image represents one measurement and as many images as possible can be used. The proposed optical method in this study is considered as an improved version of DIA. None of the assumptions used in Macari et al. (1997)'s method is needed.

## Camera Calibration

As discussed before, an ideal pinhole camera model was used for illustration of principle of photogrammetry. The ideal pinhole camera model does not include geometric distortions caused by lenses. A perfect lens would render straight lines as straight as shown in Figure 3.4a. However, in this real world, most practical lenses aren't that good, though, and instead bend lines outwards (barrel distortion as shown in Figure 3.4b) or inwards (pincushion distortion as shown in Figure 3.4c). Wide-angle and wide-range zoom lenses often suffer particularly badly from these distortions. Also, for all practical lenses, different from pinhole camera, multiple lenses are used to focus light. In addition, principal distance, principal point and format size of the image sensor are unknowns. Thus, before photogrammetric analysis, camera used for image capturing should be calibrated first to determine the characteristics of a camera so it can be used as an ideal pinhole camera to extract precise and reliable 3D geometric information from images.

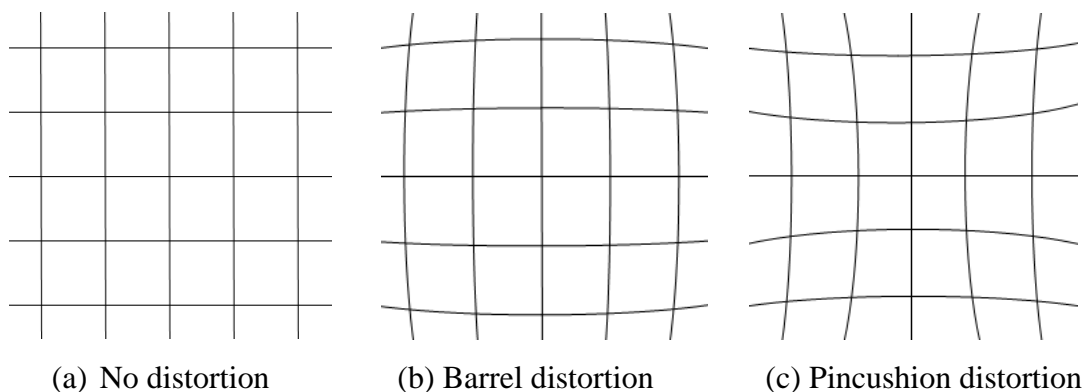


Figure 3.4 Lens distortion

Accurate camera calibration is a necessary prerequisite for the extraction of precise and reliable 3D metric information from images. The algorithms are generally based on ideal pinhole camera model, with the most popular approach being the well-known self-calibrating bundle adjustment (Triggs et al. 2000), which was first introduced to close-range photogrammetry in the early 1970s. Usually, the calibration was done by taking pictures of a calibration target which geometry is known. The evaluation algorithm calculates the intrinsic parameters (focal length, principle point, distortion

parameters) for each camera, the extrinsic parameters (translation vector and rotation matrix) as well as the uncertainties of the calibration parameters, resulting from the deviations of the detected markers from the model positions. In this study, the calibration process involved placing a calibration target (Figure 3.5) in the field of view, and collecting 12 images of the target at different camera orientations. From these images, various system parameters (e.g., actual focal length  $f$ , pixel numbers  $M$  and  $N$ , image sensor format size  $F_x$  and  $F_y$ , principal point  $P_x$  and  $P_y$ , radial lens distortion parameters  $K_1$  and  $K_2$  and decentering lens distortion parameters  $P_1$  and  $P_2$ ) were extracted. Usually, camera is suggested to be recalibrated after being used for a certain time. Table 3.1 presents the calibration results for camera with same lens before and after being used for a certain time.

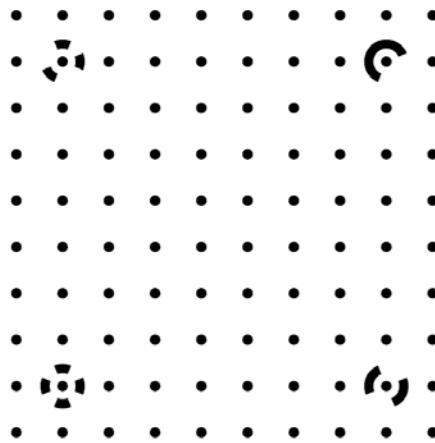


Figure 3.5 Calibration targets (from Photomodeler)

Due to the lens distortion, camera cannot be treated as a pinhole camera and images captured cannot be directly used for refraction correction. However, images can be idealized based on calibration results to eliminate the lens distortion. As can be seen in Equation 3.15, corrected image point coordinates can be determined based on its original image coordinates, radial lens distortion component (Equation 3.16) and decentering lens distortion component (Equation 3.17). After idealization, lens distortion was eliminated, principal point was centered and a new group of calibration parameters with no distortion parameters were generated as well. Then, ideal pinhole camera model can be applied for images after idealization.

$$\begin{aligned}x_c &= x + r_x + d_x \\y_c &= y + r_y + d_y\end{aligned}\tag{3.15}$$

where,

- $x, y$  = image coordinates in x and y directions,  
 $x_c, y_c$  = corrected image point coordinates in x and y directions,  
 $r_x, r_y$  = radial lens distortion correction in x and y directions (Equation 3.16),  
and  
 $d_x, d_y$  = decentering lens distortion correction in x and y directions (Equation 3.17).

$$\begin{aligned}r_x &= x \left[ K_1(x^2 + y^2) + K_2(x^2 + y^2)^2 \right] \\r_y &= y \left[ K_1(x^2 + y^2) + K_2(x^2 + y^2)^2 \right]\end{aligned}\tag{3.16}$$

$$\begin{aligned}d_x &= P_1 \left[ (x^2 + y^2) + 2x^2 \right] + 2P_2xy \\d_y &= P_2 \left[ (x^2 + y^2) + 2y^2 \right] + 2P_1xy\end{aligned}\tag{3.17}$$

where,

- $K_1, K_2$  = radial lens distortion parameters and  
 $P_1, P_2$  = decentering lens distortion parameters.

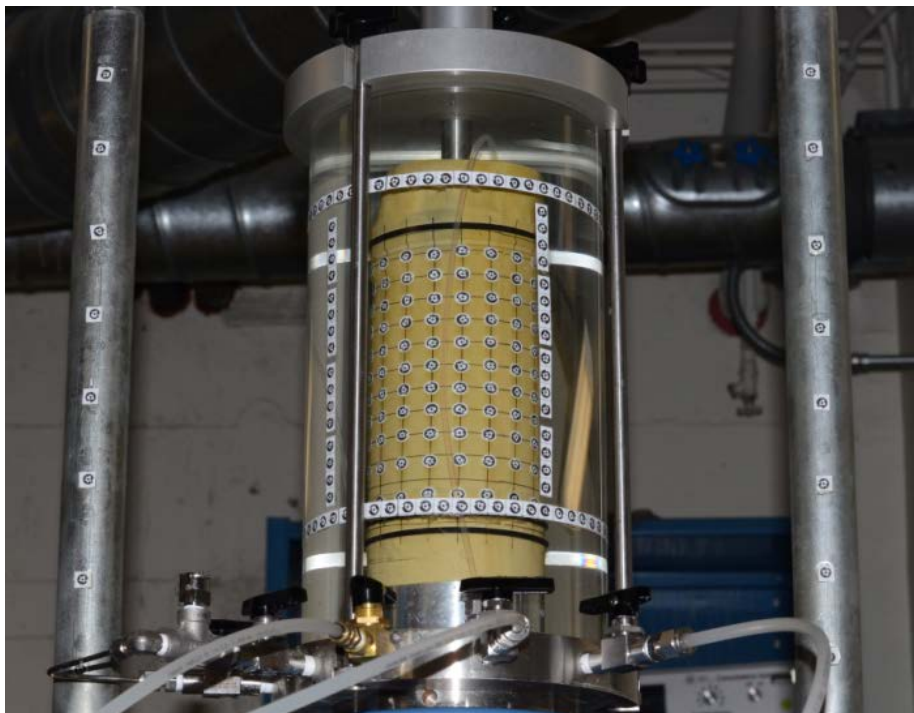
### Triaxial System Setup

In order to perform the volume change measurement on unsaturated soil specimen during triaxial testing by this optical method, some setup on the triaxial test apparatus were required to be done before measurement. The setup included posting measurement targets on specimen surface (Figure 3.6a), posting measurement targets on acrylic cell wall (Figure 3.6b), and posting measurement targets on load frame (Figure 3.6c). Measurement targets on the load frame were used to set up the global

coordinate system so that all the measurements can be compared in the same coordinate system. Measurement targets on the cell wall were used to reconstruct the 3D position and shape of the cell. Measurement targets on the specimen surface were used to monitor the deformation of the soil specimen during loading.



(a) Measurement targets on specimen      (b) Measurement targets on cell wall



(c) Measurement targets on load frame

Figure 3.6 Testing system setup

### Image Capturing and Orientation

Images can be captured from any orientations following the pattern in Figure 3.7. Camera stations that are “far away” from the testing system were used to capture images covered the load frame as shown in Figure 3.6c. Camera stations around the testing system in a circle were used to capture images only covered the acrylic cell with specimen inside. Better results were achieved by taking more than three photographs for each area/point of interest. For each test mentioned above, images capturing at different camera stations as shown in Figure 3.7 would took about 2 minutes.

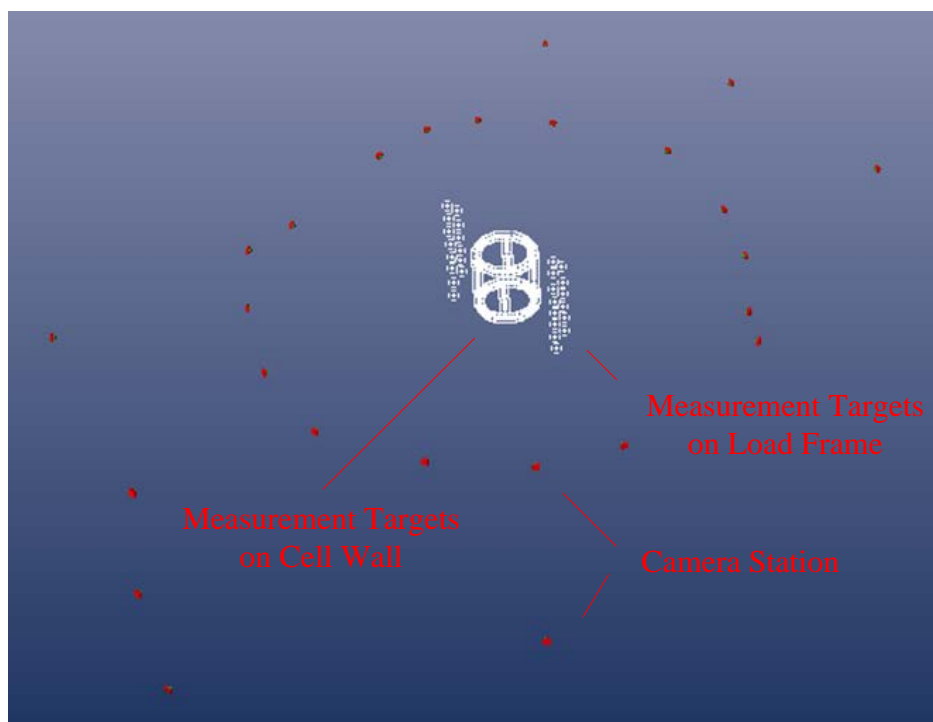


Figure 3.7 Typical camera stations

After photographing, images obtained were processed for orientations. The images were first idealized by using the camera calibration parameters to eliminate the lens distortions. Corresponding targets in different images were then used to determine the orientations of the photographs based upon the principle of photogrammetry. Only the targets on the load frame and the outside surface of the acrylic cell wall were used to

meet the requirement of the photogrammetry. Measurement targets on specimen surface cannot be used to determine the image orientation because of the distortion introduced by refraction.

### 3D Reconstruction of Acrylic Cell

Using the orientations of the photographs, the coordinates of the targets on the outside surface of the confining chamber were calculated according to the photogrammetry. These 3D coordinates defined the shape and position of the confining chamber in the global coordinate system. Experimental results indicated that the acrylic confining chamber could expand to a barrel-shape due to the applied water pressure as shown in Figure 3.8. As a result, similar to the distortion in radial direction, there were also magnification effects in the vertical direction. If a cylindrical shape is used to best-fit a barrel-shaped acrylic confining chamber, the error in the vertical direction can be as high as 0.2 mm even if the proposed method was used which is not tolerable.

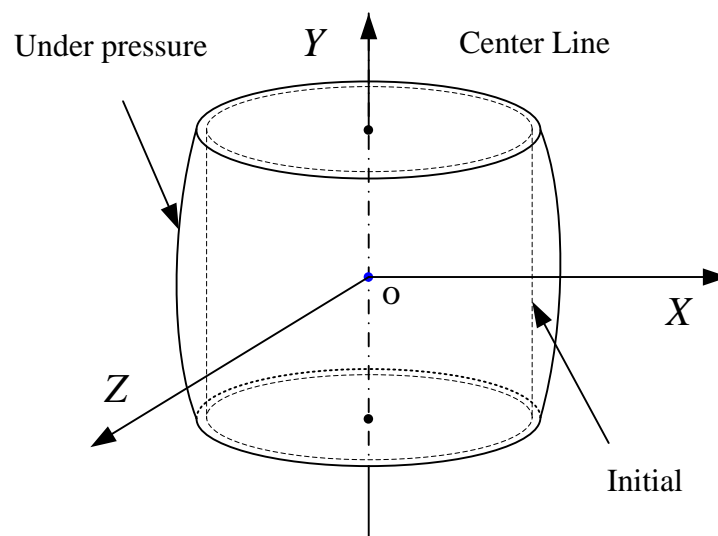


Figure 3.8 Deformation of confining chamber under pressure

Since the shape of the acrylic cell was known as cylindrical or barrel-shaped, Equations can be used to represent the cell wall. The regression to determine the function of the outside surface of the cell wall was divided in two steps. First, a cell coordinate system was built which is shown in Figure 3.8. In this coordinate system, the function for the barrel shaped acrylic cell wall can be expressed as Equation 18.

To translate the 3D coordinates of the targets to this cell coordinate system, Equation 3.19 was used. Second, the converted 3D coordinates can then be used for regression by using least square method. After regression process, coefficients  $A$ ,  $B$ ,  $C$ , as shown in Equation 3.18, the center point of the acrylic cell in the global coordinate system  $(X_r, Y_r, Z_r)'$  as well as the three directional angles  $(\kappa', \omega', \varphi)'$  can be determined.

$$X^2 + Z^2 = AY^2 + BY + C \text{ (outside)} \quad (3.18)$$

$$\begin{cases} X = a'_1 x + a'_2 y + a'_3 z - X_r \\ Y = b'_1 x + b'_2 y + b'_3 z - Y_r \\ Z = c'_1 x + c'_2 y + c'_3 z - Z_r \end{cases} \quad (3.19)$$

where,

$$\begin{pmatrix} a'_1 & a'_2 & a'_3 \\ b'_1 & b'_2 & b'_3 \\ c'_1 & c'_2 & c'_3 \end{pmatrix} = \begin{pmatrix} \cos \varphi' \cos \kappa' & \sin \omega' \sin \varphi' \cos \kappa' + \cos \omega' \sin \kappa' & \sin \omega' \sin \kappa' - \sin \varphi' \cos \omega' \cos \kappa' \\ -\cos \varphi' \sin \kappa' & \cos \omega' \cos \kappa' - \sin \omega' \sin \varphi' \sin \kappa' & \sin \varphi' \cos \omega' \sin \kappa' + \sin \omega' \cos \kappa' \\ \sin \varphi' & -\sin \omega' \cos \varphi' & \cos \omega' \cos \varphi' \end{pmatrix}$$

### Refraction Correction

After 3D reconstruction of the acrylic cell wall, optical rays from cameras to the specimen surface can be traced as shown in Figure 3.9. A specimen is located inside of the acrylic cell filled with water. Different images were captured for the specimen from different orientations (Figure 3.9a). Using camera station  $S_2$  as an example, for a specific point of interest on specimen surface, its pixel position on the corresponding image can be determined. The pixel position would then be to determine the corresponding optical ray by using Equations 3.1, 3.2, 3.3, 3.4 and 3.5. Equation 3.5 was set to be equal to  $l_1$  as shown in Equation 3.20, which is the distance between the start point and the intersection. With help of Equations 3.18 and 3.19, two solutions for  $l_1$  can be found. The little one is the correct answer which physically means the optical ray intersect with the cell wall for the first time. So, the 3D coordinates for the intersection  $C_2 = (x_o, y_o, z_o)'$  can be determined through Equation 21.

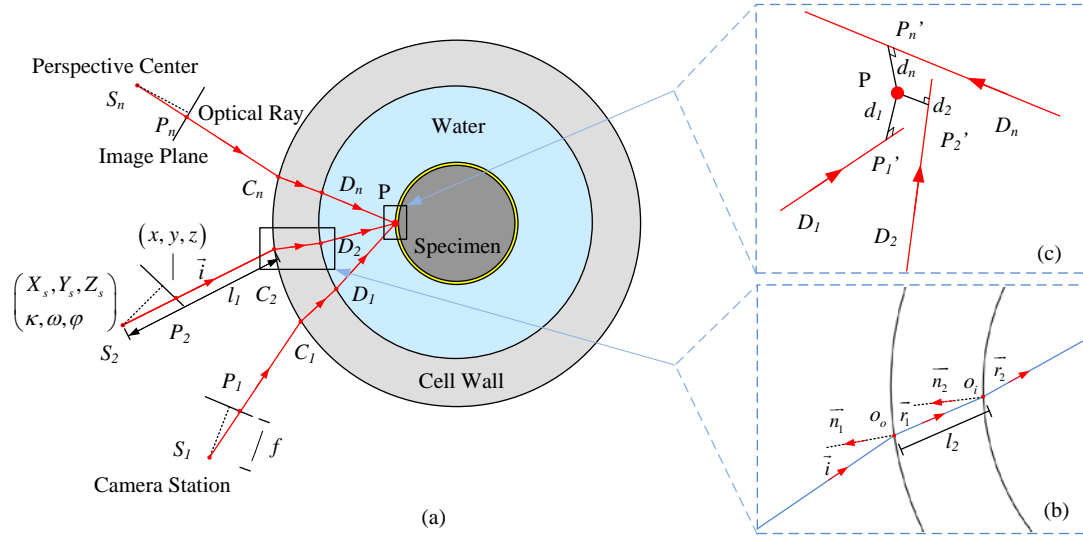


Figure 3.9 Optical-ray tracing based on Snell's law

$$\frac{x - X_s}{\alpha_a} = \frac{y - Y_s}{\beta_a} = \frac{z - Z_s}{\gamma_a} = l_1 \quad (3.20)$$

$$\begin{pmatrix} x_o \\ y_o \\ z_o \end{pmatrix} = l_1 \begin{pmatrix} \alpha_a \\ \beta_a \\ \gamma_a \end{pmatrix} + \begin{pmatrix} X_s \\ Y_s \\ Z_s \end{pmatrix} \quad (3.21)$$

The function for the outer surface is known as Equation 3.18. To determine the normal vector  $\vec{n}_1 = (\alpha_{n1}, \beta_{n1}, \gamma_{n1})'$  as shown in Figure 3.9b at the intersection  $C_2$ , partial derivatives for  $x$ ,  $y$  and  $z$  for Equation 3.18 was determined as shown in Equations 3.22 and 3.23.

$$\vec{n}_1 = \begin{pmatrix} \alpha_{n1} \\ \beta_{n1} \\ \gamma_{n1} \end{pmatrix} = \begin{pmatrix} \frac{\partial F}{\partial x} / \left( \left( \frac{\partial F}{\partial x} \right)^2 + \left( \frac{\partial F}{\partial y} \right)^2 + \left( \frac{\partial F}{\partial z} \right)^2 \right) \\ \frac{\partial F}{\partial y} / \left( \left( \frac{\partial F}{\partial x} \right)^2 + \left( \frac{\partial F}{\partial y} \right)^2 + \left( \frac{\partial F}{\partial z} \right)^2 \right) \\ \frac{\partial F}{\partial z} / \left( \left( \frac{\partial F}{\partial x} \right)^2 + \left( \frac{\partial F}{\partial y} \right)^2 + \left( \frac{\partial F}{\partial z} \right)^2 \right) \end{pmatrix}_{C_2} \quad (3.22)$$

$$\begin{pmatrix} \frac{\partial F}{\partial x} \\ \frac{\partial F}{\partial y} \\ \frac{\partial F}{\partial z} \end{pmatrix}_{C_2} = \begin{pmatrix} 2(a_1'x + a_2'y + a_3'z - X_r)a_1' + 2(c_1'x + c_2'y + c_3'z - Z_r)c_1' - 2A(b_1'x + b_2'y + b_3'z - Y_r)b_1' - Bb_1' \\ 2(a_1'x + a_2'y + a_3'z - X_r)a_2' + 2(c_1'x + c_2'y + c_3'z - Z_r)c_2' - 2A(b_1'x + b_2'y + b_3'z - Y_r)b_2' - Bb_2' \\ 2(a_1'x + a_2'y + a_3'z - X_r)a_3' + 2(c_1'x + c_2'y + c_3'z - Z_r)c_3' - 2A(b_1'x + b_2'y + b_3'z - Y_r)b_3' - Bb_3' \end{pmatrix}_{C_2} \quad (3.23)$$

Then, the vector  $\vec{r}_1 = (\alpha_{r1}, \beta_{r1}, \gamma_{r1})'$  for the optical ray  $\vec{i} = (\alpha_a, \beta_a, \gamma_a)'$  after refraction can be determined through Snell's law as shown in Equation 3.24. Since the thickness of acrylic cell wall  $t$  can be measured before testing, the function for the inside surface of the cell wall can be written as Equation 3.25.

$$\vec{r}_1 = \begin{pmatrix} \alpha_{r1} \\ \beta_{r1} \\ \gamma_{r1} \end{pmatrix} = \frac{n_a}{n_c} \vec{i} + \left( \sqrt{1 - \left(\frac{n_a}{n_c}\right)^2 \left(1 - (\vec{i} \bullet \vec{n}_1)^2\right)} - \frac{n_a}{n_c} |(\vec{i} \bullet \vec{n}_1)| \right) \vec{n}_1 \quad (3.24)$$

$$X^2 + Z^2 = AY^2 + BY + (C - 2t\sqrt{C} + t^2) \quad (\text{inside}) \quad (3.25)$$

With a new start point  $C_2 = (x_o, y_o, z_o)'$ , the intersection  $D_2$  between the refracted optical ray  $\vec{r}_1$  and the inner surface of the acrylic cell wall (Equation 3.25) can be determined through the method as addressed before. Also, the refracted optical ray  $\vec{r}_2 = (\alpha_{r2}, \beta_{r2}, \gamma_{r2})'$  after first refraction can be determined by performing optical-ray tracing technique again.

### Least Square Optimization

Snell's law is a theoretical equation and it will give the analytic solution as long as all the inputs are correct. Although the photogrammetric method has high accuracy, it is expected that there are still some errors in the obtained camera orientations and acrylic chamber positions. Consequently, it is very likely for  $D_1P$ ,  $D_2P$ , and  $D_nP$  not to intersect at the same point  $P$  as shown in Figure 3.9a. Instead, after optical ray tracing two times as shown in Figure 3.9b, they might be rays  $D_1P'$ ,  $D_2P'$ , and  $D_nP_n'$  in the 3D space with no intersection as shown in Figure 3.9c. To overcome this limitation, a least-square optimization approach is used to best approach the real

coordinate of point  $P$ . The 3D coordinate of the measurement target  $P$ , as shown in Figure 3.9c, can be set as  $(x_p, y_p, z_p)$ . Then, the distance  $d_i$  between the measurement target and each optical ray can be determined through Equation 3.26. by finding a combination of coordinate  $(x, y, z)$  which can minimize the sum of the square of the distances from the point to the optical rays as shown in Equation 3.27. At least three photographs (measurements) are needed to perform the search. The more photographs used, the higher the accuracy is. Photographs are also captured from orientation which can provide to obtain the best quality and accuracy. Using this approach, there is no need to make assumptions regarding the initial shape, position, and deformation patterns of the specimen.

$$d_i = \sqrt{(x_p - x_o)^2 + (y_p - y_o)^2 + (z_p - z_o)^2 - ((x_p - x_o)\alpha_{r2} + (y_p - y_o)\beta_{r2} + (z_p - z_o)\gamma_{r2})^2} \quad (3.26)$$

$$d_{total} = \sum_{i=1}^n d_i \quad (3.27)$$

## METHOD VALIDATION

For this proposed method, to reach a high accuracy, a digital single-lens reflex camera with a fixed focal length lens is strongly recommended. In this study, as shown in Figure 3.10, Nikon D7000 (pixel solution:  $4928 \times 3264$ ) with a fixed focal length lens (AF-S NIKKOR 50 mm f/1.4G) was adopted for the method validation. In this study, camera was calibrated and calibration results are presented in Table 3.1 (calibration 1). After being used for a while, the camera was calibrated again as shown in Table 3.2 (calibration 2).



Figure 3.10 Camera and lens

Table 3.1 Camera calibration parameters

Parameter	Calibration 1		Calibration 2	
	Before	After	Before	After
	Idealization	Idealization	Idealization	Idealization
$f$ (mm)	53.3864	53.3864	53.4027	53.4027
$M$ (pixel)	4928	4928	4928	4928
$N$ (pixel)	3264	3264	3264	3264
$F_x$ (mm)	23.9982	24.7439	23.9965	24.7875
$F_y$ (mm)	15.8961	16.3871	15.8961	16.416
$P_x$ (mm)	12.0865	12.372	12.1016	12.3937
$P_y$ (mm)	8.1022	8.1963	8.1164	8.208
$K_1$ ( $10^{-5}$ )	5.443	0	5.475	0
$K_2$ ( $10^{-9}$ )	-2.266	0	-3.751	0
$P_1$ ( $10^{-6}$ )	-3.094	0	-4.164	0
$P_2$ ( $10^{-6}$ )	2.023	0	0.7847	0

As can be seen in Table 3.1, the actual focal length of the 50 mm fixed focal length lens is 53.3864 and 53.4027 mm from the two calibrations when the camera is treated as an ideal pinhole camera model. The principle point is not exactly at the center of the image sensor. However, after idealization, lens distortions were eliminated and principle point was centered.

### Validation on Stainless Steel Cylinder

A stainless steel cylinder (Figure 3.11a) covered with measurement targets was used to validate the proposed method accuracy on 3D position and volume measurement. Different confining pressure levels ranging from 0 to 600 kPa were applied during testing. Elastic modulus of stainless steel ranges from 180 GPa to 200 GPa. With the applied maximum confining pressure of 600 kPa in this study, the volumetric strain is less than  $2 \times 10^{-6}$  and the steel cylinder can be considered as rigid. A rigid specimen provided a good reference for evaluating measurement accuracy in the validation tests. Also, drained triaxial test on a saturated sand specimen (Figure 3.6) was performed to validate the volume measurement accuracy by comparing the measured

volume change by the proposed method to the actual volume change obtained by monitoring the amount of water flow into or out of the saturated sand specimen.

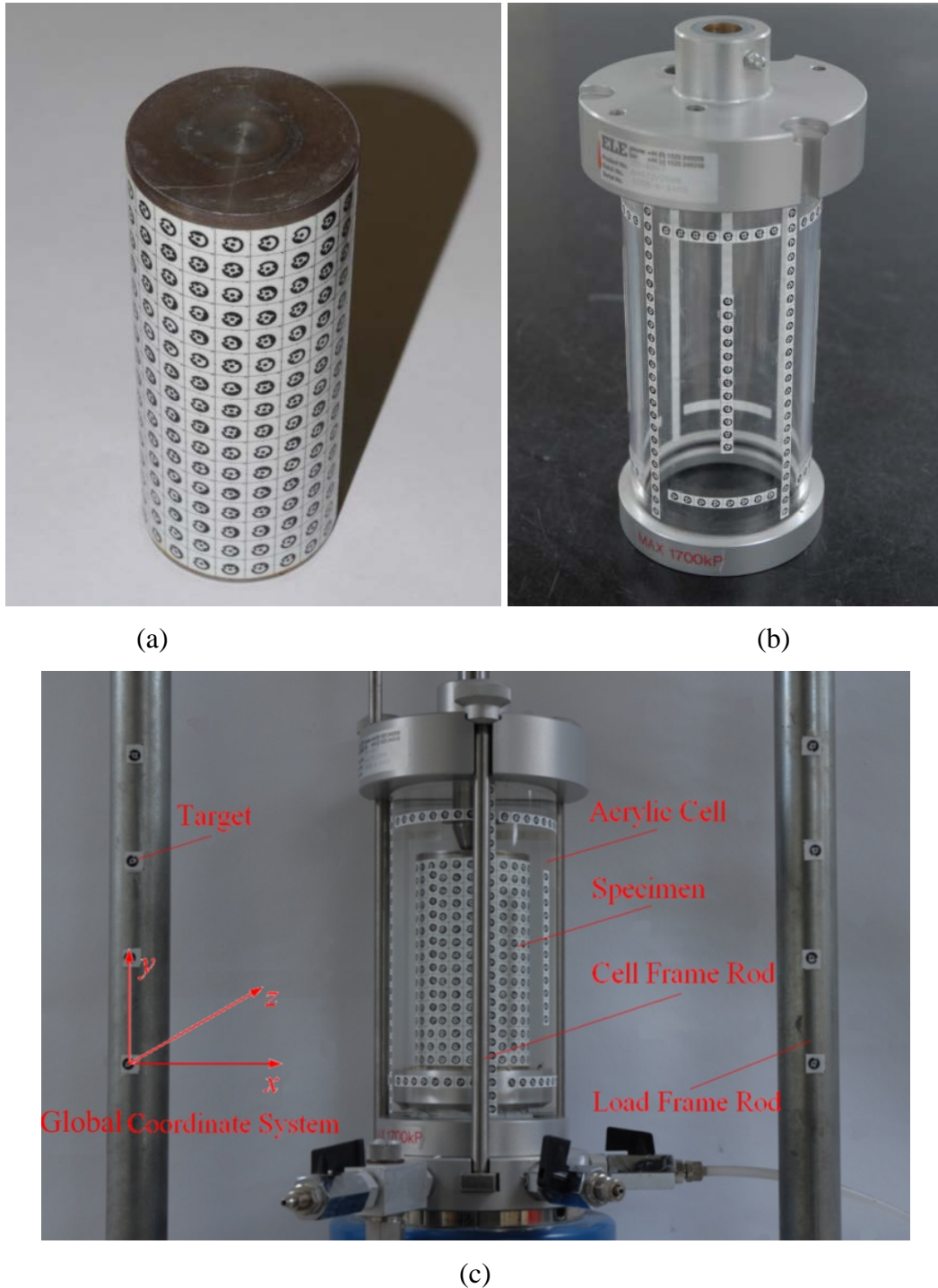


Figure 3.11 System setup: (a) Stainless steel cylinder with measurement targets; (b) Acrylic cell with measurement targets; (c) Load frame setup

For validation test on the stainless steel cylinder, the conventional ELE triaxial test apparatus for saturated soils as shown in Figure 3.11 was used to validate the

accuracy on 3D position measurement of the proposed method. The confining acrylic chamber, which has been used for years as shown in Figure 3.11b, is 8" in height, 4" in outer diameter, and 0.24" in thickness with a refractive index of 1.491. 16 measurement targets were posted on the load frame to set up the global coordinate system so that all the measurements can be compared in the same coordinate system as shown in Figure 3.11c. A total of 218 measurement targets were posted to the outside surface of the acrylic chamber, which included 2 circles (39 targets/circle) and 8 vertical stripes (12-25 targets/strip). The stainless steel cylinder in Figure 3.11a was used to as a soil specimen with 336 measurement targets (21 targets/circle $\times$ 16 circle) on its surface. Each measurement target was assigned a specific number for future identifications and comparisons.

The experimental program included reconstruction and measurements of the 3D images of the steel cylinder under the following conditions: 1. exposed in air, 2. installed in the triaxial test apparatus with 0 kPa, 200 kPa, 400 kPa, and 600 kPa confining pressure. The experiments were performed in the following way: (1) firmly fix the stainless steel cylinder on the bottom platen of the triaxial test apparatus without the confining chamber; (2) take photographs from different orientations; (3) carefully install the confining chamber and slowly fill it with water; (4) take photographs from different orientations; (5) increase the confining water pressure to 200 kPa and take photographs from different orientations; and (6) repeat step (5) with the confining water pressures changing to 400 kPa and 600 kPa. Photographs can be taken from any orientations following the pattern in Figure 3.7.

Figure 3.12 shows the diameter changes of the smaller ELE triaxial cell (the one with steel cylinder inside) under different inside water pressure. When the confining water pressure increased from 0 kPa to 600 kPa, the diameter of the confining chamber increased from approximately 100.44 mm to 100.60 mm. Assume that the height of the confining chamber does not change, for the steel cylinder used (50 mm in diameter and 100 mm in height), it caused about 2.5% error in the volumetric strain if the expansion of the confining chamber is not taken into account. Note that the above tests were performed in about 1 hour. Triaxial tests for unsaturated soils usually take

very long time (2-3 months/test). It is therefore expected that the resulted errors will be much higher due to creep of the confining chamber under pressure.

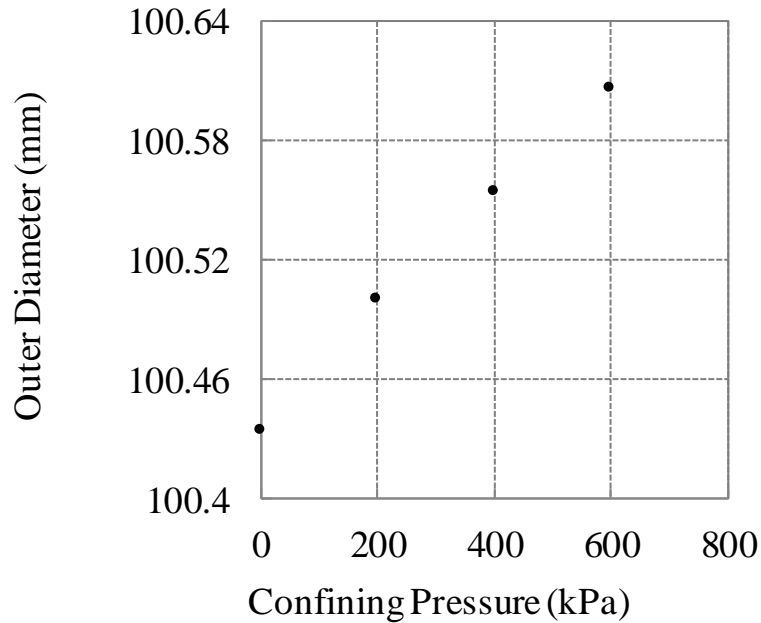


Figure 3.12 Cell deformation due to applied confining pressure

After the shape and location of the confining chambers were defined, the coordinates of the measure targets on sample surface (stainless steel cylinder and saturated sand specimen) were calculated using the optical-ray tracing and least square optimization techniques as discussed previously. A detailed example on the 3D position calculation of a specified measurement target on specimen surface could be found in Appendix A. The volumes of the samples were calculated using the AUTOCAD® Civil 3D for all the tests.

For the validation test on the stainless steel cylinder, test results were compared under the same global coordinate system as shown in Figure 3.13 with the results calculated for the steel cylinder when exposed in the air by assuming results for this test were “true” values. Table 3.2 shows the 3D coordinates results of the measurement targets on sample surface for all the tests which is also shown in Figure 3.14 for the cross sections from 1 and 16. No visible difference was found for all the test results. Using the global coordinate system as shown in Figure 3.9, measurement errors were also

estimated by calculating the displacement of each point “moving” from its position in the test exposed in the air to that in other tests when the steel cylinder subjected to different confining pressures. It was found that the average displacements (errors) for 336 targets ranged from 0.056 mm to 0.076 mm with standard deviations varying from 0.033 to 0.061mm (Table 3.2). The total volumes of the cylinder varied from 221.525 cm<sup>3</sup> (600 kPa) to 221.813 cm<sup>3</sup> (200 kPa), while the corresponding “true” value was 222.039 cm<sup>3</sup> (in air). The errors ranged from 0.131% to 0.232%. Analysis of the test results also indicated that many assumptions used in the Macari et al. (1997) cannot be satisfied. For example, without calibration, a commercial camera cannot be treated as ideal pinhole camera and it is very difficult to accurately control its position through manual installation. The confining chamber can deform under pressure and the soil specimen can never be installed at the center of the chamber.

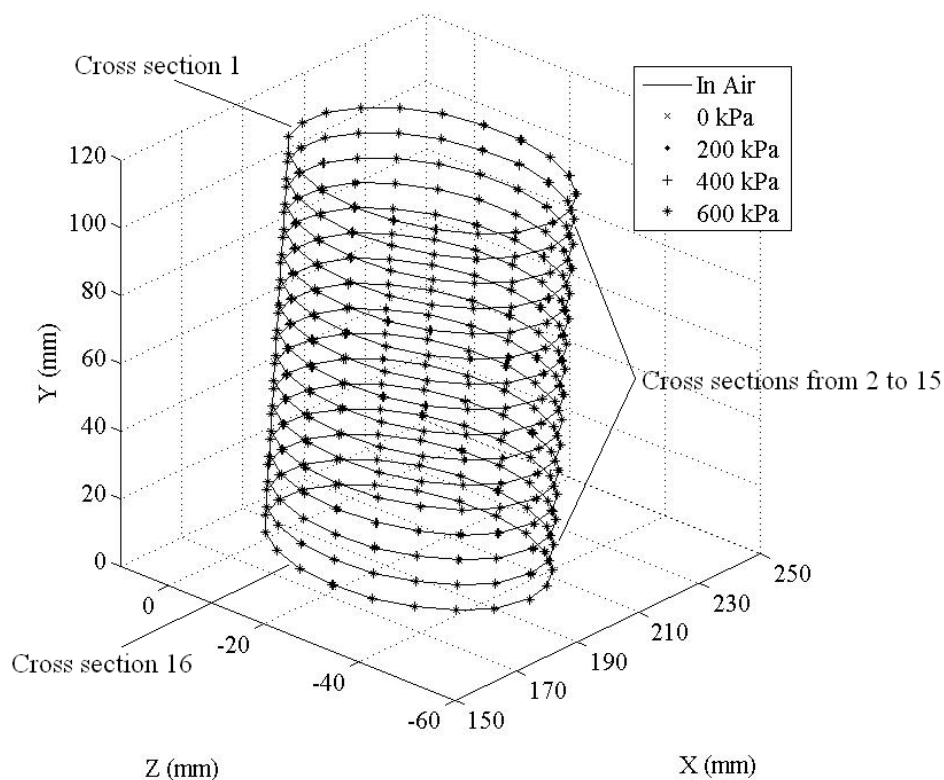
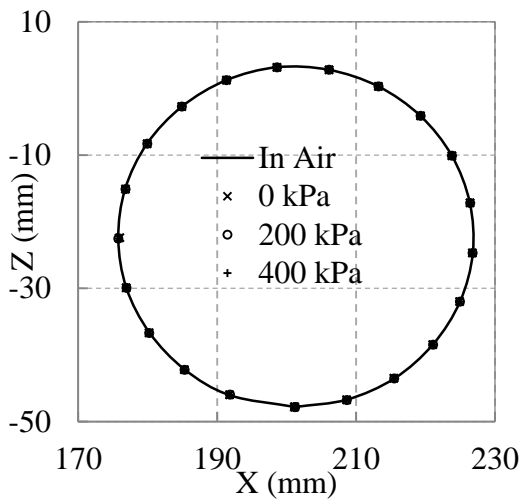


Figure 3.13 3D coordinates of the targets on specimen surface

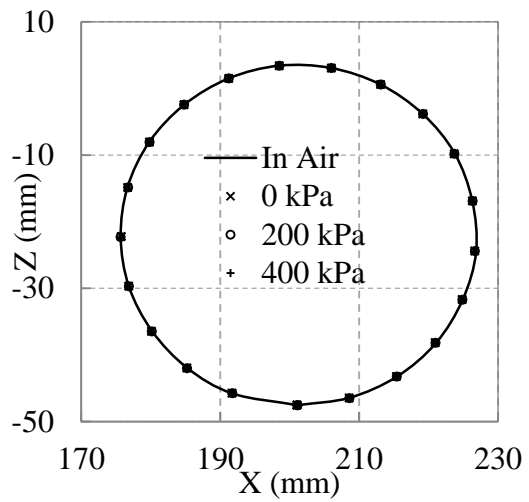
Table 3.2 Measurement accuracy under different confining pressures

Case	Displacement (mm)		Volume accuracy	
	Average	Standard deviation	Volume (cm <sup>3</sup> )	Error (%)

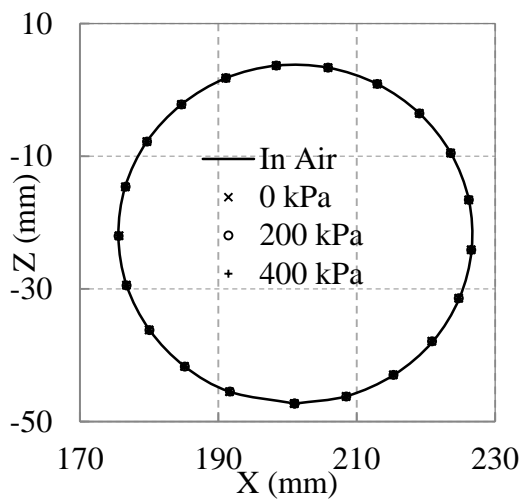
In air	0	0	222.039	0
0 kPa	0.076	0.061	221.749	-0.131
200 kPa	0.056	0.042	221.813	-0.102
400 kPa	0.063	0.033	221.766	-0.123
600 kPa	0.07	0.049	221.525	-0.232



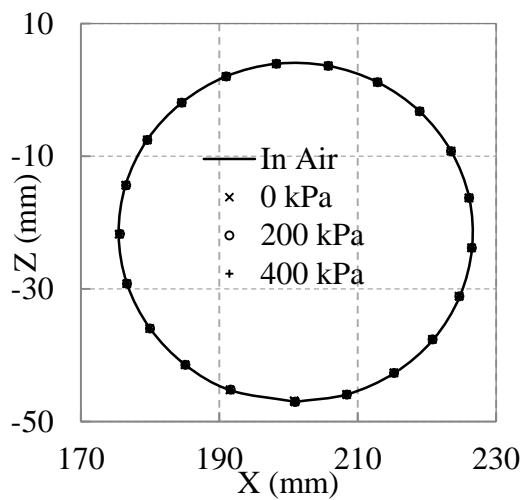
(1)



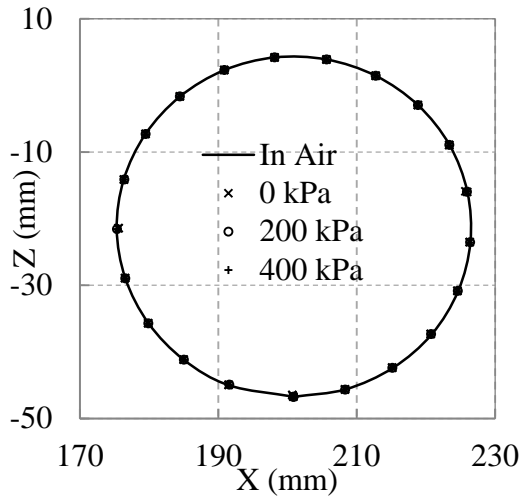
(2)



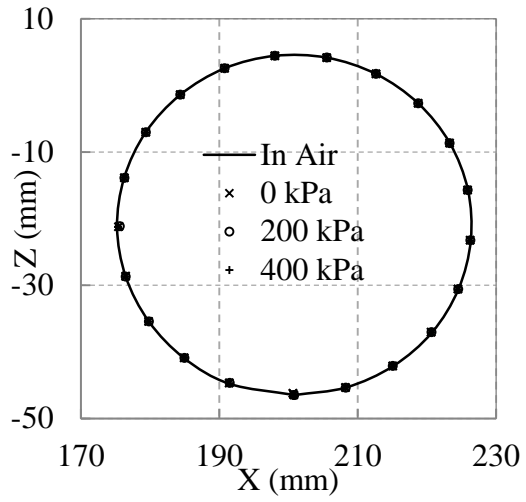
(3)



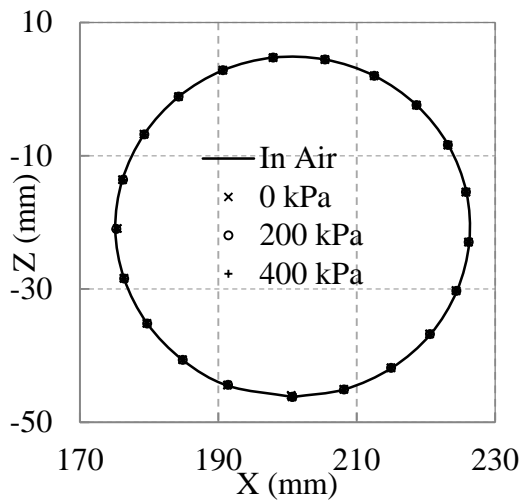
(4)



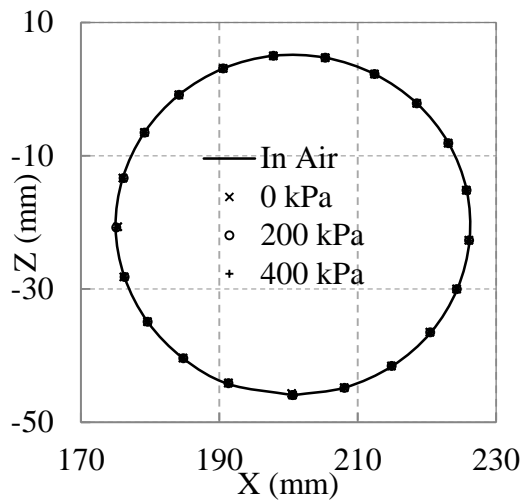
(5)



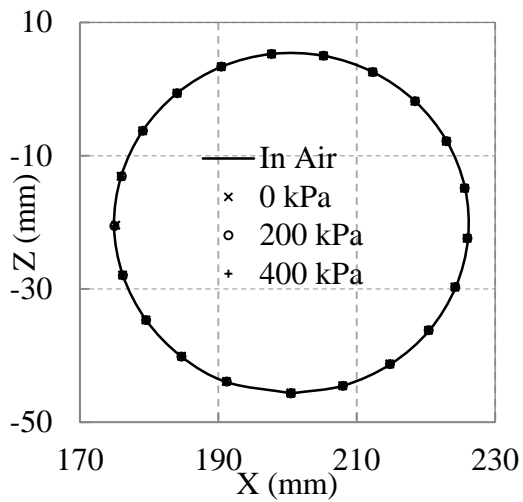
(6)



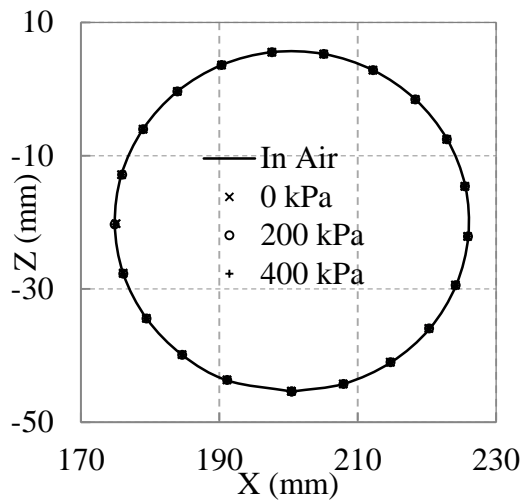
(7)



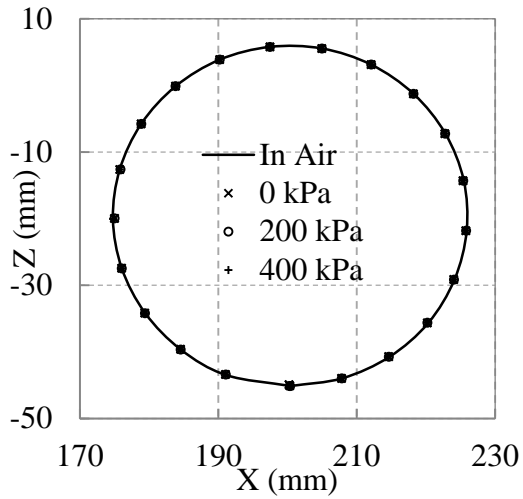
(8)



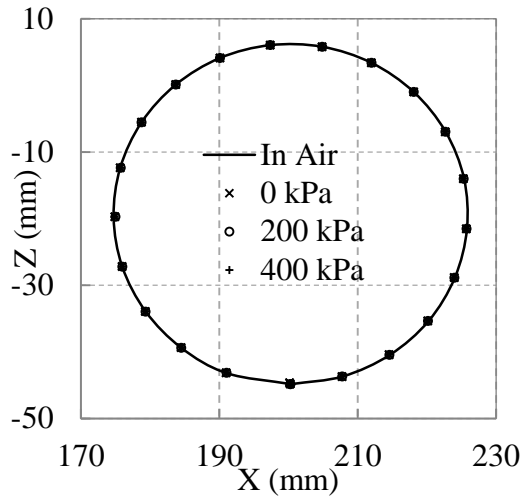
(9)



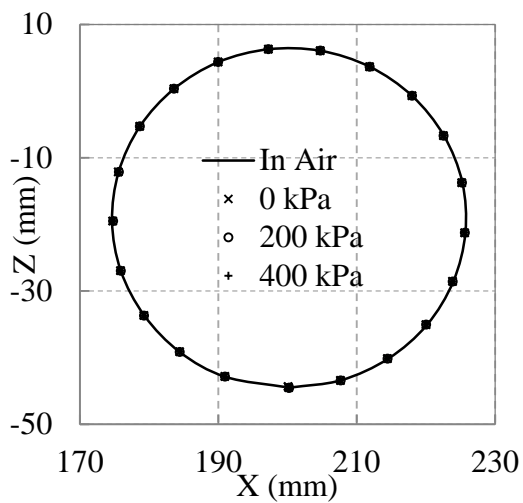
(10)



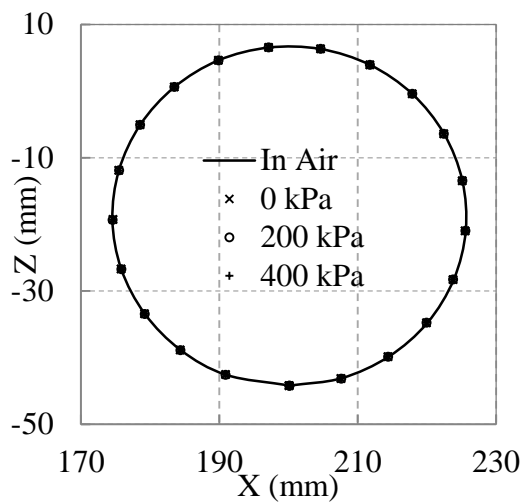
(11)



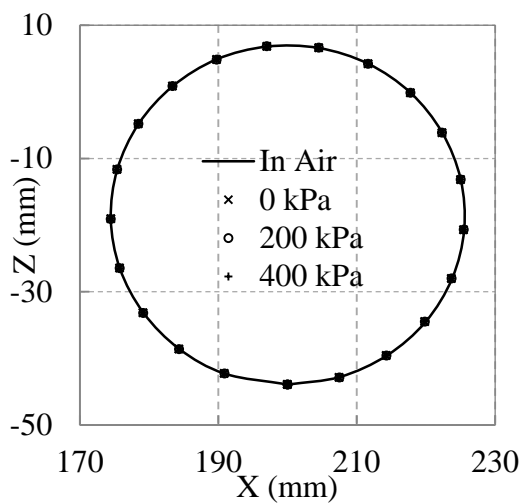
(12)



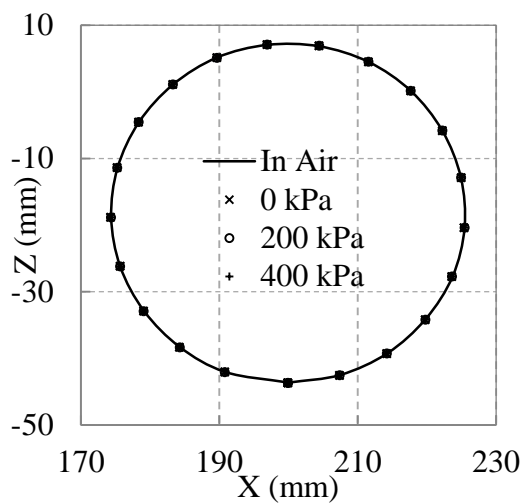
(13)



(14)



(15)



(16)

Figure 3.14 3D coordinates comparison for the 16 cross sections

### Validation on Saturated Sand Specimen

Beside the test on stainless steel cylinder, a case study by using cylindrical saturated sand specimen was conducted under drained conditions as shown in Figure 3.6. In this case, the used testing system was still the one for the validation test on stainless steel cylinder (ELE triaxial test apparatus). Instead of the 4" by 8" acrylic chamber, a brand-new confining acrylic chamber as shown in Figure 3.6b, which is 12" in height, 6.5" in outer diameter, and 0.38" in thickness with a refractive index of 1.491, was used to validate the proposed method on the saturated specimen. A total of 174 measurement targets were posted to the outside surface of the acrylic chamber, which included 2 circles (55 targets/circle) and 4 vertical stripes (16 targets/strip). Oven dried standard Ottawa fine sand (0.075 to 0.425 mm) as shown in Figure 3.12 was used for specimen preparation. Latex membrane (Figure 3.15) used was pre-gridded. A mold lined with this membrane was used to hold the specimen during compaction. After compaction, specimen (71 mm × 137 mm) was carefully mounted on the pedestal of the triaxial cell as shown in Figure 3.6a. A suction of 50 kPa was applied to hold the sand specimen in place during sealing. Then, 176 measurement targets (16 targets/circle × 11 circles) were posted on the pre-gridded membrane. To ensure that the volume change of specimen can be well represented by the movement of those measurement targets, two circles of measurement targets were posted on the top cap and the pedestal as shown in Figure 3.6a. In this way, the entire specimen was covered by the measurement targets. After this, cell chamber was installed and filled with tap water (Figure 3.6c). To short the saturation process on the sand specimen, carbon dioxide (CO<sub>2</sub>) was used to seep slowly upward from the bottom of the specimen to remove air in sand. Then, de-aired water was allowed to saturate the sand specimen from the bottom of the specimen. After this, a back pressure of 400 kPa was applied to dissolve all left air and CO<sub>2</sub> for several hours. Net confining pressure was maintained to be constant at 35 kPa during this saturation process. When a B value (0.98 in this case) greater than 0.95 was reached, saturation process was considered to be finished. Then, chamber pressure and back pressure can be simultaneously decreased to 100 kPa and 0 kPa, respectively. Drained triaxial test was performed after this.

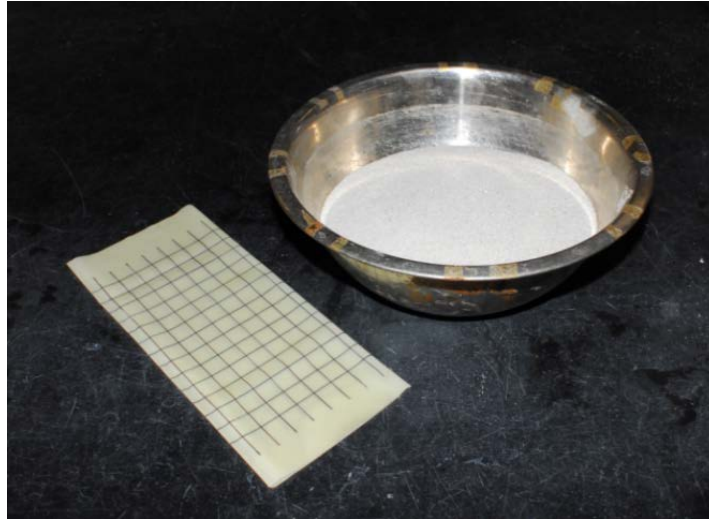


Figure 3.15 Membrane and sand used for specimen preparation

For this drained triaxial test, a confining pressure of 100 kPa was used. A loading rate of 1 mm/min was applied to generate some volume change of the saturated specimen. During loading, drain valve was kept open to allow water flow into or out of the specimen. The volume change of the specimen was recorded by monitoring the water flow. After a certain displacement, load was paused and drainage valve was closed. Then, the image capturing could be performed. In this way, there is no volume change on the specimen during image capturing. For each volume measurement by using the proposed method, 25 images around the specimen were used. The validation test was stopped when a total displacement of 10 mm was reached.

For the validation test on the saturated sand specimen, a comparison between the results of actual volume change (monitoring water flow into or out of specimen) and the volume measured by proposed method was presented in Table 3.3. Volume change detected by proposed method is very close to the actual volume change recorded by the amount of water flow into or out of the saturated specimen as shown in Figure 3.17. By comparing the differences of the volume changes between these two methods, an average and maximum error of 0.065% and 0.11% was obtained, respectively. Also, the movement of all the measurement targets on the specimen surface, as shown in Figure 3.17, were well recorded which could be used for the strain localization analysis. With increase of vertical displacement, cylindrical specimen generally turned to barrel shaped. An attempt to perform undrained test by

using saturated sand specimen turned out to be unsuccessful due to the water cavitation inside the specimen. As a result, the measured volume of the saturated sand specimen is not a constant.

Table 3.3 Measurement accuracy under shear load

Displacement (mm)	Volume Change (cm <sup>3</sup> )		Error (%)
	Actual	Proposed method	
0	0	0.00	0.000
2	-0.1	-0.25	-0.029
4	1.8	2.18	0.073
6	4.3	4.10	-0.039
8	7.5	6.94	-0.108
10	10.4	10.56	0.031

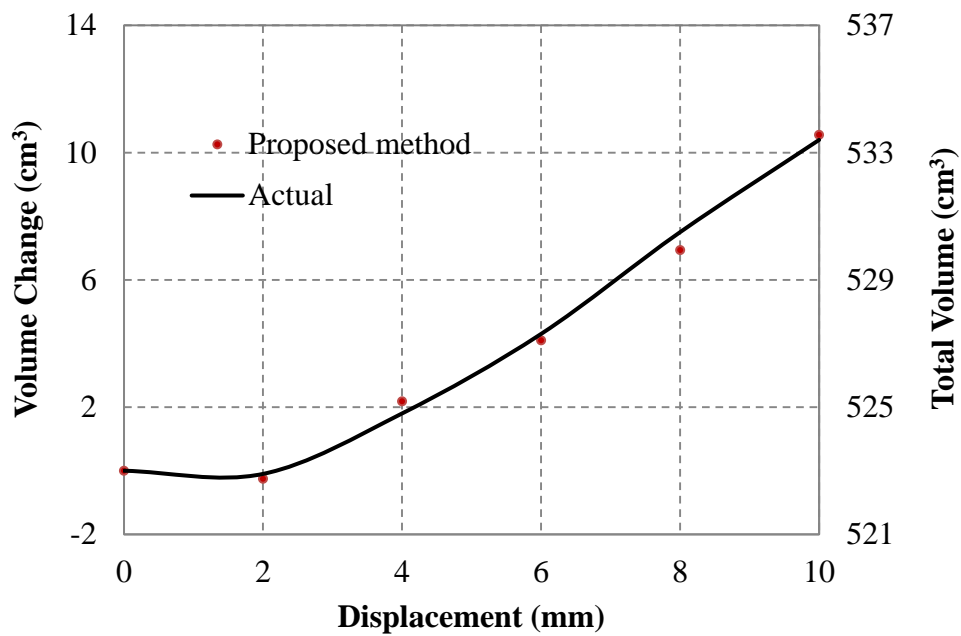


Figure 3.16 Comparison of volume change

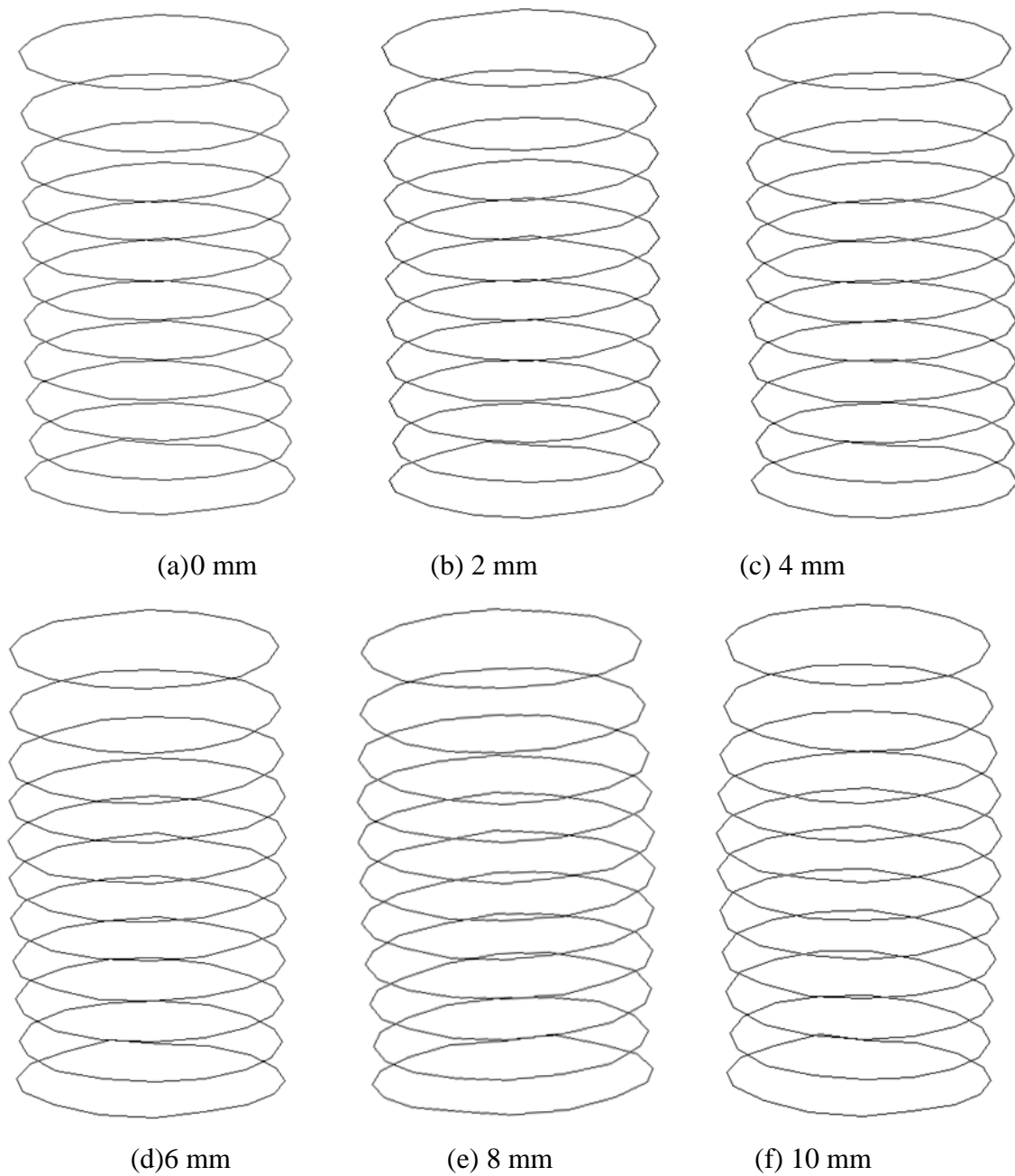


Figure 3.17 Soil deformations under shear load:  
(a) 0 mm; (b) 2 mm; (c) 4 mm; (d) 6 mm; (e) 8 mm; (f) 10 mm

### **ERROR SOURCES**

As addressed above, this proposed method is in high accuracy in terms of volume measurement for triaxial test specimen. The potential error in this method can be introduced from all over the testing procedure which is discussed in details as follows.

To perform a high accuracy measurement, all of these potential errors should be minimized.

1. Camera is clearly a very important part of any photogrammetry measurement. If a camera is suitable for photogrammetry measurement depends on several factors. Digital single-lens reflex camera with fixed focal length lens is preferred in our case. Higher pixel number and larger image sensor would lead to accurate measurement.
2. Camera calibration is one of the error sources. Image quality, camera position as well as the number of images used can influence the calibration result. And different calibration results would definitely produce different 3D measurement results. Image idealize is based on the lens distortion parameters, format size and perspective center of image sensor. These parameters are all obtained from camera calibration. Different lens calibration result could bring different pixel positions of measurement targets based on idealized images. Also, camera orientation could be affected by camera calibration results due to different focal length and format size. In other words, different group of images can bring different calibration result.
3. Different orientation process by using different reference points (targets in this study) as well as the number of the reference points can affect orientation results. This error can be minimized by using more reference points and more images from a variety of angles and distances.
4. An assumption was made for the acrylic cell wall reconstruction process. So, if the acrylic cell wall is well represented by the cylindrical or barreled shape equation or not will lead to different measurement results. Also, the thickness variation of the cell wall is another source of error. In our case, a transparent round shape cell wall with uniform thickness is highly recommended.
5. Refractive index of acrylic cell and water are an important factor which can affect accuracy of measurement significantly. However, in our case, due to the thickness of the acrylic cell is relatively small compared with the optical ray path in water,

refractive index of water is more important than that of acrylic cell. Fortunately, this refractive index can easily be determined by back-calculation method as addressed before. The refractive index of acrylic cell wall can be obtained from the testing equipment company or through internet.

6. Marking of the measurement targets can be another source of error. For the same target, view from different angles may sometimes result in different pixel position for its centroid. Even a stain on cell wall or different light conditions could cause misrecognition or inaccurate centroid of the target. To minimize the marking error, high quality images with larger depth of field are preferred. So, during image capturing, camera was set at low ISO level (100 to 200), small aperture size ( $< F9$ ) and high shutter speed ( $< 1/160$  s) with build-in flash on. In this way, high definition images could be achieved.
7. Least square method for estimation of the 3D coordinates by using least square method is the last source of error. Estimation of the 3D coordinates by using different number or group of optical rays will also generate different result. However, this potential error can be minimized by using more optical rays (greater than four is strongly suggested).

## **DIFFERENCES FROM EXISTING IMAGE BASED METHODS**

As mentioned before, some existing methods for volume measurement of unsaturated soil during triaxial test are also based image analysis. However, several features of this method listed as follows make it different from existing image based methods.

1. Camera used for this method was calibrated to determine the intrinsic parameters (focal length, principle point, distortion parameters). Based on calibration parameters, lens distortion could be eliminated and idealized images could be obtained for further photogrammetric analysis and refraction correction.
2. Photogrammetry was adopted for this method to accurately determine camera orientations. In this way, camera does not need to be mounted on tripod and

precisely adjusting for camera position is not required anymore which brings great flexibility for image capturing. With this flexibility, for a single measurement target on specimen surface, images from different distances and view angles can be captured.

3. A scaled 3D coordinate system was built for the measurement. All light rays, 3D coordinates of targets, camera positions can be well expressed in same coordinate system. Also, volume change and strain localization can be extracted based on the 3D coordinates of the measurement targets located on the surface of the specimen which makes the data analysis easier and comparable.
4. More than one image was used for the measurement of a single target. So, measurement error can be significantly reduced which is different from the other image based methods. In this study, for a single measurement points, an average of 5 images were used for its 3D coordinates estimation by least square method. Based on this estimated coordinates, the light rays relatively far from the estimated point can be deducted and least square estimation can be redo to reduce the estimation error.
5. By conducting forward intersection, 3D coordinates of measurement targets on triaxial cell can be accurately determined which is required for determine the position and shape of triaxial cell wall. The deformation of the acrylic cell wall could be introduced due to applied confining pressure. In this study, diameter variation of the acrylic cell wall was well detected under different confining pressure levels. A fairly linear relationship can be found between confining pressure and diameter of the triaxial cell. Since the position and shape of acrylic cell under different confining pressure levels can be well determined, accurate measurement on specimen in water became achievable.
6. 3D refraction correction by optical ray tracing technique was used for the refraction correction at the interfaces of air to acrylic cell and acrylic cell to water. Light rays can be traced from any camera stations. For most existing image based methods, 2D refraction correction model developed by Parker (1987) was used.

However, in this model, triaxial cell was assumed to be perfectly cylindrical without any deformation under applied confining pressure. This refraction correction only work when specimen cylinder and triaxial chamber are perfectly vertical. In this study, the author tried to vertical the specimen cylinder and triaxial cell. However, a small angle (1 to 2°) between the centerline of the triaxial cell and specimen cylinder still can be detected. Also, in this 2D refraction correction model, the camera needs to be perfectly horizontal and pass through the center of the chamber. Since the perspective center is located inside of camera, camera position cannot be accurately determined which makes the light rays from the camera undetectable. Also, the impact due to the cell deformation cannot be accounted in this 2D refraction correction model especially when cell deformed to barrel shaped.

7. Those existing image based methods only used one image for 3D position determination of the specimen. As we know, only 2D information can be obtained from a single image which means the information in depth direction was lost. So, for those image based methods, an assumption was made that the specimen deformation is perfectly along the radial direction of the specimen to find the lost depth information. In this way, the 3D position can be determined. Obviously, this radial direction deformation cannot be perfectly satisfied due to imperfect specimen and eccentric load. Thus, the measurement results based this method are questionable. However, for this proposed image based method, this assumption does not exist. For a single measurement point, 3D information can easily be found by triangulation based on different images which can also significantly raise the measurement accuracy.

## CONCLUSIOINS

In this study, a novel image based method was developed for monitoring volume change of unsaturated soil during triaxial test. For this method, photogrammetry, optical-ray tracing as well as least square estimation technique was adopted to

perform an accurate 3D measurement. Validation tests on a stainless steel cylinder under different confining pressure levels and saturated sand specimen under constant pressure level were conducted. Based on the validation results, some conclusions were drawn which are listed as follows.

1. Refraction correction is a necessary implement for Photogrammetry when used for multimedia conditions. For triaxial test, by refraction correction at the interfaces (air to acrylic cell and acrylic cell to confining fluid), 3D measurement on testing specimen can be applicable.
2. The proposed method is a low cost, real 3D, noncontact and accurate method for volume measurement on soil specimen during triaxial testing. No equipment modification is needed to perform this method by using traditional triaxial testing system for saturated soil. Also, this method can be used for both saturated and unsaturated soil.
3. The proposed image based method can be used to detect both total volume change and strain localization of soil specimen with great accuracy during triaxial testing by posting measurement targets on specimen surface anywhere if interested.
4. The accuracy of this method can be affected by several aspects. However, most of these can be minimized or even eliminated. The only error source that cannot be minimized came from the triaxial cell wall during refraction correction process. The variation of the wall thickness and the representative equations for the acrylic cell obtained from regression dominate the overall accuracy of the 3D measurement. In other words, for this proposed method, measurement accuracy could vary when using different acrylic cell. So, a clean transparent cylindrical shape cell wall with uniform thickness is highly recommended for this method.
5. The proposed image based method requires very much computation and data processing when performing camera calibration, image orientation and measurement targets identification. So, Photogrammetry software (in our case,

PhotoModeler software was used) is strongly suggested to be adopted for these processes.

## CHAPTER IV

### DEVELOPMENT OF A NEW HIGH-SUCTION TENSIOMETER

#### GENERAL

As addressed in Chapter II, high suction tensiometers were needed to monitor the suction changes of unsaturated soil specimens during undrained triaxial testing. However, due to the high mortality rate, commercial high-suction tensiometers for measuring the matric suction (below -100 kPa) on unsaturated soils are very limited. In this study, a new high-suction tensiometer was designed and fabricated based on a commercial pressure transducer. The detailed design, fabrication, saturation, and calibration process are addressed in details as follows. Also, the maximum attainable suctions were obtained through free evaporation tests.

#### HIGH-SUCTION TENSIOMETER FABRICATION

In Chapter II, it could be found that all existing high-suction tensiometers were based upon a pressure transducer. For the tensiometer developed for this study, as shown in Figure 4.1, EPXO series miniature pressure transducer was purchased from meas-spec.com with a pressure measurement up to 1500 kPa. The principle for the pressure measurement is based Wheatstone Bridge as shown in Figure 4.2. For a pressure measurement, if a pressure was applied, after pressure equilibrium, the deformation of the sensing area inward or outward will results in a change of resistance. An excitation voltage source was applied (5 V in this case) through red and black wire (ground wire). Then, a voltage output can be detected between the green and white wire which was introduced by resistors with different resistances used in the Wheatstone Bridge. If a series of known pressure were applied, a linear relationship can be built between the pressure applied on the pressure transducer and the output voltage of the Wheatstone Bridge which is referred as the calibration.

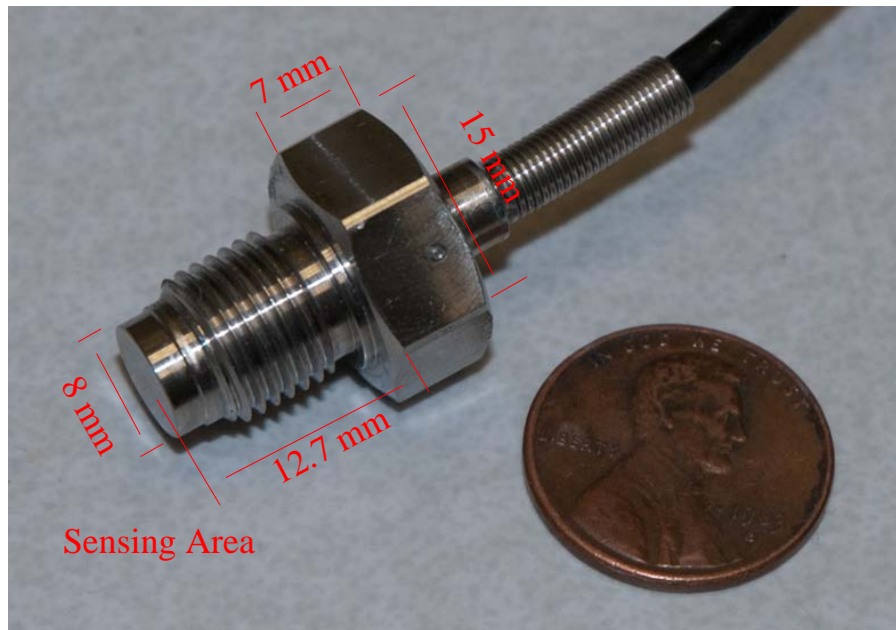


Figure 4.1 EPXO pressure transducer

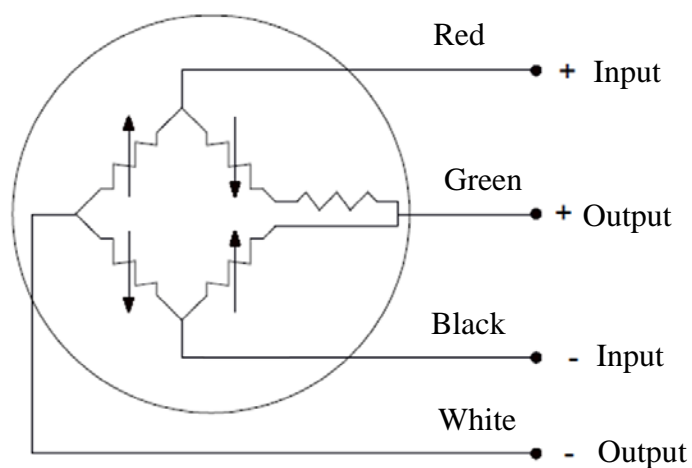


Figure 4.2 Principle of pressure measurement based on Wheatstone Bridge

Based on the literature review on existing high-suction tensiometers as shown in Chapter II, a new design for the tensiometer which incorporated with the purchased EPXO pressure transducer was generated as schematically shown in Figure 4.3. Similar to existing high suction tensiometers, the tensiometer developed in this study also included three parts which are pressure transducer, ceramic disc, and housing. However, different to the existing tensiometers, the ceramic disc was glued to a

stainless steel ring instead of glued to housing. The reasons for this design would be discussed later in this chapter.

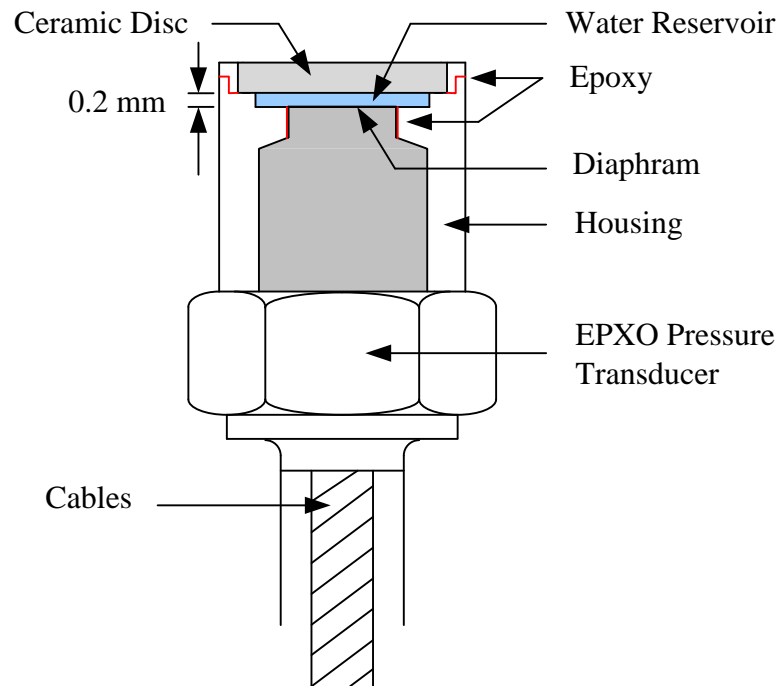


Figure 4.3 Schematic plot of the tensiometer

A pressure transducer, epoxy, housing, ceramic disc and stainless steel ring are required for the tensiometer fabrication as can be seen in Figure 4.4. The housing was designed with thread inside to incorporate with the thread on the pressure transducer. Also, a platform inside the housing, on which the stainless steel ring will rest, was used to provide a gap between the ceramic disc with the transducer diaphragm. Due to the presence of this gap, an empty room was generated which was used as a water reservoir. Ceramic disc was used as a filter to prevent air from entering the water reservoir. The fabrication process for the tensiometer can be mainly divided into three steps:

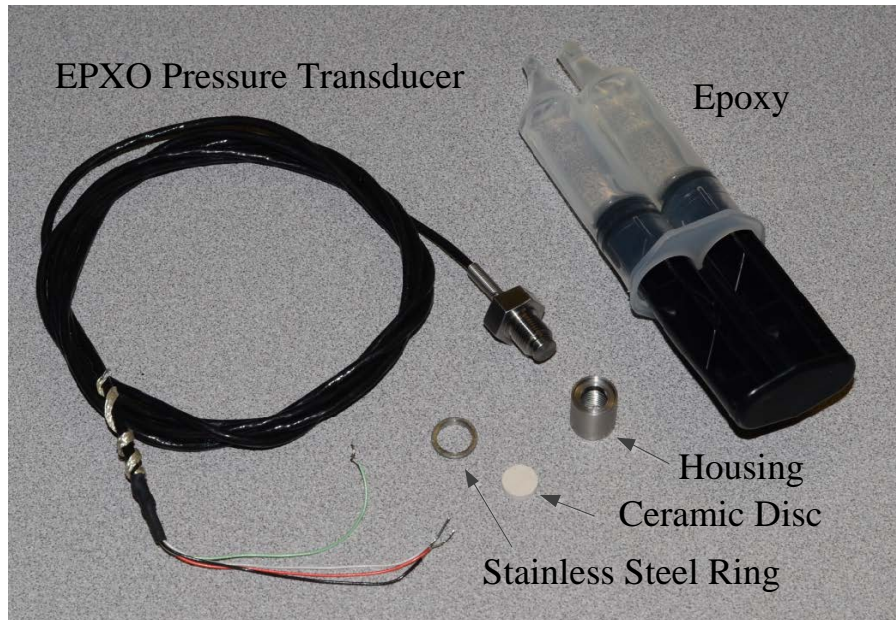


Figure 4.4 Preparation for tensiometer fabrication

1. EPXO pressure transducer, ceramic disc, stainless steel ring, and housing were carefully cleaned to remove any possible grease contamination which could weak the sealing due to the use of epoxy. A ceramic disc as shown in Figure 4.4 (2.5 mm in thickness and 10 mm in diameter) was glued to a stainless steel ring (10 mm and 13 mm in inner and outer diameters with a height of 2 mm) by using epoxy with a roughly 0.25 mm protuberance at the both sides (Figure 4.5a). During this process, to ensure a good sealing, more epoxy is encouraged to be used. Also, the stainless steeling ring was fabricated as shown in Figure 4.6. In this way, it would give us a better chance to seal the ring well. Once glued together, the ceramic disc in the ring need to be twisted to remove all possible air bubbles which could probably bring leakage to the tensiometer. After curing, epoxy on the outer side surface of the ceramic disc ring was carefully removed. Then, as shown in Figure 4.5c, the ceramic disc was grinded to 2 mm by using a 600 grit abrasive disc (Figure 4.5b) to remove the epoxy infiltrated in ceramic disc and generate a fresh surface.
2. The housing (Figure 4.4) used to hold the stainless steel ring as well as the ceramic disc in place was screwed to the pressure transducer (Figure 4.5a) with some epoxy located inside (red line in Figure 4.3). Different to the O-ring sealing

at the very end of the housing used by Ridley and Burland (1993), in this study, epoxy was used only around the sensor diaphragm. The thread is outside of the water reservoir instead of part of it which could probably reduce the possibility of cavitation according to Guan (1996). Once cured, the epoxy squeezed out to the surface of the diaphragm during assembling was carefully removed as shown in Figure 4.5c.

3. The ceramic disc ring was glued to the stainless steel housing with suitable amount of epoxy and twisted to remove trapped air as addressed before. Then, a pressure was applied on the stainless steel ring to ensure a good contact between the ring and the housing during curing process for the epoxy. Figure 4.5d shows the tensiometer after fabrication. After curing, the strength of the epoxy was fully achieved and the tensiometer can be submerged in de-aired water for saturation. In this study, a 0.2 mm thickness water reservoir ( $12.7 \text{ mm}^3$  in volume) underneath the ceramic disc ring is required for the water to provide a room for the outward deflection of the diaphragm. The volume of the water reservoir is recommended to be as small as possible to short the time for saturation process and reduce the possibility of cavitation. Also, the water reservoir cannot be too small to tolerate the outward deformation of the sensor diaphragm. When the air trapped in the water reservoir was fully dissolved into water under high pressure, the saturation process was considered to be finished.



Figure 4.5 Tensiometer fabrication

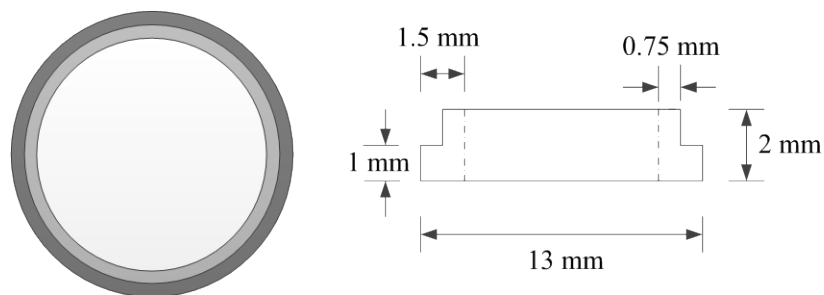


Figure 4.6 Layout of the stainless steel ring

The main difference between the design in this study and the other previous designs is the use of the stainless steel ring. Three main benefits were introduced due to the use of this ring. (1), the assembling process was divided into three steps which limited the possibility of mistakes. Also, each step is easy to perform. In other words, poor sealing is unlikely to happen in this design; (2), the quality of the assembling can be well controlled. Redundant epoxy can be removed and fresh ceramic surface can be generated to remove any stain on its surface or introduced during the assembling process which could also reduce the possibility of cavitation once saturated; and (3), if the tensiometer did not work well due to bad sealing, the ring with ceramic disc inside

can be easily detached from the pressure transducer without causing any damage to the ceramic disc.

To ensure a good contact between the tensiometer and soil specimen and hold the tensiometer in place during testing, a grommet as shown in Figure 4.7e was fabricated by using silicone rubber. Detailed fabrication process is shown in Figure 4.7. First, to prevent introducing air bubbles, silicone rubber was gently mixed as shown in Figure 4.7a. A stainless steel mold as shown in Figure 4.7b was built. After fully mixed, silicone rubber can then be poured into the mold as shown in Figure 4.7c. This process also required great patience to avoid air bubbles. Silicone rubber cured after several hours. Then, mold could be released as shown in Figure 4.7d. Edge of the grommet was trimmed as shown in Figure 4.7e. The inner diameter of the grommet is designed to be less than the outer diameter of the tensiometer housing. Therefore, the grommet can hold itself well in place. Figure 4.7f is a picture of the tensiometer with the grommet on. The grommet is suggested to be mounted on the tensiometer all the time. In case of any possible drop or collision, the silicone rubber grommet could provide absorption of the shock energy. Also, for soil specimens with high suction (>300 kPa), to prevent the tensiometer cavitation during installation and ensure a good contact between the specimen surface and the tensiometer, a thin layer of saturated Kaolin was smeared on the surface of the ceramic disk which is shown in Figure 4.8.

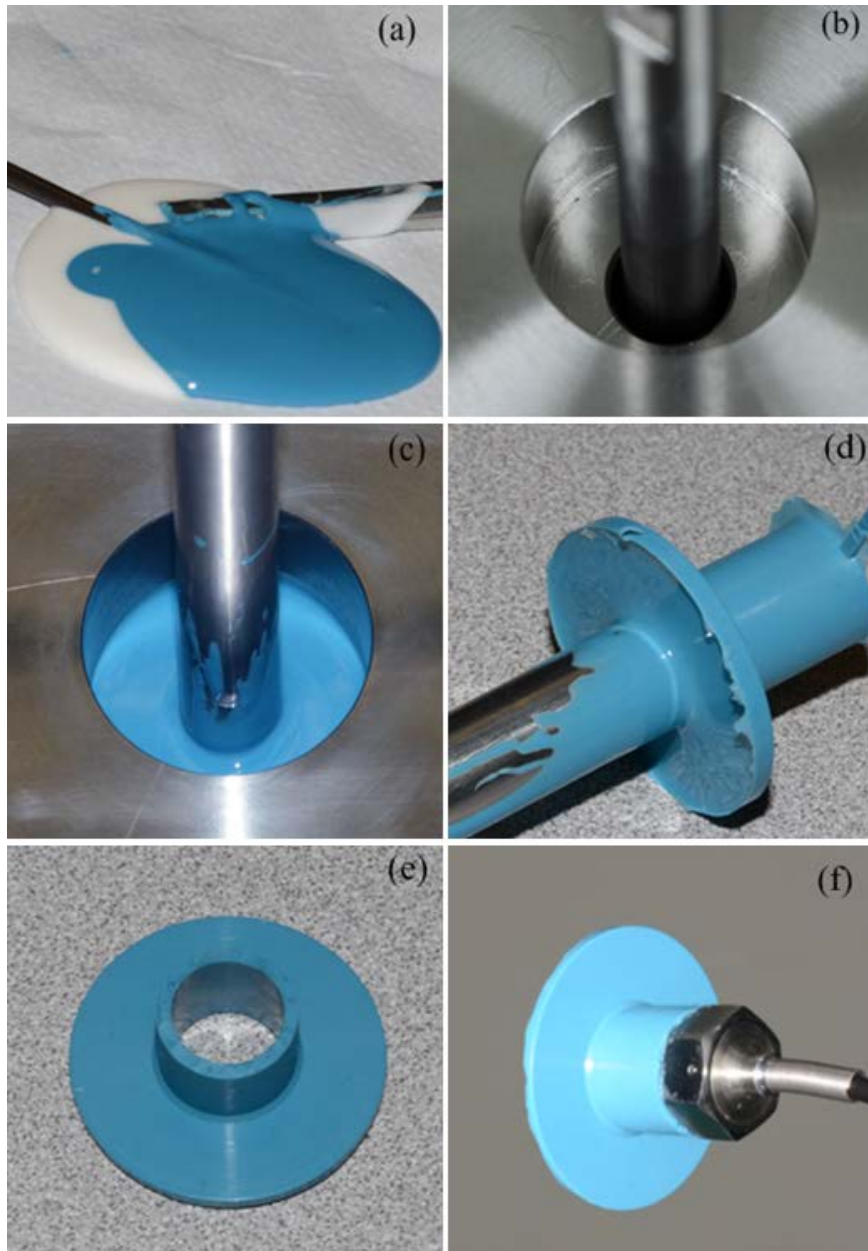
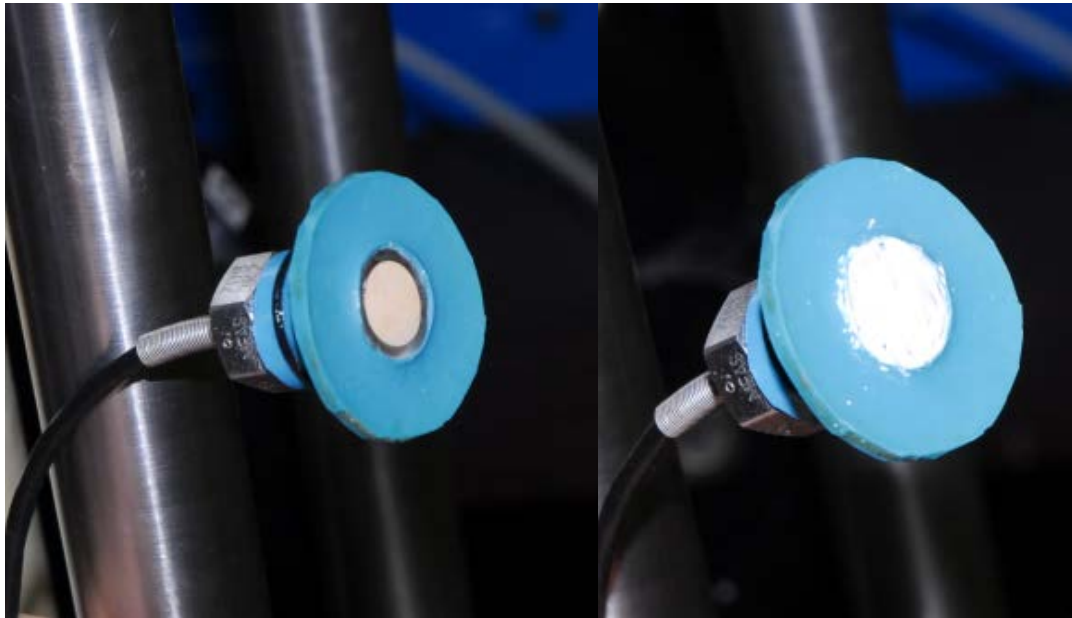


Figure 4.7 Grommet fabrication by using silicone rubber



(a) Without Kaolin

(b) With Kaolin

Figure 4.8 High-suction Tensiometer

### **HIGH-SUCTION TENSIO METER SATURATION**

In this study, two of these tensiometers were fabricated. For the saturation process, different to the other tensiometers (Ridley and Burland 1993 and Guan 1997), no special equipment is required. The tensiometer was installed to the triaxial test apparatus and submerged into de-aired water as shown in Figure 4.9. After this, a significant pressure increase of the water reservoir in the tensiometer could be observed due to the formation of a wetting front saturating the ceramic disc as long as the tensiometer was well sealed. As the wetting front moves towards the reservoir, the air trapped in the ceramic disc was progressively compressed and causing the pressure increase in the reservoir.

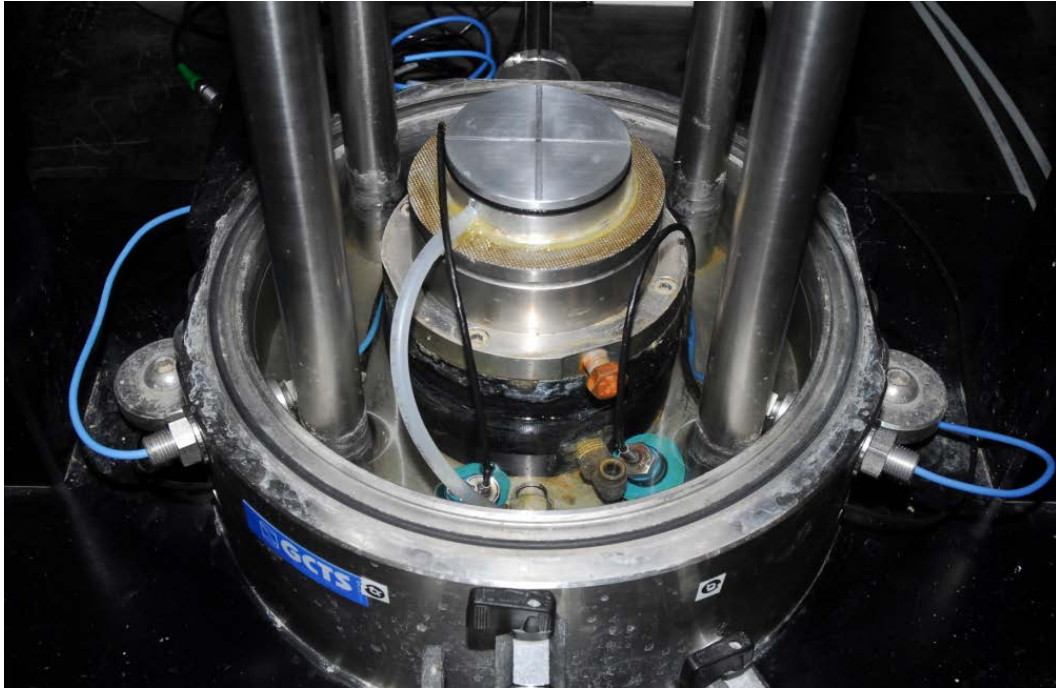


Figure 4.9 Tensiometers installation

In this study, during saturation, an air pressure of 600 kPa was applied to dissolve the air trapped in ceramic disc and underneath the ceramic disc which is commonly referred as pre-pressurization. Usually, for the initial saturation, to dissolve all the air in the ceramic disc as well as the air in the water reservoir, two to three pre-pressurization cycles in one week was required. By blowing the ceramic disc at the tensiometer tip, if the pressure quickly dropped to lower than -100 kPa, the tensiometer was considered to be saturated and can be used for suction measurement. After each suction measurement, the tensiometer was kept in water all the time. After the initial saturation, usually, several hours under a pressure of 600 kPa are sufficient to saturate the tensiometer developed in this study.

### **HIGH-SUCTION TENSIO METER CALIBRATION**

Since the presence of epoxy could possibly result in some deformation of the diaphragm due to hardening, in order to obtain an accurate measurement, calibration of tensiometer was performed after sensor saturation which is consistent with the real condition of use. For the calibration process in this study, the tensiometers were calibrated in positive pressure range. The negative pressure range calibration is based

on extrapolation which is also used and verified by some other researchers (Lourenco et al. 2008, xxxxxxx). The accuracy of the calibration can be checked by the pressure immediately after cavitation, which should be approximately -100 kPa. In other words, a tensiometer cavitation pressure reading close to -100 kPa indicates a good calibration. In this study, three cycles of cell pressure between 0 to 600 kPa were applied to calibrate the tensiometers under pressure change. When there is a cell pressure change, water flows inwards or outwards due to the pressure increases or decreases, respectively. The pressure were applied in steps and followed by waiting periods (2 minutes) to ensure the pressure equilibrium. Only the final readings, when equilibrium was achieved, were used for tensiometer calibration.

In this study, two of the tensiometers were fabricated. The calibration results for these tensiometers are tabulated in Table 4.1. By plotting those voltage output against applied pressure, a linear relationship between them can be found as shown in Figure 4.10.

Table 4.1 Tensiometer calibration

Applied Pressure (kPa)	Tensiometer Reading (mV)					
	Tensiometer 1			Tensiometer 1		
	Test 1	Test 2	Test 3	Test 1	Test 2	Test 3
0	0.654	0.66	0.657	1.131	1.133	1.131
100	1.395	1.393	1.391	1.906	1.904	1.904
200	2.127	2.122	2.12	2.671	2.667	2.667
300	2.85	2.85	2.852	3.428	3.427	3.43
400	3.578	3.578	3.571	4.189	4.189	4.183
500	4.297	4.301	4.297	4.941	4.945	4.941
600	5.01	5.016	5.014	5.687	5.691	5.691

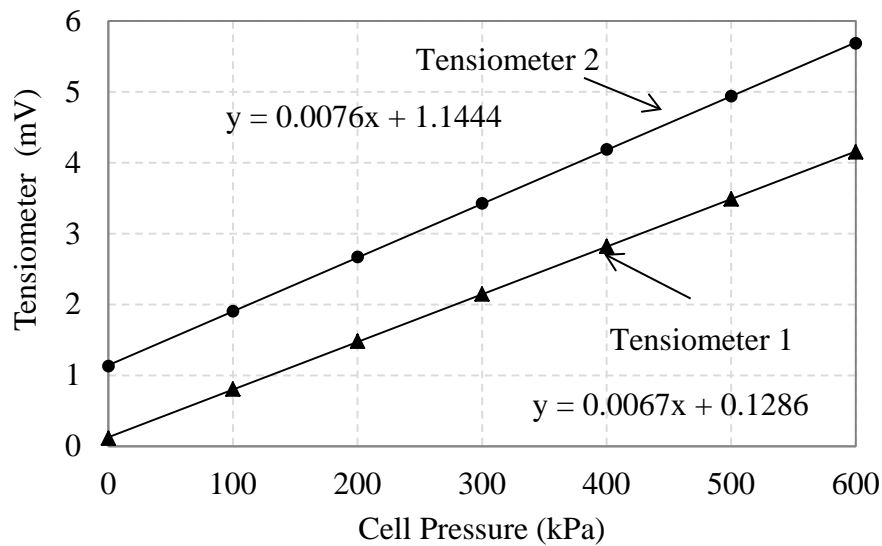


Figure 4.10 Calibration results of two tensiometers

## MAXIMUM ATTAINABLE SUCTION

The maximum attainable pressure is highly dependent on saturation process. Guan & Fredlund (1997) indicated that the maximum measurable suction could be affected by the growth of pre-existing gas bubbles, air entry value of ceramic disc, and the nucleation of vapor bubbles. In this study, it was also found that the maximum attainable suction associated with each different saturation process and tensiometers are different. Usually, a tensiometer with a high air entry ceramic disc at high degree of saturation could reach a higher suction measurement. After calibration, free evaporation test reported by Guan and Fredlund (1997) was used for the determination of the maximum attainable pressures. Due to water evaporation, the pore water pressure inside the tensiometer gradually decreased with time. The pressure right before the cavitation is the maximum attainable suction for the tensiometer. Free evaporation test results are presented in Figure 4.11. For the two tensiometers, 15 bar ceramic discs were used as the filter. The maximum attainable pressures measured are around 1130 kPa which is below 15 bar.

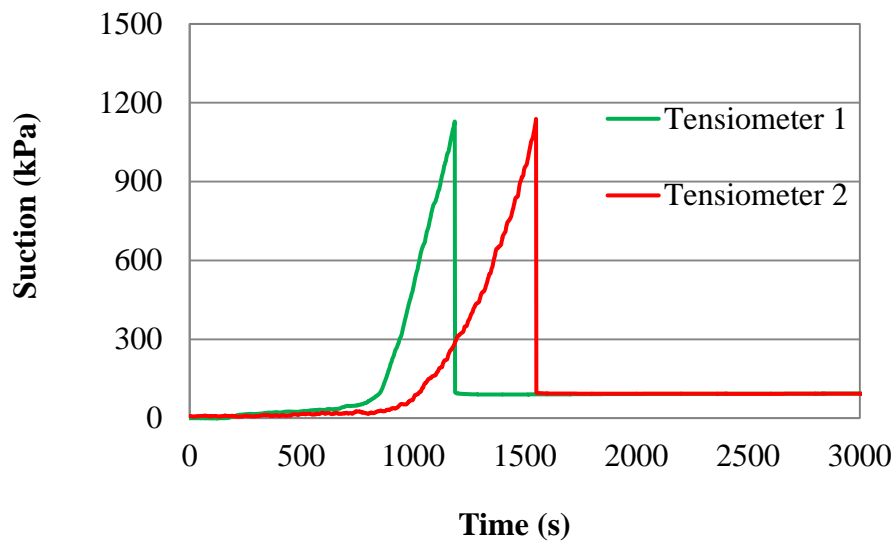


Figure 4.11 Maximum attainable pressures

## CONCLUSIONS

In this chapter, based on a review of existing high-suction tensiometers, a new high-suction tensiometer was designed, fabricated, saturated, and calibrated. The use of a stainless steel ring significantly reduced the chance of poor sealing and simplified the assembly process. Also, the tensiometer can easily be taken apart without causing any damage to the ceramic disc. To ensure a good contact between a soil specimen and the tensiometers, grommets was fabricated by using silicone rubber. After saturation and a careful calibration, the tensiometers were proved to be able to reach a maximum attainable suction at around 1100 kPa with 15 bar ceramic discs. The tensiometers developed in this study worked excellent throughout all the testing.

## CHAPTER V

### RESEARCH PROGRAMME AND PRESENTATION OF TEST RESULTS

#### GENERAL

In order to evaluate the constitutive behavior of unsaturated soil, some undrained isotropic compression and triaxial tests were conducted during which the moisture content remains constant while the suction and volume change of the soil sample were monitored. In this chapter, the sample preparation, tensiometer development, undrained isotropic compression, and shear tests were discussed in details. In this study, a new tensiometer for suction measurement of unsaturated soil during triaxial test based on a commercial EPXO pressure transducer, was designed and fabricated for this study. Also, the new method as presented in Chapter III was adopted to evaluate the volume change behavior of unsaturated soil during isotropic compression and triaxial test.

#### SAMPLE PREPARATION

To conduct the isotropic compression and triaxial tests, some soil sample with approximately the same load history and different matric suction levels were required. In this study, Fairbanks silt, collected from the side of Badger road near Brown's Hill Quarry (marked as red in Figure 5.1), was used for all the soil tests. After oven-dried, soil passed the No.16 Sieve to remove the organic and gravels. Figure 5.2 is a picture of Fairbanks silt after sieving. Some preliminary tests on Fairbanks silt were conducted which included Atterberg limits, grain size distribution, specific gravity, and compaction test.



Figure 5.1 Location of the used Fairbanks silt



Figure 5.2 Fairbanks silt



Table 5.1 Soil properties of Fairbanks silt

Soil Properties	Value
Maximum dry density	1.732 g/cm <sup>3</sup>
Optimum moisture content	15.70%
Specific gravity	2.71
Plastic limit	21.6
Liquid limit	24.7
Plastic index	3.1

### Specimen Compaction and Moisture Equalization

For the isotropic compression and shear test, cylindrical soil samples used were 2.8” in diameter and 5.6” in height. Split mold as shown in Figure 5.5a was used for compaction. Soil (Fairbanks silt) from the field was oven dried and passing the No.16 Sieve. Then soil was stored in buckets. Before using, soil was over dried again to remove moisture. Then, soil was moved out from the oven and cooled down to room temperature. Soil was mixed with tap water to desired moisture content (17.7% in our case) and stored in well-sealed buckets for moisture equilibrium for at least 12 hours. After moisture equilibrium, soil can then be used for specimen fabrication. Soil specimens were compacted in 11 layers according to the method reported by Ladd (1987). The first 10 layers were 0.5” per layer and the last layer was 0.6”. 385 g wet soil was used for each layer. After compaction for each layer, the surface of the soil was scarified to ensure a good contact between soil layers. After compaction, membranes used to cover the soil cylinders were carefully removed. Then, soil cylinders were placed in a container which is shown in Figure 5.1b for moisture equilibrium. Then, the contained was carefully sealed for the moisture equilibrium process. After two months, the moisture equilibrium considered to be reached and the samples can then be extracted for isotropic compression and triaxial tests.



(a) Compaction mold

(b) Moisture equalization

Figure 5.5 Specimen preparation

## SWCC

Soil suction is commonly referred to as the free energy state of soil water (Fredlund and Rahardjo 1993). The soil suction as quantified in terms of the relative humidity is commonly called “total suction”. Total suction is the equivalent suction derived from the measurement of the partial pressure of the water vapor in equilibrium with a solution identical in composition with the soil water, relative to the partial pressure of the water vapor in equilibrium with free pure water. It has two components, namely, matric (or capillary) and osmotic (or solute) suction. Matric suction is the equivalent suction derived from the measurement of the partial pressure of the water vapor in equilibrium with the soil water, relative to the partial pressure of the water vapor in equilibrium with a solution identical in composition with the soil water. Osmotic suction is the equivalent suction derived from the measurement of the partial pressure of the water vapor in equilibrium with a solution identical in composition with the soil water, relative to the partial pressure of water vapor in equilibrium with free pure water. In this study, matric suction was adopted to investigate the soil constitutive behavior.

SWCC is the relationship between soil water content (gravimetric, volumetric water content, or degree of saturation) and its suction.

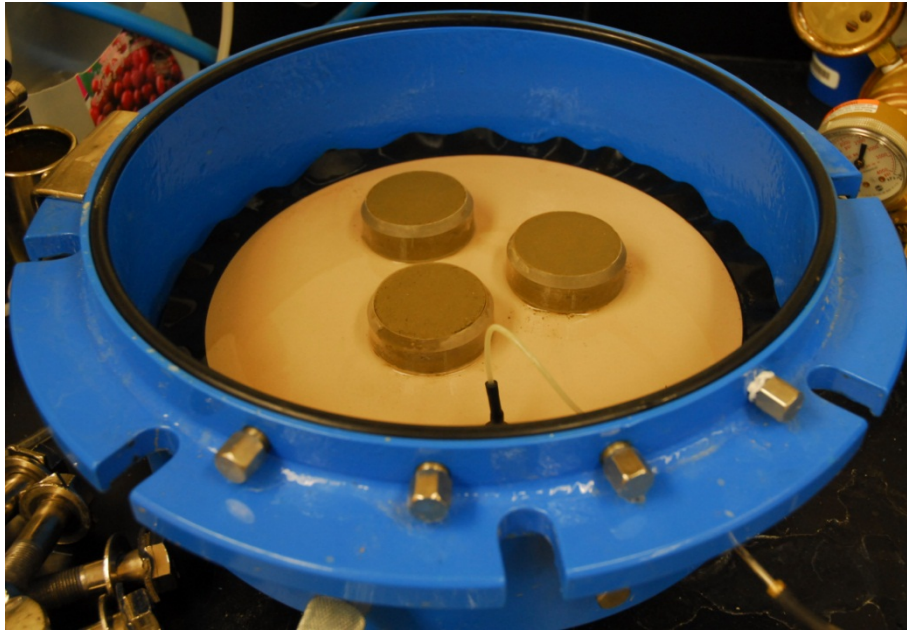
$$\psi = (u_a - u_w) + \pi \quad (5.1)$$

where,

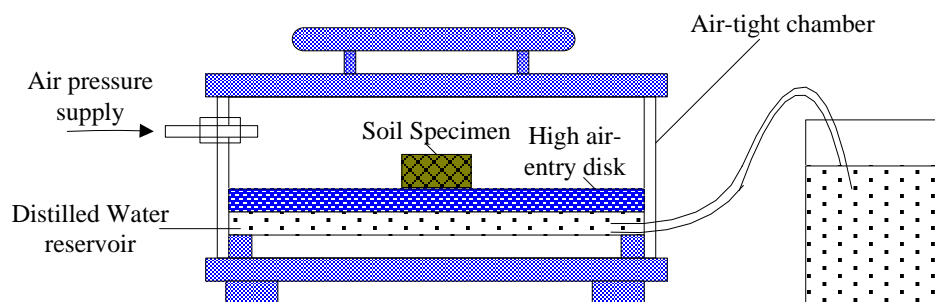
- $(u_a - u_w)$  = matric suction,
- $u_a$  = pore-air pressure,
- $u_w$  = pore-water pressure, and
- $\pi$  = osmotic suction.

To obtain SWCC of Fairbanks silt, pressure plate test was conducted. Soil specimens as shown in Figure 5.5b after compaction were shaped into 2" in diameter and 0.75" in height cylinders by using cutting rings as shown in Figure 5.6a. Before pressure plate test, soil samples were submerged in water for a week to ensure fully saturated. After saturation, samples in rings were placed on pre-saturated high air-entry ceramic disc which is also shown in Figure 5.6a. Different cell pressures ranging from 100 to 800 kPa were to determine the SWCC of Fairbanks silt. Pressure in the chamber was maintained for a week. Then, soil specimens were extracted and followed by water content determination. The matric suction was applied to a soil specimen by controlling the difference in the pore air pressure  $u_a$  and the pore water pressure  $u_w$  with both pressures being positive as shown in Figure 5.6b. The pore water pressure was controlled at an atmospheric pressure while the pore air pressure was changed to obtain the specific matric suction value. This procedure is referred to as the axis-translation technique (Hilf 1956). The main component of the pressure plate extractor is the high air entry disk as shown in Figure 5.6b that remains saturated for matric suction applications below the air entry value of the disk. The disk is always saturated and in contact with in a compartment below the compartment below the disk. The water pressure in the compartment is opened to the atmosphere to maintain at a positive pressure in the closed system. During the test soil specimen is placed on the high air entry disk. A good contact between the specimen and the disk results in the pore water pressure in the soil being controlled at the same pressure as the water

pressure in the compartment. The air pressure is then applied to the specimen in order to impose the desired matric suction.



(a) Pictures of pressure plate extractors



(b) Schematic plot of the pressure plate extractor

Figure 5.6 Pressure plate test for determination of SWCC

Theoretically, by conducting pressure plate tests with 15 bar ceramic disk, the suction of soil that can be reached is 15 bar. In reality, the soil suction that can be measured is lower than this. Thus, for SWCC of soil higher than 15 bar, another method by using salt solution, was adopted. Table 5.3 shows the osmotic suctions for different salt solutions at 25 °C. In this study, NaCl was used for the solution preparation according to Table 5.3. After preparation, solution was stored in a stainless steel bowl as shown in Figure 5.7a. Then, soil specimen slice (10 mm in height and 70 mm in diameter) as

shown in Figure 5.7b was placed in a plastic mold which is above salt solution level. Edge of the stainless steel bowl was smeared with vacuum grease. Plastic wrap was used to seal the container which is also shown in Figure 5.7b. After 15 days, the moisture equilibrium was considered to be completed. The tested soil specimen was then oven dried to determine its water content.



(a) Container with salt solution; (b) Container sealed with plastic wrap

Figure 5.7 Use of salt solution for determination of SWCC

Table 5.2 Osmotic suction for several salt solutions (Bulut et al. 2001)

<b>Molality of NaCl (m)</b>	<b>Osmotic Suction (bar)</b>	<b>Osmotic Suction (kPa)</b>	<b>Osmotic Suction (log kPa)</b>	<b>Osmotic Suction (pF)</b>	<b>Amount of NaCl (g/liter)</b>
0.01	0.4799	47.9937	1.6812	2.6897	0.5844
0.02	0.9502	95.0235	1.9778	2.9863	1.1688
0.05	2.3390	233.9024	2.3690	3.3775	2.9221
0.10	4.6232	462.3164	2.6649	3.6735	5.8442
0.20	9.1608	916.0757	2.9619	3.9704	11.6885
0.30	13.7019	1370.1870	3.1368	4.1453	17.5327
0.40	18.2658	1826.5788	3.2616	4.2702	23.3770
0.50	22.8615	2286.1486	3.3591	4.3676	29.2212
0.60	27.4942	2749.4170	3.4392	4.4478	35.0655
0.70	32.1682	3216.8152	3.5074	4.5159	40.9097
0.80	36.8870	3688.6952	3.5669	4.5754	46.7540
0.90	41.6531	4165.3100	3.6196	4.6282	52.5982
1.00	46.4691	4646.9124	3.6672	4.6757	58.4425
1.20	56.2615	5626.1507	3.7502	4.7587	70.1310
1.40	66.2798	6627.9768	3.8214	4.8299	81.8195
1.50	71.3777	7137.7693	3.8536	4.8621	87.6637
1.60	76.5384	7653.8384	3.8839	4.8924	93.5079
1.80	87.0498	8704.9848	3.9398	4.9483	105.1964
2.00	97.8247	9782.4672	3.9904	4.9990	116.8849
2.20	108.8735	10887.3465	4.0369	5.0454	128.5734
2.40	120.2025	12020.2474	4.0799	5.0884	140.2619
2.50	125.9757	12597.5653	4.1003	5.1088	146.1062

1 mole of NaCl = 58.442468 grams

## TRIAXIAL TESTING

In this study, Servo-Controlled Simple Shear Testing System (SSH-100) from GCTS (Figure 5.8), which is designed for triaxial testing on saturated soils, was modified for the unsaturated soil testing. Data acquisitions system was used to record the soil suction, cell pressure, shear load, and vertical deformation.

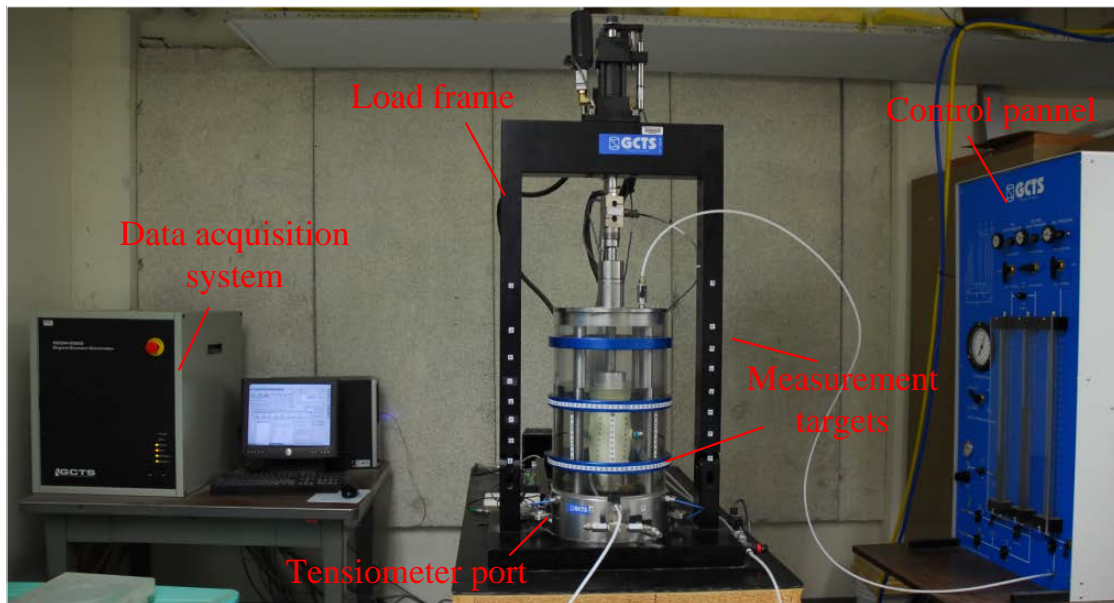
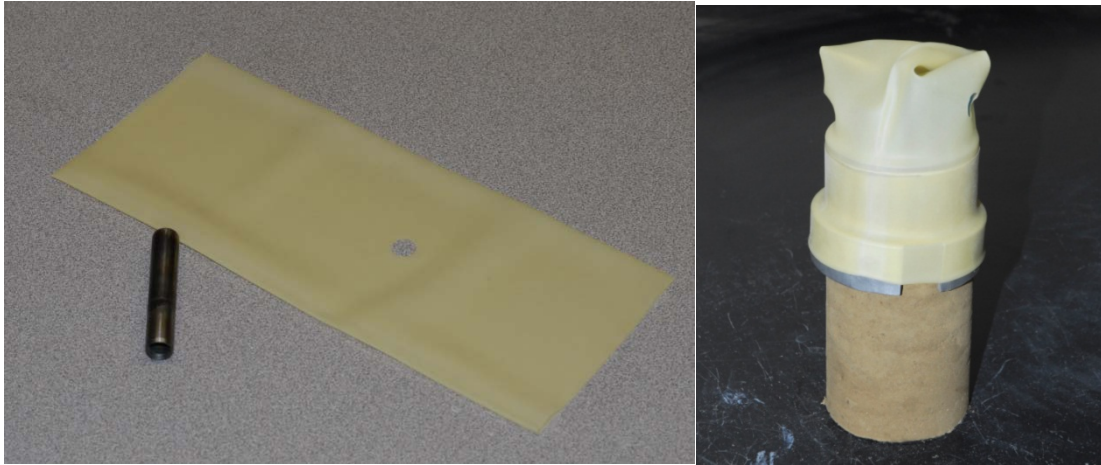


Figure 5.8 Testing system from GCTS

After saturation and calibration, tensiometers can then be used for matric suction monitoring on unsaturated soil specimen during testing. Before sample installation, dimensions of the soil specimen were determined with a caliper to an accuracy of 0.01 mm. By using the cutter as shown in Figure 5.9a, two holes were cut on the membrane which would be used to cover the soil specimen during testing. Then, soil specimen was covered with the membrane with help of an O-ring placing tool as shown in Figure 5.9b. Specimen was mounted on the pedestal of the triaxial cell and carefully sealed with O-rings as shown in Figure 5.10a. A small suction (-5 kPa) was applied after this. Some vacuum grease was smeared on the back of the grommet which was used to hold the tensiometer. In this study, two pre-saturated tensiometers were placed at the middle of the specimen which is schematically shown in Figure 5.10b. By carefully stretching the membrane, as shown in Figure 5.10a, tensiometer can be placed on sample surface (the contact area was pre-flated). The use of vacuum grease would ensure a good sealing between the grommet and membrane. Also, the applied suction will hold the sensor in place during specimen installation. After this, 36 measurement targets in four strips (Figure 5.10a) can be posted on membrane surface with help of vacuum grease which is water proof. Images were captured to determine the volume of the soil specimen. Triaxial cell wall was installed and filled with tap water as shown in Figure 5.11. A confining pressure of 50 kPa was then

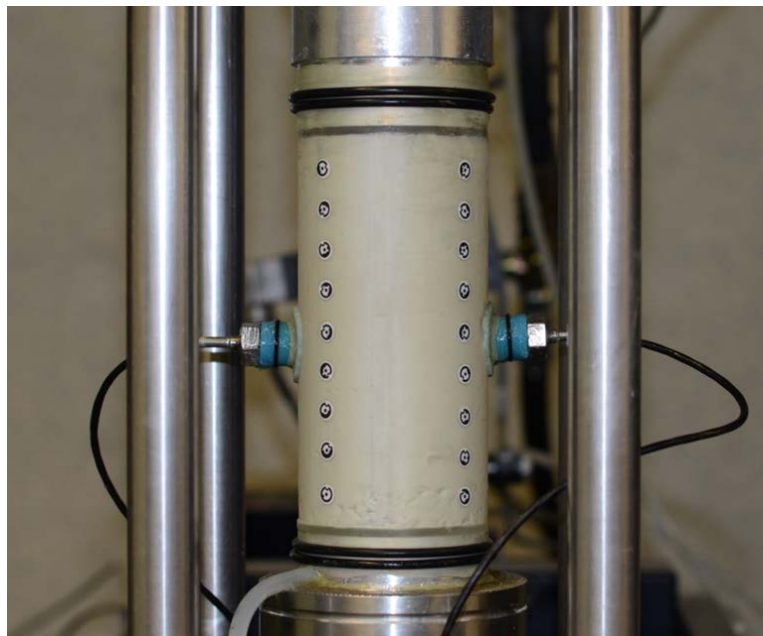
applied to hold the tensiometer in place and the applied suction was released simultaneously. Usually, 1/3 to one hour (depend on soil suction) was needed for the suction of the soil specimen to reach equilibrium.



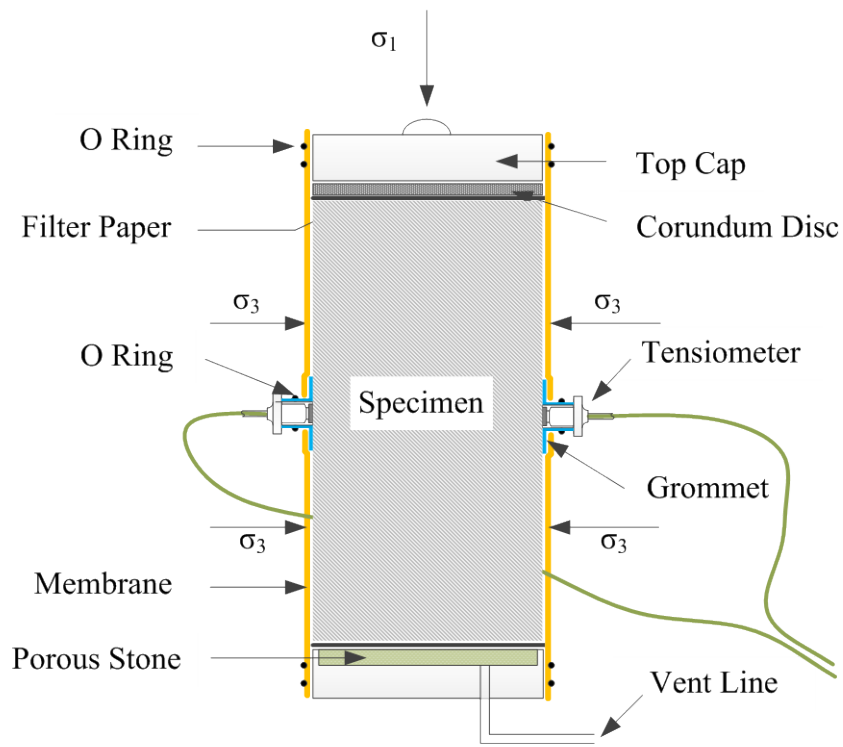
(a) Membrane and cutter

(b) O-ring placing tool

Figure 5.9 Membrane mounting on specimen



(a)



(b)

Figure 5.10 Tensiometer installation

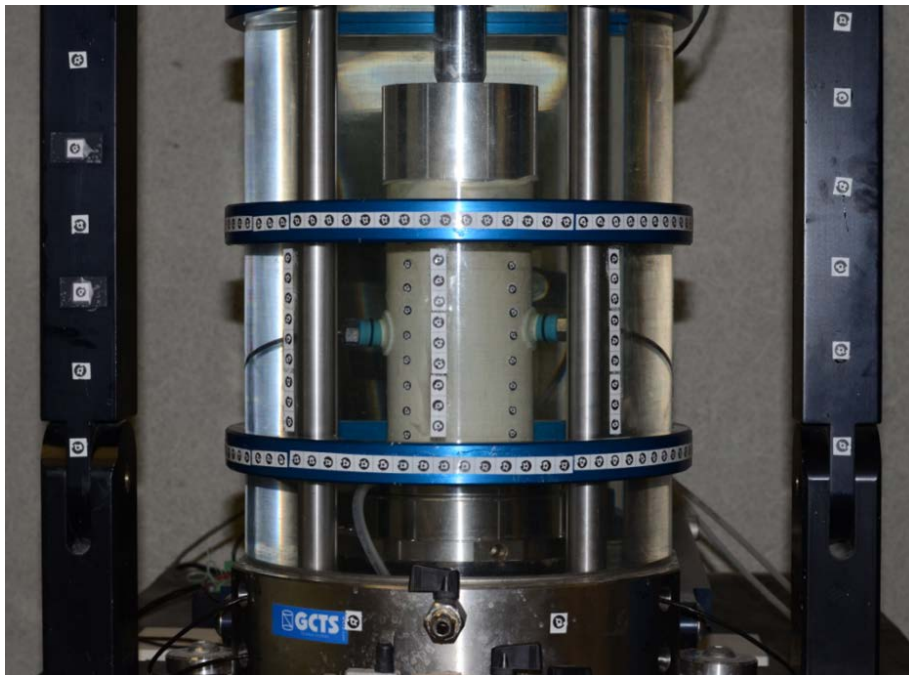
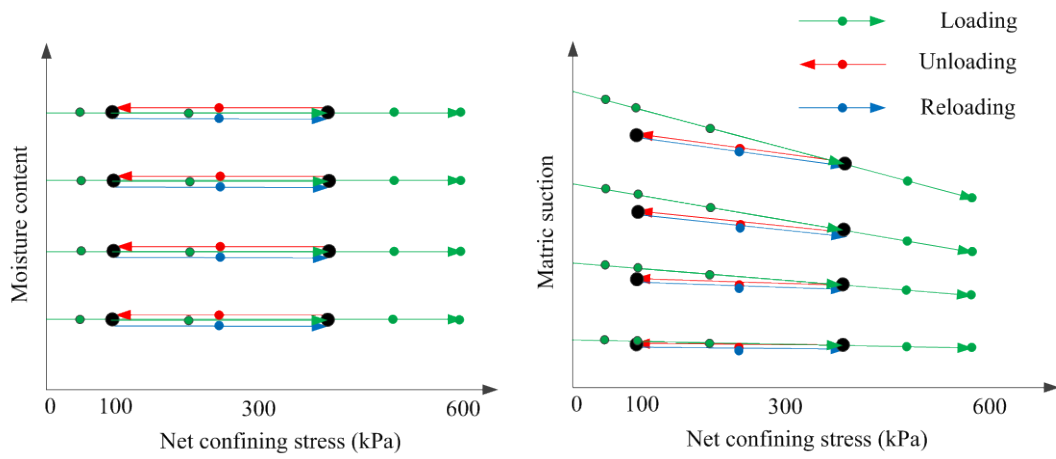
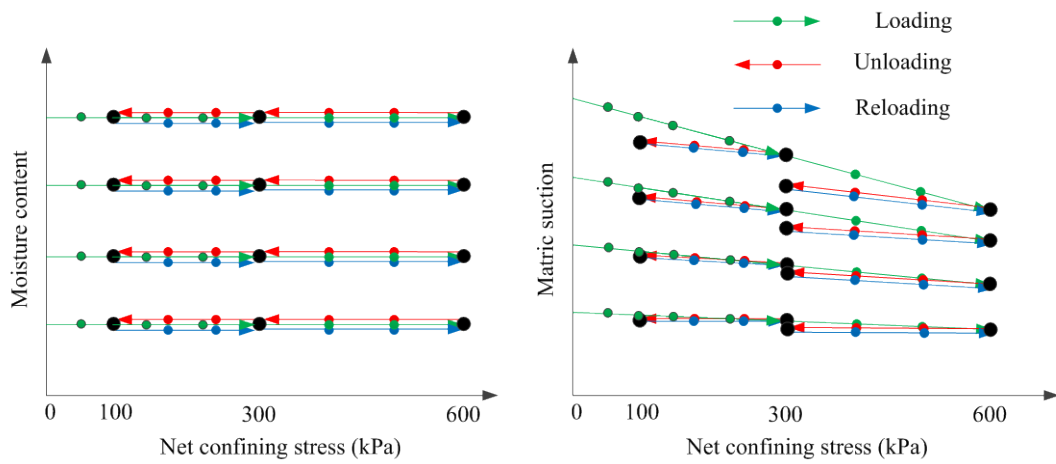


Figure 5.11 Triaxial test setup

After suction equilibrium, isotropic compression test can be performed. Confining pressure was gently increased or decreased to a target value and followed by another equilibrium period which also depends on soil suction. After suction equilibrium, volume of the soil specimen was measured by using the method as presented in Chapter III. The specific loading path used in this study is shown in Figure 5.12 and tabulated in Table 5.3. After isotropic test, shear load was applied in steps which are also shown in Table 5.3. The specimen was then dismantled from the pedestal and the membrane was removed from the specimen. Figure 5.13 is a picture of a soil specimen after shear test. The final mass of the specimen was measured immediately after removing the membrane from the specimen. Soil specimen was oven-dried right after shear test to determine its water content.



(a) Loading path A



(b) Loading path B

Figure 5.12 Isotropic loading paths

Table 5.3 Loading paths for specimens with different initial suctions

Group A		Group B	
Net confining stress (kPa)	Vertical deformation due to Shear Load (mm)	Net confining stress (kPa)	Vertical deformation due to Shear Load (mm)
50	0	50	0
200	0	125	0
400	0	200	0
250	0	300	0
100	0	230	0
250	0	160	0
400	0	100	0
600	0	160	0
600	2	230	0
600	4	300	0
600	3.4	400	0
600	5.4	500	0
600	7.4	600	0
600	9.4	500	0
600	12.4	400	0
600	15.4	300	0
600	19.4	400	0
		500	0
		600	0
		600	2
		600	4
		600	6
		600	8
		600	10
		600	13
		600	16
		600	19
		600	22



Figure 5.13 Soil specimen after testing

## **PRESENTATION OF TEST RESULTS**

This section presents the results of tests which include undrained isotropic compression and shear tests. Soil water characteristic curve (SWCC) of tested soil was determined through pressure plate test and salt solution method. Isotropic compression tests were conducted on soil specimens with different initial moisture contents. For a specific specimen, after an isotropic compression test, followed by undrained shear test on the same specimen. In other words, for one soil specimen, both undrained isotropic compression and shear tests were performed.

### **Soil Water Retaining Curve**

In this study, SWCC was obtained through pressure plate test as shown in Figure 5.14. Also, SWCC under different net confining stresses were extracted from undrained isotropic compression test. Test results are presented in Figure 5.15 at net confining stresses of 50, 200, 400, and 600 kPa. As can be seen in Figure 5.15,

suction of Fairbanks silt changed significantly at water content less than 10% due to its larger particle size when compared with clay.

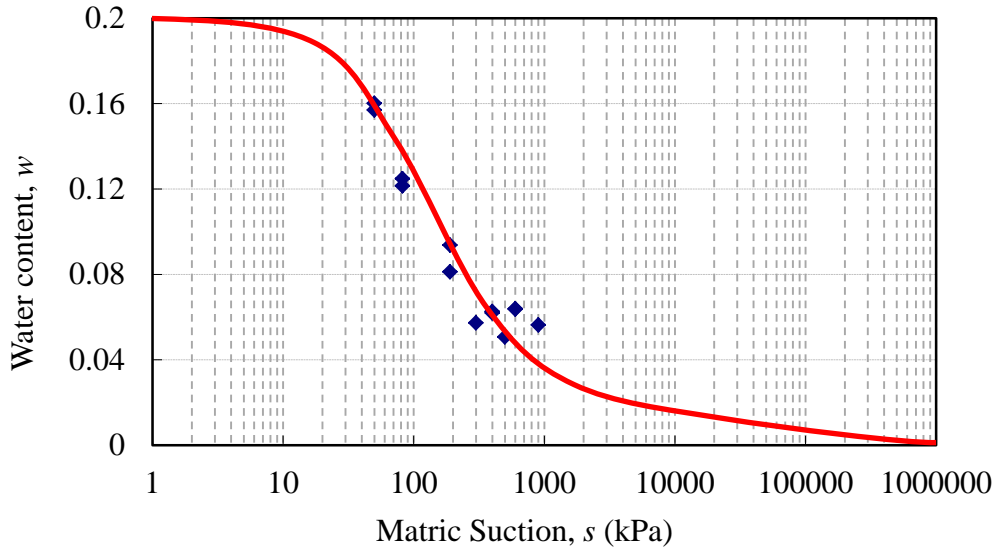
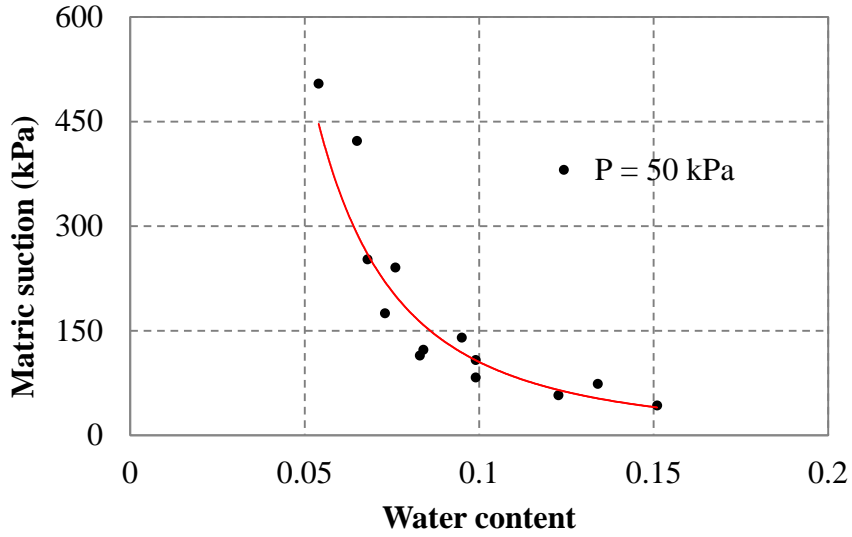
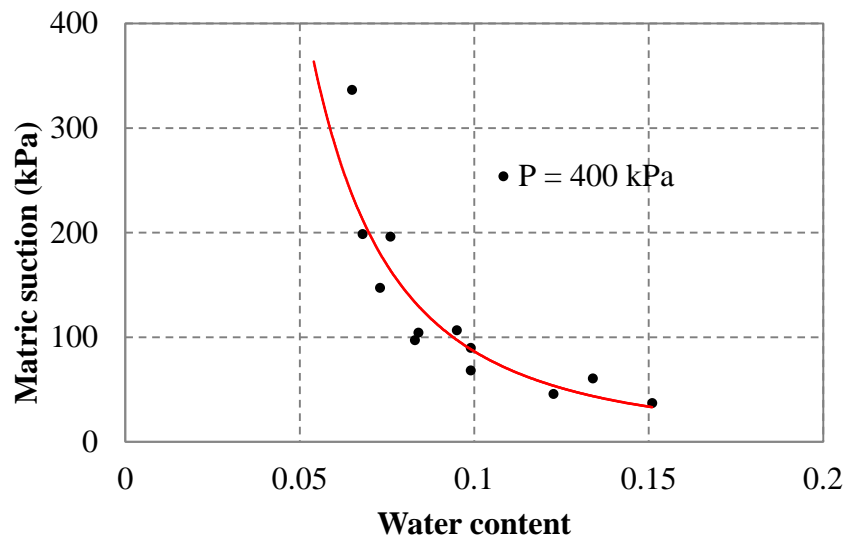


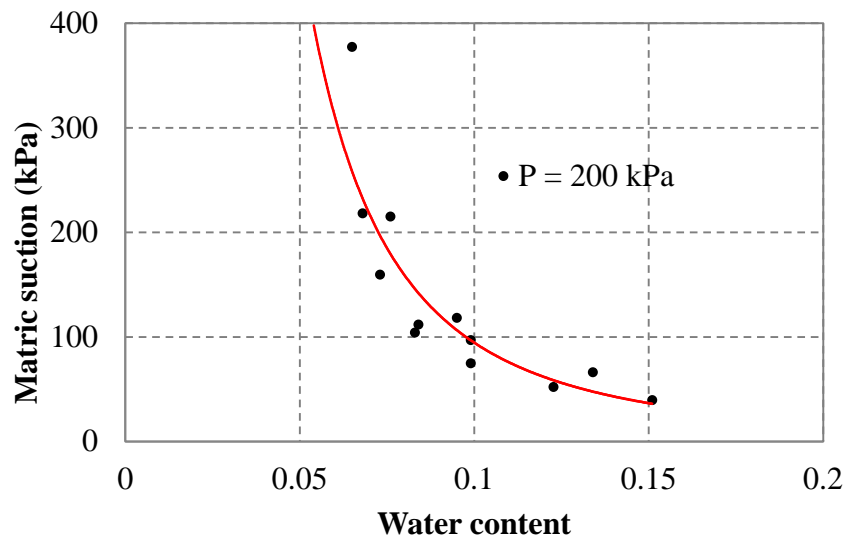
Figure 5.14 SWCC of Fairbanks silt



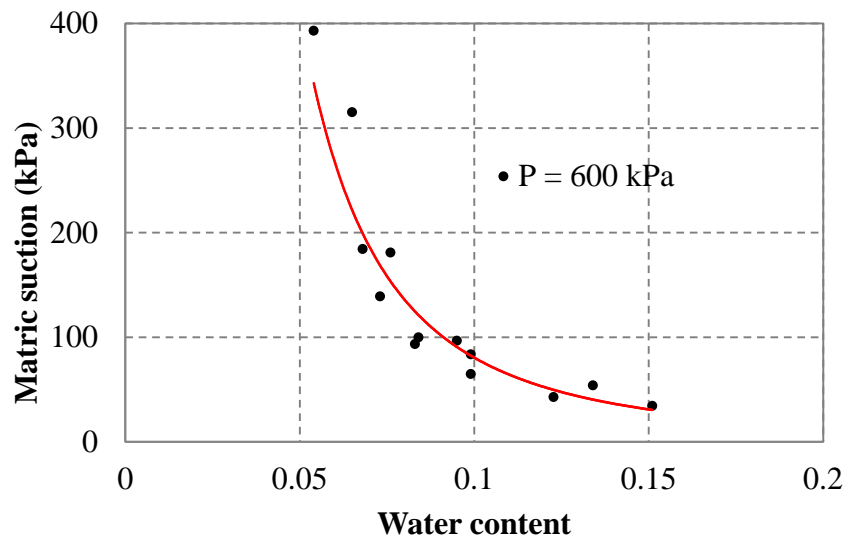
(a) 50kPa



(b) 200 kPa



(c) 400 kPa

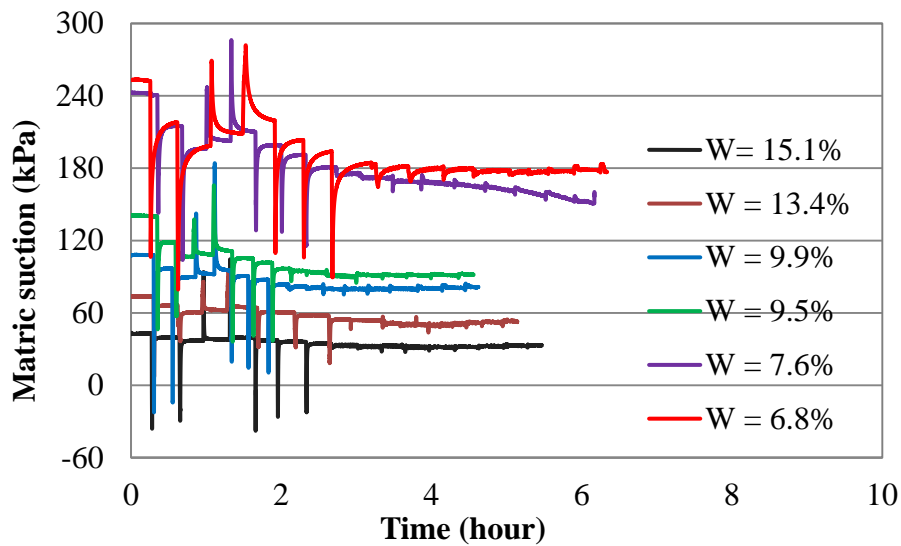


(d) 600 kPa

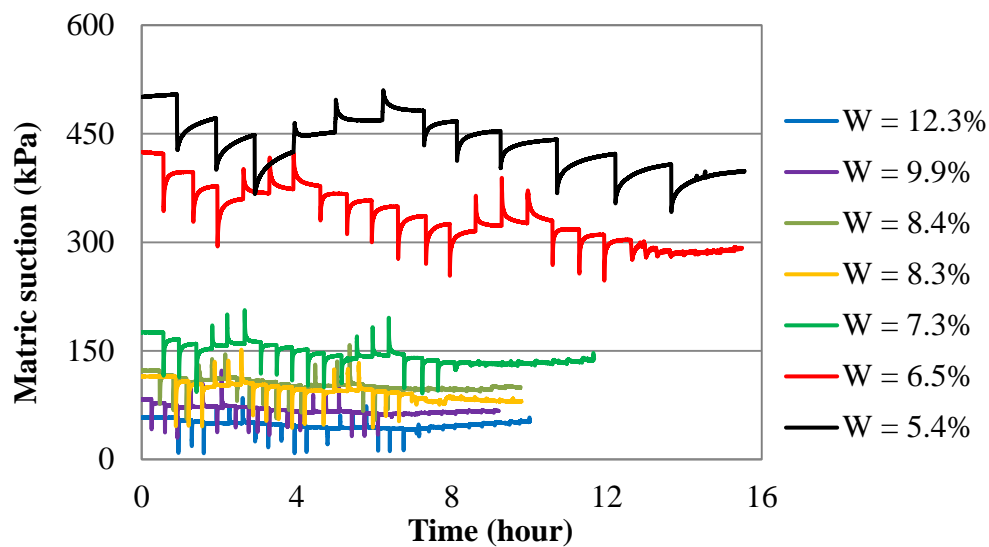
Figure 5.15 Soil water retaining curve under different confining stresses

### Undrained Isotropic Compression Test Results

Undrained isotropic compression tests were conducted on soil specimens with different initial moisture contents to evaluate the soil behavior under isotropic loading condition. Two groups of tests were performed in which different loading paths were used. As addressed before, the maximum attainable suction measured can be up to 1100 kPa. However, for real tests on silt specimens, the tests only covered specimens with suction less than 500 kPa for the following reasons: (1) due to good contact between soil specimen and the tensiometer cannot be ensured during installation process, tensiometers can easily cavitate due to water evaporation at the ceramic surface; (2) for soil with suction greater than 500 kPa, it took hours to reach a new suction equilibrium after an isotropic loading change, during which the tensiometers could also cavitate; and (3) for unloading process, if a confining stress was released, a sudden suction increase could be found in the tensiometer which could also probably cavitate the tensiometer. Therefore, this study only covers soil specimen with matric suction less than 500 kPa. For soil specimens with different initial water content, during undrained isotropic compression and shear testing, soil matric suction change due to change of load was recorded which are presented in Figure 5.16. For Figure 5.16a and 5.16b, the difference between them is the used loading paths.



(a) Loading path A



(b) Loading path B

Figure 5.16 Soil suction equalization during isotropic compression and shear test

During testing, if the isotropic load was increased or released, a sudden suction change can be found for the tensiometer reading as shown in Figure 5.16. The magnitude of the change can be affected by how quick was the load increased or released. There were two possible reasons for this phenomenon: (1) the sudden increase or release of the isotropic load would result in a change in pore air pressure in the soil specimen which could be captured by the tensiometer; (2) As can be seen in

Figure 5.17, during isotropic or shear testing, there is a contact pressure (equal to the applied confining pressure) between soil specimen and tensiometer tip. Due to this contact pressure, the pre-saturated ceramic will deform toward the water reservoir from its original position (shown in dashed line in Figure 5.17). Once suction equilibrium was reached, water would not come out of the tensiometer and a negative pressure was maintained in the water reservoir. When the contact pressure was increased, the ceramic disc will continue to deform toward the water reservoir which could lead to a significant pressure increase because of water is not compressible. This significant pressure increase will be reflected by a sudden suction decrease in the tensiometer as shown in Figure 5.16. For soil specimen at water content of 15.1%, when the applied confining pressure increased, the pressure recorded by the tensiometer jumped to positive range. A reverse process can be used to explain the sudden suction increase during a confining pressure release. After this sudden change, water in the water reservoir would flow into or out until a new suction equilibrium was reached. In Figure 5.16, it can also be found that the time needed for the suction equilibrium depended on the soil suction. The lower the soil suction, the less the time needed for suction equilibrium. For soil specimen with suction around 50 kPa, time needed for the suction equilibrium was less than 10 minutes. However, for soil specimen with suction around 150 kPa, time needed for the suction equilibrium was around 20 to 30 minutes and this suction equilibrium time was raised to hours for soils with suction higher than 500 kPa. Thus, ideally, for soil with suction around 50 kPa, the whole testing process (include isotropic compression and shear test) could be completed in 4 hours. However, this time was increased to more than 15 hours for a soil specimen with an initial suction around 420 kPa as shown in Figure 5.16.

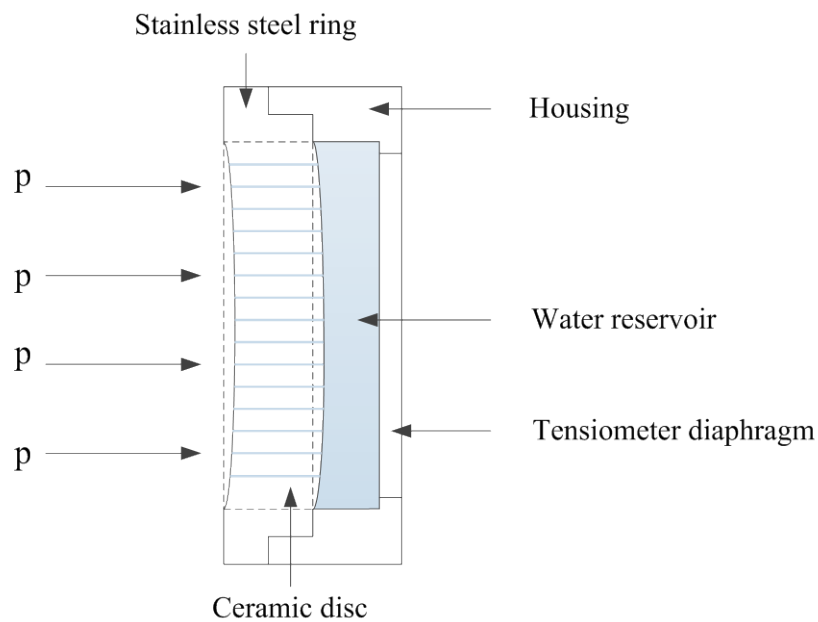
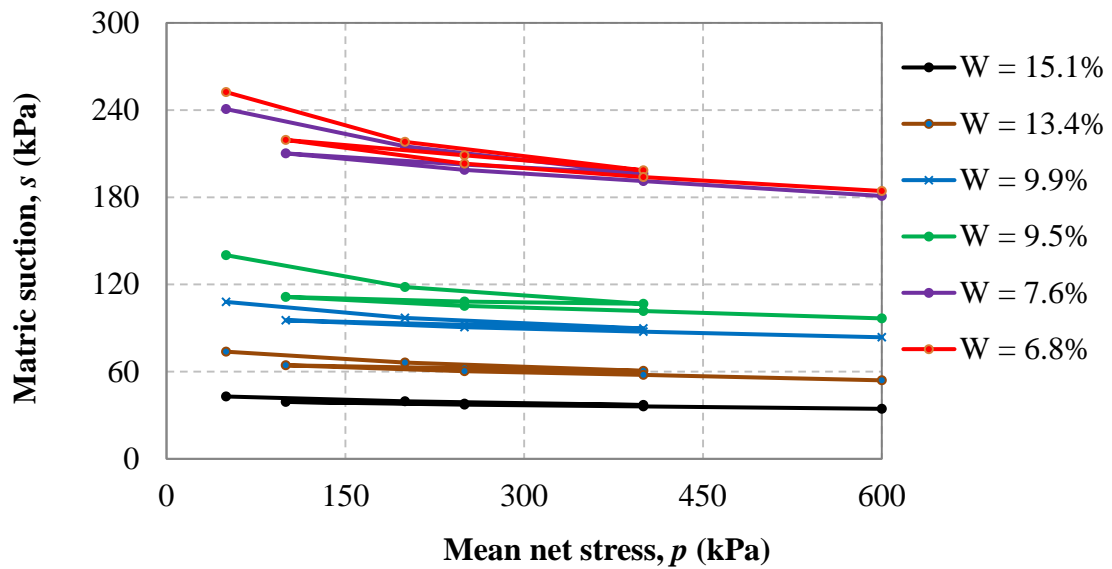


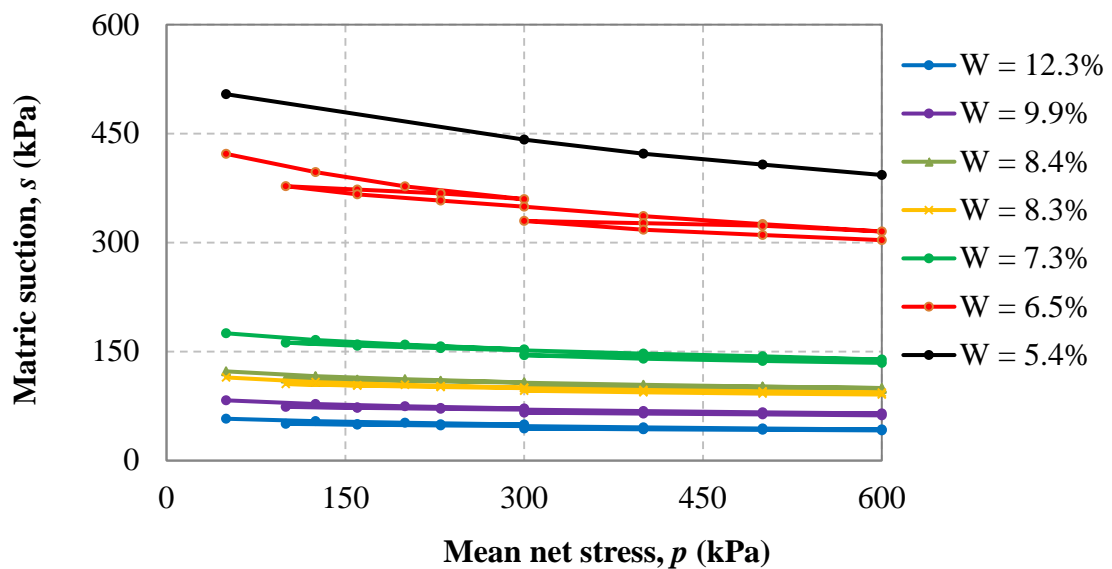
Figure 5.17 Tensiometer response to sudden increase or decrease of confining pressure

During undrained shear testing as shown in Figure 5.16, this sudden change of suction reading was not pronounced any more due to absence of the two reasons as addressed before. The shear load was applied slowly (1 mm/min) and the confining pressure was maintained to be constant during shearing. Also the time needed for suction equilibrium due to shear load was less than that due to isotropic load.

Usually, to investigate unsaturated soil behavior under loading, suction controlled triaxial test was used. However, in this study, instead of suction controlled triaxial test, suction monitored triaxial tests were performed with help of the tensiometers specially developed for high suction measurement. For isotropic compression tests, after soil suction equilibrium, suction was recorded by tensiometers. As shown in Figure 5.18, suction changes of soil specimens with different water contents under different load paths are presented on the ( $s - p$ ) plane.



(a) Loading path A



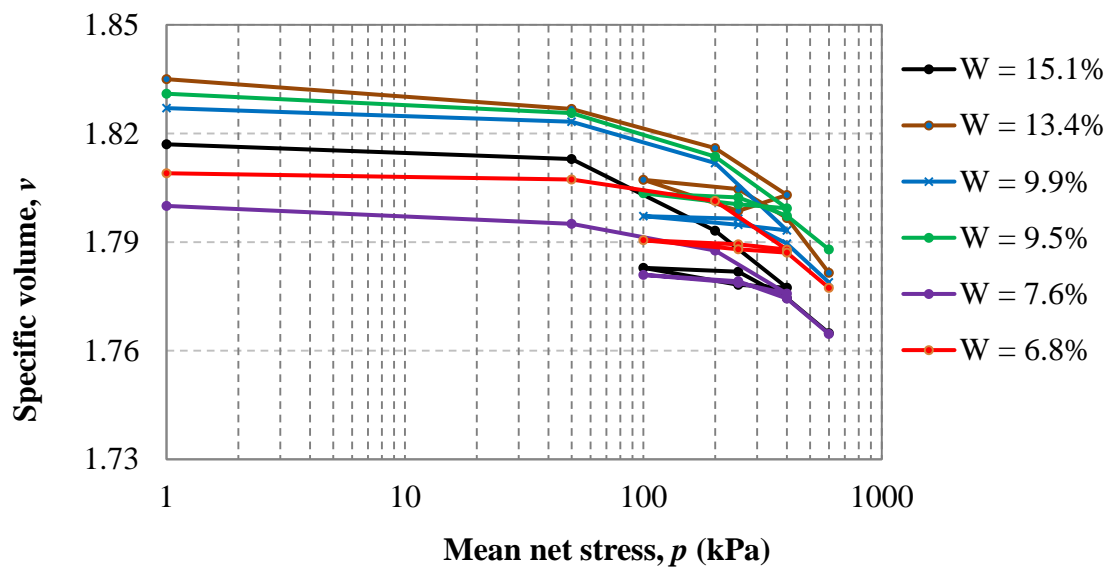
(b) Loading path B

Figure 5.18 Suction changes due to variation of net confining stress

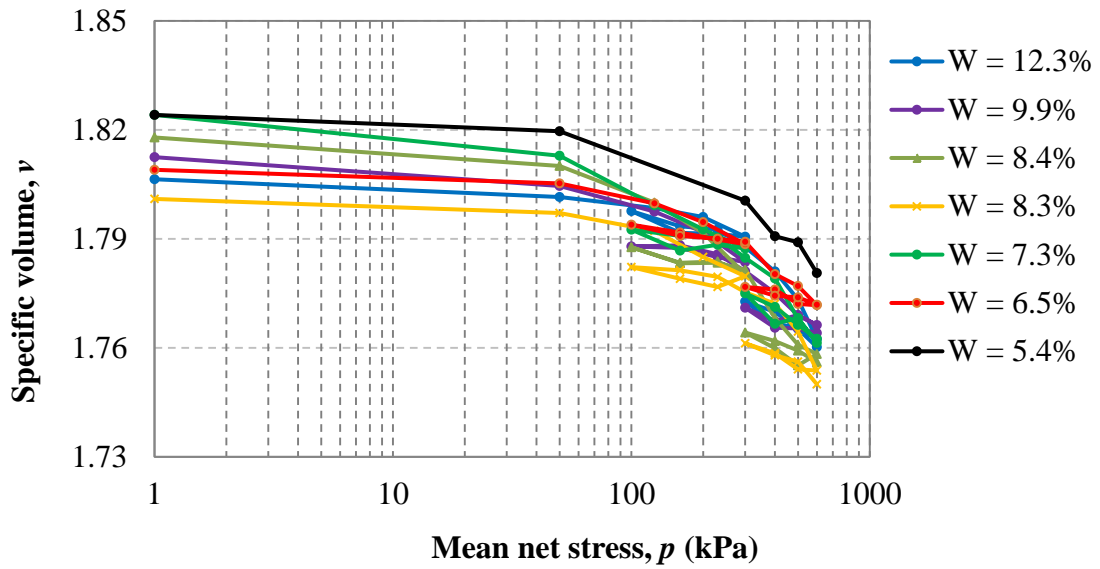
As addressed before, two idealized loading paths on  $s$ - $p$  plane were presented. After soil testing, the real loading paths used were plotted as shown in Figure 5.18. It can be found that the soil suction would decrease with an increase of confining stress and increase with a decrease of confining stress at different moisture content levels. Also, with decrease of water content, effect of mean net stress on soil suction was getting more pronounced. After unloading, there is some irrecoverable suction change. This is

because of the plastic deformation of the soil after loading. When unloading, the soil deformation was not fully recoverable which resulted in the irrecoverable suction change.

Undrained isotropic compression curves for all soil specimens with different moisture contents are plotted on the ( $v - p$ ) plane as shown in Figure 5.19. The specific volumes of all soil specimens decreased due to the increase of mean net stress. After unloading, as can be seen in Figure 5.19, there was some plastic volume change due to the loading process. Also, as shown in Figure 6.6, the yield point at a given value of suction was identified by a marked change in the slope of the continuous plot of specific volume against the logarithm of mean net stress. Yield stress of the soil specimens were determined by using Casagrande graphic determination method (1936) and plotted against soil suction as shown in Figure 5.20. Based on this method, yield stress was obtained and plotted against soil water content as shown in Figure 5.21. It can be found that the soil start to yield as the mean net stress increased to 100 to 200 kPa. Also, a clear trend can be found in Figure 5.21 that the yield stress of the soil specimens increased with an increase of matric suction with soil water contents ranging from 5.4 to 15.1%. Ideally, the pre-consolidation stresses for these soil specimens were consistent. However, yield stress of soil specimens increased due to the drying process for moisture equilibrium.



(a) Loading path A



(b) Loading path B

Figure 5.19 Volume change due to variation of net confining stress under different water contents

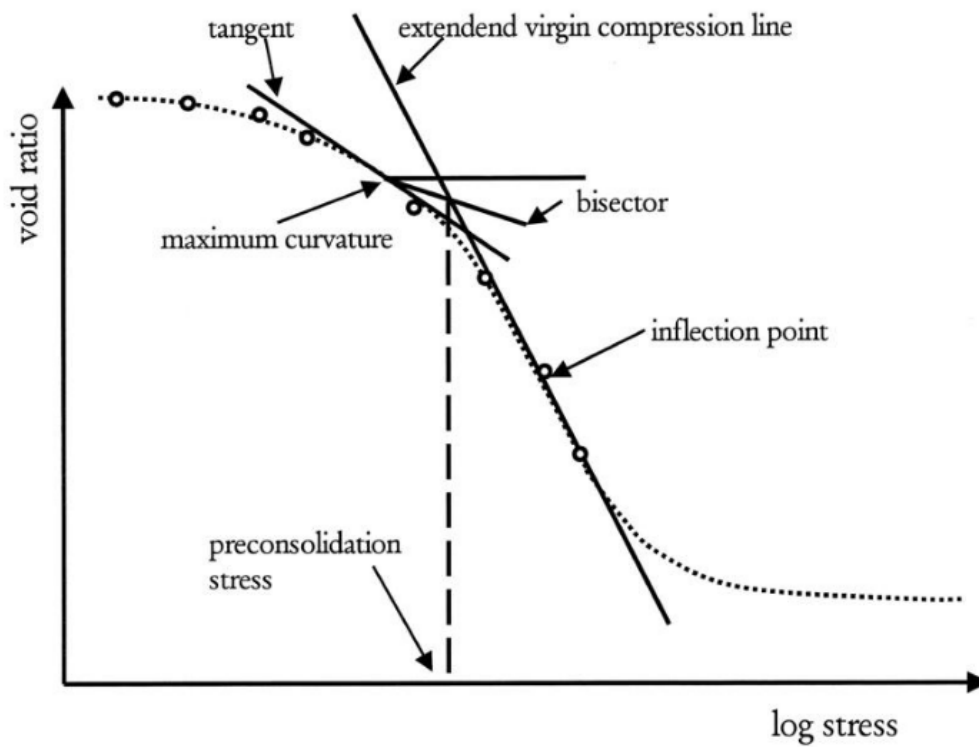


Figure 5.20 Casagrande method for determination of yield stresses

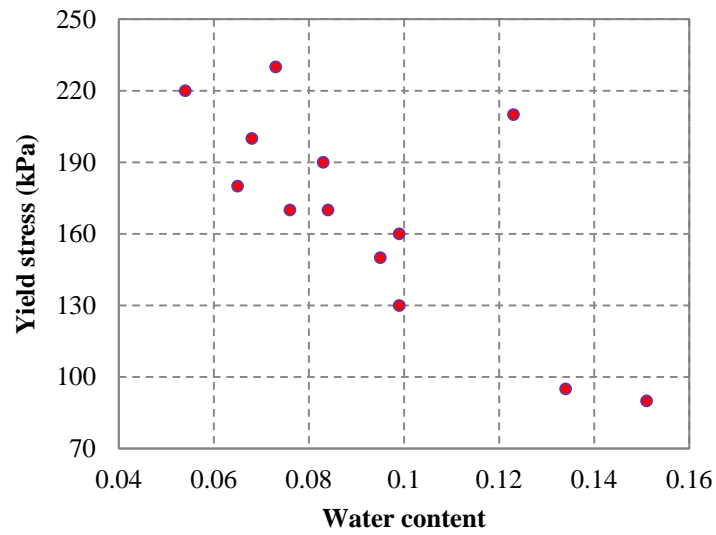
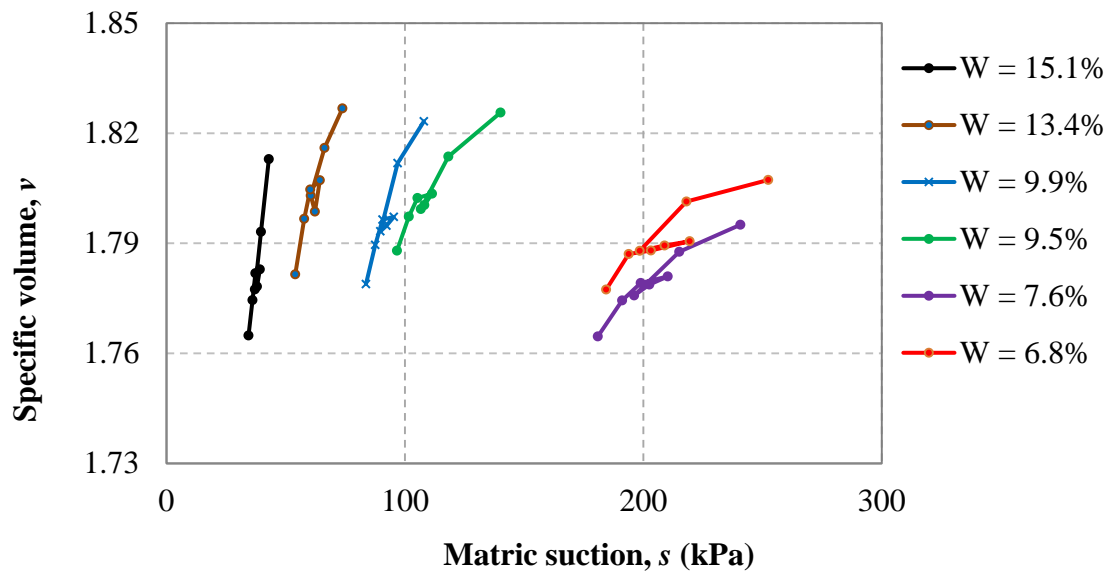
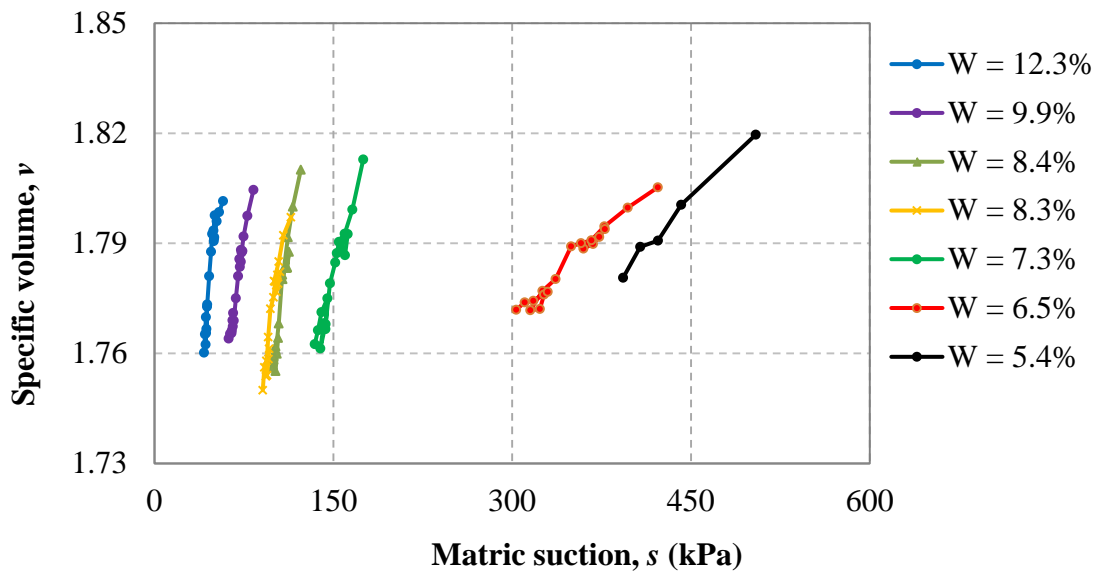


Figure 5.21 Yield stresses based on Casagrande method



(a) Loading path A



(b) Loading path B

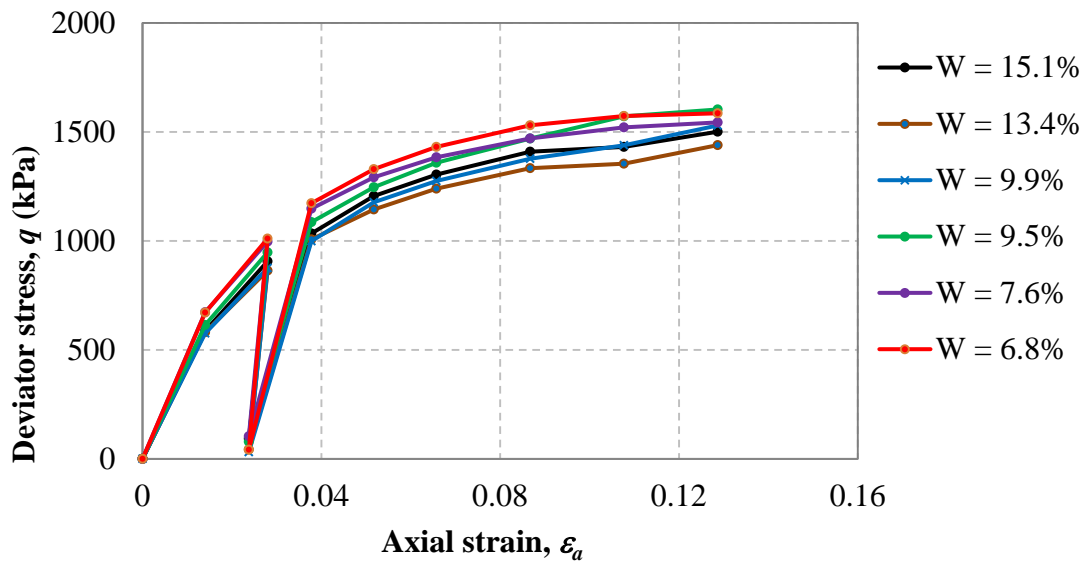
Figure 5.22 Suction changes due to variation of volume

Different from drained suction-controlled triaxial test, soil suction during testing varied in this study. It is possible to plot the stress paths of the specimens during isotropic testing under constant water content condition on the ( $v - s$ ) plane as shown in Figure 5.22. The results indicated that matric suction decreased with the decrease in specific volume under constant water content which was a result of isotropic compression.

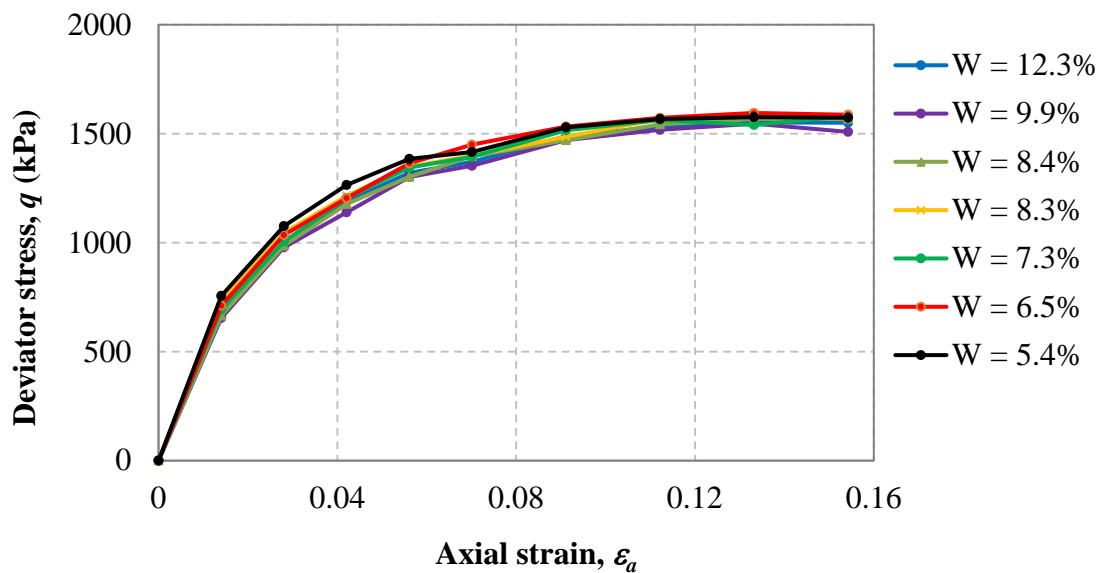
### Undrained Shear Test Results

Undrained shear tests were performed on Fairbanks silt specimens at different moisture contents under a confining pressure of 600 kPa right after the undrained isotropic compression test. A constant loading rate, which was 1 mm/min, was applied. Test was paused for a certain time to wait for the suction equilibrium and image capturing. For load path A, an unloading was performed after 4 mm of vertical displacement as shown in Figure 5.23a. It can be found that in Figure 5.23, the stress strain curves for all soil specimens are very close. Under axial strain within 15.4%, deviator stress peak was found to be at a vertical strain of 13.5% in Figure 5.23b. The deviator stress remained essentially constant after reaching the maximum value. Due

to the possible poor contact between the used tensiometers and the soil specimen surface at high strain level, the shear test was stopped at 13% and 15.4% for loading path A and B, respectively. The stiffness of the soil specimens did not varied very much under a confining pressure of 600 kPa.



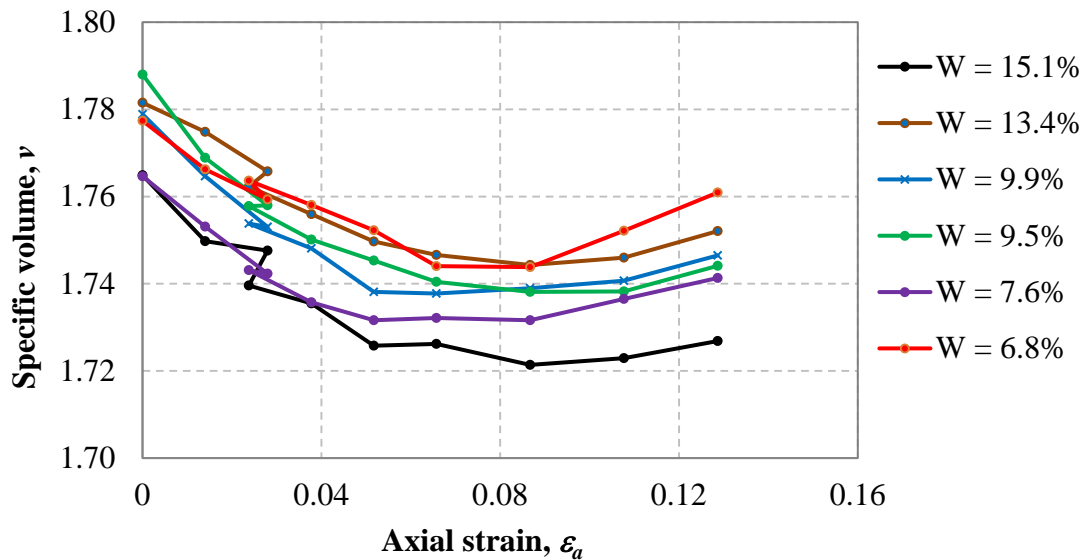
(a) Loading path A



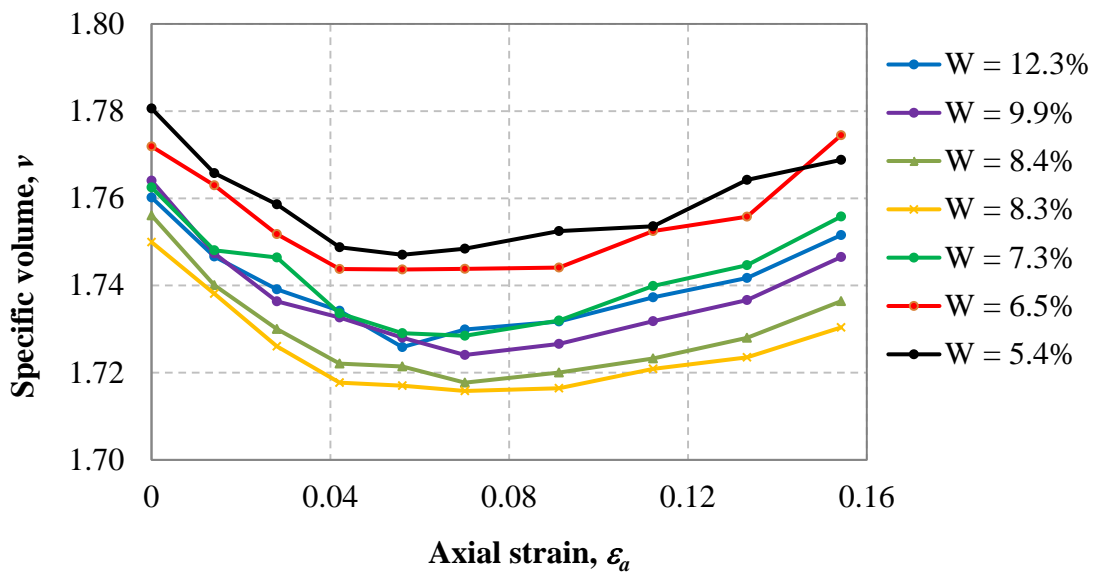
(b) Loading path B

Figure 5.23 Deviator stress versus axial strain under different moisture conditions

Besides the deviator stress change at different strain levels, volume changes of soil specimen during testing were also measured (Figure 5.24) by using the method proposed in Chapter III. The signs for the volumetric strain are negative for compression and positive for dilation. The volumetric strain of all the specimens exhibited similar characteristics. The results indicated that the specimens compressed in the early stage of shearing and then dilate afterwards.



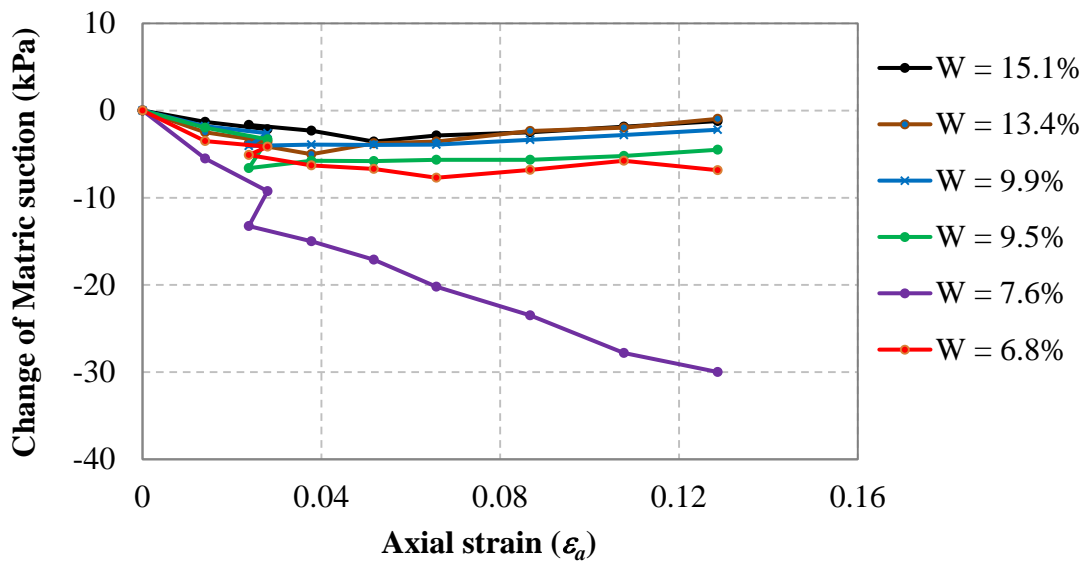
(a) Loading path A



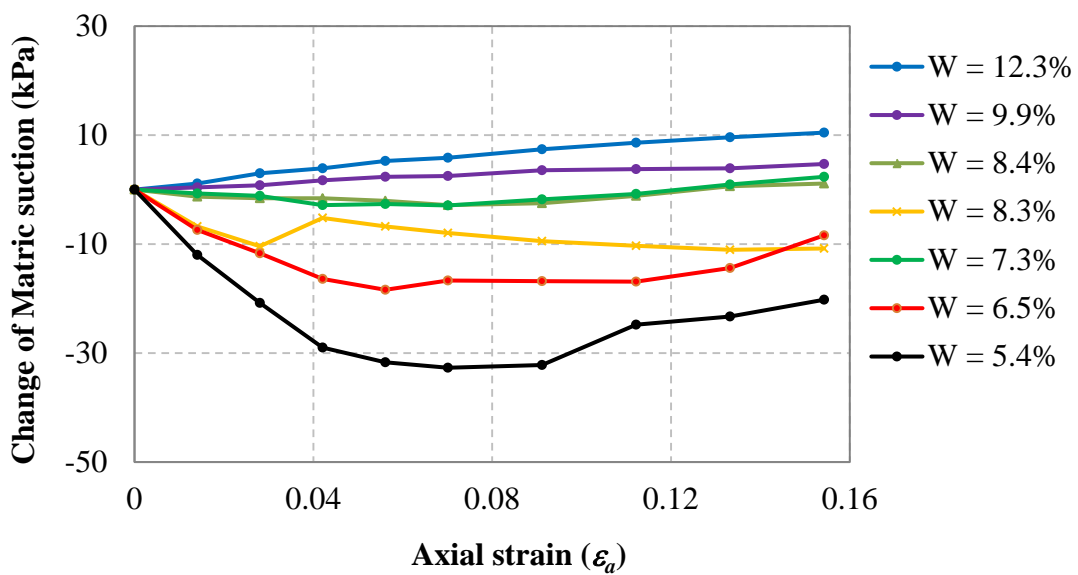
(b) Loading path B

Figure 5.24 Specific volume change versus axial strain under different moisture conditions

Change of matric suction on soil specimens with different moisture contents during undrained shear test under a confining pressure of 600 kPa are presented in Figures 5.25 and 5.26. The results indicated that matric suction decreased with the increase of deviator stress for most of the soil specimens as shown in Figures 5.25 and 5.26. For some of the soil specimens, soil suction increased throughout the test or decreased in the early stage of shearing and increased afterwards.

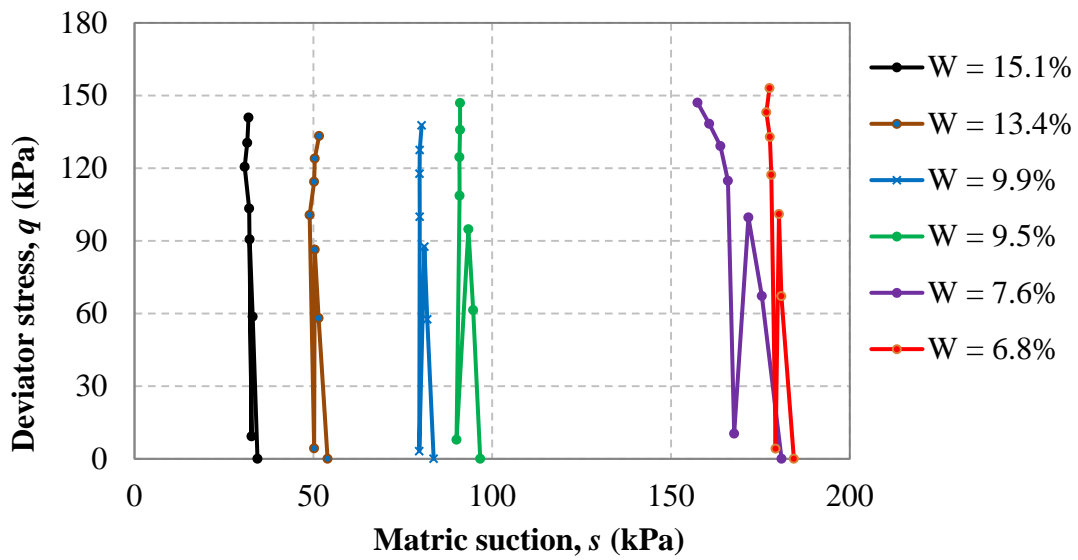


(a) Loading path A

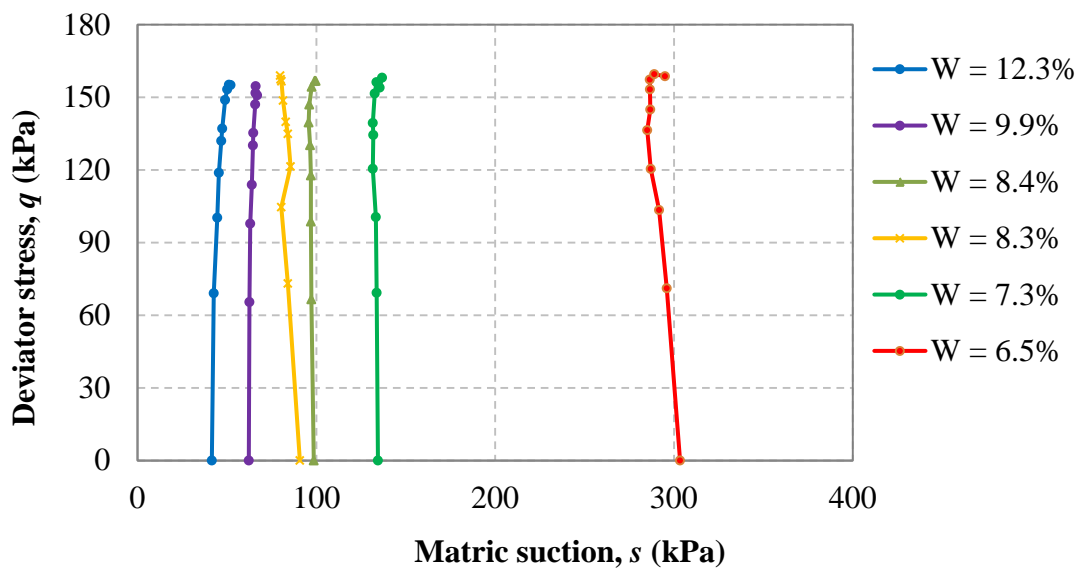


(b) Loading path B

Figure 5.25 Change of matric suction under different strain levels



(a) Loading path A



(b) Loading path B

Figure 5.26 Change of matric suction due to shear loading under different moisture conditions

## CHAPTER VI

### PRESENTATION OF RESULTS AND CONSTITUTIVE MODELLING

#### GENERAL

As discussed in Chapter II, at present, most researchers use results from suction controlled consolidated drained (SCCD) tests to perform constitutive modeling for unsaturated soils. However, SCCD tests are time-consuming due to extremely low permeability of unsaturated soils and subsequent lengthy equilibrium time. It takes five days to two weeks to bring a soil to a specific initial condition (e.g. Sivakumar 1993; Sharma, 1998; Hoyos, 1998). A simple isotropic compression test usually takes several weeks or months. For example, it took Sivakumar (1993) 959 days to complete 30 CSTs/SSP for a compacted speswhite kaolin, with an average of 32 days/test. It took Sharma (1998) 801 days to complete 20 isotropic compression tests for two compacted expansive soils under isotropic conditions with an average of 40 days/test. Although problems associated with unsaturated soils exist all over the world, SCCD tests cannot be justifiable for routine engineering projects. It is therefore important to develop alternative, cost-effective ways to characterize elasto-plastic behavior for unsaturated soils. This paper discusses possible use of results from undrained tests for the constitutive modeling of unsaturated soils.

#### THEORETIC BASIS

A constitutive model has to be able to predict soil behavior under all possible stress paths. On the other hand, results from any test reflect constitutive behavior of the soil along the specific stress path in the test and should be able to be used for constitutive modeling purposes. Compared with consolidated drained tests, some tests for unsaturated soils are easier to perform. An example is the unconfined compression test, which has been routinely performed in industrial labs and undergraduate classrooms. Often, an unsaturated soil specimen is used, although the test results are usually analyzed based on the theory of saturated soil mechanics. The test can be done in less than one hour, using any routine triaxial test apparatus for saturated soils. From the viewpoint of constitutive modeling, an unconfined compression test is an

undrained triaxial test with simultaneous changes of  $p$ ,  $q$ , and  $s$ . The variations of suction during the test are not externally specified, but internally determined by the coupling requirement that water content remains constant. In an undrained test, suction in the soil specimen will instantaneously reach equilibrium everywhere, which has been experimentally verified (Bishop et al. 1960; Rahardjo et al. 2004; Thu et al., 2006). Although having a more complicated stress path, an undrained test has the following advantages over consolidated drained tests: The tests are fast, cheap, easy to perform, and more representative of field conditions. With simultaneous change of  $p$ ,  $s$ , and  $q$ , each test can provide at least three times the information as that from a consolidated drained test, which means fewer tests are needed to provide the same amount of information. There is much less possibility of disturbance due to a short testing period, and the test results are more reliable.

Since a constitutive model must be able to predict soil behavior under any condition, including un-drained loading conditions, it is both theoretically reasonable and practically feasible to replace consolidated drained tests with undrained tests for the constitutive modeling of unsaturated soils. The only problem is that, at present, there is no method available to take full advantage of results from undrained tests for the constitutive modeling purposes. The newly proposed modified state surface approach (MSSA) (Zhang and Lytton 2009a and 2009b) can be used for the purpose. The BBM is used as an example to demonstrate the proposed method since it is the first and most influential elasto-plastic model for unsaturated soils.

## **MODIFIED STATE SURFACE APPROACH**

Zhang and Lytton (2009a and 2009b) proposed a Modified State Surface Approach (MSSA) for the constitutive modeling of unsaturated soils. The principle of the MSSA can be illustrated by Figure 6.1 (Zhang et al. 2010). Figure 6.1a shows an isotropic loading-unloading-reloading stress path under an arbitrary constant suction. The soil specimen has an initial condition of point D and an initial yield curve of  $LC_1$  with a preconsolidation stress of at  $s = 0$  kPa. The yield stress at  $s = s_2$  is at point E. The soil is loaded from D to E to V, unloaded from V to D, and then reloaded to F. Figure 6.1b illustrates a typical soil response in the  $v$ - $\ln p$  plane when the hysteresis is neglected. The following observations can be made from the process:



initial virgin consolidation curve for the soil is EVF. After loading from D to E to V, the virgin consolidation curve for the soil is VF.

2. During an elastic loading or unloading process, for example, from D to E, from V to D', or from D' to V, the shape and position of the unloading-reloading curve remain unchanged in the  $v$ - $\ln p$  plane.

3. During plastic loading process, the shape of the unloading-reloading curve remains unchanged in the  $v$ - $\ln p$  plane ( $\kappa$  is a constant), but its position will change. Specifically, the unloading-reloading curve will move downward in parallel with the original un-loading-reloading curve. The range of the elastic zone also expands due to the increase in the preconsolidation stress.

4. The yield point is the interception of the un-loading-reloading curve and the virgin consolidation curve.

Let us consider two other arbitrary stress paths from D to E, i.e. 1 and 2 as shown in Fig.2a, in the elastic zone. Since stress paths 1 and 2 are in the elastic zone, the specific volume changes are stress path independent and the results for the two stress paths should be the same. Zhang and Lytton (2009a and 2009b) proved that volume of the soil in the elastic zone is a surface in the  $v$ - $p$ - $s$  space.

Figure 6.2c shows the specific volume change for the stress paths in Figure 6.1a in the  $v$ - $p$ - $s$  space. All the elastic volume changes such as stress paths 1 and 2 and DE are in the same surface of ABEHGDA. When there is a plastic loading, similar to the previous discussion, the shape and position of the virgin consolidation curve EVF are always the same in the  $v$ - $p$ - $s$  space regardless the previous stress path and stress history. It can also be proven that when there is un-loading, any unloading stress path must fall on a lower elastic surface parallel to surface ABEHGDA. For example, if there is an unloading process from V, the unloading stress path VD' must fall on the surface D'UVW, which is in parallel with surface ABEHGDA.

Multiple normal compression tests can be performed at any arbitrary suction levels. Consequently, the virgin consolidation curves at different suction levels will also form a "plastic surface" in the  $v$ - $p$ - $s$  space such as BEHUXYZ in Figure 6.1c. The location and shape of the plastic surface will always remain the same in the  $v$ - $p$ - $s$  space and the plastic surface is unique. The uniqueness of the state boundary surface is a fundamental assumption made in the constitutive modeling of elasto-plastic soil behavior. The uniqueness of the state boundary surface for unsaturated soils has been

experimentally verified by Wheeler and Sivakumar (1995). The plastic surface BEHUXYZ in Figure 6.1c is actually the shape of the state boundary surface when the shear stress is equal to zero (isotropic conditions). Similarly, in the v-p-s space, the following criteria can be made for the elastic and plastic surfaces:

1. The shape and position of the plastic surface BEHUVWX are always the same for the soil in the v-p-s space. Plastic loading only changes the range of the plastic surface.
2. During an elastic loading or unloading process, the shape and position of the unloading-reloading elastic surface and the plastic surface remain un-changed in the v-p-s space. The volume change of any isotropic elastic loading or unloading stress path must fall on the elastic surface in the v-p-s space.
3. During a plastic loading process, the shape of the unloading-reloading elastic surface remains un-changed ( $\kappa$  and  $\kappa_s$  are constants), but its position will change. Specifically, the unloading-reloading elastic surface will move downward in parallel with the original unloading-reloading elastic surface. The volume change of any isotropic plastic loading stress path must fall on the plastic surface in the v-p-s space.
4. The yield curve is the interception of the un-loading-reloading elastic surface and the plastic surface.

### **SURFACE USED IN THE BBM**

The above criteria can be used to represent un-saturated soil behavior under isotropic loading conditions including stress path independency. Zhang and Lytton (2009a) derived the mathematical expressions of the elastic surfaces for the BBM and successfully used the MSSA to represent many un-saturated soil behavior including the stress path in-dependency under isotropic conditions. Figure 6.2 shows the elastic and plastic surfaces used in the BBM.

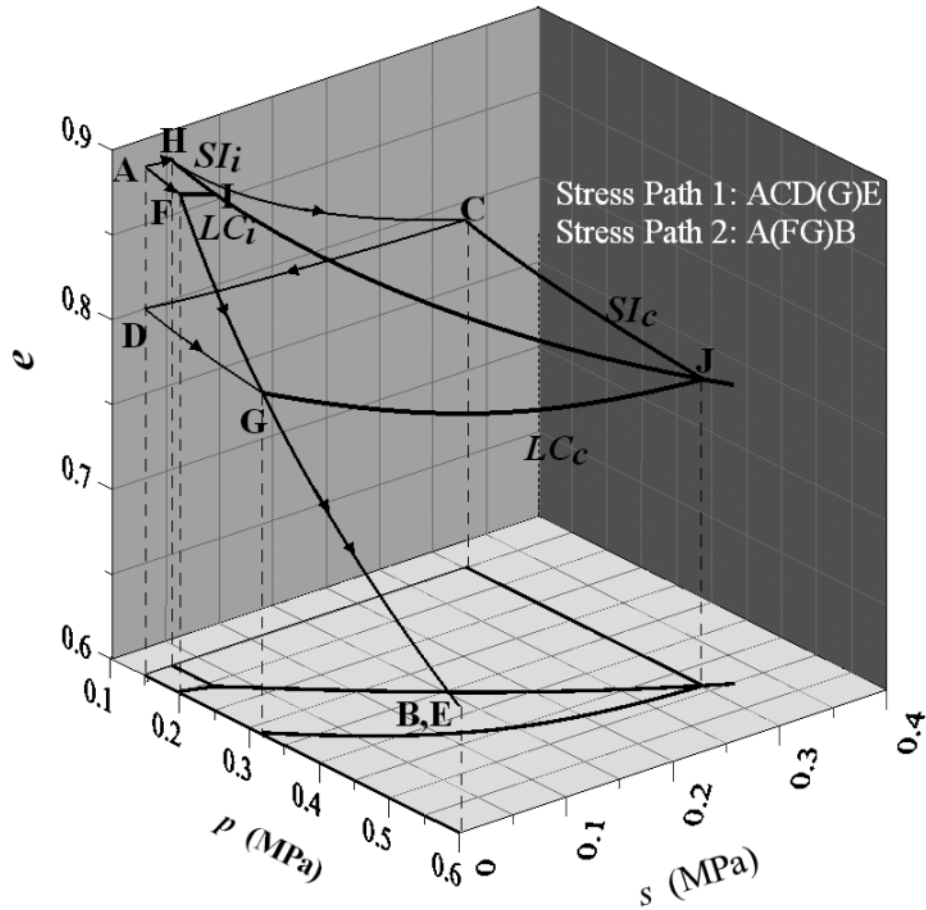


Figure 6.2 Shape of the state boundary surface for the BBM (Zhang and Lytton 2009a).

They include an elastic surface AEFG and the plastic surface which is made up of two parts: a plastic collapsible surface EFSCDHR and a plastic expansive surface GFSB.

$$e^e = C_1 - \kappa \ln p - \kappa_s \ln (s + p_{at}) \quad (6.1)$$

$$e = C_2 - \kappa_s \ln \left( \frac{s + p_{at}}{p_{at}} \right) - \lambda(s) \ln \left( \frac{p}{p^c} \right) \quad (6.2)$$

$$e = C_3 - \kappa \ln p - \lambda_s \ln (s + p_{at}) \quad (6.3)$$

Where,

$e^e$  = void ratio in the elastic zone,

$C_1$  = constants,

$C_2 = N(0)$  constants. The rest of the symbols have the same meanings as those defined in the BBM as defined in Chapter II.

Note that Figure 6.2 was plotted in scale based on the real data of Case 3 in Alonso et al. (1990), with soil parameters of  $\lambda(0) = 0.2$ ,  $\kappa = 0.02$ ,  $\lambda_s = 0.08$ ,  $\kappa_s = 0.008$ ,  $r = 0.75$ ,  $\beta = 12.5\text{MPa}^{-1}$ , and  $p^c = 0.10\text{ MPa}$ . From the initial conditions of the soil, i.e.  $p = 0.15\text{ MPa}$ ,  $s = 0\text{ MPa}$ , and  $v = 1.9$ ,  $C_1$ ,  $C_2$ , and  $C_3$  in Equations 6.1 through 6.3 are 0.844, 1.033, and 0.694, respectively.

## ANALYSIS OF AN UNDRAINED TEST USING MSSA

Let us qualitatively analyze an isotropic undrained test using the MSSA as shown in Figure 6.3. Figure 6.3a schematically shows the stress path of an undrained test. A soil specimen has an initial condition of point G in the elastic zone. The corresponding initial position of the LC yield curve is represented by HEB ( $LC_1$ ). Under an undrained loading process, the soil followed the stress path from G to E in the elastic zone, followed by a plastic undrained loading from E to C. During this process, the suction decreases due to the increase in the mechanical stress. Finally there is an undrained unloading from C to G'. Due to the irrecoverable plastic deformation, the final suction is less than the original suction as shown in Figure 6.3a. Figure 6.3b shows the corresponding changes in the specific volume is plotted in the v-p-s space. According to the MSSA, GF is on the initial elastic surface ADGHEB, and FC is on the plastic surface BEHIFC. The results from the undrained test do provide information regarding the shape of the elastic and plastic surfaces and can be used to determine the model parameters as shown in Equations 6.1 and 6.2 if the BBM model is used to simulate the soil behavior. Figure 6.3 shows results from one undrained test only. Figure 6.4 shows results from multiple undrained tests from soil specimens with identical stress histories. The elastic and plastic surfaces can be directly determined from those undrained test results. Figure 6.5 shows the results from multiple undrained tests from soil specimens with different stress histories. The virgin compression curves EC, VF, and XI can therefore be used to determine the shape of the plastic surface. The elastic surface can easily be determined by finding the constants  $\kappa$  and  $\kappa_s$  with high accuracy. As long as the shape of the elastic and elasto-plastic surfaces can be accurately determined, the shapes of yield curve and its evolutions can be accurately determined. Under this situation, only the MSSA will give correct results.

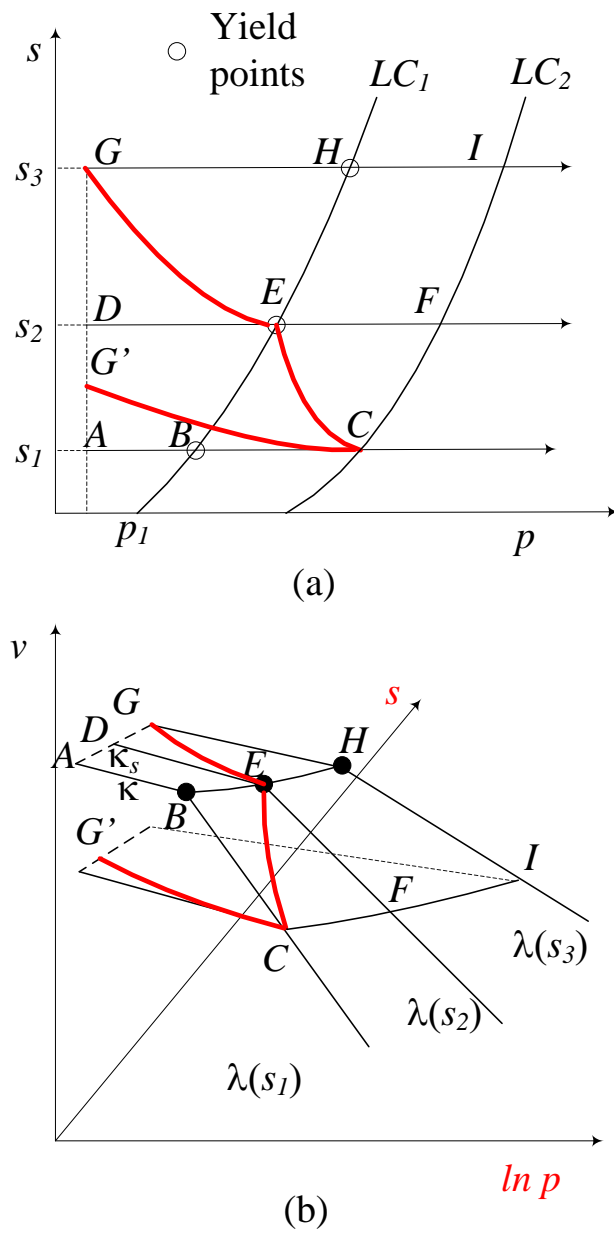


Figure 6.3. Analysis of an undrained test using the MSSA. (a) Stress path for an undrained loading and unloading test. (b) Changes in the specific volume in the  $v$ - $p$ - $s$  space for the undrained test.

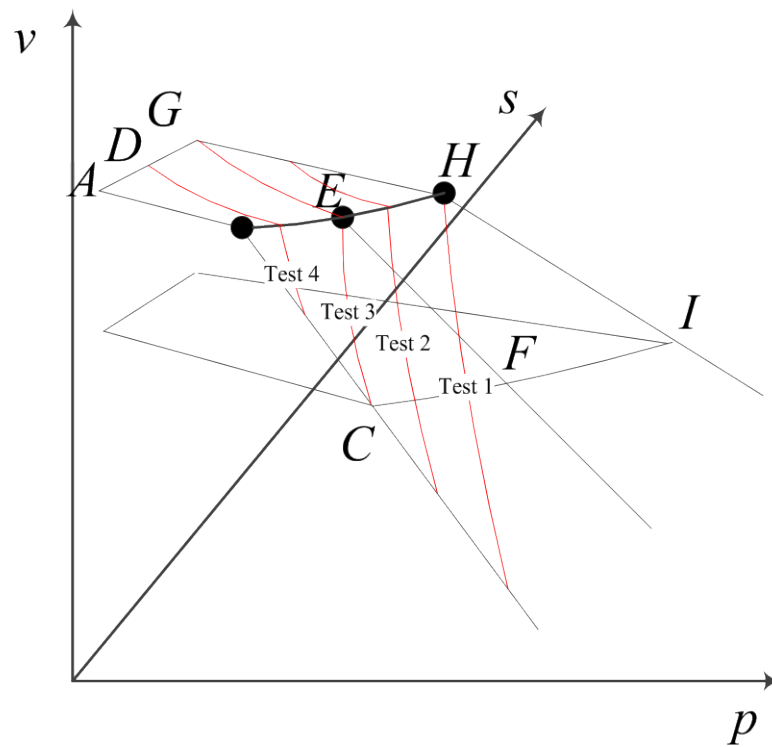


Figure 6.4. Analysis of multiple undrained tests with identical stress histories.

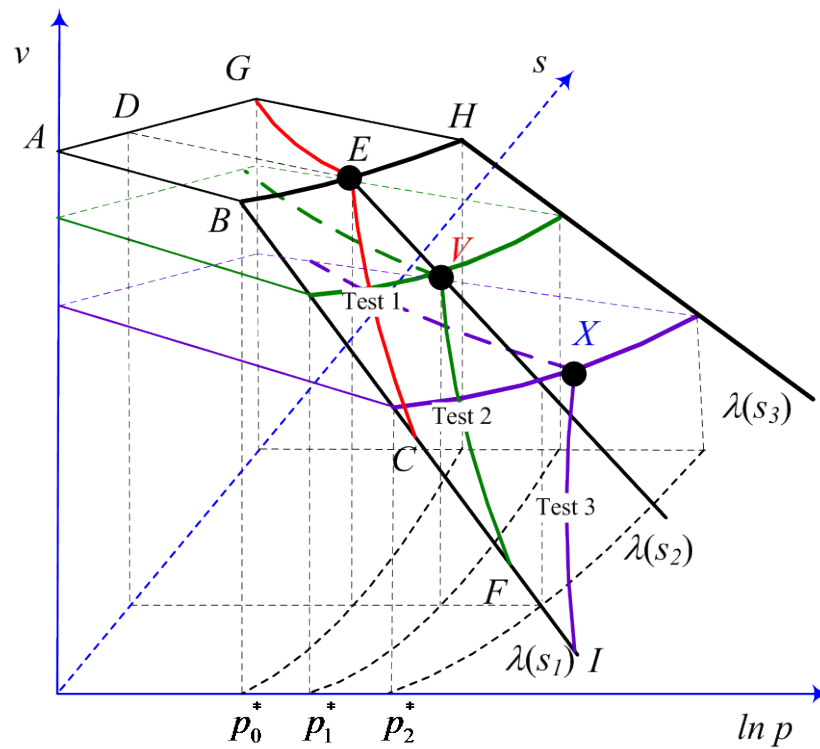


Figure 6.5. Analysis of multiple undrained tests with different stress histories

## DETERMINING PARAMETER VALUES IN BBM BY COMBINING THE MSSA AND NEWTON METHODS

The MSSA summarized the BBM under isotropic stress conditions into two concise surfaces: the elastic surface (equation 6.1) and the plastic surface (equation 6.2), if the plastic expansive surface 6.3 is not considered. While the elastic surface is easy to determine ( $C_1$  in equation 6.1 can be determined by initial condition of the soil), calibration of the BBM under isotropic stress conditions is simplified into the following problem: find a combination of the model parameters of  $N(0)$ ,  $\lambda(0)$ ,  $r$ ,  $\beta$ , and  $p^c$  to best fit the experimental results at virgin states using equation 6.2. Since all the five model parameters have physical meanings, there are also some constraints as follows:

$$N(0) > 0, \lambda(0) > 0, \beta > 0, r > 0, \text{ and } p^c > 0 \quad 6.4$$

Mathematically, the problem can be described as follows: calibration of the BBM under isotropic stress conditions is to find an appropriate combination of  $X = [N(0) \ \lambda(0) \ \beta \ r \ p^c]^T$ , which can minimize the overall difference between the experimental data at virgin states and the theoretical results as predicted by equation 6.2 for each laboratory test under the constraints of equation 6.4. The corresponding objective function can be expressed as follows using the Euclidean norm and independent state variables for all experimental points at virgin states:

$$\begin{aligned} F(X) &= \sum_{i=1}^n w_i (v_i - \hat{v}_i)^2 \\ &= \sum_{i=1}^n w_i \left\{ v_i - \left[ N(0) - \kappa_s \ln \left( \frac{s_i + p_{at}}{p_{at}} \right) - \lambda(s_i) \ln \left( \frac{p_i}{p^c} \right) \right] \right\}^2 \\ &= \sum_{i=1}^n w_i \left\{ v_i - \left[ N(0) - \kappa_s \ln \left( \frac{s_i + p_{at}}{p_{at}} \right) - \lambda(0) [(1-r) \exp(-\beta s_i) + r] \ln \left( \frac{p_i}{p^c} \right) \right] \right\}^2 \end{aligned} \quad 6.5$$

If all the experimental results have the same weight  $w_i$  of 1, the above objective function is actually the least-squares method in which the objective function is defined as the sum of the squares of the difference between the experimental value vs. theoretical values predicted by equation 6.2 (that is, the sum of the squares of the residuals). The “best” fit is defined as a combination of model parameters which

results in the least error between results from the ISC tests compared to the predicted values using equation 6.2. The least squares method finds its optimum when the sum of squared residuals,  $F(X)$ , is the minimum subject to constraints in equation 6.4. According to criterion 1 of the MSSA, the shape and position of the plastic surface are always the same for the soil in the  $v$ - $p$ - $s$  space and plastic yielding can only change the range of the plastic surface. Consequently, even if the soil specimens used in the isotropic compression tests at different suction levels have different stress histories as shown in Fig.6.5, the results can still be used to calibrate the model parameters for the BBM. Under this condition, the accurate LC yield curve can be obtained using the criterion 4 of the MSSA after the elastic and plastic surfaces are determined: that is, the yield curve is the interception of the unloading-reloading elastic surface and the plastic surface. Zhang and Xiao (2012) developed an optimization approach for simple and objective identification of material parameters in the BBM. It used the Newton or Quasi-Newton method to simultaneously determine the five parameters governing isotropic virgin behavior in the BBM. The proposed method was used in this research project to determine the model parameters based upon the test results presented in Chapter V. Table 6.1 shows the calibrated model parameters for the BBM using the test results in Chapter V under isotropic conditions.

Table 6.1 Calibrated Model Parameters for the BBM

Parameter	Unit	Best Fit
$\kappa_s$	—	0.025
$\kappa$	—	0.020
$C_2$	—	<b>1.579</b>
$\lambda(0)$	—	<b>0.136</b>
$r$	—	<b>1.758</b>
$\beta$	MPa <sup>-1</sup>	<b>2.903</b>
$p^c$	MPa	<b>3.268</b>
$p_{at}$	MPa	0.1

Figure 6.6 shows the predicted LC yield curve in the  $s$ - $p$  plane using the final results of the model parameters in table 6.1. Since the BBM with these model parameters provides a good representation of the soil behavior, an accurate prediction of the constant suction normal compression lines will automatically result in correct estimate

of the form of the LC yield curves and the hardening parameters. The LC yield curve is obtained according to criterion 4 in the MSSA: the LC yield curve is the interception of the unloading-reloading elastic surface (equation 6.1) and the plastic surface (equation 6.2). By making equation 6.1 equal to equation 6.2, the LC yield curve can be obtained by varying the value of  $C_1$  in equation 6.1. On the yield curves, the suction increases with increase of the mean net stress, which are typical for compacted soils with collapsible behavior as shown in the Alonso et al. (1990) and Zhang and Lytton (2009a and 2009b).

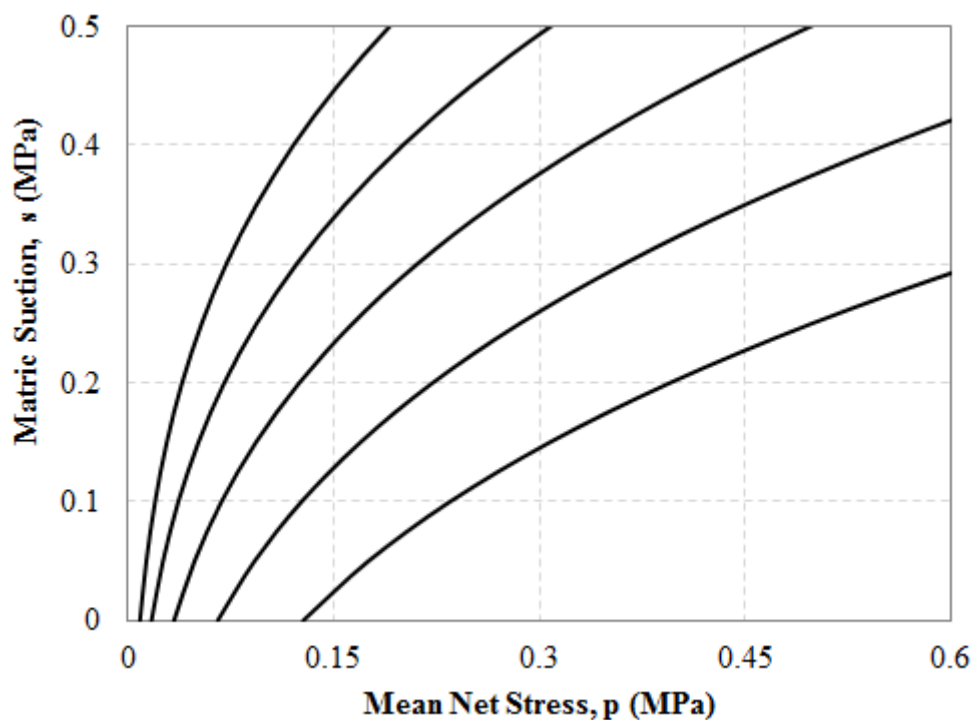
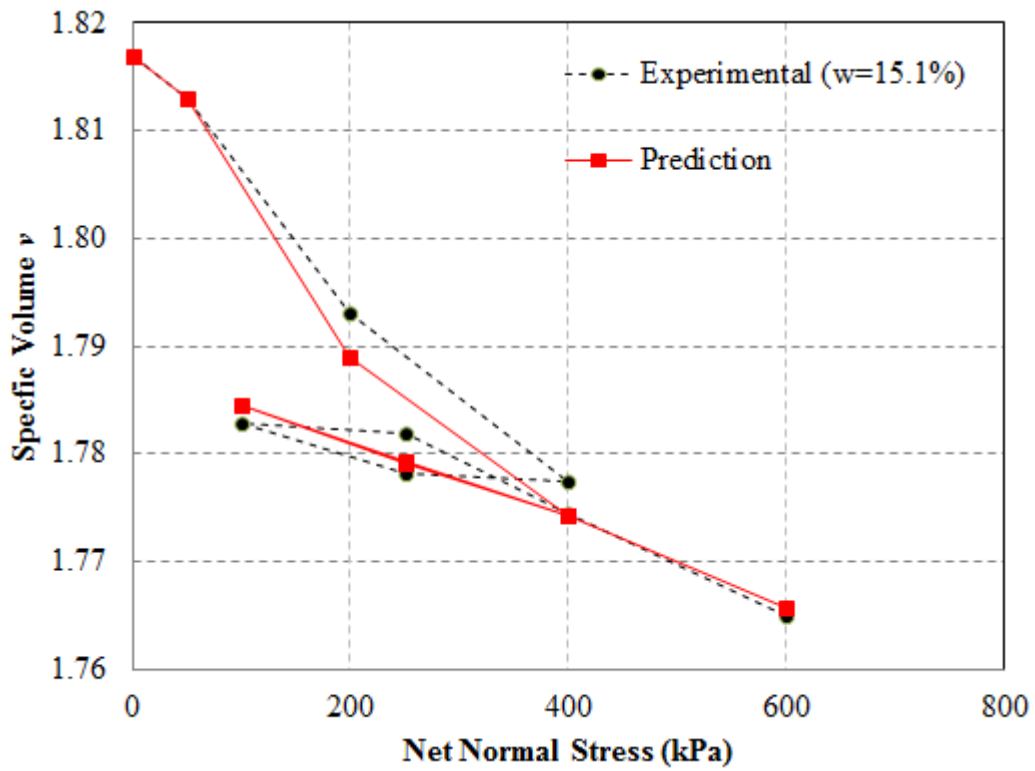
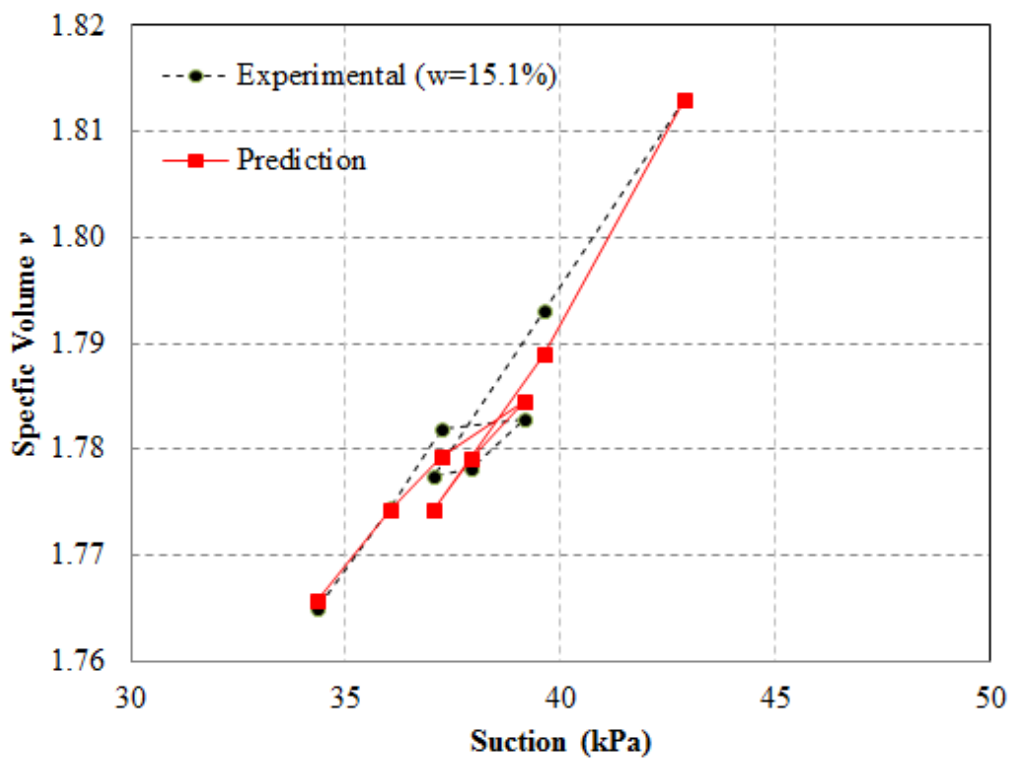


Figure 6.6 Predicted LC Yield Curve Based upon the Model Parameters

Figures 6.7 through 6.14 shows the experimental results and the predictions based upon the model parameters in Table 6.1 for undrained compression tests at constant water contents of 15.1%, 12.3%, 9.9%, 8.4%, 8.3%, 7.6%, 7.3%, and 6.5%, respectively. Inspection of these figures indicates that all the predictions reasonably matched the test results.

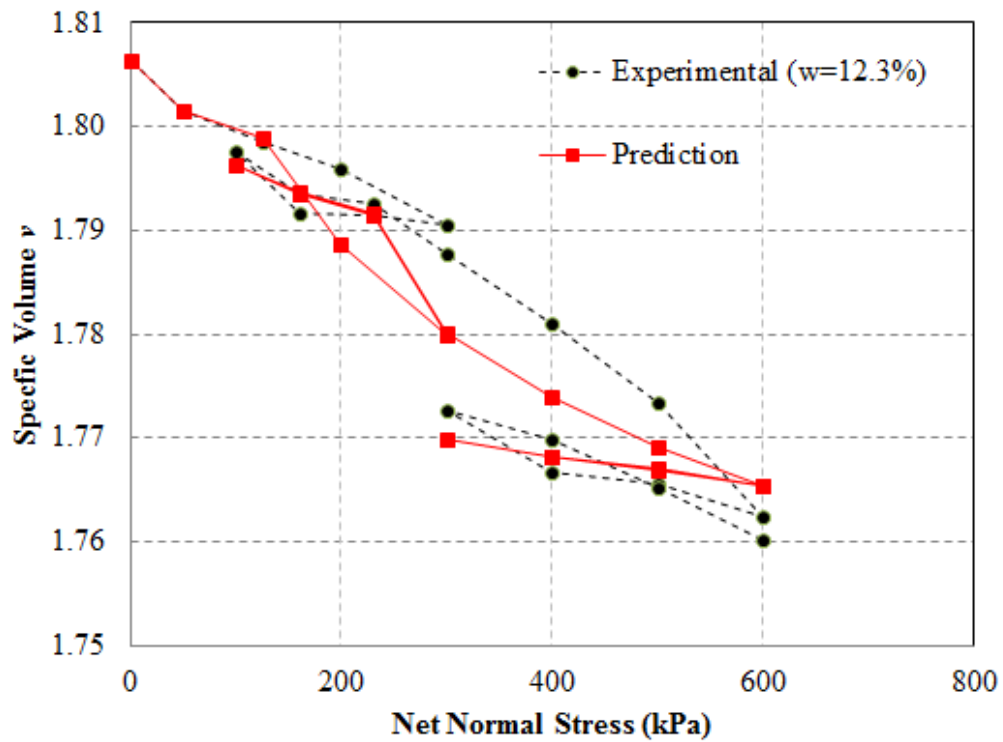


(a)

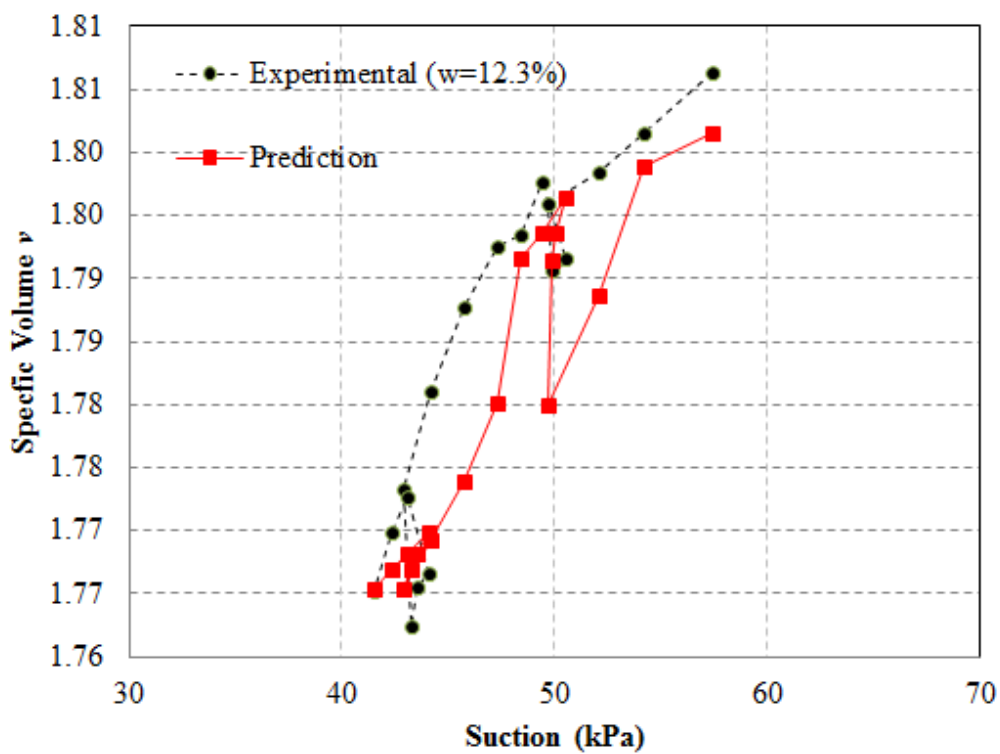


(b)

Figure 6.7 Comparison of Predicted and Experimental Results for an Undrained Test at  $w=15.1\%$ . (a) In the  $v$ - $p$  plane and (b) at in the  $v$ - $s$  plane

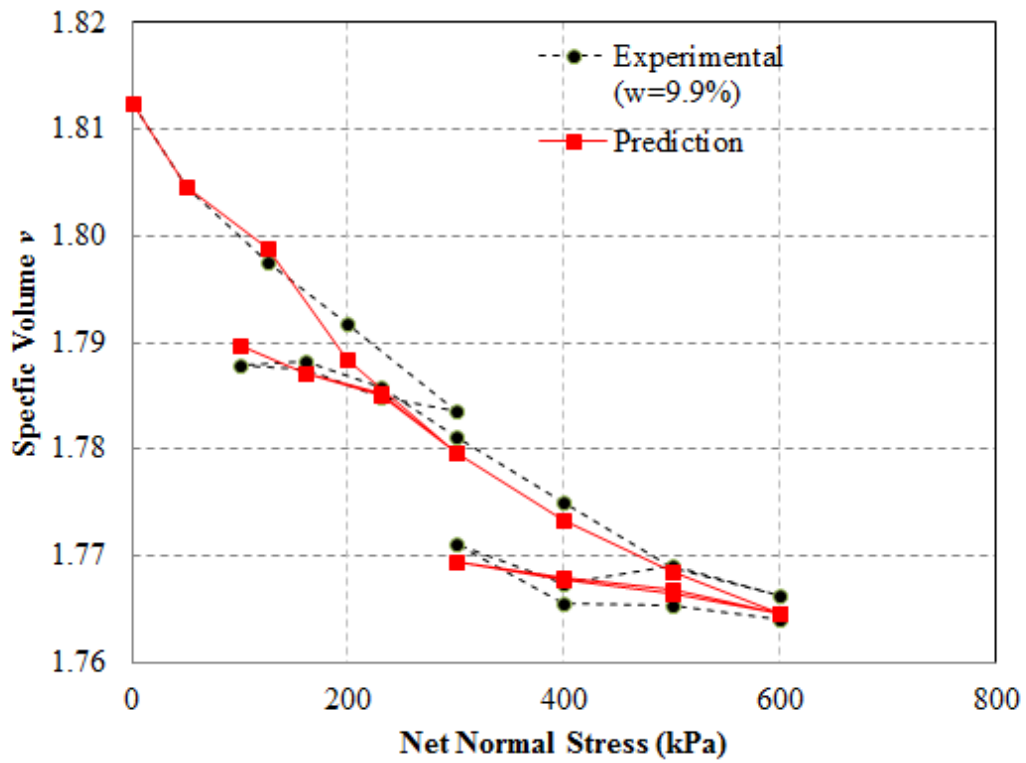


(a)

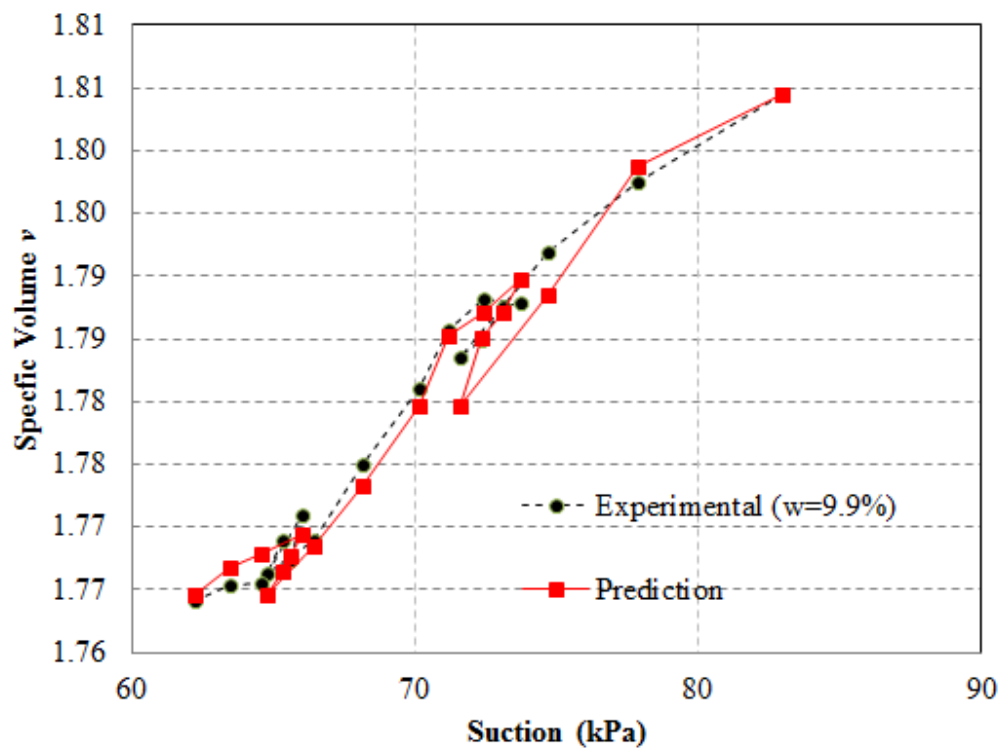


(b)

Figure 6.8 Comparison of Predicted and Experimental Results for an Undrained Test at  $w=12.3\%$ . (a) In the  $v$ - $p$  plane and (b) at in the  $v$ - $s$  plane

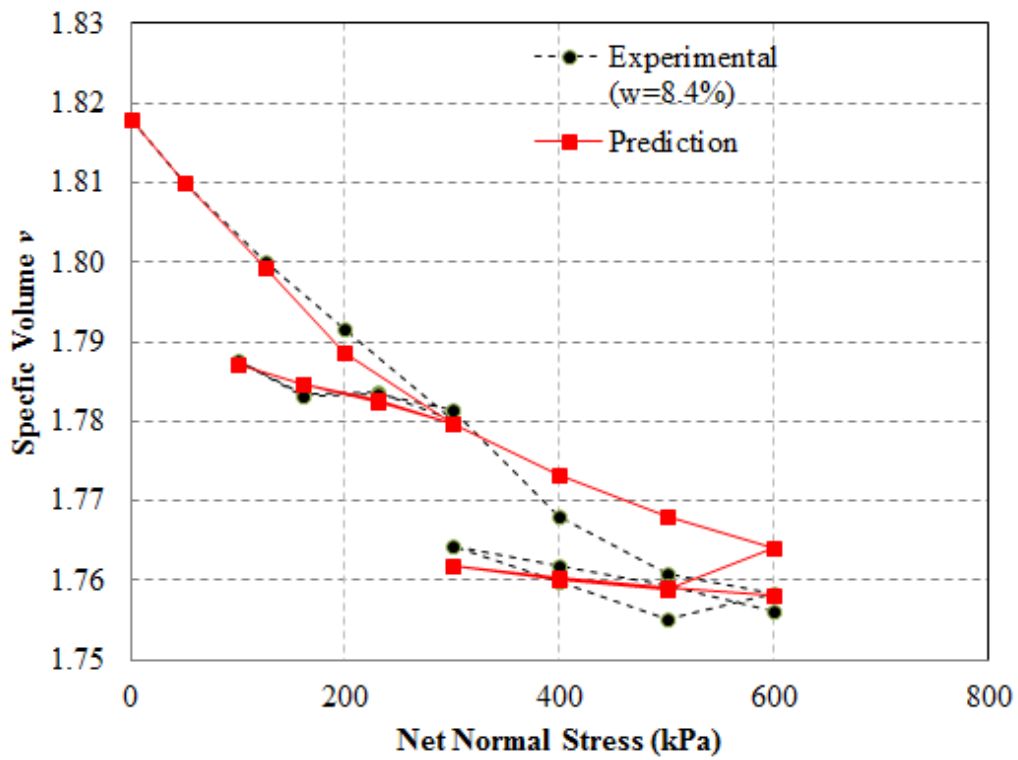


(a)

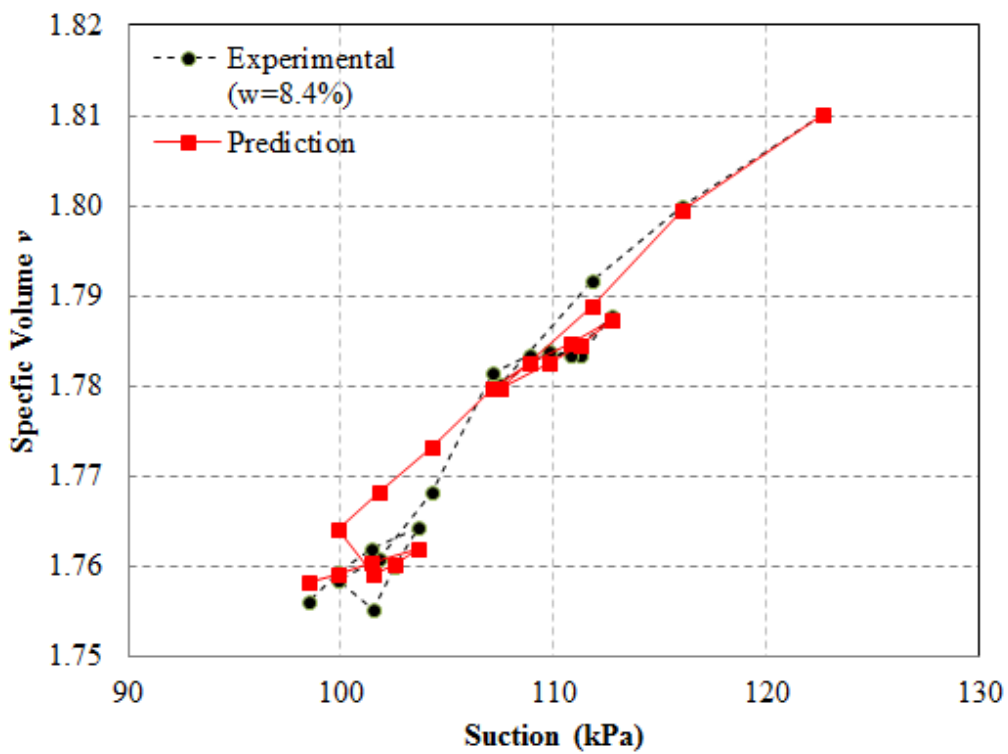


(b)

Figure 6.9 Comparison of Predicted and Experimental Results for an Undrained Test at  $w=9.9\%$ . (a) In the  $v$ - $p$  plane and (b) at in the  $v$ - $s$  plane

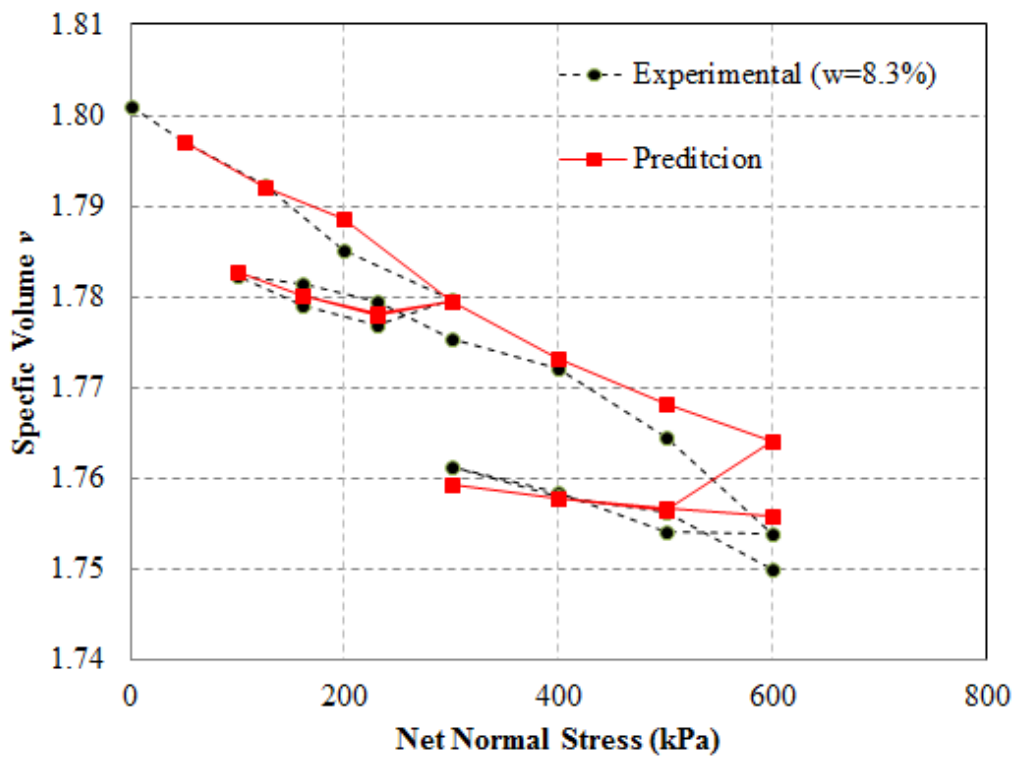


(a)

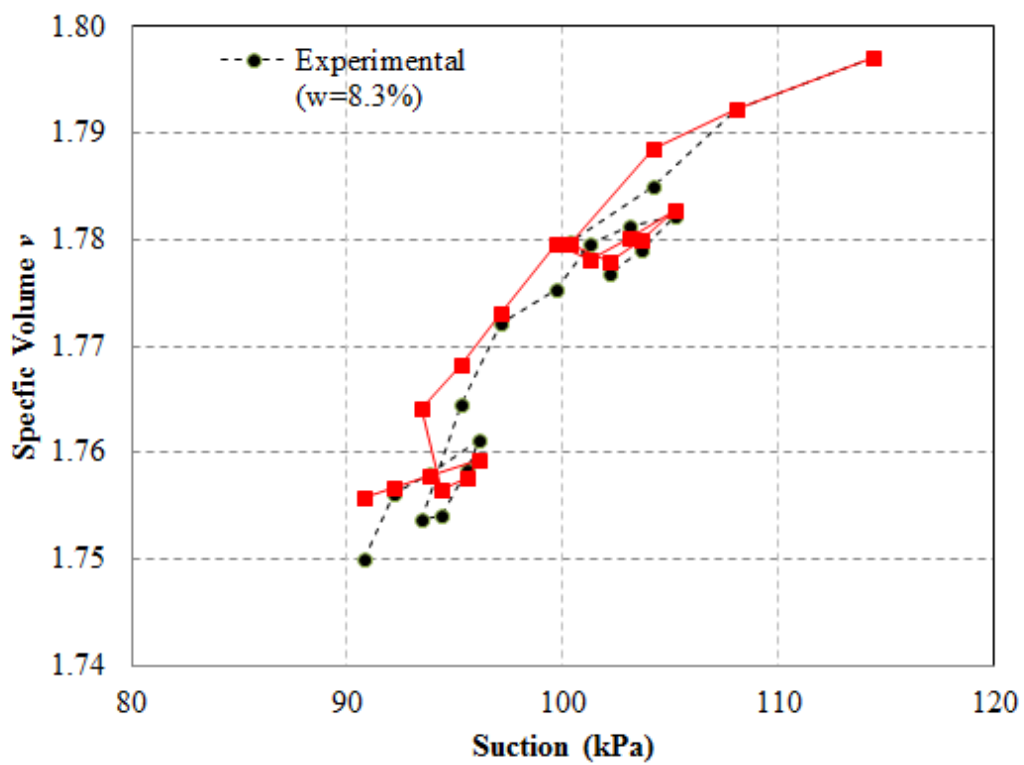


(b)

Figure 6.10 Comparison of Predicted and Experimental Results for an Undrained Test at  $w=8.4\%$ . (a) In the  $v-p$  plane and (b) at in the  $v-s$  plane

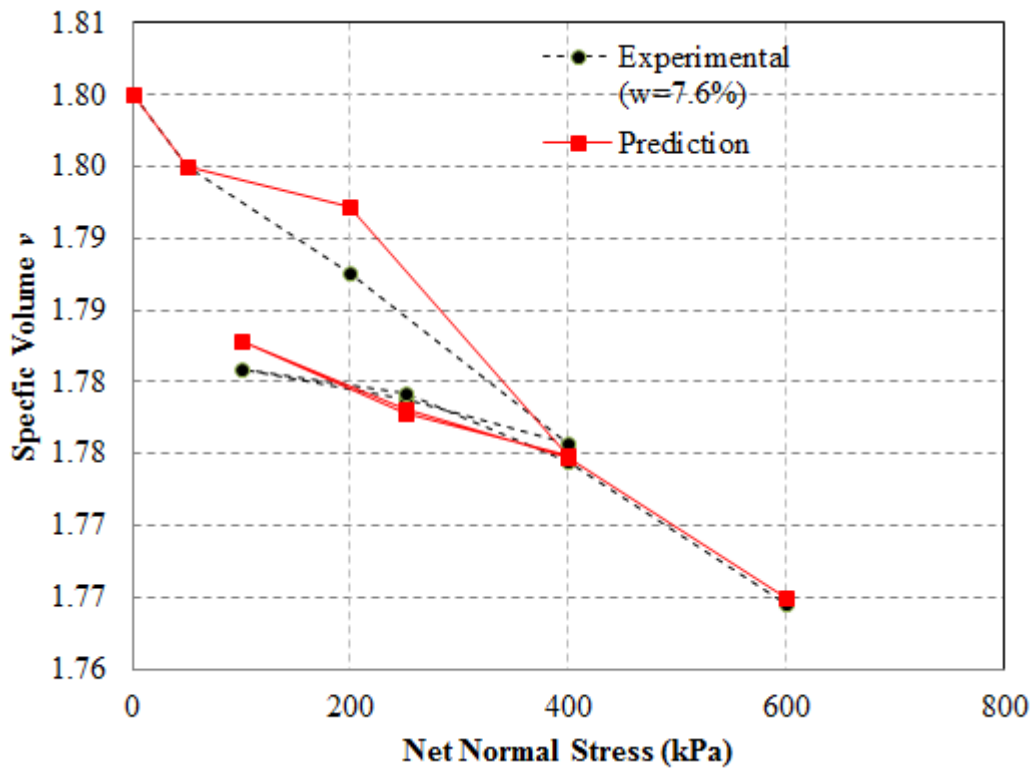


(a)

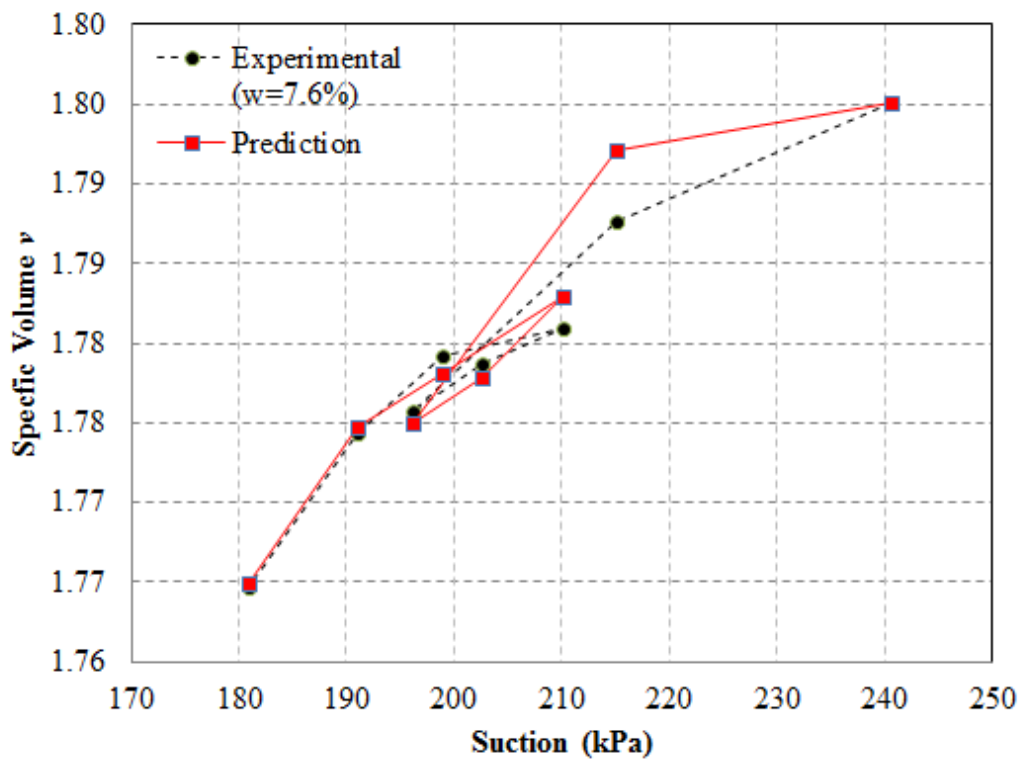


(b)

Figure 6.11 Comparison of Predicted and Experimental Results for an Undrained Test at  $w=8.3\%$ . (a) In the  $v$ - $p$  plane and (b) at in the  $v$ - $s$  plane

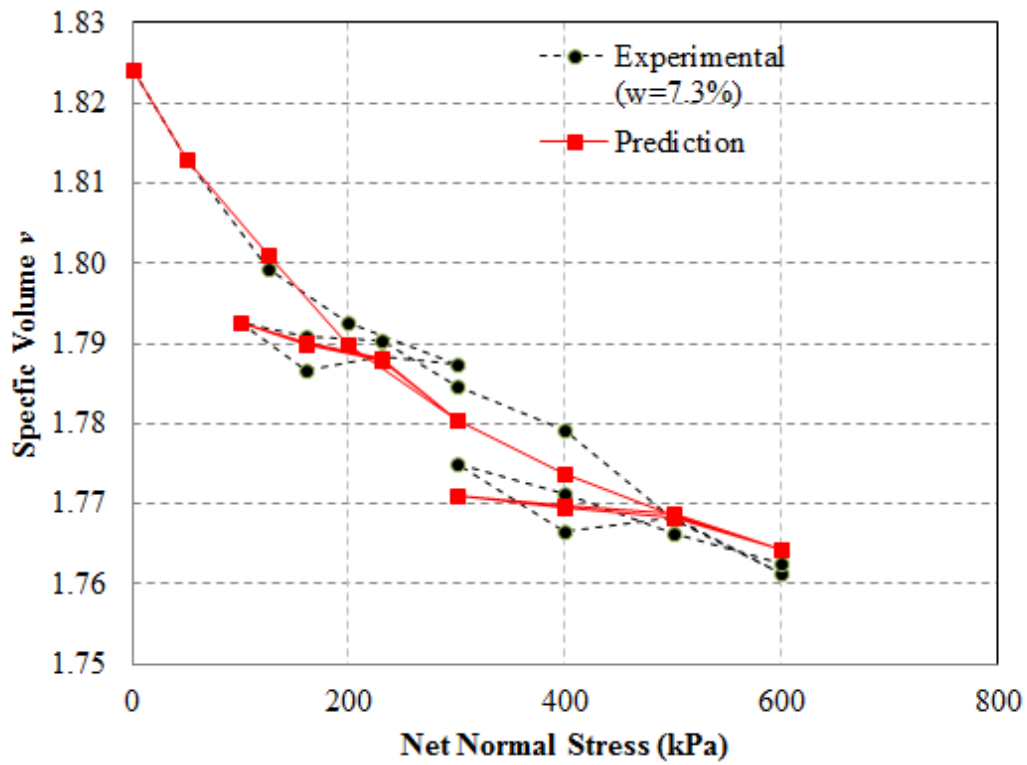


(a)

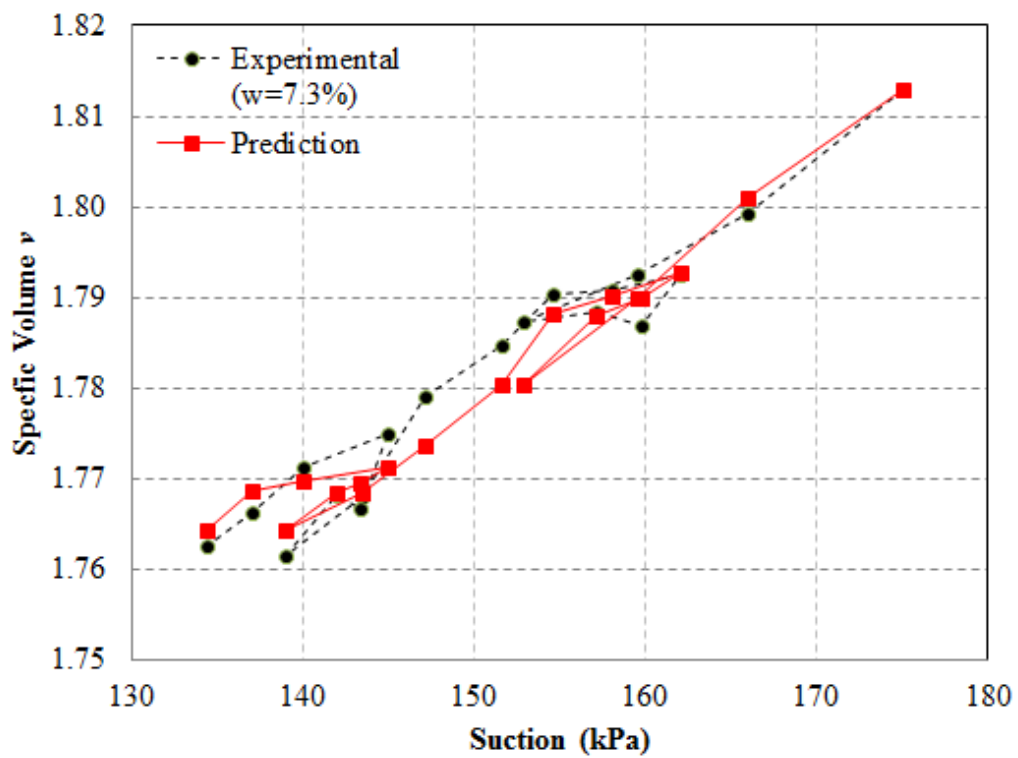


(b)

Figure 6.12 Comparison of Predicted and Experimental Results for an Undrained Test at  $w=7.6\%$ . (a) In the  $v$ - $p$  plane and (b) at in the  $v$ - $s$  plane

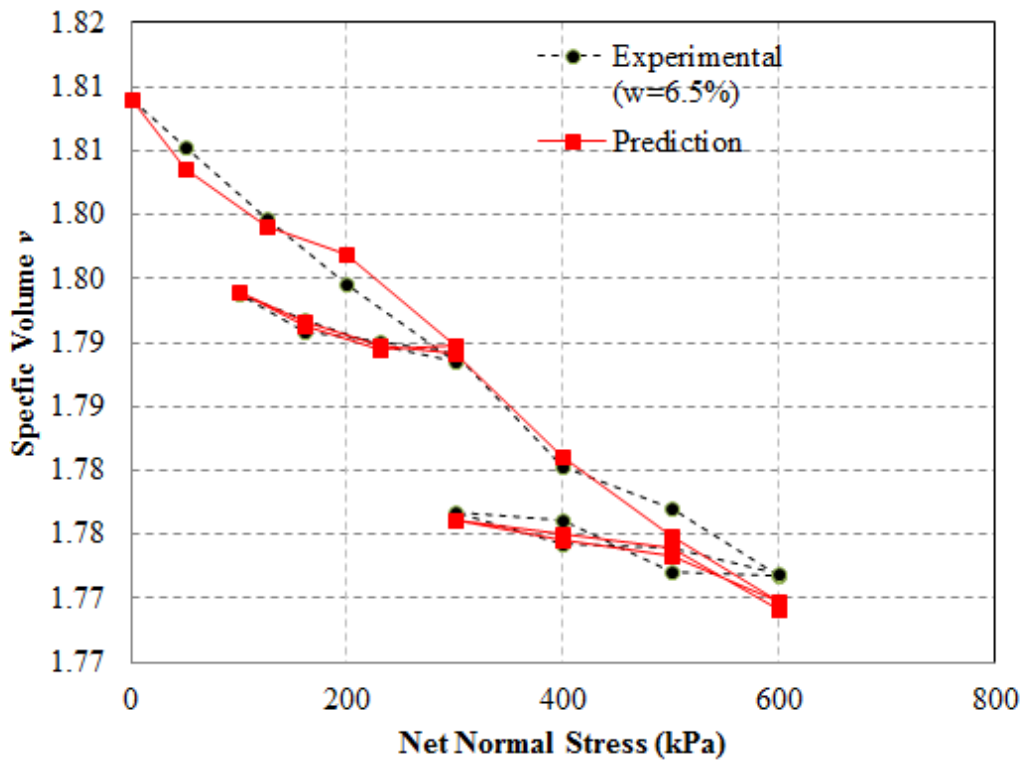


(a)

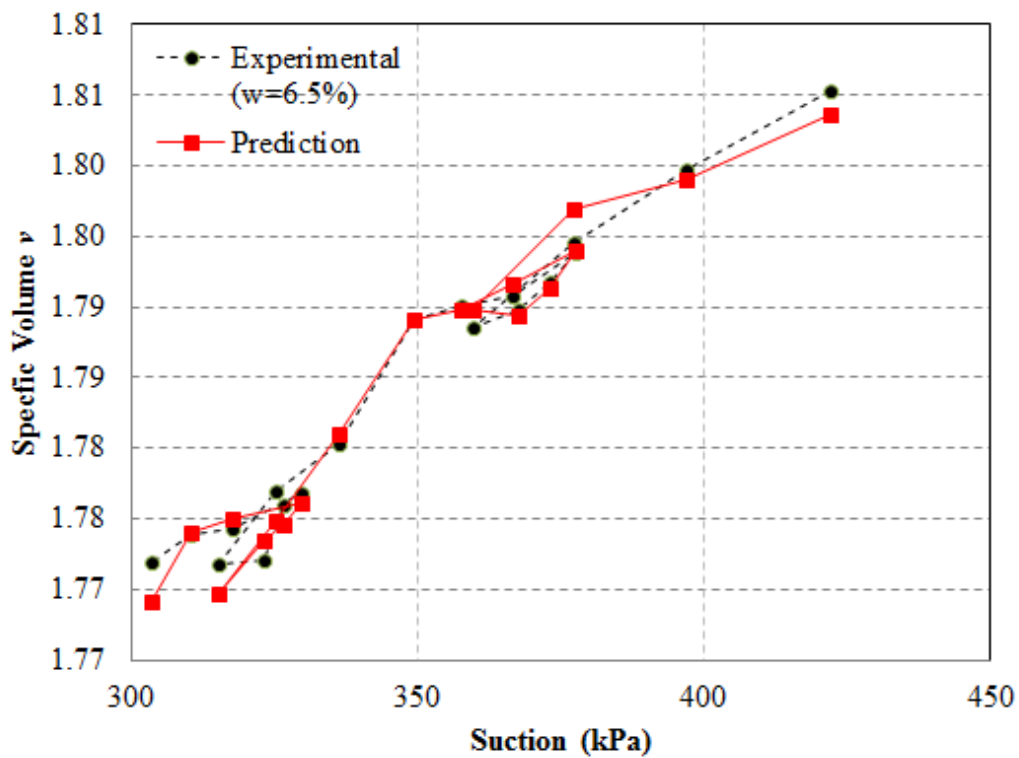


(b)

Figure 6.13 Comparison of Predicted and Experimental Results for an Undrained Test at  $w=7.3\%$ . (a) In the  $v$ - $p$  plane and (b) at in the  $v$ - $s$  plane



(a)



(b)

Figure 6.14 Comparison of Predicted and Experimental Results for an Undrained Test at  $w=6.5\%$ . (a) In the  $v$ - $p$  plane and (b) at in the  $v$ - $s$  plane

## CHAPTER VII

### CONCLUSIONS AND RECOMMENDATIONS

In this study, a method was developed to characterize constitutive behavior of unsaturated soil. Literature review on existing modeling methods were reviewed which included triaxial testing method, development of high suction tensiometers and existing elasto-plastic theories for unsaturated soils. In this study, undrained suction-monitored triaxial test was adopted to investigate unsaturated soil behavior during loading. By conducting undrained isotropic compression and shear tests on Fairbanks silt, constitutive model parameters were determined. To monitor soil suction change during loading, high-suction tensiometers were developed in this study based upon an EPXO pressure transducer from Measurement Specialties, Inc. Also, to perform the suction-monitored isotropic compression and triaxial tests by using conventional triaxial test apparatus for triaxial test on saturated soils, a new volume change measurement method was developed by integrating photogrammetry, optical-ray tracing, and least square estimation technique.

### CONCLUSIONS

The conclusions summarized from this study are listed as follows:

1. By reviewing existing suction-controlled triaxial test for constitutive modeling of unsaturated soil, it was found that drained suction-controlled triaxial test for modeling constitutive behavior of unsaturated soil was problematic. It is very time consuming to perform drained suction-controlled triaxial test low permeability of fine graded soil. Also, the test equipment (double-wall cell is most widely used) to perform the drained suction-controlled triaxial test is very expensive. All existing methods to measure soil volume change during testing have their limitations.
2. By using a miniature pressure transducer and minimizing the volume of the water reservoir, a new high-suction tensiometer was designed, fabricated, saturated, and calibrated to be used to monitor soil suction change during undrained compression and shear tests. For a fully saturated tensiometer with a 15 bar ceramic disc, the

maximum attainable suction that can be measured was around 1100 kPa which covered most volume range of natural soil.

3. A new image based method was developed to monitor soil volume change during isotropic compression and triaxial shear tests. This non-contact real 3D method was proved to be low cost and accurate.

4. In this study, to modeling constitutive behavior of unsaturated soils, undrained suction-monitored triaxial tests were performed on Fairbanks silt. These undrained tests significantly reduced the time (from one month to one day) needed to expel water out of the soil specimen for drained tests. Also, this undrained suction-monitored triaxial tests successfully overcome the limitations by using conventional drained suction-controlled triaxial test. Thus, undrained suction-monitored triaxial test can be used as an alternative to suction-controlled triaxial tests to investigate unsaturated soil behavior.

In conclusion, in this research we develop a system in which a conventional triaxial test apparatus for saturated soil can be used for triaxial test on unsaturated soil without modification. Both total volume change and strain localization can be determined. This significantly reduced the cost for testing unsaturated soils when compared with double-wall cell apparatus. It took only several hours (or at most one day) to complete one undrained test, while it takes several months to finish a suction controlled consolidated drained test. The cost for suction controlled double cell triaxial test equipment is also higher.

## **RECOMMENDATIONS**

1. A high-suction tensiometer was developed for the suction measurement during testing. For the 70 mm × 140 mm specimen used in this study, to ensure a good contact between specimen surface and the tensiometer, contact area on specimen surface was pre-flatted before tensiometer installation. The tensiometer is relatively big for small specimens (50 mm × 100 mm). It is recommended that smaller miniature pressure transducers be used for the fabrication of high-suction tensiometer. By using a smaller tensiometer, specimen size can be reduced to 50 mm × 100 mm which is consistent with previous studies. Also, by using smaller tensiometer, contact between soil specimen and tensiometer can be easily satisfied.

2. For a fully saturated tensiometer with a 15 bar ceramic disc, the maximum attainable suction that can be measured was around 1100 -2600 kPa. It is recommended that thermal coupled psychrometers be used for suction higher than 1500kPa.
3. A new image based method was proposed in this study to accurately monitor soil volume change during triaxial testing. This method excelled all existing volume change measurement methods in different ways. However, there is still room for improvements. In the existing method, it requires a number of measurement targets to be posted on soil specimen, which limited number of measurement points. It is recommended that in the future, the membrane on specimen surface be painted with different textures and image correlation method be used to determine the pixel positions of the texture on membrane. In this way, no measurement target is needed to be posted on the membrane. Also, a denser surface (point cloud), which represent the specimen surface, could be generated. Thus, more accurate measurement result could be reached. In addition, strain localization could be more accurately extracted from the shape change of the dense surface.
4. The application of this proposed image based measurement method could potentially be expanded to other multi-media situations.
5. In this study, undrained triaxial test was used to investigate unsaturated soil behavior during loading. Method has been developed to analyze the soil behavior under isotropic conditions based upon the modified state surface approach. There is a great need to extend the method to triaxial stress conditions of true-triaxial stress conditions.
6. The method developed was used to develop constitutive models for unsaturated soils. It seems that as similar approach can be developed to simplify the characterization and modeling of saturated soil behavior since saturated soil is a special case of unsaturated soils.

## REFERENCES

- Geiser, F., Laloui, L., and Vulliet, L. (2000). On the volume measurement in unsaturated triaxial test. In *Unsaturated soils for Asia*. Edited by H. Rahardjo, D.G. Toll, and E.C. Leong. A.A. Balkema, Rotterdam, Netherlands, 669–674.
- Bishop, A. W. & Donald, I. B. (1961). The Experimental Study of Partly Saturated Soil in the Triaxial Apparatus. *Proceedings of the 5th International Conference on Soils Mechanics*, Paris, Vol. 1, 13–21.
- Estabragh, A.R., Javadi, A.A. & Boot, J.C. (2004). Effect of compaction pressure on consolidation behavior of unsaturated silty soil. *Canadian Geotechnical Journal* 41, 540–550.
- Cui, Y.J. & Delage, P. (1996). Yielding and plastic behaviour of an unsaturated compacted silt. *Géotechnique* 46, No.2, 291–311.
- Ng, C.W.W., Zhan, L.T. & Cui, Y.J. (2002). A new simple system for measuring volume changes in unsaturated soils. *Canadian Geotechnical Journal* 39, No.3, 757–764.
- Zhang, X., Mavroulidou, M. & Gunn, M.J. (2011). A novel non-contacting laser displacement transducer technique for volume change measurements of unsaturated soils. *Unsaturated Soils* Edited by Antonio Gens CRC Press 2011, 751–756.
- Wheeler, S.J. (1986). *The stress-strain behavior of soils containing gas bubbles*. Ph.D. thesis, Oxford University, Oxford, U.K.
- Geiser, F. (1999). *Comportement mécanique d'un limon non saturé: étude expérimentale et modélisation constitutive*. Ph.D. thesis, Swiss Federal Institute of Technology, Lausanne, Switzerland.
- Scholey, G.K., Frost, D.J., Lo Presti, D.C.F., & Jamiolkowski, M. (1995). A Review of Instrumentation for Measuring Small Strains During Triaxial Testing of Soil Specimens. *Geotechnical Testing Journal* 18, No. 2, 137-156.
- Cunningham, M. R., Ridley, A. M., Dineen, K., and Burland, J. B., (2003). The Mechanical Behavior of A Reconstituted Unsaturated Silty Clay. *Géotechnique* 53, No. 2, 183–194.
- Sun, D. A., Matsuoka, H., & Xu, Y. F. (2004). Collapse Behavior of Compacted Clays In Suction-Controlled Triaxial Tests. *Geotechnical Testing Journal* 27, No. 4, 362–370.

- Blatz, J. & Graham, J. (2000). A System for Controlled Suction in Triaxial Tests. *Geotechnique* 50, No. 4, 465–469.
- Romero, E., Facio, J. A., Lloret, A., Gens, A., and Alonso, E. E. (1997). A New Suction and Temperature Controlled Triaxial Apparatus. *Proceedings of the 14th International Conference on Soil Mechanics and Foundation Engineering*, Hamburg, Vol. 1, 185–188.
- Macari, E.J., Parker, J.K., & Costes, N.C. (1997). Measurement of volume changes in triaxial tests using digital imaging techniques. *Geotechnical Testing Journal* 20, No.1, 103–109.
- White, D., Take, W., & Bolton, M. (2001). ‘Measuring soil deformation in geotechnical models using digital images and PIV analysis. *Proc., 10th Int. Conf. on Computer Methods and Advances in Geomechanics*, Tuscon, Ariz., Balkema, Rotterdam, The Netherlands, 997–1002.
- Desrues, J., Chambon, R., Mokni, M. & Mazerolle, F. (1996). Void ratio evolution inside shear bands in triaxial sand specimens studied by computed tomography. *Géotechnique* 46, No. 3, 529– 546.
- Gachet, P., Klubertanz G., Vulliet L. & Laloui L. (2003). Interfacial behaviour of unsaturated soil with smallscale models and use of image processing techniques. *Geotechnical Testing Journal* 26, No.1, 12–21.
- Romero, E. (1999). *Characterization and thermohydromechanical behaviour of unsaturated Boom clay: an experimental study*. Ph.D thesis. Barcelona: Universitat Politecnica de Catalunya.
- Li, R.X., Li, H.H., Zou, W.h., Smith, R.G. & Curran, T.A. (1997). Quantitive Photogrammetric Analysis of Digital Underwater Video Imagery. *IEEE Journal of Oceanic Engineering* 22, No.2, 364–375.
- Yamashita, A., Hayashimoto, E., Kaneko, T. & Kawata, Y. (2003). 3D Measurement of Objects in a Cylindrical Glass Water Tank with a Laser Range Finder. *Proceedings of the 2003 IRRR/RSJ, Intl. Conference on Intelligent Robots and Systems*, 1578–1583.
- Parker, J.K. (1987). Image processing and analysis for the mechanics of granular materials experiment. *ASME Proceedings of the 19<sup>th</sup> SE Symposium on System Theory*, Nashville, TN, March 2, ASME, New York.
- ASCE. (2009). “ASCE’s Infrastructure Report Card.” *ASCE News*, 34(2), 1-4.

- Wray, W.K. and Meyer, K.T. (2004). "Expansive clay soil... a widespread and costly geohazard." *GeoStrata*, ASCE GeoInstitute. Vol. 5, No. 4, October, pp. 24-25, 27-28.
- Spiker, E.C., and Gori, P.L. (2003). "National landslide hazards mitigation strategy – A framework for loss reduction." *United States Geological Survey Circular* 1244, 48 pp.
- Holt, M. (2008). "Civilian Nuclear Waste Disposal." *CRS report number RL33461*. Resources, Science, and Industry Division.
- Wong, T.T., Fredlund, D.G., and Krahn, J. (1998). "A numerical study of coupled consolidation in unsaturated soils." *Canadian Geotechnical Journal*, 35: 926–937.
- Zhang, X., and Briaud, J. L. (2006) "Mandel-Cryer effect for unsaturated soils." In: *Proc. of the 4th International Conference on Unsaturated Soils*, April 2006, Carefree, AZ, Geotechnical Special Publication No.147, pp. 2063–2074.
- Bishop, A. W., and Donald, I. B. (1961). "The experimental study of partly saturated soil in the triaxial apparatus." In: *Proc., 5th Int. Conf. Soil Mech.*, 1, 13–21.
- Delage, P (2002). "Experimental unsaturated soil mechanics." *Proc. 3rd Int. Conf. on Unsaturated Soils, UNSAT*, (3) 973-996, Juca JFT, De Campos TMP, Marino FAM, Recife, Brazil, Balkema.
- Alonso, E. E., Gens, A., and Josa, A. (1990). "A constitutive model for partially saturated soils." *Geotechnique*, 40(3), 405–430.
- Delage, P., and Graham, I. (1995). "State of the art report-understanding the behavior of unsaturated soils requires reliable conceptual models." In: *Proc. of 1st International Conference on Unsaturated Soils*, Paris, 3, pp. 1323–1256.
- Sheng, D., Sloan, S. W., and Gens, A. (2004). "A Constitutive model for unsaturated soils: thermomechanical and computational aspects." *Computational Mechanics*, 33(6), 453–465.
- Gens, A., Sánchez, M., and Sheng, D. (2006). "On constitutive modelling of unsaturated soils." *Acta Geotechnica*, 1(3), 137–147.
- Zhang, X. (2010). "Limitations to the use of stress path controlled consolidated drained tests in the characterization of unsaturated soils." Submitted to *Geotechnique*.
- Zhang, X., and Lytton, R. L. (2009). "A modified state surface approach on unsaturated soil behavior study (I): Basic concept." *Canadian Geotechnical Journal*, 46(5), 536–552.

Zhang, X., and Lytton, R. L. (2009). "A modified state surface approach on unsaturated soil behavior study (II): General formulation." *Canadian Geotechnical Journal*, 46(5), 553–570.

Zhang, X., and Lytton, R. L. (2009). "Modeling of coupled hydro-mechanical behavior using modified state surface approach." *Canadian Geotechnical Journal* (under second round review).

Zhang X., Liu, J. and Li, P. (2010). "A New Method to Determine the Shapes of Yield Curves for Unsaturated Soils," *Journal of Geotechnical and Geoenvironmental Engineering*, ASCE, Volume 136, Issue 1, pp. 239-247.

Zhang, X. (2010). "Use of Results from Undrained Tests for the Constitutive Modeling of Unsaturated Soils." *5th International Conference on Unsaturated Soils, September 6-8, 2010, Barcelona, Spain. Unsaturated soils- Alonso & Gens (eds)*. Vol. 2, pp. 1009-1014.

Zhang, X. (2010). "Analytical Solution of the Barcelona Basic Model." *Experimental and Applied Modeling of Unsaturated Soils* (Geotechnical Special Publication No. 202) *GeoShanghai 2010 International Conference, June 3-5, 2010, Shanghai, China*. pp.96-103.

Hilf, J. W. (1956). "An Investigation of Pore-Water Pressure in Compacted Cohesive Soils." *Ph.D. dissertation*, Technical Memorandum No. 654, U.S. Department of the Interior, Bureau of Reclamation, Design and Construction Division, Denver, Colorado.

Bishop, A. W., Alpan, I., Blight, G. E., and Donald, I. B. (1960). "Factors controlling the shear strength of partly saturated cohesive soil." In: *Proc., ASCE Research Conf. on Shear Strength of Cohesive Soils*, Univ. of Colorado, Boulder, CO, pp. 503–532.

Bishop, A. W., and Blight, G. E. (1963). "Some aspects of effective stress in saturated and unsaturated soils." *Geotechnique*, 13(3), 177–197.

Aitchison, G. D. (1961). "Relationship of moisture and effective stress functions in unsaturated soils." In: *Proc., Conference on Pore Pressure and Suction in Soils*. London: Butterworths, pp. 47–52.

Aitchison, G. D., and Donald, I. B. (1956). "Some preliminary studies of unsaturated soils." *Proc., 2nd Australia-New Zealand Conference on Soil Mechanics and Foundation Engineering*. Technical Publications for the New Zealand Institution of Engineers, Wellington, New Zealand, 192–199.

- Jennings, J. E., and Burland, J. B. (1962). "Limitations to the use of effective stresses in partly saturated soils." *Geotechnique*, 12(2), 125–144.
- Matyas, E. L., and Radhakrishna, H. S. (1968). "Volume change characteristics of partially saturated soils." *Geotechnique*, 18, 432–448.
- Fredlund, D. G., and Morgenstern, N. R. (1977). "Stress state variables for unsaturated soils." *ASCE J. Geotech. Eng. Div.*, GT5, 103, 447–466.
- Fredlund, D. G., and Morgenstern, N. R. (1976). "Constitutive relations for volume change in unsaturated soils." *Canadian Geotechnical Journal*, 13(3), 261–276.
- Fredlund, D. G. (1979). "Appropriate concepts and technology for unsaturated soils." *Canadian Geotechnical Journal*, 16(1), 121–139.
- Fredlund, D. G., and Hasan, J. U. (1979). "One-dimensional consolidation theory: Unsaturated soils." *Canadian Geotechnical Journal*, 16(3), 521–531.
- Dakshanamurthy, V., Fredlund, D. G., and Rahardjo, H. (1984). "Coupled three-dimensional consolidation theory of unsaturated porous media." Preprint of Papers: *5th Int. Conf. Expansive Soils, Institute of Engineers, Adelaide, South Australia, May*, pp. 99-104.
- Fredlund, D.G., and Xing, A. (1994). "Equations for the soil water characteristic curve." *Canadian Geotechnical Journal*, 31, 533-546.
- Fredlund, D. G., Morgenstern, N. R., and Widger, R. A.(1978). "The shear strength of unsaturated soils." *Can. Geotech. J.*, vol. 15, no. 3, pp. 313-321.
- Fredlund, D. G., and Rahardjo, H. (1993). *Soil Mechanics for Unsaturated Soils*. New York: John Wiley and Sons.
- Lloret, A., and Alonso, E. E. (1980). "Consolidation of unsaturated soils including swelling and collapse behavior." *Geotechnique*, 30(4), 449–477.
- Lloret, A., and Alonso, E. E. (1985). "State surfaces for partially saturated soils." In: *Proc. 11th Int. Conf. Soil Mech. Fdn. Engng.* San Francisco, 2, pp. 557–562.
- Vu, H.Q. and Fredlund, D.G. (2004), "The prediction of one-, two- and three-dimensional heave in shrink-swell soils." *Canadian Geotechnical Journal*, 41:713-737.
- Pereira, J.H.F. (1996). "Numerical analysis of the mechanical behavior of collapsing earth dams during first reservoir filling." *Ph.D dissertation*, University of Saskatchewan, Saskatoon, Canada.

- Alonso, E. E., Gens, A., and Hight, D. W. (1987). "Special problem soils-general report." In: *9th European Conference on Soil Mechanics*, Dublin, Vol. 3, pp. 1087–1146.
- Wheeler, S. J. (1996). "Inclusion of specific water volume within an elastoplastic model for unsaturated soil." *Can. Geotech. J.*, 33, 42–57.
- Gens, A., and Alonso, E. E. (1992). "A framework for the behavior of unsaturated expansive clays." *Canadian Geotechnical Journal*, 29, 1013–1032.
- Alonso, E. E., Gens, A., and Gehling, W. Y. Y. (1994). "Elasto-plastic model for unsaturated expansive soils." *Numerical models in geotechnical engineering*. Balkema, 11–18.
- Alonso, E. E., Vaunat, J., and Gens, A. (1999). "Modeling the mechanical behavior of expansive clays." *Engineering Geology*, 54(1–2), 173–183.
- Wheeler, S. J., and Sivakumar, V. (1995). "An elasto-plastic critical state framework for unsaturated soil." *Geotechnique*, 45(1), 35–53.
- Cui, Y. J., and Delage, P. (1996). "Yielding and plastic behaviour of an unsaturated compacted silt." *Geotechnique*, 46(2), 291–311.
- Dangla, O. L., Malinsky, L., and Coussy, O. (1997). "Plasticity and imbibition-drainage curves for unsaturated soils: a unified approach." In: *6th international conference on numerical models in geomechanics*, Montreal. Balkema, Rotterdam, pp 141–146.
- Bolzon, G., Schrefler, B. A., and Zienkiewicz, O. C. (1996). "Elastoplastic soil constitutive laws generalised to partially saturated states." *Geotechnique*, 46, 279–289.
- Geiser, F., Laloui, L., and Vulliet, L. (2000). "Modelling the behaviour of unsaturated silt." In: *Experimental Evidence and Theoretical Approaches in Unsaturated Soils*. Rotterdam: Balkema, pp. 155–175.
- Vaunat, J., Romero, E, and Jommi, C. (2000). "An elastoplastic hydro-mechanical model for unsaturated soils." In: *Experimental Evidence and Theoretical Approaches in Unsaturated Soils*. Rotterdam: Balkema, 121–138.
- Buisson, M. S. R., and Wheeler, S. J. (2000). "Inclusion of hydraulic hysteresis in a new elasto-plastic framework for unsaturated soils." In: *Experimental Evidence and Theoretical Approaches in Unsaturated Soils*. Balkema, Rotterdam, pp. 109–119.

- Jommi, C. (2000). "Remarks on the constitutive modelling of unsaturated soils." In: *Experimental Evidence and Theoretical Approaches in Unsaturated Soils*. Rotterdam: Balkema, pp. 139–153.
- Wheeler, S. J., Gallipoli, D., and Karstunen, M. (2002). "Comments on use of the Barcelona Basic Model for unsaturated soils." *Int. J. Numer. Anal. Meth. Geomech.*, 26, 1561–1571.
- Blatz, J. A., and Graham, J. (2003). "Elastic-plastic modeling of unsaturated soil using results from a new triaxial test with controlled suction." *Geotechnique*, 53(1), 113–122.
- Gallipoli, D., Gens, A., Sharma, R., and Vaunat, J. (2003). "An elastoplastic model for unsaturated soil incorporating the effects of suction and degree of saturation on mechanical behaviour." *Geotechnique*, 53, 123–135.
- Gallipoli, D., Wheeler, S. J., and Karstunen, M. (2003). "Modeling the variation of degree of saturation in a deformable unsaturated soil." *Geotechnique*, 53(1), 105–112.
- Wheeler, S. J., Sharma, R. S., and Buisson, M. S. R. (2003). "Coupling of hydraulic hysteresis and stress–strain behaviour in unsaturated soils." *Geotechnique*, 53, 41–54.
- Macari, E. J., Arduino, P., and Hoyos, L. R. (2003). "Constitutive modeling of unsaturated soil behavior under axisymmetric stress states using a stress/suction-controlled cubical test cell." *International Journal of Plasticity*, 19(10), 1481–1515.
- Tamagnini, R. (2004). "An extended Cam-clay model for unsaturated soils with hydraulic hysteresis." *Geotechnique*, 54, 223–228.
- Sheng, D., Sloan, S. W., Gens, A., and Smith, D. W. (2003a). "Finite element formulation and algorithms for unsaturated soils. Part I: theory." *Int. J. Numer. Anal. Meth. Geomech.*, 27, 745–765.
- Sheng, D., Smith, D. W., Sloan, S. W., and Gens, A. (2003b). "Finite element formulation and algorithms for unsaturated soils. Part II: verification and application." *Int. J. Numer. Anal. Meth. Geomech.*, 27, 767–790.
- Sheng, D., Fredlund, D. G., and Gens, A. (2008a) "A new modelling approach for unsaturated soils using independent stress variables." *Canad. Geotech. J.*, 45(4), 511–534.
- Sheng, D., Gens, A., Fredlund, D. G., and Sloan, S. W. (2008b). "Unsaturated soils: from constitutive modelling to numerical algorithms." *Computers and Geotechnics*, 35(6), 810–824.

- Sanchez, M., Gens, A., Guimaraes, L. D. N, and Olivella, S. (2005) “A double structure generalized plasticity model for expansive materials.” *Int. J. Numer. Anal. Meth. Geomech.*, 29, 751–787.
- Costa, L. M., and Alonso, E. E. (2009). “Predicting the Behavior of an Earth and Rockfill Dam under Construction.” *Journal of Geotechnical & Geoenvironmental Engineering*, Vol. 135,( Issue 7), pp851–862.
- Sun, D. A., Sheng, D. C., Xiang, L., and Sloan, S.W. (2008). “Elastoplastic prediction of hydro-mechanical behaviour of unsaturated soils under undrained conditions.” *Computers and Geotechnics*: 35: 845-852.
- Khalili, N., Geiser, F., and Blight, G. E. (2004). “Effective stress in unsaturated soils: review with new evidence.” *International Journal of Geomechanics, ASCE*. Vol. 4, No. 2, 115–126
- Gens, A. (1995). “Constitutive modelling: Application to compacted soil.” In: *Proc. of 1st International Conference on Unsaturated Soils*, Paris, 3, pp. 1179–1200.
- Wheeler, S. J., and Karube, D. (1995). “State of the art report-constitutive modeling.” In: *Proc. of 1st International Conference on Unsaturated Soils*, Paris, 3, pp. 1323–1356.
- Vaunat, J. (2005). “Elastoplastic framework to model unsaturated materials.” *1 st. MUSE School "Fundamentals of Unsaturated Soils"*. Barcelona, Spain, 1–2 June 2005. <http://muse.dur.ac.uk/>
- Zhang, X., and Lytton, R. L. (2008). “Discussion of a new modeling approach for unsaturated soils using independent stress variables.” *Canadian Geotechnical Journal*, 45(12), 1784–1787.
- Brackley, I. J. (1975). “Swell under load.” In: *Proc., 6th Regional Conference for Africa on Soil Mechanics and Foundation Engineering*, Durban, Vol. 1, pp. 65–70.
- Justo, J. L., Delgado, A., and Ruiz, J. (1984). “The influence of stresspath in the collapse-swelling of soils at the laboratory.” In: *5th International Conference on Expansive Soils*, Haifa, Vol. 1, pp. 201–208.
- Pousada, E. (1984). “Deformabilidad de arcillas expansivas bajo succión controlada.” *Doctoral Thesis*. Universidad Politécnica de Madrid, Spain.
- Dif, A. E., and Bluemel, W. F. (1991). “Expansive soils under cyclic drying and wetting.” Technical note, *Geotech. Test. J.*, 14(1), 96–102.

- Olivella, S., Carrera, J., Gens, A., and Alonso, E. E. (1994). "Nonisothermal multiphase flow of brine and gas through saline media." *Transp. Porous. Media*, 15, 271–293.
- Olivella, S., Gens, A., Carrera, J., and Alonso, E. E. (1996). "Numerical Formulation for a Simulator (CODE\_BRIGHT) for the Coupled Analysis of Saline Media." *Engineering Computations*, 13(7), 87–112.
- Collins, I. F., and Houlsby, G. T. (1997). "Application of thermomechanical principles to the modelling of geotechnical materials." *Proc. R. Soc. Lond., A* 453, pp. 1975–2001.
- Khalili, N., and Loret, B. (2001). "An elasto-plastic model for nonisothermal analysis of flow and deformation in unsaturated porous media: Formulation." *Int. J. Solids Struct.*, 38, 8305–8330.
- Gens, A., and Olivella, S. (2001). "THM phenomena in saturated and unsaturated porous media." *Revue franc, aise de ge ´nie civil* 5, 693–717.
- Lloret, A., Sanchez, M., Gens, A., Pintado, X., and Alonso, E. E. (2003). "Mechanical behavior of heavily compacted bentonite under high suction changes." *Geotechnique*, 53(1), 27–40.
- Sanchez, M., and Gens, A. (2005). "Final report on thermo-hydromechanical modelling." *Deliverable D19-3*, Febex II Project, EC Contract FIKW-CT-2000-00016.
- Rao, K. R. (2001). "Radioactive waste: The problem and its Management." *Current Science*, 81(12): <http://www.ias.ac.in/currsci/dec252001/1534.pdf>
- Lambe, T. W., and Whitman, R. V. (1969). *Soil Mechanics*. New York: John Wiley & Sons.
- Lu, N. (2008). "Is matric suction a stress variable?" *Journal of Geotechnical and Geoenvironmental Engineering, ASCE*, Volume 134, Issue7, pp.899-905.
- Khalili, N., Geiser, F., and Blight, G. E. (2004). "Effective stress in unsaturated soils: review with new evidence." *International Journal of Geomechanics, ASCE*. Vol. 4, No. 2, 115–126
- Sivakumar, V. (1993). "A critical state framework for unsaturated soil." *Ph.D. Thesis*, University of Oxford.
- Sharma, R. S. (1998). "Mechanical behaviour of unsaturated highly expansive clays." *D.Phil. thesis*, University of Oxford, UK.

- Das (2008). *Advanced Soil Mechanics*. 3<sup>rd</sup> Edition. Taylor & Francis Group
- Gallipoli, D., Toll, D., Augarde, C., Tarantino, A., Degennaro, V., Vaunat, J., Wheeler, S. J., and Mancuso, C. (2006), "The MUSE Network: sharing research expertise on unsaturated soils across Europe", *4th International Conference on Unsaturated Soils*, 2–6 April, Arizona, USA, ASCE, ISBN: 0-7844-0802-5, pp. 2075–2085.
- Ridley, A.M. and Burland, J.B. (1994). "Discussion: A new instrument for the measurement of soil moisture suction." *Geotechnique*, 44(3), 551 – 556.
- Ridley, A.M. and Burland, J.B. (1996). "A pore pressure probe for the in situ measurement of soil suction." In *Advances in Site Investigation Practice*, London, 1995, C. Craig (ed), Thomas Telford, London, pp. 510 – 520.
- Rahardjo, H., Heng, O. B., and Leong, E. C. (2004). "Shear strength of a compacted residual soil from consolidated drained and the constant water content triaxial tests." *Can. Geotech. J.* 41, 1–16.
- Thu, T. M., Rahardjo, H., and Leong, E. C. (2006). "Shear strength and pore-water pressure characteristics during constant water content triaxial tests." *Journal of Geotechnical and Geoenvironmental Engineering*, 132( 3), 411–419.
- Karube, D. (1986). "New concept of effective stress in unsaturated soil and its proving tests." *ASTM Symp. on Advanced Triaxial Testing of Soil and Rock*, ST 977, 539–552.
- Wheeler, S. J. (1986). "The Stress-Strain Behaviour of Soils Containing Gas Bubbles." D.Phil Thesis, University of Oxford.
- Mun, B. (2005). "Unsaturated soil behaviour under monotonic and cyclic stress states." *Ph.D. Dissertation*, Department of Civil Engineering, Texas A&M University, College Station, TX.
- Ridley, A.M. and Burland, J.B. (1993). "A new instrument for the measurement of soil moisture suction." *Geotechnique*, 43(2), 321 – 324.
- Ridley, A.M. and Burland, J.B. (1999). "Discussion: Use of tensile strength of water for the direct measurement of high soil suction." *Canadian Geotechnical Journal*, 36, 178 – 180.
- Tarantino, A. and Mongiovi, L. (2001). "Experimental procedures and cavitation mechanisms in tensiometer measurements." *Geotech. and Geol. Eng.* 19, 189 – 210

Tarantino, A., and Mongiovi, L. (2002). "Design and construction of a tensiometer for direct measurement of matric suction." In: *Proc. Third Int. Conf. on Unsaturated Soils*, Recife 1, 319–324.

Tarantino, A., and Mongiovi, L. (2003). "Calibration of tensiometer for direct measurement of matric suction." *Geotechnique*, 53(1), 137–141.

Rahardjo, H. and Leong, E. C. (2006). "Suction measurements." In: *Proc. of the 4th International Conference on Unsaturated Soils*, April 2006, Carefree, AZ, Geotechnical Special Publication No.147, pp. 81–104.

Briaud, J. L. and Zhang, X. and Moon, S. (2003). "The shrink test – water content method for shrink and swell predictions." *Journal of Geotechnical and Geoenvironmental Engineering, ASCE*. Vol. 129, No.7, pp.590-600.

Dafalias, D. F. and Hermann, L. R. (1982). "Bounding surface formulation of soil plasticity." *Soil mechanics - Transient and cyclic loads*, G. N. Pande and O. C. Zienkiewicz, eds., John Wiley & Sons, book chapter 10, 253–282.

*ABAQUS/Standard User's Manual* (2004). Version 6.8, Hibbit, Karlsson and Sorenson, Inc., Pawtucket, RI.

UPC (2002). *CODE BRIGHT, A 3-D program for thermo-hydro-mechanical analysis in geological media, USER's GUIDE*.

Zhang, X. (2004). "Consolidation theories for saturated-unsaturated soils and numerical simulations of residential buildings on shrink-swell soils." *Ph.D. Dissertation*, Department of Civil Engineering, Texas A&M University, College Station, TX.

Zhang, X., and Briaud, J. L. (2008). "A total stress-pore water pressure formulation of coupled consolidation analysis for saturated soils." *International Journal of Geotechnical Engineering*, 3, 171–185.

Zhang, X., Lytton, R. L., and Briaud, J. L. (2005). "Coupled Consolidation Theory For Saturated-Unsaturated Soils." Third Biot Conference on Poromechanics (Biot Centennial), University of Oklahoma, Norman, Oklahoma, USA, 2005. Abousleiman, Y., Cheng, A.H.-D., and Ulm, F.-J. (eds.) Pp.323-330.

Zhang, X. and Lytton, R. L. (2006). "Stress State Variables for Saturated and Unsaturated Soils." *Proceedings of the Fourth International Conference on Unsaturated Soils*, April 2006, Carefree, AZ, Geotechnical Special Publication No.147, pp. 2380-2391.

Zhang, X. and Lytton, R. L. (2007). "One Dimensional Consolidation for an Unsaturated Collapsible Soil." Presented at 85th Transportation Research Board Annual Meeting, Washington, D.C., January 2006.

Zhang, X. and Briaud, J. L. (2007). "Slab moment distributions of a residential building." 3rd Asian Conference on Unsaturated Soils, (UNSAT-ASIA 2007) Nanjing, China, April 2007.

Zhang, X. and Liu, J.(2008) "Numerical Simulation of Influence of Climatic Factors on Concrete Pavements Built on Expansive Soil." Geocongress 2008, New Orleans, LA.

Zhang, X., Chen, L., and Li, L. (2009). "Remarks on Constitutive Modeling of Unsaturated Soils" ASCE GeoHunan 2009, August 3-6, Hunan, China. ASCE Geotechnical Special Publication No.189. pp 13-19.

Zhang, X., Li, L., and Chen, L. (2009). "Impact of a Tree on a Residential Building on Expansive Soils: A Numerical Approach." International Foundation Engineering Congress and Equipment Expo '09 (ICFEE09) March 15-19, Orlando, FL ASCE Geotechnical Special Publication No.187. pp.614-621.

Zhang, X. and Lytton, R.L. (2009). "Discussion of Analysis of Deep Moisture Barriers in Expansive Soils. II: Water Flow Formulation and Implementation." ASCE International Journal of Geomechanics, Volume 9, Issue 2, pp 84-87.

Zhang, X. and Lytton, R.L. (2009). "Discussion of Analysis of Deep Moisture Barriers in Expansive Soils. I: Constitutive Model Formulation." ASCE International Journal of Geomechanics, Volume 9, Issue 2, pp 82-83.

Zhang, X. (2011). "Some Limitations in the Constitutive Modeling of Unsaturated Soils and Solutions." ASCE International Journal of Geomechanics (in press) [http://dx.doi.org/10.1061/\(ASCE\)GM.1943-5622.0000076](http://dx.doi.org/10.1061/(ASCE)GM.1943-5622.0000076).

Liu, J., Zhang, X., and Zollinger, D.G.. (2007). "A Two-Step Fracture Mechanics-based Approach for Assessing Early-age Delamination Distress." Transportation Research Record: Journal of the Transportation Research Board, No. 2016, pp. 76-84.

Zhang, X. and Briaud, J. L. (2008). "Coupled Water Content Method for Shrink and Swell Predictions." International Journal of Pavement Engineering Published on: 16 October 2008. DOI: 10.1080/10298430802394154.

Zhang, X. and Briaud, J. L. (2008). "Improved Approach to Construct Constitutive Surfaces for Stable-Structured Soils Covering Both Saturated and Unsaturated

Conditions” *Journal of Geotechnical and Geoenvironmental Engineering*, ASCE, Volume 134, Issue 6, pp. 876-882.

Zhang, X. and Briaud, J. L. “Three Dimensional Numerical Simulation of Residential Buildings on Expansive Soils in Response to Climatic Conditions: (I) Theory.” *Journal of Geotechnical and Geoenvironmental Engineering*, ASCE (under review).

Zhang, X. and Briaud, J. L. “Three Dimensional Numerical Simulation of Residential Buildings on Expansive Soils in Response to Climatic Conditions: (II) Application.” *Journal of Geotechnical and Geoenvironmental Engineering*, ASCE (under review).

**APPENDICES**

**Data Details**

## Appendix A

As discussed before, this method can be used for measurement of underwater object. Thus, if the 3D coordinates of the underwater object is known, this method could be used to back-calculate the refractive index of water. The following experiment was designed and performed to accurately determine the refractive index of the tap water. As shown in Figure A.1a, several measurement targets were glued to a stainless steel container. Targets at the edge of the container were used to build the coordinate system. The four targets at the bottom of the container were used to back-calculate the refractive index of water. Image capturing was performed first to determine the 3D coordinates of those targets by photogrammetric method. Then, as shown in Figure A.1b, container was filled with water and some more measurement targets were placed at the water surface. After this, image capturing was performed again.



(a) without water

(b) with water

Figure A.1 Container with and without water

For the second group of images, 3D coordinates of targets at water surface and edge of the water container can also be determined by photogrammetric method in the same coordinate system. The 3D coordinates of the four targets at the bottom of the container were determined from the first groups of images. 3D coordinates of the targets on top of the water were used to determine the water surface by least square method. Just like eyes of human being, the optical ray was also considered to be a straight line for camera. Thus, for an underwater object, two points which are the perspective center of the camera station and the object coordinates in the image can define an optical ray. Based on this, the optical rays for the underwater targets can be

determined. Thus, given the optical rays, interface and the object coordinates, the refractive index of the used tap water can be back-calculated to be 1.339 by least square method.

## Appendix B

To address the mathematic 3D coordinates calculation of a single measurement target, an example is presented for the drained triaxial test on the saturated sand specimen under a confining pressure of 100 kPa with no shear load. After photogrammetric analysis, all images obtained were idealized based on the calibration results as shown in Table 3.1. By processing image orientation, all camera positions and orientations for each image were determined as shown in Table B.1. Also, 3D coordinates for all measurement targets on acrylic cell in the global coordinate system were determined as shown in Table B.2. Based on these 3D coordinates, regression can be processed to determine the parameters in Equations 3.17 and 3.18 which represent the shape of the outside acrylic cell wall. Since the triaxial cell used for this test is brand-new and under a low confining pressure of 100 kPa, a function for the cylindrical shaped cell was used for the regression. The regression results are presented in Table B.3.

Table B.1 Camera stations

Picture ID	3D Coordinates (mm)			Rotation Angles (degree)		
	$X_s$	$Y_s$	$Z_s$	$\kappa$	$\omega$	$\varphi$
1	197.276	12.671	1529.483	0.031	-0.310	-0.628
2	189.256	305.667	1436.547	0.224	-12.353	-0.721
3	202.527	-371.998	1477.686	-0.264	14.336	-0.139
4	-753.624	3.638	1014.935	-0.422	-0.398	-43.464
5	1143.568	-1.716	978.379	-0.250	0.389	43.340
6	998.928	40.886	364.492	93.435	-3.600	64.250
7	843.272	36.984	570.823	92.018	-2.464	47.425
8	572.708	37.832	759.643	93.370	-2.122	25.857
9	234.078	41.455	825.782	90.812	-1.881	1.835
10	-87.136	47.815	770.335	89.413	-2.517	-20.339
11	-348.243	22.654	539.275	89.231	-1.834	-45.296
12	-463.997	37.553	349.359	86.898	-2.386	-61.632
13	-453.070	25.433	203.199	84.188	-5.752	-71.205
14	-632.377	22.055	-256.221	-86.809	-177.175	-73.174
15	-575.045	45.986	-384.515	-85.242	-174.212	-63.692
16	-438.337	57.128	-592.990	-86.081	-175.409	-47.752
17	-153.596	54.674	-732.853	-87.994	-176.539	-25.768
18	214.719	54.205	-776.019	-88.606	-176.643	1.093
19	493.724	53.223	-713.704	-90.575	-176.669	22.653
20	663.325	45.610	-600.446	-92.347	-175.869	37.840
21	805.201	48.968	-372.163	-93.715	-174.187	58.658
22	952.235	35.656	-299.874	83.981	-173.457	68.883
23	728.918	14.621	-1159.361	179.823	-178.706	25.231
24	202.433	30.046	-1196.233	179.981	-178.818	0.381
25	-440.738	27.049	-1024.387	-178.337	-178.425	-32.127

Table B.2 3D coordinates for measurement points on cell wall (1)

Point ID	3D Coordinates (mm)			Point ID	3D Coordinates (mm)		
	x	y	z		x	y	z
760	260.989	98.835	-68.586	809	125.430	101.671	-47.225
761	254.144	98.850	-75.092	810	129.913	101.681	-55.457
762	246.589	98.855	-80.759	811	135.415	101.689	-63.048
780	282.874	99.205	1.141	812	159.382	101.360	60.791
782	283.517	99.103	-17.825	814	144.236	101.657	49.744
783	282.278	99.026	-27.242	815	137.644	101.819	42.953
784	240.240	100.881	61.624	816	195.467	101.070	71.594
785	248.311	100.698	56.762	817	186.097	101.160	70.526
786	255.716	100.497	50.908	818	176.877	101.253	68.379
787	262.398	100.291	44.293	819	168.001	101.323	65.163
788	266.337	98.178	-62.382	820	248.032	45.950	56.806
789	271.741	98.234	-54.676	821	248.163	36.502	56.644
790	276.246	98.301	-46.433	822	248.283	27.060	56.473
791	279.619	98.318	-37.662	823	248.444	17.582	56.356
792	281.034	99.004	9.982	824	141.891	101.318	-70.270
793	278.151	99.286	18.923	825	148.895	100.931	-76.554
794	274.253	99.575	27.501	826	156.602	100.523	-82.004
795	269.280	99.795	35.545	828	202.408	99.170	-94.610
796	238.781	98.583	-85.216	829	192.980	99.432	-94.337
797	230.173	98.670	-89.065	830	183.695	99.671	-92.974
798	221.150	98.744	-91.969	831	174.643	99.871	-90.537
799	211.918	98.818	-93.885	832	232.467	100.606	65.321
800	131.374	102.129	34.818	833	223.597	100.773	68.432
801	126.592	102.155	26.665	834	214.434	100.963	70.514
802	122.759	102.184	18.034	835	205.045	101.129	71.534
803	119.936	102.228	8.987	836	247.270	86.918	57.382
804	118.008	102.258	-0.721	837	247.346	77.493	57.338
805	117.364	102.202	-10.130	838	247.391	68.020	57.257
806	117.840	102.164	-19.584	839	247.439	58.584	57.177
807	119.310	102.099	-28.876	840	152.820	-24.619	-79.677
808	121.964	101.633	-38.444	841	152.876	-15.170	-79.751

Table B.2 3D coordinates for measurement points on cell wall (2)

Point ID	3D Coordinates (mm)			Point ID	3D Coordinates (mm)		
	x	y	z		x	y	z
842	152.983	-5.723	-79.744	873	265.160	67.556	-63.623
843	153.055	3.758	-79.786	874	265.237	76.952	-63.577
844	152.521	45.787	-79.333	875	265.277	86.398	-63.495
845	152.541	36.371	-79.319	876	152.171	-37.253	-79.275
846	152.501	26.924	-79.402	877	152.160	-46.676	-79.304
847	152.501	17.525	-79.423	878	152.076	-56.153	-79.441
848	248.098	-23.452	56.513	879	152.068	-65.588	-79.473
849	248.116	-14.016	56.482	880	133.760	-25.674	38.277
850	248.154	-4.628	56.470	881	133.728	-16.227	38.168
851	248.247	4.760	56.540	882	133.674	-6.777	38.068
852	153.073	58.378	-79.625	883	133.604	2.703	38.004
853	153.064	67.766	-79.666	884	133.865	16.522	38.238
854	153.112	77.166	-79.642	885	133.740	25.938	38.096
855	153.130	86.613	-79.661	886	133.632	35.384	37.934
856	247.745	-65.972	56.619	887	133.523	44.794	37.795
857	247.905	-56.544	56.567	888	133.573	57.617	37.866
858	248.044	-47.069	56.474	889	133.449	67.042	37.734
859	248.215	-37.628	56.415	890	133.341	76.428	37.590
860	264.745	-38.032	-64.055	891	133.279	85.805	37.409
861	264.672	-47.485	-64.078	892	134.084	-66.610	38.802
862	264.626	-56.925	-64.108	893	133.957	-57.224	38.706
863	264.568	-66.404	-64.138	894	133.911	-47.821	38.554
864	265.135	4.543	-63.644	895	133.843	-38.376	38.411
865	265.048	-4.875	-63.651	896	247.240	-78.676	56.968
866	265.032	-14.332	-63.707	897	254.743	-78.572	51.249
867	265.031	-23.726	-63.773	898	261.559	-78.457	44.641
868	265.007	46.167	-63.829	899	267.534	-78.342	37.360
869	264.916	36.735	-63.884	900	135.997	-78.533	41.167
870	264.857	27.350	-63.973	901	130.301	-78.700	33.641
871	264.785	17.965	-64.046	902	125.566	-78.884	25.477
872	265.143	58.168	-63.717	903	121.921	-79.129	16.728

Table B.2 3D coordinates for measurement points on cell wall (3)

Point ID	3D Coordinates (mm)			Point ID	3D Coordinates (mm)		
	<i>x</i>	<i>y</i>	<i>z</i>		<i>x</i>	<i>y</i>	<i>z</i>
904	203.716	-79.577	71.507	928	135.703	-79.052	-64.090
905	194.300	-79.383	71.341	929	142.028	-79.159	-71.093
906	184.924	-79.220	70.099	930	149.114	-79.262	-77.246
907	175.822	-79.054	67.794	931	156.858	-79.366	-82.550
908	166.545	-78.866	64.385	932	193.898	-79.076	-94.460
909	158.134	-78.685	60.220	933	184.583	-79.059	-93.226
910	150.366	-78.494	54.914	934	175.452	-79.053	-90.988
911	143.192	-78.333	48.844	935	166.636	-79.084	-87.738
912	239.819	-79.088	61.424	936	202.714	-79.519	-94.706
913	231.323	-79.107	65.442	937	212.106	-79.356	-93.886
914	222.435	-79.128	68.504	938	221.381	-79.214	-91.988
915	213.200	-79.152	70.514	939	230.343	-79.094	-89.021
916	119.146	-78.805	7.204	940	282.279	-78.191	2.088
917	117.460	-78.823	-2.083	941	280.146	-78.382	11.241
918	116.943	-78.835	-11.559	942	277.028	-78.574	20.179
919	117.517	-78.855	-20.996	943	273.016	-78.757	28.789
920	238.705	-78.991	-85.342	944	279.715	-79.089	-35.730
921	246.801	-78.936	-80.485	945	281.939	-78.935	-26.565
922	254.238	-78.892	-74.656	946	283.200	-78.750	-17.233
923	261.065	-78.836	-68.081	947	283.291	-78.599	-7.808
924	119.104	-79.205	-30.281	948	267.630	-78.695	-60.255
925	121.672	-79.087	-39.365	949	272.634	-78.953	-52.274
926	125.323	-78.986	-48.086	950	276.757	-79.211	-43.839
927	130.008	-78.912	-56.227				

Table B.3 Regression parameters for acrylic cell wall

A	B	C	$X_r$	$Y_r$	$Z_r$	$\kappa$ (deg.)	$\omega$ (deg.)	$\varphi$ (deg.)
0	0	6915.455	200.674	100.000	2.526	0.136	-0.056	-4.008

The measurement point on soil specimen surface with an ID number of 177 was used as an example to describe the calculation for its 3D position. After orientation for each camera station, pixel positions for point 177 in the corresponding images (after idealization) could be determined as shown in Table B.4. A total number of eight

images were found to have point 177. Then, based upon Equations 3.12 and 3.13, 3D coordinates of point 177 on each image plane in the global coordinate system can be calculated from their pixel positions by using calibration results from Table 3.1 (calibration 2). Since the camera positions for each pictures was known as shown in Table B.1, by connecting the camera station with the corresponding point on its image plane, all the unit vectors  $\vec{i}$  for each optical ray can be determined as shown in Table B.4.

Table B.4 Point information on each corresponding image

Point ID	Picture ID	Pixel Position (Pixel)		3D Coordinates (mm)			Vector $\vec{i}$		
		$m_o$	$n_o$	$x$	$y$	$z$	$\alpha_a$	$\beta_a$	$\gamma_a$
177	1	2502.93	1610.76	198.058	12.489	1476.086	0.0146	-0.0034	-0.9999
	2	2552.38	1566.75	190.371	294.567	1384.320	0.0209	-0.2078	-0.9779
	3	2557.29	1557.91	203.128	-358.416	1426.040	0.0113	0.2543	-0.9671
	6	2334.50	1205.18	949.914	38.771	343.277	-0.9170	-0.0396	-0.3969
	8	2419.61	1654.54	549.531	35.834	711.573	-0.4340	-0.0374	-0.9001
	9	2356.86	1774.29	233.091	39.175	772.430	-0.0185	-0.0427	-0.9989
	10	2362.24	2018.21	-66.758	45.115	721.006	0.3813	-0.0505	-0.9231
	11	2485.39	2156.30	-308.432	21.584	503.600	0.7446	-0.0200	-0.6672

Since the parameters needed to determine the shape and location of the acrylic cell wall was determined from the regression as shown in Table B.3, combined with the optical rays (defined by the corresponding camera station and unit vector  $\vec{i}$ ), the distance  $l_i$  between the camera station and the interception for each ray can be computed as shown in Table B.5. Then, the 3D coordinates of the interceptions can be determined which are also shown in Table B.5. The normal vector  $\vec{n}_1$  for the eight interceptions can be determined through Equation 3.21 and the results are shown in Table B.5. By applying optical ray tracing technique as addressed before, optical rays  $\vec{r}_1$  after refraction can be determined as presented in Table B.5. Repeating the ray tracing process, the eight optical rays  $\vec{r}_2$  after two times of refractions are presented in Table B.6. By conducting the least square estimation as shown in Equation 3.25, a best estimation for point 177 was found in Table B.7. As presented in Table B.7, all

the eight distances  $d$  between the estimated point and optical ray after two times of refractions are less than 0.04 mm which indicated an accurate estimation.

Table B.5 First optical-ray tracing (air to acrylic cell) results

Interception point			$l_1$	Normal vector $\vec{n}_1$			Vector $\vec{r}_1$		
$x$	$y$	$z$		$\alpha_{n1}$	$\beta_{n1}$	$\gamma_{n1}$	$\alpha_{r1}$	$\beta_{r1}$	$\gamma_{r1}$
218.633	7.697	69.631	1460.017	-0.2195	0.0015	-0.9756	-0.0638	-0.0018	-0.9980
218.449	15.160	69.683	1397.699	-0.2171	0.0015	-0.9762	-0.0600	-0.1389	-0.9885
218.912	-1.703	69.553	1456.099	-0.2231	0.0015	-0.9748	-0.0690	0.1711	-0.9828
261.225	9.053	45.191	804.470	-0.7316	0.0025	-0.6817	-0.8657	-0.0257	-0.4998
236.922	8.889	63.203	773.705	-0.4394	0.0019	-0.8983	-0.4358	-0.0244	-0.8997
220.076	9.117	69.295	757.307	-0.2368	0.0015	-0.9716	-0.0917	-0.0281	-0.9954
201.495	9.564	71.653	756.919	-0.0134	0.0010	-0.9999	0.2511	-0.0335	-0.9674
177.257	8.532	68.380	705.756	0.2781	0.0002	-0.9606	0.6012	-0.0133	-0.7990

Table B.6 Second optical-ray tracing (air to acrylic cell) results

Interception point			$l_2$	Normal vector $\vec{n}_2$			Vector $\vec{r}_2$		
$x$	$y$	$z$		$\alpha_{n2}$	$\beta_{n2}$	$\gamma_{n2}$	$\alpha_{r2}$	$\beta_{r2}$	$\gamma_{r2}$
218.005	7.679	59.813	9.838	-0.2399	0.0015	-0.9708	-0.0434	-0.0022	-0.9991
217.853	13.780	59.860	9.938	-0.2377	0.0015	-0.9713	-0.0390	-0.1548	-0.9872
218.224	0.004	59.747	9.978	-0.2432	0.0015	-0.9700	-0.0482	0.1903	-0.9805
252.573	8.796	40.196	9.993	-0.7105	0.0024	-0.7037	-0.8803	-0.0289	-0.4736
232.693	8.651	54.473	9.703	-0.4398	0.0019	-0.8981	-0.4354	-0.0274	-0.8998
219.175	8.840	59.516	9.825	-0.2558	0.0016	-0.9667	-0.0726	-0.0315	-0.9969
204.035	9.224	61.870	10.114	-0.0497	0.0011	-0.9988	0.2856	-0.0375	-0.9576
183.556	8.392	60.007	10.479	0.2290	0.0004	-0.9734	0.6407	-0.0149	-0.7677

Table B.7 Least square estimation for the point

Point ID	Picture ID	$d$ (mm)	3D Coordinates (mm)		
			$x$	$y$	$z$
177	1	0.021	216.321	7.611	20.694
	2	0.029			
	3	0.032			
	6	0.005			
	8	0.028			
	9	0.026			
	10	0.008			
	11	0.040			